Aeromechanics of Coaxial Rotor Helicopters using the Viscous Vortex Particle Method

by

Puneet Singh

A dissertation submitted in partial fulfillment
of the requirements for the degree of
Doctor of Philosophy
(Aerospace Engineering)
in The University of Michigan
2020

Doctoral Committee:

Professor Peretz P. Friedmann, Chair
Professor Carlos E. S. Cesnik
Professor Bogdan I. Epureanu
Associate Professor Krzysztof J. Fidkowski

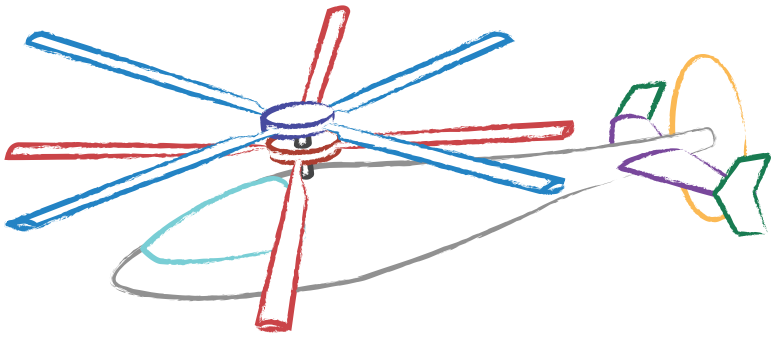

Puneet Singh

punsingh@umich.edu

ORCID iD: 0000-0001-6015-9601

ਦੇਇ ਮੁਹਾਰ ਲਗਾਮੁ ਪਹਿਰਾਵਉ ॥
ਸਗਲ ਤਜੀਨੁ ਗਗਨ ਦਉਰਾਵਉ ॥੧॥

ਗਉੜੀ ਕਬੀਰ ਜੀ - ਪੰਨਾ ੩੨੯ - ਸ਼੍ਰੀ ਗੁਰੂ ਗ੍ਰੰਥ ਸਾਹਿਬ ਜੀ

I have grasped the reins (of love) and attached the bridle (on my mind);
Abandoning everything, I now ride through the skies (in Your praise).

Gauri Kabir Ji - Page 329 - Sri Guru Granth Sahib Ji

Acknowledgments

For many years, I have thought of my research as an individual pursuit of knowledge towards understanding a small set of physical laws that govern the behavior of an exotic flying machine. Looking back, it is impossible to ignore the role of all those who have supported me and provided a nourishing environment for my intellectual and personal growth.

My interest in coaxial helicopters began a decade ago, when I received a toy coaxial helicopter as a gift from my father JP Singh. That toy led me to publish my first journal paper while still an undergraduate, writing a masters thesis, traveling to Japan for a research internship and now completing a doctorate in the field. I owe my interest in engineering and mathematics to him. My mother, Ravinder Kaur, instilled in me a love of reading and scientific curiosity, which has helped me remain steadfast and sincere towards my research. My parents and brother have faced major health crises and financial insecurity without me by their side and let me pursue my passion. I am indebted to them for their unwavering and steadfast support for my education and career.

Years of physical separation from one's family takes a huge toll. I regret being unable to attend the last rites of my paternal grandparents, Prakash Kaur and Sant Singh. Their personal history as refugees surviving the the partition of the Indian subcontinent in 1947, Bangladesh Liberation War in 1971, and the brutal anti-Sikh genocide in 1984, has inspired me to persevere among all odds. I never had the opportunity to spend time with my maternal grandparents, Kartar Kaur and Pratap Singh, during their lives. Their values have lived on in their children and grand children. My eldest maternal uncle Dr. Pritam Singh was the first to obtain a doctorate in the family and he built a fruitful life and family as an immigrant in New Zealand and the US. I am grateful to the rest of my extended family in the US, my uncles Harbhajan Singh and Dr. GP Singh, aunts, cousins, nieces and nephews, who are a source of immense joy and laughter during my short visits.

The current pandemic has made it clear how physical proximity with your friends and family are so crucial to our functioning as a society. I am grateful to Sriram Ganesan, a fellow aerospace enthusiast, friend and mentor who encouraged me to come join him in Michigan. The Sikh community in Michigan welcomed me into its homes, and provided me with well-needed nutritional and spiritual nourishment. I am honored to have shared an innumerable number of laughs and tears with my friends from the Michigan Branch of the Telluride Association, Aixa, Anurag, Chris, Deja, James, Koustav, Makenzie, Marianna, Nadiya, Natasha, Peiyu, Raghav, Robert, and so many others. My friends in the Aerospace department, Adam, Alasdair, Alex, Anil, Anna, Austin, Corey, Chris, Christina, Cristina, Devina, Eirikkur, Gurmeet, John, Leanne, Marco, Mike, Neil, Nomita, Patricia, Pedro, Prince, Renato, Shamsheer, Shardul, Siddhartha, Vishnu, Yingqian and many others, have made my time here memorable. Abhinav, Ashwani, Daning, Eric, Michael, Nicolas and Ryan were excellent lab and office mates. I am especially grateful for Abhinav's happy-go-lucky attitude, Ashwani's calming support, Daning's perfectionist thinking, and Ryan's patience with my crazy antics.

I am grateful to Profs. John Shaw, Veera Sundaraghavan and Tony Waas, who have been incredible mentors and have taught me by example how to be good teachers. Prof. Ken Powell has been an exceptional ally in diversity, equity and inclusion affairs in the department. I am also grateful to Profs. Duraisamy, Krasny, Martins, Roe, Scruggs and Veerapaneni who I learned a lot from through their courses and research. I am thankful to my committee members, Profs. Carlos Cesnik, Bogdan Epureanu and Krzysztof Fidkowski. I am in awe of Prof. Cesnik's incredible teaching skills, breadth of aerospace research, and his passion for flying. Prof. Fidkowski and his students have always been role models as researchers for me. The departmental staff: Chris, Dave, Denise, Gwen, Jessica, Kathy, Kim, Sam, Terry, Tom and the custodians, do an incredible job in keeping the department running, and I miss having the opportunity to personally thank them for their service to the students.

The acknowledgements will not be complete without my sincere gratitude towards the patient and unwavering support of Prof. Peretz Friedmann. Prof. Friedmann gave me an incredible opportunity to work on a topic of my choosing, with the freedom to find my own way and make my own mistakes. His unrelenting attitude towards perfection and precision has had an immense effect on my research and writing. I have been able to pursue my research though financial support provided by the FXB

Center for Rotary and Fixed Wing Air Vehicle Design (FXB-CRFWAD) at the University of Michigan.

The PhD journey is not easy, especially being someone who is visibly distinct as an observant Sikh. There are many layers of ignorance, bias and prejudice, both implicit and explicit, which I have learned to navigate in the academic environment. Many others before me have faced harder challenges, and have paved the way to create a supportive environment that I was able to enjoy. I owe a profound gratitude to them, whom I have never known or may have forgotten.

Finally, I would like to acknowledge the divinity in the laws of the universe that have led me to this milestone.

Table of Contents

List of Figures

FIGURE

List of Tables

TABLE

List of Appendices

APPENDIX

List of Abbreviations

2D	two-dimensional.
3D	three-dimensional.
AAS	Armed Aerial Scout.
ABC	Advancing Blade Concept.
AFDD	Aero-Flight Dynamics Directorate.
ARRIM	Active-Receiving Rotor Inflow Model.
AVCS	Active Vibration Control System.
AVINOR	Active VIbration and NOise Reduction.
BEMT	Blade Element Momentum Theory.
BVI	Blade Vortex Interaction.
CAMRAD II	Comprehensive Analytical Model of Rotorcraft Aerodynamics and Dynamics.
CD&RR	Competitive Demonstration and Risk Reduction.
CFD	Computational Fluid Dynamics.
CFD-RFA	CFD based Rational Function Approximation.
CG	center of gravity.
CHARM	Comprehensive Hierarchical Aeromechanics Rotorcraft Model.
CL	collocation point.
CSD	Computational Structural Dynamics.
DES	Detached Eddy Simulation.
DL-RFA	Doublet-Lattice based Rational Function Approximation.
DoD	Department of Defense.
DS	dynamic stall.
FAA	Federal Aviation Administration.
FARA	Future Attack Reconnaissance Aircraft.
FBW	Fly By Wire.
FE	Finite Element.
FFT	Fast Fourier Transform.
FGT	Fast Gauss Transform.
FLRAA	Future Long-Range Assault Aircraft.
FM	Figure of Merit.
FMM	Fast Multipole Method.
FVL	Future Vertical Lift.
FVW	Free Vortex Wake.
GENUVP	GENeral Unsteady Vortex Particle.

GPU	Graphics Processing Units.
GSL	GNU Scientific Library.
HALE	High Altitude Long Endurance.
HPC	High Performance Computing.
JMR	Joint Multi Role.
LE	leading edge.
LES	Large Eddy Simulation.
LO	Lift Offset.
MFW	Maryland Free Wake.
NASA	National Aeronautics and Space Administration.
ODE	ordinary differential equations.
OpenMP	Open Multi-Processing.
OVERFLOW	Overset Grid CFD Flow Solver.
PCHIP	piecewise cubic hermite interpolating polynomial.
PDE	partial differential equations.
PIV	Particle Image Velocimetry.
PRASADUM	Parallelized Rotorcraft comprehensive Analysis for Simulation And Design.
PSE	Particle Strength Exchange.
QC	quarter chord.
RANS	Reynolds Averaged Navier Stokes.
RCAS	Rotorcraft Comprehensive Analysis System.
RFA	rational function approximation.
RK4	fourth-order Runge-Kutta method.
ROM	reduced order model.
RotUNS	Rotor Unstructured Navier-Stokes.
RPM	revolutions per minute.
SAS	Stability Augmentation System.
SIAM	Society for Industrial and Applied Mathematics.
SMR	single main rotor.
STM	state transition matrix.
TE	trailing edge.
TVD	Total Variation Diminishing.
UAM	Urban Air Mobility.
UMARC	University of Maryland Advanced Rotorcraft Code.
UVLM	Unsteady Vortex Lattice Method.
VPM	Vortex Particle Method.
VTM	Vorticity Transport Model.
VTOL	Vertical Take-Off and Landing.
VVPM	Viscous Vortex Particle Method.
X2TD	$X2^{TM}$ Technology Demonstrator.

List of Symbols

Roman letters

a	offset between feathering axis and mid-chord
a_d	empirical parameter in ONERA-DS model
$a_{F/L/T}$	generalized flap/lag/torsional degree of freedom
$\boldsymbol{a}$	generalized structural degrees of freedom vector
$\boldsymbol{a}_r$	acceleration of a point at $\boldsymbol{r}$
A	area of cross section
A_1	XH-59A lateral control parameter
$\boldsymbol{A}$	angular impulse of a system of vortex particles
$[\boldsymbol{A}_a]$	state-space matrix used in CFD-RFA
$\boldsymbol{\mathcal{A}}_k$	k^{th} column vector of the linearized system matrix
$[\boldsymbol{\mathcal{A}}]$	linearized system matrix
b	airfoil semi-chord
B_1	XH-59A longitudinal control parameter
c	airfoil chord
$C(k)$	Theodorsen's lift deficiency function
C_d	airfoil drag coefficient
C_{d_f}	flat plate drag coefficient
C_{D_F}	fuselage drag coefficient
ΔC_d^k	change in k$^{\text{th}}$ airfoil coefficient due to static stall
C_F	rotor hub force coefficient
C_l	airfoil lift coefficient
C_{l_α}	airfoil lift curve slope
C_m	airfoil moment coefficient
C_M	rotor hub moment coefficient
C_{q_0}	ideal helicopter torque coefficient
C_T	rotor thrust coefficient
C_W	helicopter weight coefficient
$\boldsymbol{C}$	hub center
$\boldsymbol{CL}$	collocation point
$\boldsymbol{C}_p$	vector location of propulsor center
$[\boldsymbol{C}_n]$	n$^{\text{th}}$ RFA coefficient matrices
d	skin thickness
d_p	distance between neighboring vortex particles
$\boldsymbol{d}$	displacement vector between vortex filament endpoint and $\boldsymbol{r}$

D_f	drag force on a fuselage
$[\boldsymbol{D}_{a/d}]$	state-space matrix used in ROM
$\mathcal{D}$	blade sectional drag force
e	hub offset distance
e_d	empirical parameter in ONERA-DS model
$\widehat{\boldsymbol{e}}$	unit vector in k^{th} dimension
E	kinetic energy of a flow field
E_σ	semi-regularized kinetic energy of a flow field
$E_{\sigma,f}$	semi-regularized kinetic energy of a divergence-free flow field
EI	bending stiffness
$[\boldsymbol{E}_{a/d}]$	state-space matrix used in CFD-RFA
$\mathcal{E}$	enstrophy of a flow field
$\mathcal{E}_\sigma$	semi-regularized enstrophy of a flow field
$\mathcal{E}_{\sigma,f}$	semi-regularized enstrophy of a divergence-free flow field
f	fuselage area
fC_{d_f}	equivalent fuselage flat plate area
$\boldsymbol{f}$	generalized force vector
F	revolution averaged rotor hub forces
$F_\sigma(s)$	vortex particle regularized vortex stretching function
$\boldsymbol{F}_{a/d}$	vector of attached/separated flow aerodynamic loads
$\boldsymbol{F}_b$	net force at hub due to blade
$\boldsymbol{F}_h$	net force at hub due to rotor
$\boldsymbol{g}$	non-linear system of governing equations of rotor blade aeroelasticity
$\boldsymbol{g}_d$	state-space vector used in ONERA-DS
$\boldsymbol{G}_{a/d}$	vector of attached/separated flow blade bound circulation
$\boldsymbol{\mathcal{G}}$	Laplace transform of generalized force
GJ	torsional stiffness
h	vertical separation between upper and lower rotor
h_d	empirical parameter in ONERA-DS model
h_{res}	resolution parameter for vortex particle discretization
$h_{u/l}$	vertical distance between helicopter CG and upper/lower rotor hub
$\boldsymbol{h}$	generalized motion vector
$\mathcal{H}$	helicity of a flow field
$\mathcal{H}_\sigma$	semi-regularized helicity of a flow field
$\boldsymbol{\mathcal{H}}$	Laplace transform of generalized motion
i	unit imaginary number $\sqrt{-1}$
i	index used for summations
$\hat{\boldsymbol{i}}$	unit vector along $\boldsymbol{x}$ axis
I	area moment of inertia
I_m	mass moment of inertia
$\boldsymbol{I}$	linear impulse of a system of vortex particles
$[\boldsymbol{I}]$	identity matrix
j	index used for summations
$\hat{\boldsymbol{j}}$	unit vector along $\boldsymbol{y}$ axis
J	torsional stiffness constant

k	reduced frequency of oscillations
$\hat{\boldsymbol{k}}$	unit vector along $\boldsymbol{z}$ axis
K_d	empirical parameter in ONERA-DS model
$\boldsymbol{K}_\sigma(s)$	vortex particle regularized Biot - Savart function
$[\boldsymbol{K}]$	stiffness matrix
l	blade length
$\boldsymbol{l}$	displacement vector between two consecutive points on a blade
LO	lift offset
$\mathcal{L}$	blade sectional lift force
m	mass per unit length of blade
$m_{F/L/T}$	number of non-rotating flap/lag/torsional mode shapes
m_p	number of particles discretized from a vortex filament
M	revolution averaged rotor hub moments
M_c	Mach number
M_p	propulsor torque
$\boldsymbol{M}_b$	net moment at hub due to blade
$\boldsymbol{M}_h$	net moment at hub due to rotor
$[\boldsymbol{M}]$	mass matrix
$\mathcal{M}$	blade sectional pitching moment
n_c	number of layers in vortex ring core
n_{dof}	number of degrees of freedom per blade
$n_{F/L/T}$	number of uncoupled rotating flap/lag/torsional mode shapes
n_p	number of RFA poles
n_s	number of cross sectional locations per blade
n_ψ	number of azimuthal slices of vortex ring
$\hat{\boldsymbol{n}}$	unit vector normal to enclosed area
N_b	number of blades
N_c	number of particle clusters in FMM
N_f	total number of vortex filaments in the coaxial rotor
N_p	number of vortex particles
N_s	total number of cross sectional locations in the coaxial rotor
$\boldsymbol{O}$	vector location of CG
p	blade sectional force
$p_{d_{0,1}}$	empirical parameters in ONERA-DS model
p_m	number of terms in multipole expansion
$\boldsymbol{p}$	blade sectional force vector
P	pressure
$\boldsymbol{P}$	point on the undeformed blade elastic axis
$\boldsymbol{P'}$	location of point $\boldsymbol{P}$ after structural deformation
q	blade sectional moment
$q_\sigma(s)$	regularized kernel of Biot - Savart function
$\boldsymbol{q}$	blade sectional moment vector
$\boldsymbol{Q}$	blade root
$[\boldsymbol{\mathcal{Q}}]$	matrix transfer function relating generalized motion to generalized force

r	radial distance from hub center on rotor plane
r_0	vortex core discretization radius
r_c	vortex core radius
r_d	empirical parameter in ONERA-DS model
r_l	half the thickness of each vortex core layer
r_v	radial coordinate in vortex core
$\boldsymbol{r}$	position vector of a point on a blade cross section
R	rotor radius
R_0	vortex ring radius
Re	Reynolds number
$[\boldsymbol{R}_{a/d}]$	state-space matrix used in ROM
s	radial distance
$\bar{s}$	Laplace domain variable
$\boldsymbol{s}$	displacement vector between $\boldsymbol{S}$ and $\boldsymbol{r}$
$\boldsymbol{S}$	point on vortex filament closest to $\boldsymbol{r}$
$\bar{t}$	non-dimensional time
t	time
t_0	time at which vortex particle is generated
t_h	airfoil thickness
T	time period
T_c	centrifugal force at blade section
T_p	propulsor thrust
$\boldsymbol{T}_c$	centrifugal force vector at blade section
u	axial displacement due to elastic deformation
$\widetilde{U}$	approximate rotating axial deformation mode shape
U	magnitude of relative velocity $\boldsymbol{U}$ at blade cross section
U_p	component of $\boldsymbol{U}$ along $-\boldsymbol{z}_d$ axis
U_R	vortex ring speed
U_t	component of $\boldsymbol{U}$ along $-\boldsymbol{y}_d$ axis
$\boldsymbol{U}$	relative velocity of air at blade cross section
v	lag displacement due to elastic deformation
$\boldsymbol{v}$	fluid velocity
$\boldsymbol{v}_B$	velocity induced by vortex filament
$\boldsymbol{v}_{\boldsymbol{P}/\boldsymbol{P}'}$	velocity of point on undeformed/deformed blade
$\boldsymbol{v}_\sigma$	regularized velocity using VVPM
V	uncoupled rotating lag mode shape
$\boldsymbol{V}_w$	vector of wake induced velocities
$\mathcal{V}$	fluid volume
$\mathcal{V}_p$	volume associated with vortex particle
w	flap displacement due to elastic deformation
W	uncoupled rotating flap mode shape
W_f	helicopter weight
$\mathcal{W}_{0/1}$	generalized normal velocity distributions over airfoil
x	spanwise location
$\boldsymbol{x}$	position vector of a point in the flow

$\boldsymbol{x}_{a/d}$	vector of attached/separated flow aerodynamic states
$\boldsymbol{x}_p$	position vector of a vortex particle
$\boldsymbol{X}_{a/d}$	vector of attached/separated aerodynamic states
$\boldsymbol{X}_s$	vector of structural states
$\boldsymbol{X}_w$	vector of wake inflow states
y	coordinate along airfoil center-line
$\boldsymbol{y}$	combined blade states
z	coordinate perpendicular to airfoil center-line
$\boldsymbol{z}_k$	k^{th} column vector of the state transition matrix
$\mathbb{Z}$	set of all integers

Greek symbols

α	angle of attack
α_0	magnitude of angle of attack oscillations
α_{cr}	critical angle of attack
$\alpha_{d_{0,1}}$	empirical angle of attack parameter in ONERA-DS model
α_f	fuselage tilt angle
$\boldsymbol{\alpha}_p$	particle vorticity strength
β	angle between $\boldsymbol{r}$ and ends of a vortex filament
β_p	blade precone angle
$\delta(s)$	Dirac delta function
δ_t	tolerance for trim calculations
ϵ	residual of equation using Galerkin method
ε	error estimate
$\eta_\sigma(s)$	heat equation kernel
$\boldsymbol{\epsilon}$	vector of residuals of equations using Galerkin method
ϕ	elastic twist
ϕ_{in}	induced angle at blade section
Φ	uncoupled rotating torsional mode shape
φ	non-rotating torsional shape function
$[\boldsymbol{\Phi}(T,0)]$	state transition matrix at the end of time period T
γ	exponent of N_p for computational time complexity
γ_n	n^{th} RFA pole
Γ	bound circulation
Γ^0	harmonic mean of vortex filament bound circulation
Γ^1	spanwise change of vortex filament bound circulation
Γ_v	vortex ring circulation strength
λ	characteristic exponent
Λ	characteristic multiplier
μ	advance ratio
ν	kinematic viscosity
η_k	k^{th} entry of the reduced eigenvector $\boldsymbol{\eta}$
$\boldsymbol{\eta}$	reduced form of of the eigenvector $\boldsymbol{\xi}$
ω	frequency of oscillations
$\boldsymbol{\omega}$	vorticity

$\boldsymbol{\omega}_{b/d}$	angular velocity of blade rotation/deformation
$\boldsymbol{\omega}_{\sigma}$	regularized vorticity using VVPM
Ω	rotational speed
$\boldsymbol{\Omega}$	total vorticity of a system of vortex particles
θ	local blade pitch angle
$\Delta\theta_0$	differential collective pitch angle
θ_0	collective pitch angle
$\Delta\theta_{1c}$	differential lateral cyclic pitch angle
θ_{1c}	lateral cyclic pitch angle
$\Delta\theta_{1s}$	differential longitudinal cyclic pitch angle
θ_{1s}	longitudinal cyclic pitch angle
θ_{tw}	built-in pre-twist
θ_v	polar angle coordinate in vortex core
ρ	density of air
ρ_b	density of blade
ψ	blade azimuth angle
σ	vortex particle smoothing radius
ς	root of transcendental equation of cantilever beam
Ψ	rotor phasing parameter
ϑ	non-rotating bending shape function
τ_d	time delay in ONERA-DS model
ξ_k	k^{th} entry of the eigenvector $\boldsymbol{\xi}$
$\boldsymbol{\xi}$	eigenvector of state transition matrix $[\boldsymbol{\Phi}(T,0)]$
$\boldsymbol{\chi}$	generalized coordinates of non-rotating mode shapes
ζ	real part of characteristic exponent
$\zeta_\sigma(s)$	vortex particle vorticity regularization function

Subscripts

a	attached flow
B	bound circulation induced velocity
d	separated flow
F	flap modes
$\mathbb{I}$	imaginary part
l	lower rotor
L	lag modes
o	root of blade
$\mathbb{R}$	real part
S	structural deformation
T	torsional modes
u	upper rotor
W	wake induced velocity
y	axis along airfoil center-line
z	axis perpendicular to airfoil center-line
∞	free-stream velocity
Ω	blade rotation

σ	regularized

Superscripts

A	aerodynamic
C	circulatory
$\mathcal{D}$	drag
E	elastic
I	inertial
J	induced
K	kinematic
$\mathcal{L}$	lift
$\mathcal{M}$	moment
NC	non-circulatory

Coordinate systems

$(\boldsymbol{x}_b, \boldsymbol{y}_b, \boldsymbol{z}_b)$	undeformed blade coordinate system
$(\boldsymbol{x}_d, \boldsymbol{y}_d, \boldsymbol{z}_d)$	local blade section coordinate system after elastic deflections
$(\boldsymbol{x}_h, \boldsymbol{y}_h, \boldsymbol{z}_h)$	hub fixed coordinate system
$(\boldsymbol{x}_r, \boldsymbol{y}_r, \boldsymbol{z}_r)$	hub rotating coordinate system
$(\boldsymbol{x}_t, \boldsymbol{y}_t, \boldsymbol{z}_t)$	local airfoil coordinate system including built-in and elastic twist
$(\boldsymbol{X}, \boldsymbol{Y}, \boldsymbol{Z})$	body fixed coordinate system
$(\boldsymbol{X}_o, \boldsymbol{Y}_o, \boldsymbol{Z}_o)$	coordinate system aligned with ground reference frame

Special symbols

$\widetilde{(\bullet)}$	approximation of $(\bullet)$
$\overline{(\bullet)}$	blade property including effects of blade twist
$\dot{\overline{(\bullet)}}$	partial derivative with respect to non-dimensional time $\bar{t}$
$\ddot{\overline{(\bullet)}}$	partial second derivative with respect to non-dimensional time $\bar{t}$
$\dot{(\bullet)}$	partial derivative with respect to time t
$\ddot{(\bullet)}$	partial second derivative with respect to time t
$\hat{(\bullet)}$	unit vector
$[\bullet]^{-1}$	matrix inverse
$(\bullet)'$	dummy variable used for integration of variable $(\bullet)$
$(\bullet)^*$	clockwise rotating system
$(\bullet)^T$	transpose of vector or matrix
$(\bullet)_{,x}$	partial derivative with respect to spanwise coordinate x
$(\bullet)_{,xx}$	partial second derivative with respect to spanwise coordinate x

Abstract

Coaxial rotor helicopters are a candidate for the next generation of rotorcraft due to their ability to achieve high speeds without compromising hover performance. Coaxial rotors are designed to offload the retreating side of the rotor in high speed flight to delay the effects of reverse flow and blade stall which limit the speed of conventional single main rotor helicopters. The proximity of the two rotors induces periodic blade passage effect loads and unsteady rotor wake interactions absent in single rotor configurations. Coaxial rotors employ stiff composite hingeless blades to prevent the possibility of blade strike. At high speeds, the coaxial rotor operates at reduced RPM to avoid the drag penalty on the advancing blade tip. This combination of rotor lift distribution, periodic blade passage effect, unsteady rotor wake interaction, combined with stiff hingeless blades and reduced rotor RPM implies that a coaxial rotor system requires a specialized aeromechanical analysis.

The goal of this dissertation is to develop a comprehensive aeromechanical analysis capable of modeling the aeroelasticity of stiff hingeless counter-rotating blades and the complex rotor-wake interactions present in a coaxial rotor system. The rotor wake is modeled with the Viscous Vortex Particle method, a grid free approach for calculating vortex interactions over long distances. The spanwise blade loading in attached flow is obtained from a computational fluid dynamics based rational function approximation unsteady aerodynamic model. The ONERA dynamic stall model is extended to capture three dimensional effects due to flow separation. The combination of the viscous vortex particle method with reduced order models for spanwise

loading captures the unsteady coaxial rotor loads with computational efficiency. Trim procedures are developed to determine control inputs for a coaxial rotor to maintain equilibrium in hover and forward flight. In forward flight, two different trim conditions are considered: trim with propulsor off, and trim at level attitude. The two trim conditions have a significant impact on the vibratory hub loads, rotor inflow distribution and the aeroelastic stability. A unique aspect of the coaxial rotor is that its stability in both hover and forward flight are governed by equations with periodic coefficients. Therefore, a periodic aeroelastic stability analysis based on Floquet theory is applied. A new graphical method is developed to identify coupling between the blade modes of the two rotors.

The aeromechanical formulation is applied to a rotor resembling the Sikorsky X2TD coaxial helicopter. In hover, the rotor experiences 8/rev blade passage loads due to oscillations in the blade bound circulation induced inflow. Increasing the collective pitch increases the coupling between the flap and lag modes of the blade. The aerodynamic interactions lead to an inter-rotor coupling of the first flap modes. In forward flight, the effects of trim condition, advance ratio, lift offset, and separated wake on the hub loads, inflow distribution and aeroelastic stability are examined. The results indicate that the aeroelastic stability of the lag mode is reduced in forward flight at a level attitude compared to hover.

This study provides an improved physical understanding of the aeroelastic interactions in coaxial rotors. The work presented in this dissertation has the potential to facilitate design and development of future high speed coaxial rotorcraft.

CHAPTER 1

Introduction, Background and Objectives

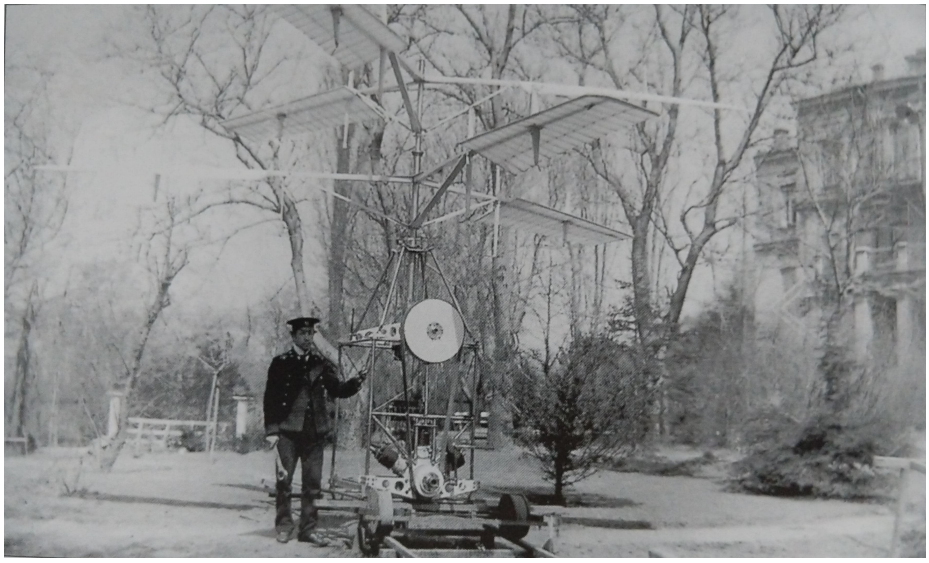

Figure 1.1: Igor Sikorsky's H-2 coaxial helicopter in 1910 [1]

In 1908, just five years after the first controlled flight of a heavier-than-air powered aircraft by the Wright brothers, 19 year old Igor Sikorsky designed H-1, his first Vertical Take-Off and Landing (VTOL) aircraft. The aircraft used two counter-rotating rotors mounted on a single shaft - a coaxial helicopter (Fig. 1.1). The contraption never flew, but managed to generate just enough thrust to lift itself without a pilot [1]. Igor Sikorsky abandoned the project and went on to a successful career designing fixed-wing transport and amphibious aircraft.

Three decades later, he decided to try his hand again at rotary wing vehicles

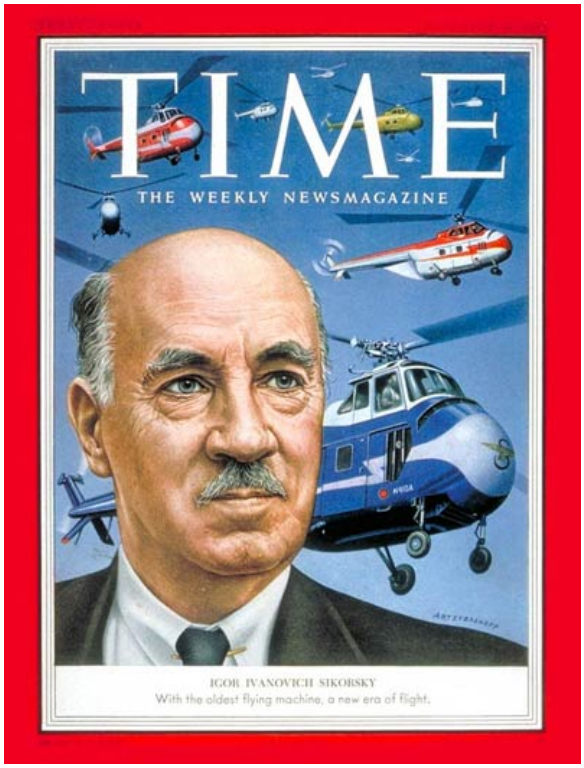

Figure 1.2: Cover of Time Magazine from November 16, 1953 [2]

and built the VS-300: the first successful single main rotor (SMR) helicopter. The helicopter was quickly adopted by military and civilian authorities for passenger transport, cargo delivery and rescue operations. The rapid success of the vehicle brought Igor Sikorsky such fame that in November of 1953, he was on the cover of Time magazine [2] (Fig. 1.2). He was asked why the SMR helicopter configuration (one main rotor to generate thrust and one tail rotor to balance yaw moment) had succeeded.

> *Most earlier helicopter builders (like some today) killed torque by using sets of two or more rotors which revolved in opposite directions. But Sikorsky put his faith in one rotor. "One woman in the kitchen is fine," he says. "Two women in the kitchen get in each other's way." He decided to keep his fuselage from spinning simply by hanging a vertical fan on an outrigger at the tail.*

Since 1941, nearly 95% of all helicopters manufactured have been of the SMR

configuration perfected by Igor Sikorsky [1]. Today, the company he founded has decided to pursue the coaxial rotor configuration for the next generation of helicopters. Sikorsky, a Lockheed Martin company, is competing for the U.S. Army Future Long-Range Assault Aircraft (FLRAA) program with the SB>1 Defiant (Fig. 1.3c), and for the Future Attack Reconnaissance Aircraft (FARA) program with the Raider-X (Fig. 1.3d). The FLRAA and FARA are part of the Future Vertical Lift (FVL) program of the U.S. Department of Defense (DoD) to develop the next generation of high speed helicopters. The SB>1 Defiant and Raider-X are based on the coaxial compound Sikorsky X2^{TM} Technology Demonstrator (X2TD) (Fig. 1.3a), which exceeded 250 knots in 2010, a helicopter speed record.

High speed forward flight has always been a challenge for conventional SMR helicopters. The coaxial configuration has the potential to revolutionize vertical flight because of its ability to achieve high speeds ($>$ 200 knots), while maintaining hover efficiency. The ability to hover is a unique advantage of VTOL vehicles because they can take-off and land in confined spaces, which makes them ideal for insertion and rescue missions. In rescue missions, high speed is a necessity because critically injured passengers need to reach a specialized medical facility urgently for treatment. High speed is also necessary for military helicopters used in stealth and attack missions.

It has taken over a century to overcome challenges associated with coaxial rotors to make them competitive and exceed the performance of conventional SMR helicopters. This chapter briefly describes the history of coaxial helicopters, current challenges in their modeling, and defines the scope of the work presented in this thesis.

(a) X2^{TM} Technology Demonstrator [6]

(b) S-97 Raider [7]

(c) SB>1 Defiant [8]

(d) Raider-X [9]

Figure 1.3: Modern coaxial helicopters designed by Sikorsky, a Lockheed Martin company

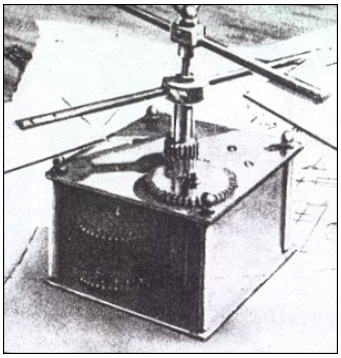

(a) Lomonosov, 1754 [10]

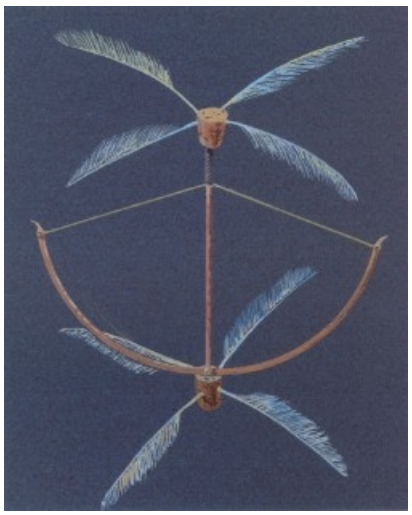

(b) Launoy-Bienvenu, 1783 [11]

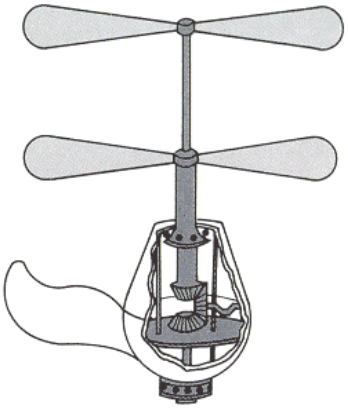

(c) Henry Bright, 1861 [12]

Figure 1.4: First known coaxial rotor model helicopters

1.1 Brief history of coaxial rotor helicopters

The first flying model helicopter was the Chinese Top. Several inventors modified the toy to have coaxial rotors [13]. Some of the earliest models are shown in Fig. 1.4. Mikhail Lomonosov from Russia built a small coaxial rotor toy powered with a wound-up spring device in 1754 (Fig. 1.4a). Launoy, a French naturalist, along with Bienvenu, a mechanic, built a similar coaxial rotor Chinese top powered by a string pulled in tension by a cross-bow (Fig. 1.4b). In 1861, Henry Bright published a coaxial design shown in Fig. 1.4c. Igor Sikorsky, at age 12, built a rubber band powered coaxial helicopter in 1901 [1].

1909 - 1920

The first attempts to build coaxial rotor helicopters were unsuccessful primarily because of the lack of engine power. Igor Sikorsky built the H-1 coaxial helicopter in the summer of 1909, which was followed by the H-2 (Fig. 1.1) in 1910. Both aircraft were unable to fly. Konstantine Antonov, the famous Russian aeronautical engineer, built a coaxial helicopter around 1910 (Fig. 1.5a). The aircraft used triangular shaped blades for the rotor and had a propeller for forward propulsion. The aerodynamicist Joukowski and his students built a primitive coaxial helicopter at Moscow University in 1910. In 1912, the Danish aviation pioneer, Jacob C. Ellehammer designed a coaxial helicopter which featured six short rotor blades attached to the periphery of two large circular rings (Fig. 1.5b). The helicopter took several short hops but never completed a properly controlled free flight [18]. Another famous aerodynamicist, Theodore von Kármán, along with the Austrian Stephan Petroczy, built a coaxial helicopter which accomplished tethered vertical flights during 1917-1920 (Fig. 1.5c). In 1919, Henry Berliner built a coaxial helicopter which made brief uncontrolled hops and reached a height of about 4 ft (Fig. 1.5d).

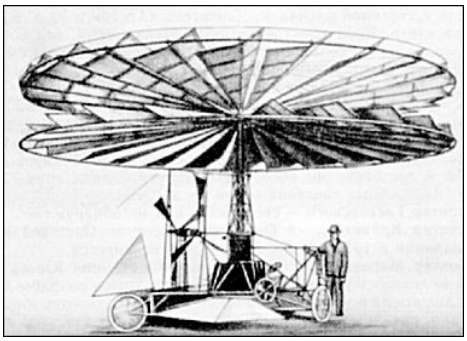

(a) Helicoplane, 1910 [14]

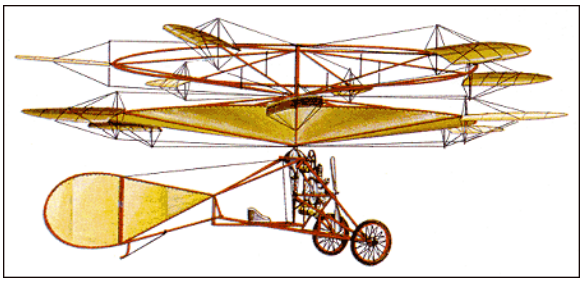

(b) Ellehammer Helicopter, 1912 [15]

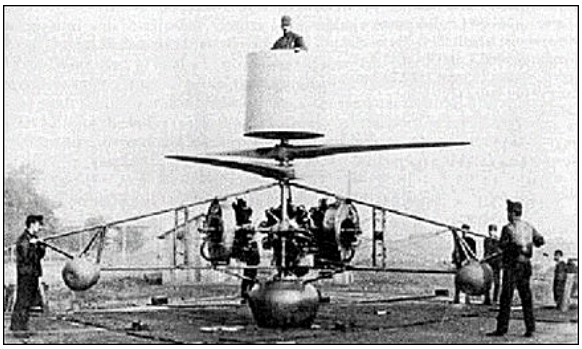

(c) PKZ-2, 1918 [16]

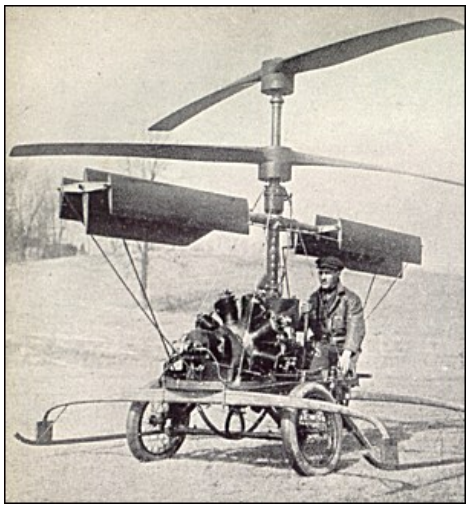

(d) Berliner Helicopter, 1919 [17]

Figure 1.5: Early coaxial rotor helicopters lacked sufficient power for sustained flight

Figure 1.6: Cierva C1 gyroplane, 1920 [3]

Juan de la Cierva, inventor of the successful Autogiro aircraft, had initially experimented with coaxial rotors for his gyroplanes (Fig. 1.6). However, the aerodynamic interactions between the rotors resulted in different upper and lower rotor speeds, which prevented the necessary roll moment balance required and the aircraft crashed.

1920 - 1950

In the 1920s, engine technology had sufficiently advanced to allow sustained hover and low speed flight. Adequate controllability of the vehicles still remained a challenge. Raul Pescara, an Argentinian living and working in Spain and France, built a coaxial helicopter with bi-plane type rotor blades (Fig. 1.7a). In 1930, Corradino d'Ascanio from Italy built a coaxial helicopter with two-bladed rotors (Fig. 1.7b). Louis Breguet and René Dorand built a coaxial helicopter in 1935 which flew for 62 minutes and 27 miles (Fig. 1.7c).

In the 1940s and 1950s, the SMR configuration had gained popularity because of its simpler design and control. During this time, several coaxial helicopters were built and flown, however they did not find wide acceptance. In 1944, 19 year old

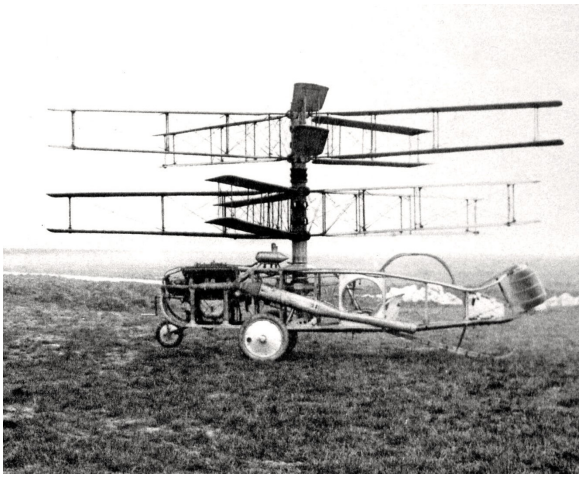

(a) Pescara Helicopter, 1923 [19]

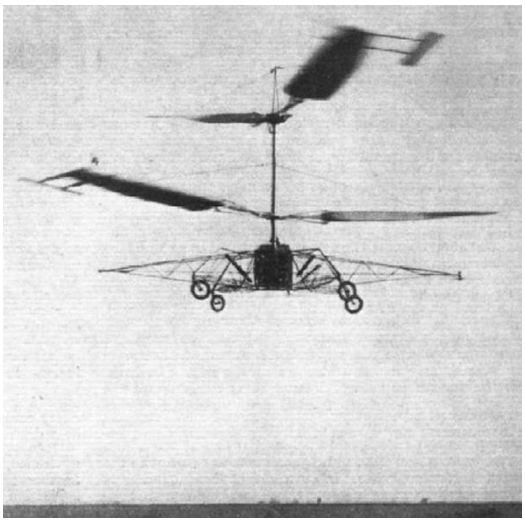

(b) D'AT3, 1930 [20]

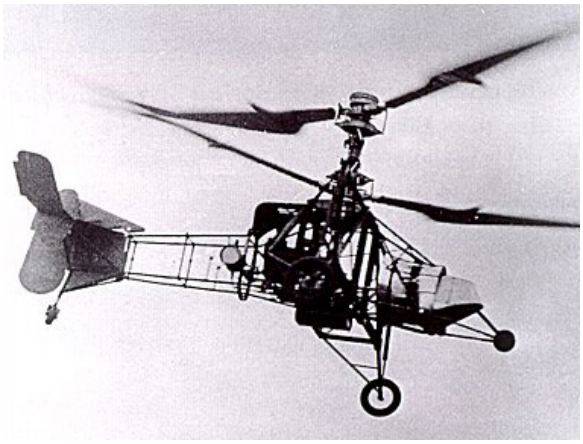

(c) Gyroplane-Laboratoire 1, 1933 [21]

(d) XH-44 Hiller-Copter, 1944 [22]

(e) Bell Model 30, 1945 [23]

(f) Bendix Model K, 1945 [24]

Figure 1.7: First successful coaxial helicopters (1920-1950)

(a) Gyrodyne Model 2C, 1952 [25]

(b) XRON Rotocycle, 1955 [26]

(c) Kamov Ka-15, 1955 [27]

Figure 1.8: Coaxial helicopters adopted for specialized missions (1950 - 1960)

Stanley Hiller Jr. designed, built, and test flew the first coaxial rotor helicopter to fly successfully in the United States (Fig. 1.7d). Arthur Young, working for the Bell helicopter company, conducted several experiments with a coaxial helicopter (Fig. 1.7e) in 1945-46. Major General Chia-Jen Chu, designed and built the CJC-1A and CJC-1B Hummingbird coaxial helicopters in China in 1945 and 1948 respectively. The Bendix Helicopters' Model K (Fig. 1.7f) made its maiden flight in June 1945. The Model K was followed by Bendix Model J in 1949 but the company was forced to close soon after. The Brantly helicopter company built its first aircraft, the Brantly B-1, a coaxial helicopter, in 1946, but then switched to manufacturing SMR helicopters.

Figure 1.9: Sikorsky XH-59A / S-69A, 1981 [4]

1950 - 2000

In the 1950s, a few coaxial helicopters achieved moderate success and were utilized for specialized missions. The Gyrodyne company successfully demonstrated a coaxial rotor helicopter (Fig. 1.8a) for the U.S. Navy in the 1950s. This led to the development of the XRON-I/YRON-I Rotorcycle (Fig. 1.8b), a single-seat helicopter for observation and tactical maneuvers. In 1960, the company produced the Gyrodyne QH-50A, an anti-submarine coaxial rotor drone for the U.S. Navy. The Kamov company built the Ka-15 (Fig. 1.8c) and Ka-18 coaxial rotorcraft in the mid 1950s. It has commercially produced several light and medium weight versions for civil and military applications since then.

In 1964, development began on the Advancing Blade Concept (ABC) [28], a coaxial rotor system with rigid hingeless blades. The ABC marked a significant step in the development of coaxial helicopters because of its ability to achieve much higher speeds compared to SMR helicopters. Experiments conducted on a 40ft diameter rigid coaxial rotor at NASA Ames were promising, and confirmed the improved performance of the ABC rotor. The U.S. Army awarded Sikorsky Aircraft a contract to design and build the XH-59A/S-69A (Fig. 1.9). The XH-59A had three bladed ro-

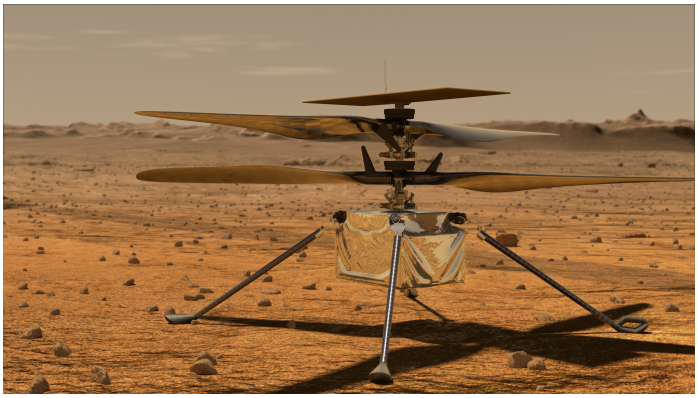

Figure 1.10: Mars Helicopter "Ingenuity" [5]

tors with a diameter of 36 ft. Auxiliary forward thrust was provided by two turbojet engines. The first aircraft built was badly damaged during a test flight in 1973. The accident was unrelated to the ABC technology. The second aircraft was test flown for over 100 hours. It achieved a maximum level speed of 238 knots. However, the vehicle experienced high levels of vibration and fuel consumption. The program was discontinued in 1981.

After the XH-59A program ended, coaxial helicopters did not receive much attention for many years. During this time, the Kamov company, produced several versions of articulated coaxial helicopters in Russia. Several home/kit-built coaxial helicopters were designed and flown under the Federal Aviation Administration (FAA) experimental category certification.

2000 - Today

In 2004, the Sikorsky Aircraft initiated preliminary design for an advanced technology demonstrator designated the X2TD, shown in Fig. 1.3a. The X2TD first flew in 2008. In 2010, it exceeded 250 knots during flight tests, an unofficial speed record for a helicopter. The record is considered unofficial because the X2TD uses a propulsor for thrust augmentation, and is therefore not a "pure" helicopter. The X2TD was

successful compared to the XH-59A because of an Active Vibration Control System (AVCS) which significantly reduced fuselage vibrations. In addition, auxiliary thrust was provided by a propulsor instead of turbojet engines. The X2TD was retired in 2011. The design and development of the X2TD led to a spurt in research activity which continues today, concurrent with the development of advanced coaxial helicopters shown in Fig. 1.3.

In 2010, Sikorsky started working on the S-97 Raider (Fig. 1.3b) for the Armed Aerial Scout (AAS) program. Under the Joint Multi Role (JMR) Technology Demonstrator program, Sikorsky teamed up with Boeing to develop the SB>1 Defiant (Fig. 1.3c) in 2014. In March 2020, the U.S. Army selected the SB>1 Defiant to move forward in the FLRAA Competitive Demonstration and Risk Reduction (CD&RR) program. The SB>1 Defiant achieved flight speeds of 205 knots in June 2020 with 50% power available in reserve. The U.S. Army has also selected the Raider-X (Fig. 1.3d) as a FARA candidate for the next phase of detailed design, prototype build and testing. The Raider-X is based on the S-97 Raider demonstrator (Fig. 1.3b) which has already achieved 207 knots in flight testing. Therefore, the future of coaxial helicopters based on the ABC and X2TD technology is promising.

Most recently, the coaxial configuration has been selected for the Mars Helicopter "Ingenuity" to perform the first extra-terrestrial (fixed or rotary-wing) atmospheric flight of humankind as part of the Mars 2020 mission [29–31]. The objective of the Mars Helicopter is to demonstrate technologies needed for planetary exploration through a series of low-altitude flights in 2021.

Based on this historical overview, it is evident that Sikorsky's X2TD configuration has the potential to replace current rotorcraft due to its exceptional high speed and

hover performance. As shown in the literature review provided in this chapter, the aeromechanical aspects of a coaxial helicopter is an evolving area and therefore this dissertation is specifically focused on coaxial rotor systems with stiff hingeless blades and a propulsor for auxiliary thrust.

1.2 Key features of a coaxial rotor system

The coaxial helicopter produces a very complex operating environment as shown in Fig. 1.11. A coaxial rotor system consists of two vertically spaced rotors spinning in opposite directions to generate thrust. The *counter-rotation* cancels out the torque from each rotor and provides *yaw trim* for the vehicle. Since the total weight is supported by two rotors, the rotor diameter can be reduced, and the vehicle is compact compared to a conventional SMR helicopter.

In SMR helicopters, a portion of the engine power is diverted towards the operation of the tail rotor, which does not contribute to generating lift. Due to the inherent yaw trim of the coaxial configuration, a tail rotor is not needed and therefore additional power is available. Single rotor helicopters have losses associated with the momentum transferred in the azimuthal direction of the wake, known as *swirl*. The counter-rotation of the coaxial rotors reduces the effective swirl and improves hover performance.

In forward flight, SMR systems reduce loads on the advancing blades and increase loads on retreating blades to maintain roll moment equilibrium. The retreating side operates at lower dynamic pressure and high angles of attack causing some regions of the blade to experience *retreating blade stall*. Therefore, the forward speed is limited by the lift capability of the retreating side. In addition, the advancing tip experiences

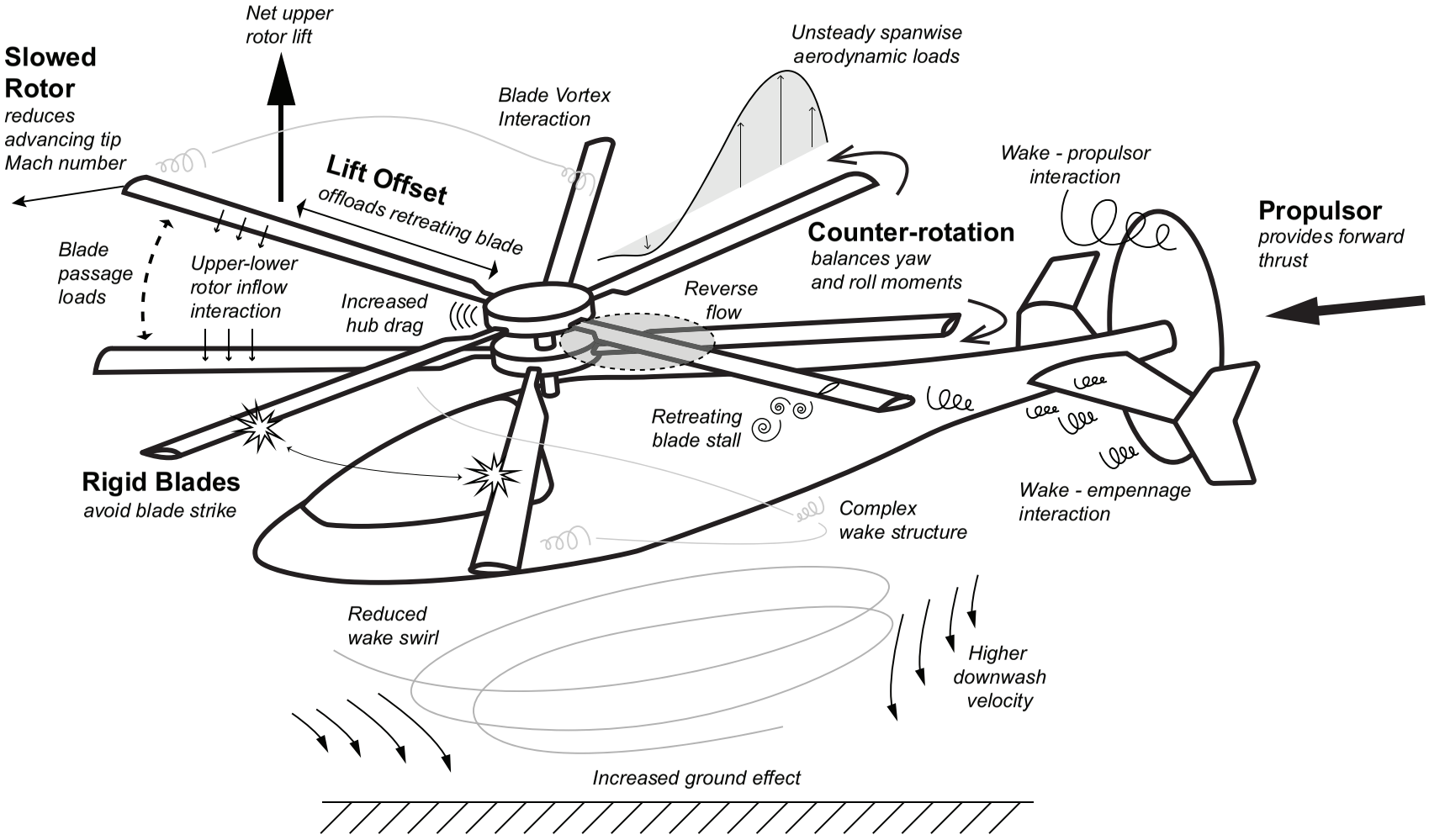

Figure 1.11: Coaxial helicopters produce a complex operating environment

high Mach numbers and can exceed the *drag-divergence* limit.

In a coaxial rotor, the rolling moments developed by the upper and lower rotor are in opposite directions. The retreating blades can be offloaded and stall is avoided. The net lift of each rotor acts at a location displaced from the hub, known as the Lift Offset (LO) shown in Fig. 1.11. Therefore, the coaxial rotor lift distribution is different when compared to the SMR and the blade needs to be designed appropriately. The advancing blade tip Mach number can be reduced with *slowed rotors*. A propulsor provides additional forward thrust and can compensate for the loss of main rotor thrust due to reduction in rotor RPM.

Despite its advantages, the coaxial configuration also has some drawbacks. The lower rotor experiences the inflow induced by the upper rotor. The upper rotor is also affected by the airflow through the lower rotor. This decreases the effective angle of attack encountered at various sections, and increases the required induced power. Downwash velocities are typically higher because the total weight of the vehicle is supported over a smaller disk area. Higher downwash velocities lead to increased dynamic pressure experienced by an obstacle in the wake. Therefore, *ground effect* and *empennage interactions* are intensified.

The vertical spacing between the rotors plays an important role in determining the characteristics of the coaxial rotor system. A large vertical separation between the rotors requires a large coaxial hub that generates excessive drag at high speeds. However, decreasing the separation increases the aerodynamic interaction between the two rotors. The aerodynamic interaction reduces the thrust efficiency and increases the vibratory loads. A small vertical separation also enhances the possibility of *blade strike*. Blade strike occurs when the blade tip paths intersect due to the

anti-symmetric flapping of blades of each rotor. Therefore, coaxial rotor blades are designed to be structurally rigid. However, rigid blades transfer larger moments at the hub and thus increase vibratory loads.

The rotor loads are tightly coupled with the rotor wake. The inflow distribution over the rotor is determined by the velocities induced by the wake vortices. The inflow distribution determines the angle of attack at each blade section, and hence determines the blade loads. The strength of the tip and shed vortices depends on the radial and azimuthal distribution of blade loads. The radial flow on the blades influence the boundary layer and in turn, the viscous drag. The three-dimensional (3D) effects on the flow due to the centrifugal force result in a thinner boundary layer and delay *flow separation* and stall. The periodic impulsive loading due to repeated attachment and separation of flow is referred to as dynamic stall (DS).

In a coaxial system, the upper and lower rotor wakes interact with each other, as well as with blades of either rotor. The tip vortices from the upper rotor intersect with the lower rotor blades. The shed vorticity from inboard sections of the upper blade interacts with the lower rotor. These vortex sheets modify the loads and inflow over both rotors. Blade Vortex Interaction (BVI) is a phenomena which occurs when tip vortices from preceding blades strike or pass in close proximity to a rotor blade. For SMR helicopters, BVI commonly occurs during descending forward flight, where it significantly affects vibration and noise. In contrast, BVI can occur at nearly all flight conditions of a coaxial helicopter due to the proximity of the upper and lower rotors.

The upper and lower rotor blades pass each other several times in each revolution and generate periodic loads. The periodic loading is known as *blade passage effect*,

and has been referred to in literature as the *overpressure effect*, *cross-over effect* and *venturi effect*. The blades pass each other $2N_b$ times during every revolution, where N_b is the number of blades per rotor. The azimuthal location at which the blades first overlap is referred to as the coaxial *rotor phase* or *indexing*. The rotor phase determines the magnitude of the vibratory pitch and roll moments at the hub. These rotor interaction effects are responsible for the excessive vibrations associated with coaxial helicopters.

The control of a coaxial rotor system is complex when compared to a SMR helicopter. Typically, each rotor has its own swashplate that provides collective and cyclic inputs. The design of two swashplate units that change pitch on counter-rotating rotors in a coaxial shaft system is mechanically complex and contributes to hub drag. The controls need to be coupled such that the vehicle has favorable handling characteristics. The thrust variation is obtained by changing the collective on both rotors simultaneously. However, the aerodynamic conditions on each rotor are not identical. Therefore a differential collective is required to maintain torque balance and total thrust. Similarly, the cyclic controls need to be coupled to maintain pitch and roll moment equilibrium in forward flight.

Due to the nature of aerodynamic interactions, and the structural and dynamic response of the blades in a rotating system, the aeroelastic coupling is highly nonlinear and changes with advance ratio. The rotor tilt can be adjusted based on the forward thrust distribution between the coaxial rotor system and the propulsor. However, the ingestion of the coaxial rotor wake into the propulsor depends on vehicle tilt and can lead to adverse aerodynamic interactions and excessive vibrations.

1.3 Literature review

A comprehensive review of the state of art of coaxial rotor research was published in a NASA report by Coleman in 1997 [32]. This widely cited report summarized developments in coaxial research across the world. It focused on early experimental work and methods of analyses used. The survey has become outdated as a result of the significant progress made during the last two decades. An updated comprehensive review is presented next.

1.3.1 Experimental studies

Harrington [33] published the first experimental study on coaxial rotor hover performance. Full scale rotors with differential collective pitch for trim were tested. The same setup was used in forward flight by Dingledein [34]. The power requirements of the coaxial rotor were predicted well by momentum theory. The power required in level flight exceeded that of an equivalent single rotor. References 33 and 34 are two of the few sources containing experimental loads data on full scale coaxial rotors.

Another experimental study considered the wake geometry of a Kamov helicopter and compared it with a vortex wake model code ULYSS-6 [35]. Results showed that the upper rotor wake contracted to only 85% of the rotor radius, while the lower rotor wake contracted to 91% of the rotor radius.

A coaxial rotor with highly twisted scaled XV-15 blades was studied experimentally by McAllister and Tung [36]. Particle Image Velocimetry (PIV) was used for flow visualizations. The wake geometries of each rotor differed significantly from that of a single rotor. As indicated in Ref. 35, the wake from the upper rotor contracted to a smaller radius compared to the lower rotor. The tip vortex position was found to

become erratic with increasing wake age. The magnitude of wake velocity was found to be higher in the coaxial configuration compared to a SMR.

A study conducted at NASA Ames [37] presented a comparison of experimental results from several coaxial rotor tests. It reviewed some conflicting observations in previous experimental studies. Experiments were conducted to resolve these contradictions, using blades similar to those used in Ref. 36. Momentum theory relations between thrust and power were found to be valid only if there was no upflow near the rotor tips. The lower rotor influence on the upper rotor performance was found to be significant, contrary to previous experimental and simulation studies. The effect of reduced swirl in the coaxial rotor was shown to be beneficial because it reduced power consumption by nearly 5%. The rotor phasing was found to significantly influence the swirl losses.

A Mach-scaled coaxial rotor has been tested in hover and forward flight at UT Austin and University of Maryland, respectively. Tip vortices in hover were visualized using PIV [38]. Vortex filaments underwent 3D short wave and long wave perturbations. Considerable scatter in the instantaneous positions of the vortices was observed, similar to the result of Ref. 36. The unsteadiness increased with vortex age. The lower rotor vortices were highly strained when compared to upper rotor vortices.

The performance and vibratory hub loads in hover were reported in Ref. 39. Results were compared with a free wake model. Coaxial rotors had higher vibratory loads compared to the SMR. The lower rotor thrust showed significant azimuthal variation due to the interaction with the upper rotor. The transient loading introduced by upper rotor blade passage led to increased vibratory loads on the lower rotor.

Additional measurements of hub loads and blade deformations were conducted in Ref. 40. Significant vibrations occurred at a frequency of $2N_b$/rev, and had a magnitude equal to 11% of the mean thrust. The twist and bending deformations measured on the lower rotor were much higher compared to the SMR. Torque balance was difficult to achieve due to the unsteadiness of the flow.

Further experiments in forward flight were conducted in Ref. 41. The effects of rotor collective, LO and rotor phasing on the performance and loads were studied. The upper rotor loads were found to be insensitive to the state of the lower rotor. Increasing the LO increased the available thrust at high advance ratios. However, changing the LO was ineffective in improving performance at low advance ratios. Increasing the LO reduced the tip clearance, therefore blade strike limited the maximum allowable LO for a coaxial rotor. The hub forces and yaw moment decreased with increase in LO, however the vibratory $2N_b$/rev rolling and pitching moments increased. For the coaxial system, the vibrations were dependent on the phase angle between the rotors.

Recently, flight tests have been conducted on a German coaxial rotorcraft with teetering blades [42, 43]. Rotor-fuselage interaction effects were found to be prominent during hover. The vibratory loads due to upper and lower rotor interaction effects were highest at very low speed flight ($\leq$ 10 kts), due to the upper rotor inflow passing through the lower rotor. At speeds above 50 kts, the interactions began increasing again because the wake of the upper rotor passed through the lower rotor due to the nose down attitude of the helicopter.

1.3.2 Advancing Blade Concept research

The Advancing Blade Concept term was coined by Sikorsky Aircraft in the late 1960s. An introduction to the ABC concept described the advantages of this configuration [44]. Experiments were conducted on dynamically scaled rotors to understand the wake structure in hover and forward flight. Measured blade loads indicated that the vibrations were greater than those from a SMR. Analytical studies were conducted for the design of a full scale model. The use of slowed rotors and stiff blades were studied. The study concluded that the ABC was a feasible solution for a high speed helicopter.

The ABC configuration was implemented on the XH-59A three-bladed prototype, flown for the first time in 1973. A non-fatal accident revealed that the required forward cyclic pitch control was larger than predicted because the rotor inflow was underestimated in the analysis. During XH-59A flight tests, the 3/rev vibrations were excessive at high speeds. The vibration level was found to be dependent on the phase difference between the two rotors. When the blades from the two rotors crossed at 0^{o} azimuth, the 3/rev roll and yaw moments and the side forces would cancel each other out. By contrast when they crossed at a 30^{o} azimuth, the vertical forces, longitudinal forces and the pitching moments would cancel out. The vehicle was tested in the NASA Ames 40 by 80 foot wind tunnel [45]. Aerodynamic forces and moments, rotor control positions, structural loads and vibrations were measured. Despite substantial improvements in design and performance, the funding for the next phase XH-59B was not approved.

In 2005, Sikorsky restarted efforts to build a coaxial rotor helicopter using modern materials and avionics technology that culminated in the development of the four bladed compound Sikorsky X2TD. During the development of the Sikorsky X2TD,

several studies including experimental and design analyses were conducted [46–49].

The aerodynamic design of the rotor blades was considered in Ref. 46. The blades were optimally designed to exploit the advancing region, due to offloading of the retreating side. The main features of the blade design consisted of: non-uniform planform, positive and negative twist gradients and distribution of modern airfoils. The X2TD blade was designed to overcome shortcomings of the XH-59A rotor that experienced high profile and compressibility drag at high speeds. The high rigidity of the X2TD blades allowed close proximity of the two rotors and prevented the risk of blade strike. The closely spaced rotors decreased the mast size and hence reduced parasite drag. The rigid blades of the coaxial rotor system combined with high forward speed and variable rotor speed produced a complex dynamic environment resulting in high vibration levels.

The vibratory loads of the X2TD were considered in Ref. 47. Experimental results indicated that even with optimum blade phasing, cockpit vibrations at a cruise speed of 225 knots were of the order of 0.5g in the vertical and 0.75g in the lateral directions. An AVCS with force generating actuators in the fuselage was employed to reduce vibrations to acceptable levels. References 48 and 49 describe the ground, hover and high speed flight testing program of the X2TD. Fuselage and hub drag was studied in Ref. 50.

Wind tunnel tests on a scaled S-97 Raider coaxial helicopter were described in Ref. 51. The inboard regions of the S-97 Raider blades have double-ended airfoils for improved performance in reverse flow. However, there was a large amount of separated flow that complicated flow measurements. Scale model wind tunnel tests of the SB>1 Defiant were conducted in Ref. 52. The airframe loads and aerodynamic

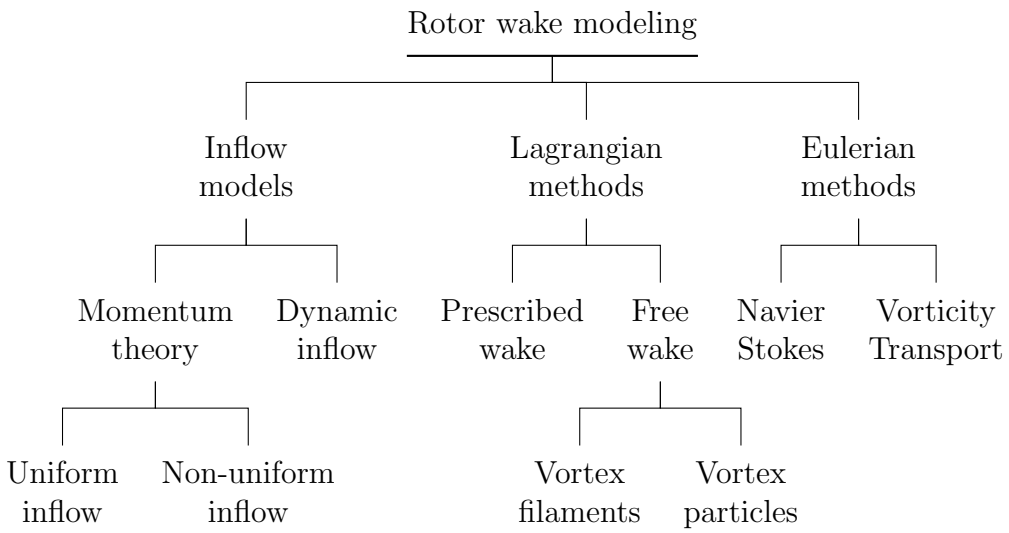

Figure 1.12: Classification of commonly used rotor wake modeling approaches

interactions between the propulsor and empennage were quantified to substantiate projected aircraft performance. Manufacturing technologies used in the SB>1 Defiant have been discussed in Ref. 53.

Sikorsky has developed and applied a comprehensive set of tools for the design and analysis of the JMR aircraft [54]. These tools include Overset Grid CFD Flow Solver (OVERFLOW), HELIOS, Rotorcraft Comprehensive Analysis System (RCAS), NASTRAN and FLUENT. The coupled Computational Fluid Dynamics (CFD)-Computational Structural Dynamics (CSD) analysis combining RCAS and OVERFLOW was found to be most promising for predicting vibratory loads for coaxial configurations. Fuselage and empennage testing for the SB> 1 Defiant was discussed in Ref. 55. A detailed CFD analysis of the S-97 Raider using STAR-CCM+ was published in Ref. 56. The study examined the component wise contributions to lift and drag, as well as the effect of rotor wake interactions on propulsor efficiency.

1.3.3 Rotor wake modeling

The complex aerodynamic environment over the rotor is governed by its wake system. Various methods have been considered for analysis and simulation of the coaxial rotor wake. Several existing SMR models have been modified for use on coaxial rotors. The rotor wake modeling approaches can be broadly divided into inflow models, Lagrangian methods, and Eulerian methods, shown in Fig. 1.12. Inflow models provide a distribution of induced velocities over the rotor disk based on analytical expressions or differential equations, without solving the rotor wake flow field itself. The parameters for the models are typically extracted from experiments or higher fidelity rotor wake simulations.

In Lagrangian methods, the rotor wake is represented using vortex elements that are tracked over time. The most common Lagrangian approach is the *free wake* method using vortex filaments. More recently, free wake methods have used vortex particle representations as well. To facilitate the distinction between the two approaches in this document, the term Free Vortex Wake (FVW) is used exclusively for *vortex filament* free wake methods and the term Vortex Particle Method (VPM) is used for *vortex particle* free wake methods.

Eulerian methods solve fluid dynamics equations over a grid or multiple connected grids over the rotor wake. The term Computational Fluid Dynamics (CFD) generally refers to grid based methods. However strictly speaking, Lagrangian methods are also considered as examples of CFD. In this document, the term CFD is used exclusively to refer to the Eulerian approach.

The list of methods presented in Fig. 1.12 is not exhaustive, and only represents

some of the most common approaches used in the literature of coaxial rotor wake modeling. Note that in practical engineering analyses, these methods are often combined. The hybrid approaches depend on the desired accuracy and computational efficiency requirements. The following subsections briefly describe the methods and their application to coaxial rotor wake modeling.

1.3.3.1 Inflow models

Inflow models are computationally fast and easy to use. Therefore, these are used in rotorcraft design and flight simulation codes because they provide quick estimates of rotor thrust and power.

Momentum theory

Momentum theory is a basic inflow modeling approach [13, 57, 58]. In hover, uniform inflow is a reasonable assumption for SMR helicopters. However, it does not provide radial or azimuthal variation of loads. Non-uniform inflow momentum theory, such as Blade Element Momentum Theory (BEMT) provides an improved physical explanation of the radial distribution of loads and inflow on the rotors. However detailed aspects of the rotor wake are not modeled. Thus, momentum theory is not suitable for computing unsteady blade loads.

Initial research on the coaxial rotor focused on momentum theory. Reference 32 provides a brief description of work done in Russia and Japan that included expressions for rotor inflow and interaction factors based on modified momentum theory for coaxial rotors. However, these models provide a limited understanding of the flow features of the rotor wake and their dependence on rotor loading, solidity and separation.

Leishman and collaborators examined the applicability of momentum theory to

coaxial rotors in Refs. 59–61. Momentum theory and FVW methods were compared for coaxial *proprotors* in hover and axial flight in Ref. 59. The proprotor is a convertible rotor concept that can transition between generating lift to generating propulsive thrust. Optimum performance was achieved when both rotors had uniform disk loadings and equal torque. Performance improvement due to the recovery of the swirl momentum was only evident at high disk loading. Uniform inflow momentum theory was found to be unreliable. By comparison, BEMT results correlated better with experiments, except near the tip and the region of impingement of the upper rotor wake on the lower rotor.

Subsequently, the definition of an appropriate Figure of Merit (FM) for coaxial rotors was considered in Ref. 60. The study indicated that the comparison of SMR and coaxial rotor performance depends on how the FM is defined. Momentum theory was used at different thrust and torque conditions to calculate induced power interference factors. The results confirmed that coaxial rotor performance could be predicted using SMR expressions corrected with interference factors. The under-prediction of rotor power was attributed to the assumption that the lower rotor did not affect the upper rotor. In a similar study, expressions of mutual inflow interference were derived using BEMT in Ref. 62. These expressions were used with a variational approach to optimize the blade design of coaxial rotors.

The BEMT approach was explored further and compared with the FVW approach for optimizing the design of a coaxial system [61]. Rotor separation had minimal effects on the performance. It was noted that the optimum design for efficient axial flight could not be obtained due to the large number of design variables associated with multiple rotors, and constraints for maintaining torque balance while avoiding stall.

In Ref. 63, the vortex wake system of a hovering isolated and coaxial rotor was incorporated in a momentum theory based actuator disk model for the rotor. The wake was approximated by axisymmetric contracting vortex rings. The predicted non-uniform inflow distribution at hover was consistent with numerical and analytical solutions in literature. The study concluded that the approach accurately captured influence of the lower rotor on the upper rotor as well as the effect of the contracted upper rotor wake in the outboard region of the lower rotor disk.

Dynamic inflow

In dynamic inflow, the effect of the wake on the rotor disk is modeled as a set of ordinary differential equations (ODE). Dynamic inflow models are based on the assumptions of incompressible-inviscid flow and a rigid cylindrical wake. The induced velocity at different points on the rotor disk is obtained from a state-space model with rotor loads as the input. The state-space form of dynamic inflow models is convenient to use in flight simulation codes. Several research groups have adapted these models for coaxial rotors.

Analytical formulations of coaxial rotor dynamic inflow models have been derived in Refs. 64 and 65. Reference 64 combined two single rotors using superposition to represent a coaxial rotor dynamic inflow model in hover. An analytical time delay equation was derived to incorporate the interaction effects between the upper and lower rotor. The analytical model was compared with the Viscous Vortex Particle Method (VVPM) [66]. The results indicated that the analytical model over-predicted the inflow at the lower rotor because viscous dissipation is not included. In Ref. 65, the sensitivity of the hub loads and flapping response to coaxial rotor dynamic inflow parameters was studied. Results were compared for articulated and stiff coaxial ro-

tors. The study provided corrections to the dynamic inflow model for a non-zero LO coaxial rotor. Recently, a simple dynamic inflow model was coupled with centrally hinged root spring flapping blade structural dynamics for coaxial rotors [67].

Several studies have used FVW models to extract paramters for coaxial rotor dynamic inflow models [68, 69]. In Ref. 68, a coaxial rotor dynamic inflow model was derived from the GT-Hybrid FVW code. The rotor interference effects were used to augment influence coefficient matrices in Active-Receiving Rotor Inflow Model (AR-RIM), a finite state, potential theory based state space model. Hover thrust and power were accurately predicted. However, the model could not represent the complex aerodynamic interactions in forward flight. A similar approach was employed using the Maryland Free Wake (MFW) model to extract a coaxial rotor dynamic inflow model [69]. It was found that the first-order models were not sufficiently accurate. Therefore, time delays were incorporated to capture missing effects.

Similarly, the VVPM was used to develop a finite state dynamic inflow model for coaxial rotors [70–72]. The blade structural dynamics and airloads were obtained using the FLIGHTLAB simulation environment. The dynamic inflow model was capable of capturing disk loading and power consumption of the SMR and coaxial rotors. For flight dynamics applications, the low frequency response of the inflow model is the most important component. Therefore, the accuracy of the dynamic inflow model was demonstrated only in the low frequency range. Results indicated that the first order state-space inflow model captured accurately the physics of inflow dynamics for the coaxial system.

The most recent development in dynamic inflow models for coaxial rotors is the application of CFD to extract inflow coefficients in hover and forward flight [73]. The

results had good agreement with the VVPM calculations for the Harrington rotor [33].

1.3.3.2 Lagrangian methods

Rotor wake simulation is a coupled convection-diffusion problem suitable for a Lagrangian formulation. A variety of vortex methods exist for solutions of the rotor wake. Typically, tip and root vortices are discretized as vortex filaments, and shed vorticity from the blades is modeled as vortex sheets. The effects of viscosity are included using empirical parameters that control the size and strengths of these vortices as a function of time.

In the prescribed wake model, a fixed cylindrical helical structure for the tip vortices is assumed. The strengths or locations of the vortex filaments do not change with time. Only a limited number of studies have applied a prescribed wake approach to coaxial rotors. Free wake methods are associated with numerical instabilities. They do not always converge rapidly to a periodic solution. Therefore efforts have focused on improving empirical models, and accelerate convergence to the correct solution. However, additional physical effects such as the interaction of physical boundaries with the vortices cannot be modeled conveniently. This is critical for accurate rotor wake prediction in the vicinity of the rotor. The modeling of additional physical factors such as the rotor hub and fuselage also becomes important since they significantly alter the path of the rotor wake.

Free wake modeling using vortex filaments

Reference 74 presents a detailed geometrical description of a coaxial rotor wake. Methods based on momentum theory and simplified FVW are derived for the complex wake geometry and the interaction between the rotors. It is notable that this study rep-

resents one of the earliest attempts to characterize the rotor wake geometry for a coaxial rotor.

A comprehensive study detailing the formulation of a wake model for multi-rotor systems was developed by Bagai and Leishman [75]. A predictor-corrector approach was used for time integration. The maximum intensity of mutual interaction and distortions between wake vortices occurred at low advance ratios, consistent with experimental and simulation studies. The upper rotor wake contracted radially at a faster rate than the lower rotor and was ingested into the lower rotor stream tube. The presence of the inner vortex tube axially contracted the outer vortex spirals from the lower rotor. The severity of axial distortion of the tip vortices was increased compared to the SMR. The distortion of each rotor's wake was found to increase due to mutual interference. However, the rotor wakes retained their individual concentric structures, and did not intertwine or coalesce into combined vortex bundles. The tip vortices rolled up into two distinct bundles and orbited each other as they convected downstream.

In another study, the Comprehensive Hierarchical Aeromechanics Rotorcraft Model (CHARM) rotorcraft code was used to model a coaxial rotor system [76]. The CHARM code is an extensively validated comprehensive rotorcraft analysis code that combines a full-span FVW model with a fast lifting surface panel analysis. This code uses hierarchical fast vortex and fast panel techniques that achieve a computational time complexity of $\mathcal{O}(N \log N)$, instead of $\mathcal{O}(N^2)$ for N number of computational elements. CHARM includes a linear finite element structural analysis for rotor blade mode shapes, and can generate blade dynamic response. A predictor-corrector method is available for maneuvering and aperiodic flight. The CHARM results for a coaxial rotor indicated that the coaxial rotor wake has a larger degree of symmetry

in forward flight when compared to the SMR. However, the results displayed poor correlation with experiments at high advance ratios. Initially the absence of a fuselage in the simulations was considered to be the source of the discrepancy. However, incorporation of these effects did not produce significant differences. Errors were also attributed to inconsistencies in the experiments conducted in Refs. 33, 34. Noise comparisons between isolated and coaxial rotor were also conducted by combining CHARM with WOPWOP [76].

A time-marching free-wake method for the rotor wake analysis was used in Ref. 77, using an unsteady source-doublet panel method and a time marching free wake model. SMR performance results were within 2.4% of experimental data. The axial descent rate of coaxial rotor tip vortices was faster compared to SMR tip vortices. Radial contraction of the lower rotor tip vortices was slower than the upper rotor. The tip vortices oscillated along the azimuth angle due to the varying relative positions of blades of the two rotors. The interaction between the strong starting vortex and the wake created at the rotor hub was identified as the source of wake instability.

Hover performance calculation of coaxial rotors using Comprehensive Analytical Model of Rotorcraft Aerodynamics and Dynamics (CAMRAD II) FVW was conducted in Ref. 78. The free wake model provided satisfactory correlation with Harrington [33], Aero-Flight Dynamics Directorate (AFDD) coaxial rotor [36] and XH-59A [44] experiments. The axial wake displacement of the upper rotor wake was twice that of the lower rotor. The outer helicoidal wake convected with the downwash velocity of the lower rotor. The upper and lower rotor wake geometries remained distinct and did not diffuse into each other. The Reynolds number correction improved the performance prediction substantially. The simulations failed to capture trends of the ground effect on a coaxial rotor. The effect of rotor spacing was found to be small

when in close proximity to the ground.

Free wake using vortex particles

The need for developing improved tools for rotor wake dynamics led to the application of the Viscous Vortex Particle Method. To accurately simulate a complex rotor wake, it is necessary to preserve coherent vorticity structures over large distances without numerical dissipation, while retaining physical diffusion and dissipation due to viscosity and turbulence for wake decay. VPM has been used for modeling Kelvin-Helmholtz instabilities, separated flows [79, 80], evolution of vortex rings and in plasma physics [81]. The application of VVPM to helicopter wakes was proposed several decades ago [82], however it has received significant research interest relatively recently. In the last few years, VVPM has been used to examine propeller-wing effects in High Altitude Long Endurance (HALE) [83, 84] and Urban Air Mobility (UAM) aircraft [85].

The VVPM is a grid free approach for solving the vorticity-velocity form of the incompressible Navier-Stokes equations [86–88]. In some studies, viscosity is ignored, therefore they are referred to as just VPM. Artificial numerical dissipation is avoided because VVPM is a grid free method. The method solves for the vorticity strength and motion of vortex particles present in the flow field. This is a N-body problem which requires $\mathcal{O}(N^2)$ calculations per time step. However the use of fast algorithms such as the TreeCode and the Fast Multipole Method (FMM) allow the computations to be performed in $\mathcal{O}(N \log N)$ or $\mathcal{O}(N)$ time. The vorticity in the field originates from the rotor blade and body surfaces. VVPM can be coupled with CFD or lifting line models to obtain blade sectional aerodynamic loads, which are required to determine the vorticity generation.

One of the first studies to apply VVPM for rotor wakes was Ref. 89. The study

examined the wake structure of a two bladed SMR. The study showed excellent agreement with experimental data of the tip vortex trajectories. It was noted that a slowly starting rotor gives rise to a stable wake structure in the simulation, compared to an impulsively started rotor.

A combined unsteady panel method and vortex particle wake was applied to rotorcraft aerodynamics and aeroacoustics in Refs. 90 and 91. The studies described the GENeral Unsteady Vortex Particle (GENUVP) code developed as a component for the aeroelastic and aeroacoustic modeling of the NASA/Army/MIT Active Twist Rotor. Viscous interactions between particles were not modeled. The vortex particle calculations were accelerated using the particle-mesh technique. In this method, the particle quantities are projected on a cartesian grid, where the solution is calculated and then interpolated back to the particles. The computational cost is reduced from $\mathcal{O}(N^2)$ to $\mathcal{O}(N \log N)$ for N particles. However due to errors introduced by the method, the particle-mesh was applied only for the far wake region beyond the fuselage of the helicopter. The code was verified by comparisons with CAMRAD II and DYMORE for blade spanwise loading in hover and forward flight. Acoustic results also showed good correlation with experimental data.

A detailed description of the use of VPM for rotorcraft applications was presented in Ref. 92. The study compared different formulations for vorticity generation from lifting surfaces. Engineering corrections to account for separated flow and boundary layer effects on the airfoil surface were discussed. The use of CFD grids near boundary surfaces was considered for superior accuracy. Results indicated reasonable agreement with measurements of blade surface pressure distribution for a SMR. Errors near the inboard region of the blades were attributed to the absence of the hub in simulations.

In Refs. 93, 94 and 70, the lifting line representation was used with the local angle of attack, Mach number and dynamic pressure to obtain blade loads. Bound circulation on the blades was obtained from the Kutta-Joukowski theorem. The total vorticity generated at each time step was shed as vortex particles along the blade trajectory. The SMR wake and dynamic response were accurately predicted in Ref. 93. Sensitivity studies were conducted on the modeling parameters to identify adequate size and spacing of vortex particles.

The VVPM was implemented in the FLIGHTLAB environment [94]. To decrease computational expense, a two-loop trim algorithm was used. The inner loop included the vehicle dynamics and aerodynamics employing a finite state inflow model. The outer loop simulated the rotor wake using the VVPM. Good correlation was found with SMR downwash results at different heights. Ground effect and ship landing calculations were also found to be accurate.

The use of a hybrid CFD method allows accurate modeling of viscous flow near the blades, and a non-dissipating rotor wake over large distances [95, 96]. The VVPM vorticity information was obtained from the Navier-Stokes CFD solution on unstructured grids around the blade. The influence of the rotor wake was applied on the far field boundary of the CFD domain. Each rotor was solved independently using CFD, however the interaction between rotors was based exclusively on the VVPM. Results from this study produced reasonable agreement with experimental flow field measurements.

In another study, VVPM calculations on a rigid coaxial rotor [97] were compared with CFD-CSD sectional airloads from Ref. 98. The results were in good agreement. However, the computational runtime of the CFD-CSD results was 9600 CPU hours

compared to only 155 CPU hours for the VVPM approach. The study concluded that as flight speed increases, the blade passage effect on the loads of the coaxial rotor become more pronounced.

1.3.3.3 Eulerian Methods

The limitations of inflow models and Lagrangian methods has led to the application of Eulerian methods, i.e. conventional CFD to analyze coaxial rotors aerodynamics. A well-developed CFD computation can capture all the important features present in the flow, including viscous and compressible effects on surfaces. However, there are several limitations to this method, especially for rotorcraft. Complex grids are required to adequately represent blade geometry because of varying Reynolds number and Mach number over the blade span. Additionally, blade grids need to be rotating while maintaining connectivity with the rest of the domain. Due to the inherent numerical diffusion in Cartesian grids, vorticity structures present in the flow are artificially dissipated. Fine grids are required to capture wake vortices with sufficient resolution. The grid size is extensive because the wake extends a considerable distance beyond the rotor. These requirements can prohibit practical applications. Currently, CFD is computationally too expensive to use for vibration control or design optimization studies. Only with recent increase in availability of computational power, it has become possible to simulate the counter-rotating multiple blade coaxial rotor system.

Navier Stokes CFD solutions

The first high-resolution CFD analysis for coaxial rotors using a compressible RANS solver OVERTURNS on structured overset meshes was conducted in Ref. 99. Sliding meshes were required for the counter-rotating blades. The CFD calculations provided good correlation with SMR experiments. Results indicated that the upper rotor contributes 55% of the total thrust, consistent with experiments and other simulations.

Both rotors had degraded performance compared to the SMR. Unsteadiness in the thrust and torque varied between 5-10% of the mean values. The high frequency vibration in the loads was attributed to the venturi effect (blade passage effect). The vibrations were more impulsive for the upper rotor compared to the lower rotor. The location of coaxial BVI in hover depended on the thrust coefficient. Due to the wake interaction, blade spanwise loading was shifted outboard. A complex flow field was produced by the interaction of the upper rotor vortex with the bottom rotor blades, and the interaction between the tip vortices and the inboard sheet. The upper rotor vortices became distorted after impinging on the blade.

A hybrid CFD method for coaxial rotors was considered in Ref. 100. A 3D unsteady viscous compressible flow solver using Reynolds Averaged Navier Stokes (RANS) was used to obtain a time accurate, finite volume solution on a curvilinear body-fitted coordinate system over the blades. The hybrid Spalart-Allmaras turbulence model with Detached Eddy Simulation (DES) was employed. Outside of the rotor grid, the wake structure was represented using vortex filaments. The DYMORE code was used for CSD calculations. Computational cost was reduced using parallel processors to obtain coupled CFD-CSD solutions overnight. The coaxial rotor validation with XH-59A data was poor compared to the SMR case. For the SMR, performance results were similar to BEMT calculations. It was postulated that modeling a rectangular root blade spar was required for accurate prediction of drag and power. Other alternatives of improvement included better turbulence modeling and transition modeling for the unsteady separated flow. A denser spanwise and surface normal grid was required to capture 3D flow and dynamic stall effects, respectively.

A detailed numerical simulation of unsteady flow around a coaxial rotor helicopter in forward flight was conducted in Ref. 101. The unsteady Euler equations were

solved on unstructured dynamic overset grids. Hence, viscosity and turbulence were not included. Both rotors of the coaxial system had degraded performance compared to SMRs. There was good agreement with the performance results from experiments conducted in Japan [32]. The magnitude of the thrust oscillations for the upper rotor was slightly larger than those calculated for the lower rotor. The downwash velocity at the plane of the lower rotor was also larger than that of an SMR.

The CFD code HELIOS was coupled with RCAS to simulate a coaxial rotor to analyze unsteady forces and blade deflection [102]. The results were compared with experimental data from Ref. 40. The thrust sharing varied between 53%-56%, consistent with experiments. The lower rotor had comparatively less oscillations in forces and moments due to the blade passage interactions. However, it experienced additional coaxial BVI from the upper rotor tip vortex. The percentage variation with respect to the mean thrust for each rotor was approximately equal to 8%. By comparison, the magnitude of the oscillation in thrust was 0.05% for the SMR. The impulsive loads due to the rotor interaction did not have significant effect on the vertical deflections of the blades. However, the upper rotor had larger flap deflections compared to the lower rotor, due to the greater amount of thrust.

A comparative study of BEMT, FVW and CFD applied to a coaxial rotor in hover to analyze performance and blade loading was conducted in Ref. 103. Results were compared with experimental data from Ref. 36. The BEMT analysis used table look-up for 2D airfoils that included corrections for Mach number, Reynolds number and stall effects. A prescribed inflow model was used. The FVW analysis employed was based on the MFW [104]. The CFD computations used OVERFLOW2 with structured overset grids. A sizable center body was required to prevent counter-rotating blade root vortices from combining and forming an unrealistic upwash. BEMT and

FVW predicted the blade loading distribution well, however CFD overestimated it by 8%.

Reference 103 concluded that BEMT should be used for preliminary design and performance. FVW can be used for modeling unsteadiness and 3D effects that are useful for blade design. CFD is essential for obtaining airfoil pressure distributions, and allows viscous unsteady flow modeling. The study indicated the advantages of combining different methods. FVW can be used to correct BEMT, and CFD can be used to improve FVW by providing tailored table look-ups of airfoil coefficients, calibration of semi-empirical unsteady airfoil models and simple vortex evolution models.

The blade passage effect on a coaxial rotor was examined using CFD in a series of studies [105–108]. The OVERFLOW CFD code was used to develop an understanding of the pressure field around two airfoils traveling in opposite directions. The results indicated that airfoil thickness, vertical separation and Mach number were key parameters in predicting the magnitude and azimuthal variation of the impulsive loading. The 3D incompressible unstructured RANS code Rotor Unstructured Navier-Stokes (RotUNS) was used for modeling the coaxial rotor in hover and forward flight. The 3D study was aimed at determining the effect of number of blades and planform on rotor acoustics and performance. The predicted performance correlated well with CAMRAD II computations.

Reference 109 used an extensive CFD-CSD framework to analyze the effect of coaxial rotor-fuselage interaction. The CSD solver Parallelized Rotorcraft comprehensive Analysis for Simulation And Design (PRASADUM) developed at University of Maryland was coupled with the CREATE-AV Helios CFD framework. The CFD grids used for the fuselage and rotor exceeded 100 million points. The computa-

tional cost of a typical coaxial simulation was of the order of 9600 CPU hours. Three fuselage configurations were tested: a simple X2TD shaped body, body with tail empennage, and body with tail empennage and rotor mast. Rotor thrust increased in the presence of the fuselage. The lower rotor produced larger thrust than the upper rotor in forward flight. The total thrust and power was same for all three fuselage configurations. The difference between the configurations was only apparent in the local distribution of loading at sections inboard of 30% of the blade span. The lateral asymmetry in fuselage loads resulted in a net yawing moment. The study concluded that refined fuselage geometry had minimal direct effect on the rotor sectional airloads.

Another study used the CFD code OVERFLOW to investigate the interactional effects of rotor spacing and fuselage on the performance and efficiency of coaxial systems [110]. A hybrid RANS/Large Eddy Simulation (LES) turbulence model, DES was employed for the CFD calculations. The XV-15 rotor system was modeled in hover, using structured overset grids with approximately 67-86 million grid points. The results indicated that overall thrust increased with decrease in rotor spacing. The reduction of thrust in the lower rotor at large rotor spacing was attributed to increase in turbulence in the lower rotor wake.

A hybrid CFD-FVW approach to analyze coaxial rotor performance in hover was presented in Ref. 111. The compressible flow solver GT-Hybrid was used to solve the Navier Stokes equations in the vicinity of the rotor. The wake was captured with FVW in the near field and prescribed trajectories in the far field. The vortex-induced velocities from the wake were applied at the boundary of the CFD grid and vortex elements were generated from CFD calculations into the free wake. A coarse grid with approximately 400,000 grid points, and a fine grid with approximately 3.3 million grid

points were employed for comparison with experimental data of Ref. 33. The trends for thrust, power and figure of merit were captured well, although the results were not as good when compared to other methods such as Vorticity Transport Model (VTM) [112] and VVPM [70]. Discrepancies in inflow and vortex descent rate were attributed to numerical diffusion and grid density.

The CFD-CSD framework developed in Ref. 109 was applied to a notional X2TD configuration in high speed flight [113]. The computations captured blade passage loads that were previously not captured with a simple lifting-line model. The CFD results provided improved predictions of retreating blade reverse flow at high advance ratios including blade pitching moments for elliptic airfoil sections. This work was further extended to a full helicopter configuration, i.e., including the fuselage, empennage and propulsor [114]. The study was computationally expensive: approximately 7 million grid points were required for the rotor, 15 million for the fuselage, 13 million for the propulsor, and 115 million for the off body domain. The results indicated that the blade passage loading was the dominant source of vibratory loads. The aerodynamic interaction between the fuselage and rotor wake increased the N_b/rev loads.

Vorticity Transport Model

The Vorticity Transport Model (VTM) is considered an intermediate fidelity approach between conventional RANS based CFD and FVW methods. The VTM approach is a time dependent computational solution of the vorticity-velocity form of the incompressible Navier Stokes equations in the Eulerian representation. The discretized equations are solved using the finite volume Total Variation Diminishing (TVD) method over a Cartesian adaptive grid surrounding the vehicle. The flow is inviscid everywhere, except on solid surfaces which generate vorticity.

The main advantage of this approach is its ability to deal effectively with the issue of numerical dissipation of vorticity on grids. Instead of solving the governing equations of the flow in conservative variable form like conventional CFD, the results are computed directly in terms of vorticity and velocity. Therefore, VTM is well suited for long range aerodynamic interactions between two main rotors and geometrically well separated components of the aircraft. This approach was used in a series of studies [112, 115–121] aimed at understanding and modeling the coaxial rotor wake system.

Coaxial rotor performance and wake dynamics in steady and maneuvering flight were analyzed in Ref. 115. The results were found to be sensitive to profile drag characteristics. There was increased drag near the highly loaded tip of the rotor. At zero thrust, the predicted power consumption was lower than the experimental results. This implied that there is viscous interaction between the upper and lower rotors. The systematic underprediction of power at all advance ratios was attributed to experimental inaccuracies [34]. The blade passage effect loads were larger on the lower rotor compared to the upper rotor. The variability in the loads was attributed to low-frequency fluctuations in the geometry of the rotor wake. This was a natural consequence of the periodic interactions between the blades of the two rotors. The wake geometry affected the induced power. The tip vortices from the upper and lower rotor interweaved in the gap between rotors, leading to a complicated pattern of coaxial BVI. The inter-rotor BVI persisted in forward flight and was found to be prominent on the advancing side. Increasing the load factor increased the influence of vortices shed from the blade root, especially on the rear of the rotors. The study also noted that the improved performance of the coaxial system came at the cost of significantly higher vibration levels.

A generic thrust compounded hingeless rigid 3 blade ABC rotor was considered in Ref. 118. The rotors were phased such that the blades overlapped over the centerline of the fuselage. The increased hub stiffness modified the strength of BVI, and affected intensity and directivity of the BVI noise. Decreasing the LO increased BVI and power requirement. The lower rotor inflow was influenced by both its own and the upper rotor tip vortices. The interaction was found to be strongest at an advance ratio of 0.15. Periodic ingestion of the coaxial rotor wake caused fluctuations in the thrust produced by the propulsor. The thrust fluctuation was at the N_b/rev frequency. The propulsor was a significant source of dynamic excitation. The BVI impulses originated almost entirely from the lower rotor. The rear quadrant of the advancing side of each rotor was highly loaded, and therefore contributed significantly to noise. The propulsor influenced the directionality of the noise signals from the vehicle.

Reference 121 presented an improved approach for comparing single and coaxial rotors. The variability between Harrington [33] and Dingeldein [34] experimental drag characteristics was identified as a major obstacle in the comprehensive validation of numerical predictions. A separate study compared the coaxial and conventional rotor performance using VTM [112]. The coaxial rotor wake was found to maintain its helical structure for longer periods and therefore was more stable than a SMR wake. This led to increased tail-shake and rotor-fuselage interaction. The relative merits between the coaxial and the SMR configurations were closely tied to the position and strength of tip vortex collision with the blades of the rotor.

1.3.4 Aeromechanics studies

The combination of complex unsteady aerodynamic interaction and stiff hingeless blades leads to a unique aeromechanical environment for the coaxial rotor system.

While many studies have focused on predicting rotor performance, relatively few studies have combined structural and aerodynamic components of a coaxial rotor to examine the vibrations and aeroelastic stability of such configurations.

Reference 122 used University of Maryland Advanced Rotorcraft Code (UMARC) to predict dynamic response of the coaxial rotor examined in Ref. 40. The UMARC code employs 2nd order, nonlinear isotropic Euler-Bernoulli beam for modeling the blade with coupled flap, lag, torsion and axial motion. The Weissinger-L lifting line theory and time accurate free wake were used for computing blade loads and rotor wake. The airfoil properties were obtained from a CFD enhanced table look-up. The calculated performance compared well with the Harrington rotor experiments [33]. The blade bending stresses were greater for the lower rotor when compared to the upper rotor, and increased with advance ratio. Increasing the phase angle in the cyclic coupling alleviated the overall bending stresses in the blades. Results showed that a larger rotor LO provided significant benefits in power and thrust. However, the advantages came at the cost of increased blade loads.

This study was extended to forward flight in Ref. 123 complementing the experimental study in Ref. 41. It focused on the effect of LO on the coaxial rotor performance and loads. The far-wake FVW model described in Ref. 75 was employed as part of the modified UMARC. The simulation correctly predicted the superior thrust performance of the lower rotor compared to the upper rotor as observed in Ref. 41, although its magnitude was under-predicted. The side force results correlated poorly with experimental measurements, an effect attributed to inadequate modeling of the rotor aeroelasticity. The study illustrated that there are fundamental deficiencies in using conventional rotor aerodynamic models for predicting vibratory loads. Important trends may be captured, however the magnitude of loads calculated was found

to be inaccurate.

The effect of LO on a coaxial rotor was examined in detail in Refs. 124 and 125. The LO increased the maximum thrust of a rotor at a given speed by modifying the lift distribution around the rotor disk. The improved efficiency came at the cost of increased blade loads. Inter-rotor aerodynamic interactions decreased significantly with increasing speed. In hover, the upper rotor is more efficient compared to the lower rotor. However, the lower rotor thrust efficiency increases with forward speed and becomes more efficient than the upper rotor. The relative phase of the two rotors modified the resultant total loads significantly.

A study on small unmanned coaxial helicopters [126] analyzed the flapping motion of the rotor blades. The stabilizer bar dynamics, lower rotor cyclic pitch control and variable RPM were included in the model. The structural model assumed centrally hinged spring restrained rigid blades. The aerodynamic model included quadratic airfoil lift and drag coefficients coupled with BEMT. The main contribution of this study is the derivation of a closed form simple aeroelastic model for the coaxial rotor.

Fuselage aerodynamics and rotor structural dynamics of a coaxial helicopter were studied using VTM in Ref. 117. The rotor model consisted of rigid, centrally hinged spring restrained blades. Coupled flap-lag-feather dynamics were considered. The structural tailoring had little effect on modifying the inherent vibrational characteristics of the vehicle. The unsteady aerodynamic forcing produced pitch and heave excitation at the blade passage frequency. The improvement in performance compared to an equivalent SMR came at the cost of vibrations and noise. The aerodynamic environment was dominated by the direct impingement of the upper rotor wake on the lower rotor. Fluctuations were noted in the propulsor thrust due to main rotor

wake ingestion. Noise studies were also performed in Refs. 116 and 118.

RCAS simulations of the XH-59A helicopter were conducted in Ref. 127 to compare performance, loads and vibrations at different trim settings. The blades were modeled with finite elements, and table look-up was used for aerodynamic loads. A prescribed wake model was used to reduce computational cost, however no indication on its ability to capture rotor wake interaction effects was provided. Due to the availability of additional control variables such as rotor speed and propulsive thrust, several trim combinations of aircraft pitch attitude and thrust could be studied for a given advance ratio. Significant power savings were indicated by slowing the rotor between 40%-65% of the nominal RPM, and at a higher aircraft pitch attitude. It was noted that using the main rotor transmission to drive the propulsor could reduce total power requirement and vibratory loads significantly. Vibrations were dominant at 3/rev due to the three bladed rotors.

1.4 Objectives of the dissertation

The literature survey indicates that a major portion of prior coaxial rotor research has focused on evaluating rotor thrust and power in hover and forward flight. Although excessive vibrations have been a practical challenge for the XH-59A and Sikorsky X2TD, relatively few studies have analyzed loads and vibrations of the coaxial rotors. Furthermore, previous studies have not addressed the aeroelastic stability of stiff hingeless coaxial rotor configurations.

Coaxial rotors experience significant vibrations due to blade-wake interactions and blade passage effect. Therefore, accurate rotor wake modeling is a key element in the analysis of coaxial rotors and this topic is far from being well understood. A

variety of Eulerian and Lagragian methods have been applied to model the complex flow field of the coaxial rotor wake. Conventional CFD still remains computationally expensive for design and control studies. Furthermore, wakes computed using CFD suffer from excessive numerical dissipation. Vortex filament based FVW methods are computationally efficient, however they fail to completely capture the near wake system of the coaxial rotor. Both FVW and VTM methods use empirical corrections to include viscous effects in their solutions. VVPM can represent the complete trailing and shed wake of the coaxial rotor including physical viscous diffusion effects, and therefore is a more effective approach when compared to vortex filaments based FVW.

Another important element missing in previous studies is the accurate modeling of unsteady aerodynamic spanwise loading along the blade. Most studies employ some form of a quasi-steady lifting line method to determine blade spanwise loads. The error in computing unsteady blade loads propagates to the rotor wake structure due to the interdependence of blade loads and rotor wake [128]. These errors are particularly significant in the highly complex flow field of a coaxial rotor system. Hence, a higher fidelity approach for calculating unsteady aerodynamic loads is required.

From the review of previous research, it is evident that the aeromechanical behavior of coaxial rotors is still not well understood. This is due to the lack of an efficient comprehensive analysis which can accurately capture the structural dynamics, aerodynamic loads and rotor wake. The goal of this dissertation is to address these challenges by developing a coaxial rotor aeroelastic formulation and applying it to a rotor resembling the Sikorsky X2TD. The specific goals of this dissertation are:

1. Development and application of VVPM to model a coaxial rotor wake system, with an unsteady spanwise aerodynamic load distribution that is valid for both attached and separated flow.

2. Formulation and solution of the coaxial rotor trim problem in hover and forward flight.

3. Development of a periodic aeroelastic stability analysis for stiff hingeless coaxial rotor blades in hover and forward flight.

4. Examination of aeromechanical behavior of a coaxial rotor resembling the Sikorsky X2TD, emphasizing the effects of LO on inflow, hub loads, aeroelastic stability and blade response.

1.5 Key contributions of the dissertation

The work presented in this dissertation has produced several novel contributions to the state-of-the-art coaxial rotor research. These contributions are summarized below:

1. Developed a modular comprehensive analysis for coaxial rotors that combines non-linear hingeless blade structural dynamics with a reduced order model (ROM) for aerodynamic loads and VVPM based rotor wake modeling. The comprehensive analysis is also applicable to the SMR configuration. Therefore, the characteristics of both configurations can be compared and enhance our understanding of the fundamental behavior of coaxial rotors.

2. Derived analytical expressions for vortex particle interactions with blade bound circulation. Also, provided corrections to the original formulation of diagnostic terms in a generic VVPM flow field [86]. These corrections lead to differences in previously reported validation studies on vortex ring modeling using VVPM.

3. Developed a systematic analysis of blade bound circulation and wake induced velocities on the rotor disk, and examined their individual contribution to mean and oscillatory hub loads.

4. Presented a novel approach to model DS by integrating the ONERA-DS model with VVPM and generate leading edge separated wake structures present on a coaxial rotor in high speed flight.

5. Formulated free-flight/propulsive trim analysis for coaxial rotor helicopters in forward flight incorporating propulsor thrust and fuselage tilt.

6. Identified the coaxial rotor in hover as a periodic system due to the blade passage effect, for the first time in the literature. As a consequence, Floquet theory has to be applied to determine coaxial rotor aeroelastic stability in hover.

7. Developed a unique graphical approach for systematic identification of coaxial rotor aeroelastic modes and facilitate the determination of coupling between rotors.

1.6 Dissertation outline

The dissertation is divided into 8 chapters. A brief history, literature review, and scope of the thesis is presented in Chapter 1. The aeromechanical formulation and aerodynamic modeling approach are described in Chapters 2 - 4. Chapter 2 provides the overall aeroelastic formulation for the coaxial rotor system. The blade coordinate systems, equations of motion and spanwise loads are described for counter-rotating hingeless blades. Chapter 3 describes the ROMs for determining the unsteady spanwise aerodynamic loads on the blade. The transformation of the two-dimensional (2D) airfoil loads to the spanwise blade loads and bound circulation distribution is presented. Chapter 4 contains the first-principles formulation of VVPM. The generation of vortex particles from the rotor blade in attached as well as separated flow are described. The solution procedure is provided in Chapter 5. The chapter contains the formulation and analysis of coaxial rotor trim in hover and forward flight. It presents

the aeroelastic stability analysis of the periodic system together with a new graphical approach for identifying blade modes and determine aeroelastic coupling. Chapters 6 - 7 present the results of the computational simulations. Chapter 6 describes the notional Sikorsky X2TD rotor used in the study. The results are analyzed to determine distribution of inflow and loads between the upper and lower rotor, and their aeroelastic stability in hover. Chapter 7 presents results for the X2TD rotor in forward flight. The rotor inflow distribution, vibratory loads, blade response and aeroelastic stability are examined at different advance ratios and LOs. Chapter 8 summarizes the work presented together with the new contributions made in the dissertation and provides recommendations for future work.

CHAPTER 2

Overview of Aeromechanical Modeling

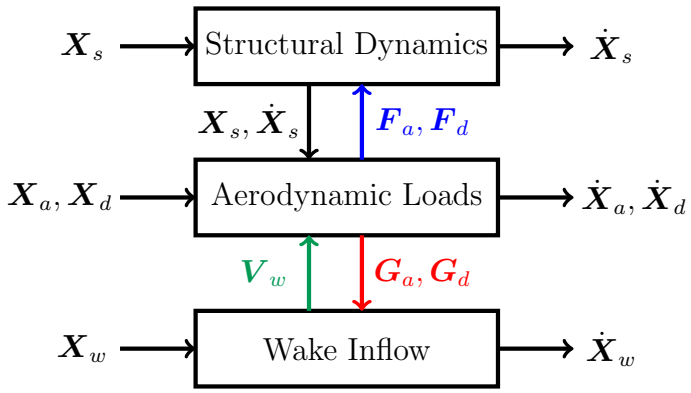

Figure 2.1: Schematic of aeroelastic solver and exchange of state variables

The aeromechanics of a coaxial rotor combines the aeroelasticity of counter-rotating blades with unsteady rotor-wake interactions. The aeromechanical formulation combines three essential components as shown in Fig. 2.1: *structural dynamics*, *aerodynamic loads*, and the *wake inflow*. Each component determines the rate of change $\dot{\boldsymbol{X}}$ given a current state vector $\boldsymbol{X}$. The states of the three components are coupled in a non-linear manner. The time response of the system is obtained through time integration of the rate of the combined state vector.

The structural dynamics module determines the elastic and inertial blade loads due to the blade deformation states ($\boldsymbol{X}_s$, $\dot{\boldsymbol{X}}_s$). The aerodynamic loads module determines the attached flow ($\boldsymbol{F}_a$) and DS loads due to flow separation ($\boldsymbol{F}_d$). The CFD based Rational Function Approximation (CFD-RFA) is used to compute the

attached flow spanwise aerodynamic loads. The ONERA-DS model is used to calculate the spanwise aerodynamic loads in separated flow. The aerodynamic loads are determined by the attached flow aerodynamic states ($\boldsymbol{X}_a$), DS states ($\boldsymbol{X}_d$), and the total velocities and accelerations at each blade section. The total velocities and accelerations are obtained from the blade motion, the structural deformation velocities and acceleration ($\boldsymbol{X}_s$, $\dot{\boldsymbol{X}}_s$), and the velocities induced by the wake ($\boldsymbol{V}_w$) at the blade section. The aerodynamic loads provide the distribution of bound circulation due to attached flow circulation ($\boldsymbol{G}_a$) and DS circulation ($\boldsymbol{G}_d$) to the wake inflow module. The wake inflow is computed using VVPM. New particles are generated based on the bound circulation on the blade. The particle positions and vorticity strengths are assembled into the wake state vector ($\boldsymbol{X}_w$). The velocities of the particles and rate of change of strength ($\dot{\boldsymbol{X}}_w$) are determined by inter-particle interactions and velocities induced by the bound circulation. The combined states are integrated in time to obtain the dynamic response of the blades.

A detailed description of the modeling of aerodynamic loads is provided in Chapter 3. The wake modeling using VVPM is presented in Chapter 4.

2.1 Rotor modeling assumptions

1. The coaxial rotor consists of two vertically separated counter-rotating rotors. The rotors are attached to separate hollow shafts on a single axis which allow them to spin in opposite directions. The shafts are not modeled in the analysis. Each rotor has N_b hingeless blades.

2. The hingeless blades are cantilevered at their root with a hub offset e from the axis of rotation.

3. The blade feathering axis and elastic axis are coincident. They are preconed by

an angle β_p at the blade root.

4. The undeformed blade is straight with a built-in pre-twist distribution θ_{tw} about the blade elastic axis.

5. The blade has no sweep, droop or torque offset.

6. The blade cross section is symmetric about its principal axes.

7. The blade chord c, thickness t_h, mass per unit length m, principal cross section mass moments of inertia I_{m_y} and I_{m_z}, bending stiffnesses EI_y and EI_z, and torsional stiffness GJ vary along the blade span.

8. The blade is inextensible. Elastic bending deflections are moderate and the strains are small.

9. The rotational speed Ω of the upper and lower rotors is equal and constant, i.e., $\dot{\Omega} = 0$.

10. The rotor shaft is rigid, and fuselage degrees of freedom are ignored.

2.2 Coordinate systems

The aeroelastic formulation for a coaxial rotor requires several coordinate systems. The upper and lower rotor require separate rotating frames of reference because the blades rotate in opposite directions. The non-rotating hub fixed coordinate systems are shown in Fig. 2.2. The upper rotor hub is located at the point $\boldsymbol{C}_u$. The lower rotor hub is located at the point $\boldsymbol{C}_l^*$. The vertical separation between the two rotor hubs is h. The upper rotor blades rotate counter-clockwise. The lower rotor blades rotate clockwise, therefore the coordinate system follows the left-hand rule instead of the conventional right-hand rule. The two coordinate systems and the relations between them are described next.

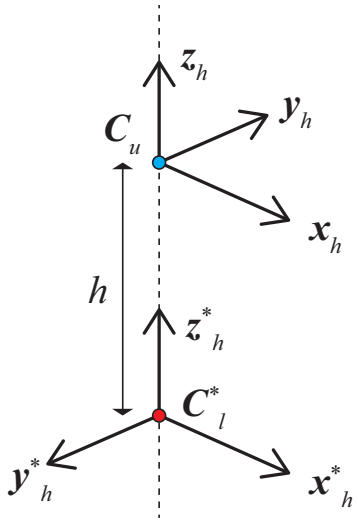

Figure 2.2: Coaxial rotor non-rotating hub fixed coordinate systems

2.2.1 Counter-clockwise rotating blade

The coordinate systems for a counter-clockwise rotating blade are illustrated in Fig. 2.3. The hub is located at the point $\boldsymbol{C}$. The **non-rotating hub fixed** frame $(\boldsymbol{x}_h, \boldsymbol{y}_h, \boldsymbol{z}_h)$ is colored black. The $\boldsymbol{x}_h$ axis points towards the rear of the helicopter. The $\boldsymbol{y}_h$ axis points towards the starboard side of the helicopter.

The **rotating hub-fixed** coordinate system $(\boldsymbol{x}_r, \boldsymbol{y}_r, \boldsymbol{z}_r)$ is in blue in Fig. 2.3. The axes are rotated about the hub along the $\boldsymbol{z}_h$ axis by the azimuthal angle ψ. The transformation from the hub fixed system to the rotating frame is:

$$\begin{Bmatrix} \widehat{\boldsymbol{i}}_r \\ \widehat{\boldsymbol{j}}_r \\ \widehat{\boldsymbol{k}}_r \end{Bmatrix} = \begin{bmatrix} \cos\psi & \sin\psi & 0 \\ -\sin\psi & \cos\psi & 0 \\ 0 & 0 & 1 \end{bmatrix} \begin{Bmatrix} \widehat{\boldsymbol{i}}_h \\ \widehat{\boldsymbol{j}}_h \\ \widehat{\boldsymbol{k}}_h \end{Bmatrix} \tag{2.1}$$

where $\widehat{\boldsymbol{i}}, \widehat{\boldsymbol{j}}, \widehat{\boldsymbol{k}}$ are the unit vectors along the $\boldsymbol{x}, \boldsymbol{y}, \boldsymbol{z}$ axes respectively.

The **undeformed blade** coordinate system $(\boldsymbol{x}_b, \boldsymbol{y}_b, \boldsymbol{z}_b)$ is rotated by the precone

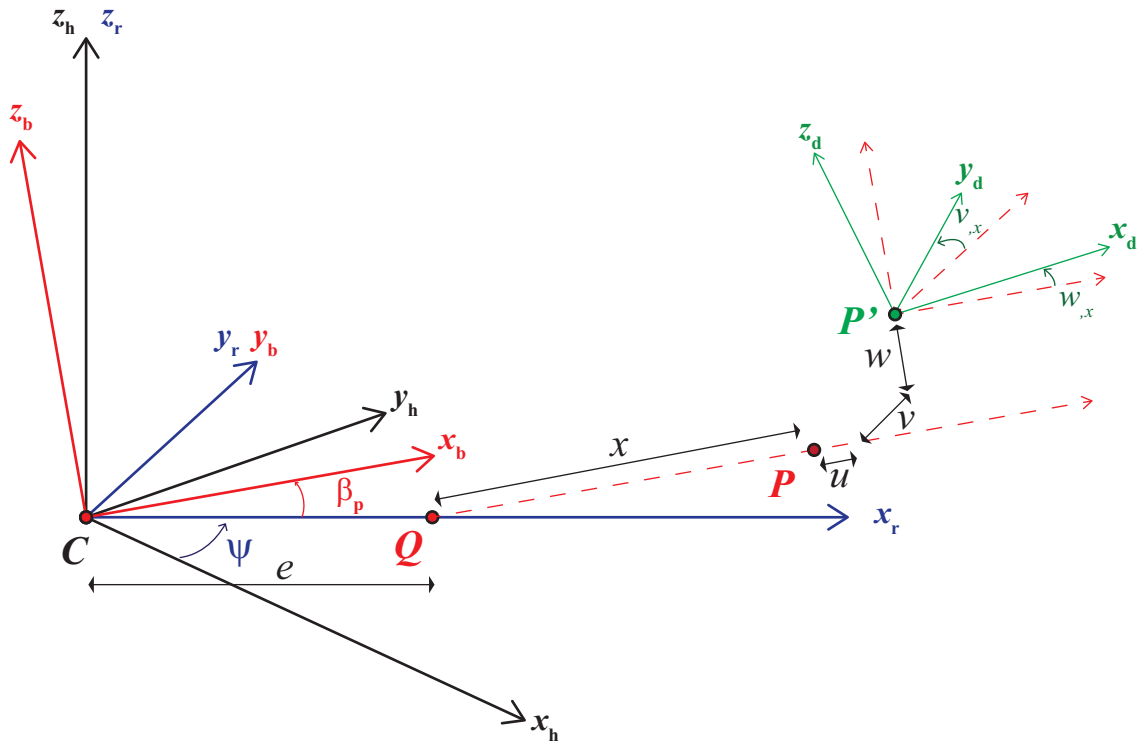

Figure 2.3: Coordinate systems for counter-clockwise rotating blade

angle β_p about the $\boldsymbol{y}_r$ axis. These axes are in red. Note that the $\boldsymbol{x}_b$ axis is parallel to the elastic and feathering axes of the blade. The coordinate system rotations are represented by the transformation:

$$\begin{Bmatrix} \widehat{\boldsymbol{i}}_b \\ \widehat{\boldsymbol{j}}_b \\ \widehat{\boldsymbol{k}}_b \end{Bmatrix} = \begin{bmatrix} \cos\beta_p & 0 & \sin\beta_p \\ 0 & 1 & 0 \\ -\sin\beta_p & 0 & \cos\beta_p \end{bmatrix} \begin{Bmatrix} \widehat{\boldsymbol{i}}_r \\ \widehat{\boldsymbol{j}}_r \\ \widehat{\boldsymbol{k}}_r \end{Bmatrix} \tag{2.2}$$

The root of the hingeless blade is attached to the rotor hub at the point $\boldsymbol{Q}$. The hub offset e is the distance between the hub center $\boldsymbol{C}$ and point $\boldsymbol{Q}$.

$$e = |\boldsymbol{Q} - \boldsymbol{C}| \tag{2.3}$$

The length l of the blade is defined:

$$l = R - e \tag{2.4}$$

The coordinates of a point $\boldsymbol{P}$ at a distance x from the root on the undeformed elastic axis of the blade are:

$$\boldsymbol{P} = \boldsymbol{C} + e\widehat{\boldsymbol{i}}_r + x\widehat{\boldsymbol{i}}_b \tag{2.5}$$

The point $\boldsymbol{P}$ is translated to $\boldsymbol{P'}$ due to structural deformations u, v, w in the axial, lead-lag and flap directions respectively. The location of the new point is:

$$\boldsymbol{P'} = \boldsymbol{C} + e\widehat{\boldsymbol{i}}_r + (x+u)\widehat{\boldsymbol{i}}_b + v\widehat{\boldsymbol{j}}_b + w\widehat{\boldsymbol{j}}_b \tag{2.6}$$

Due to the deformation, the coordinate system attached to the point $\boldsymbol{P'}$ undergoes rotations in the flap and lag directions. The **deflected blade** coordinate system $(\boldsymbol{x}_d, \boldsymbol{y}_d, \boldsymbol{z}_d)$ is in green in Fig. 2.3. The order of the rotations is 1) an angle of $w_{,x}$ about the negative $\boldsymbol{y}_b$ axis, and 2) an angle of $v_{,x}$ about the $\boldsymbol{z}_b$ axis. Therefore:

$$\begin{Bmatrix} \widehat{\boldsymbol{i}}_d \\ \widehat{\boldsymbol{j}}_d \\ \widehat{\boldsymbol{k}}_d \end{Bmatrix} = \begin{bmatrix} \cos w_{,x} \cos v_{,x} & \sin v_{,x} & \sin w_{,x} \cos v_{,x} \\ -\cos w_{,x} \sin v_{,x} & \cos v_{,x} & -\sin w_{,x} \sin v_{,x} \\ -\sin w_{,x} & 0 & \cos w_{,x} \end{bmatrix} \begin{Bmatrix} \widehat{\boldsymbol{i}}_b \\ \widehat{\boldsymbol{j}}_b \\ \widehat{\boldsymbol{k}}_b \end{Bmatrix} \tag{2.7}$$

Figure 2.4 illustrates the coordinate systems viewed along the plane of the blade cross section. The $(\boldsymbol{x}_d, \boldsymbol{y}_d, \boldsymbol{z}_d)$ coordinate system is rotated by an angle of $(\theta+\phi)$ about the $\boldsymbol{x}_d$ axis to obtain the **twisted blade** coordinate system $(\boldsymbol{x}_t, \boldsymbol{y}_t, \boldsymbol{z}_t)$ marked in violet in Fig. 2.4.

$$\begin{Bmatrix} \widehat{\boldsymbol{i}}_t \\ \widehat{\boldsymbol{j}}_t \\ \widehat{\boldsymbol{k}}_t \end{Bmatrix} = \begin{bmatrix} 1 & 0 & 0 \\ 0 & \cos(\theta+\phi) & \sin(\theta+\phi) \\ 0 & -\sin(\theta+\phi) & \cos(\theta+\phi) \end{bmatrix} \begin{Bmatrix} \widehat{\boldsymbol{i}}_d \\ \widehat{\boldsymbol{j}}_d \\ \widehat{\boldsymbol{k}}_d \end{Bmatrix} \tag{2.8}$$

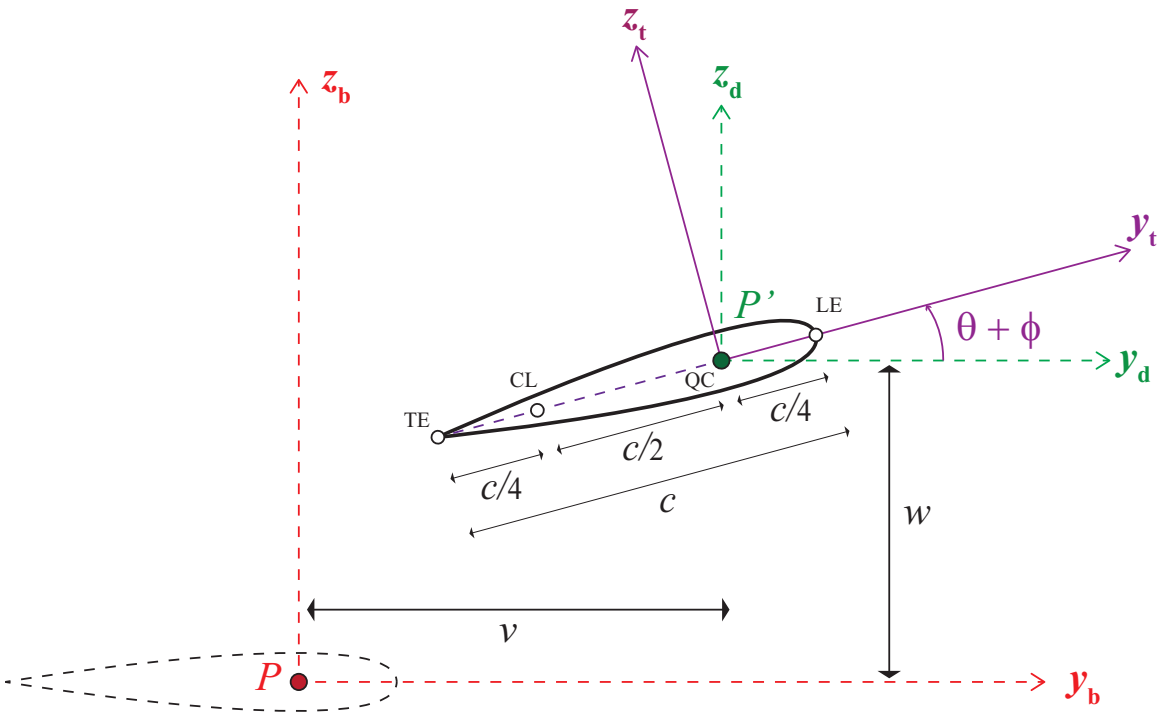

Figure 2.4: Blade cross section coordinate systems

The elastic axis and the feathering axis are assumed to be coincident. The feathering axis passes through the quarter chord (QC) of the airfoil. The leading edge (LE), QC, collocation point (CL) and trailing edge (TE) all lie along the $\boldsymbol{y}_t$ axis. The locations of these points are given by:

$$\mathbf{LE} = \boldsymbol{P'} + \left(\frac{c}{4}\right)\widehat{\boldsymbol{j}}_t \tag{2.9}$$

$$\mathbf{CL} = \boldsymbol{P'} - \left(\frac{c}{2}\right)\widehat{\boldsymbol{j}}_t \tag{2.10}$$

$$\mathbf{TE} = \boldsymbol{P'} - \left(\frac{3c}{4}\right)\widehat{\boldsymbol{j}}_t \tag{2.11}$$

2.2.2 Clockwise rotating blade

The coordinate systems for a clockwise rotating blade are illustrated in Fig. 2.3. The hub is located at the point $\boldsymbol{C}^*$. The **non-rotating hub-fixed** coordinate system $(\boldsymbol{x}_h^*, \boldsymbol{y}_h^*, \boldsymbol{z}_h^*)$ is shown in black. The $\boldsymbol{x}_h^*$ axis points towards the rear of the helicopter.

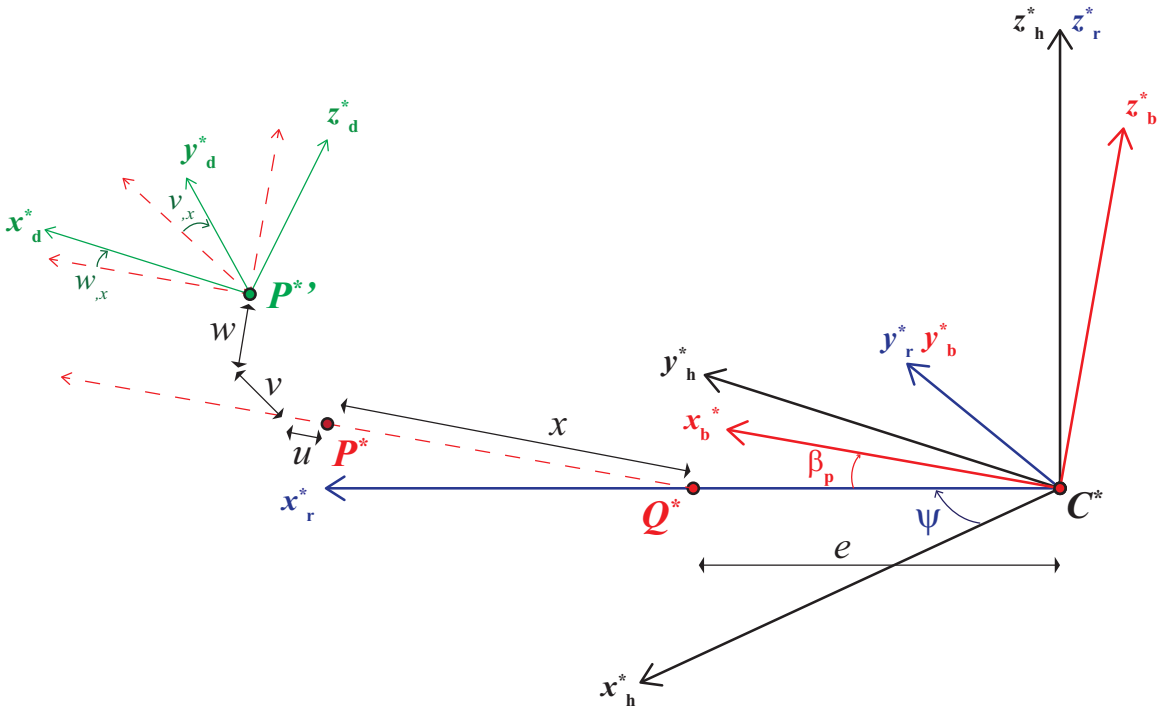

Figure 2.5: Coordinate systems for clockwise rotating blade

The $\boldsymbol{y}_h^*$ axis points towards the port side of the helicopter. Note that this is no longer a right handed coordinate system. Therefore, $\widehat{\boldsymbol{i}}_h^* \times \widehat{\boldsymbol{j}}_h^* = -\widehat{\boldsymbol{k}}_h^*$. The advantage of using a left-handed coordinate systems is that the rotational transformations and position vectors derived for the counter-clockwise rotor blade are the same in this new system. Therefore, the equations can be conveniently re-used in the computer code. The transformation from the **non-rotating hub-fixed** system to the **rotating hub-fixed** system is:

$$\begin{Bmatrix} \widehat{\boldsymbol{i}}_r^* \\ \widehat{\boldsymbol{j}}_r^* \\ \widehat{\boldsymbol{k}}_r^* \end{Bmatrix} = \begin{bmatrix} \cos\psi & \sin\psi & 0 \\ -\sin\psi & \cos\psi & 0 \\ 0 & 0 & 1 \end{bmatrix} \begin{Bmatrix} \widehat{\boldsymbol{i}}_h^* \\ \widehat{\boldsymbol{j}}_h^* \\ \widehat{\boldsymbol{k}}_h^* \end{Bmatrix} \tag{2.12}$$

The **undeformed blade** coordinate system $(\boldsymbol{x}_b^*, \boldsymbol{y}_b^*, \boldsymbol{z}_b^*)$ in red is represented by the transformation:

$$\begin{Bmatrix} \widehat{\boldsymbol{i}}_b^* \\ \widehat{\boldsymbol{j}}_b^* \\ \widehat{\boldsymbol{k}}_b^* \end{Bmatrix} = \begin{bmatrix} \cos\beta_p & 0 & \sin\beta_p \\ 0 & 1 & 0 \\ -\sin\beta_p & 0 & \cos\beta_p \end{bmatrix} \begin{Bmatrix} \widehat{\boldsymbol{i}}_r^* \\ \widehat{\boldsymbol{j}}_r^* \\ \widehat{\boldsymbol{k}}_r^* \end{Bmatrix} \tag{2.13}$$

The coordinates of a point $\boldsymbol{P}^*$ on the undeformed elastic axis is:

$$\boldsymbol{P}^* = \boldsymbol{C}^* + e\widehat{\boldsymbol{i}}_r^* + x\widehat{\boldsymbol{i}}_b^* \tag{2.14}$$

The point $\boldsymbol{P}^*$ after deformation is $\boldsymbol{P}^{*\prime}$:

$$\boldsymbol{P}^{*\prime} = \boldsymbol{C}^* + e\widehat{\boldsymbol{i}}_r^* + (x+u)\widehat{\boldsymbol{i}}_b^* + v\widehat{\boldsymbol{j}}_b^* + w\widehat{\boldsymbol{j}}_b^* \tag{2.15}$$

The **deflected blade** coordinate system $(\boldsymbol{x}_d^*, \boldsymbol{y}_d^*, \boldsymbol{z}_d^*)$ is shown in green in Fig. 2.5.

$$\begin{Bmatrix} \widehat{\boldsymbol{i}}_d^* \\ \widehat{\boldsymbol{j}}_d^* \\ \widehat{\boldsymbol{k}}_d^* \end{Bmatrix} = \begin{bmatrix} \cos w_{,x}\cos v_{,x} & \sin v_{,x} & \sin w_{,x}\cos v_{,x} \\ -\cos w_{,x}\sin v_{,x} & \cos v_{,x} & -\sin w_{,x}\sin v_{,x} \\ -\sin w_{,x} & 0 & \cos w_{,x} \end{bmatrix} \begin{Bmatrix} \widehat{\boldsymbol{i}}_b^* \\ \widehat{\boldsymbol{j}}_b^* \\ \widehat{\boldsymbol{k}}_b^* \end{Bmatrix} \tag{2.16}$$

For the clockwise rotating blade, the blade twist $(\theta + \phi)$ is in the negative $\boldsymbol{x}_d^*$ axis. Therefore, the transformation from the **deflected blade** coordinate system $(\boldsymbol{x}_d^*, \boldsymbol{y}_d^*, \boldsymbol{z}_d^*)$ to the **twisted blade** coordinate system $(\boldsymbol{x}_t^*, \boldsymbol{y}_t^*, \boldsymbol{z}_t^*)$ is.

$$\begin{Bmatrix} \widehat{\boldsymbol{i}}_t^* \\ \widehat{\boldsymbol{j}}_t^* \\ \widehat{\boldsymbol{k}}_t^* \end{Bmatrix} = \begin{bmatrix} 1 & 0 & 0 \\ 0 & \cos(\theta+\phi) & \sin(\theta+\phi) \\ 0 & -\sin(\theta+\phi) & \cos(\theta+\phi) \end{bmatrix} \begin{Bmatrix} \widehat{\boldsymbol{i}}_d^* \\ \widehat{\boldsymbol{j}}_d^* \\ \widehat{\boldsymbol{k}}_d^* \end{Bmatrix} \tag{2.17}$$

The locations of the LE, CL and TE are:

$$\mathbf{LE}^* = \boldsymbol{P}'^* + \left(\frac{c}{4}\right)\widehat{\boldsymbol{j}}_t^* \tag{2.18}$$

$$\mathbf{CL}^* = \boldsymbol{P}'^* - \left(\frac{c}{2}\right)\widehat{\boldsymbol{j}}_t^* \tag{2.19}$$

$$\mathbf{TE}^* = \boldsymbol{P}'^* - \left(\frac{3c}{4}\right)\widehat{\boldsymbol{j}}_t^* \tag{2.20}$$

In the subsequent sections, the descriptions and derivations are the same for the clockwise and counter-clockwise blades unless specified otherwise.

2.3 Hingeless blade structural dynamics

The rotor blade is modeled as a slender cantilever beam composed of a linearly elastic homogeneous material undergoing moderate deflections with fully coupled flap-lag-torsional dynamics [129], which are suitable assumptions for a coaxial rotor with stiff hingeless blades. The formulation has been described in previous work [130–134]. The equations presented in this dissertation are identical except for the change in symbols.

2.3.1 Cross section structural modeling

The Sikorsky X2TD blade (Fig. 2.6) has a non-uniform taper, twist and thickness distribution [46]. Therefore, the sectional mass, inertia moments, and stiffness properties change along the blade span. The blade structural modes and frequencies depend on the spanwise distribution of these structural properties. Due to the limited availability of data, the structural properties were estimated by matching the known structural frequencies of the rotating blade. Therefore, a suitable blade cross section model was assumed.

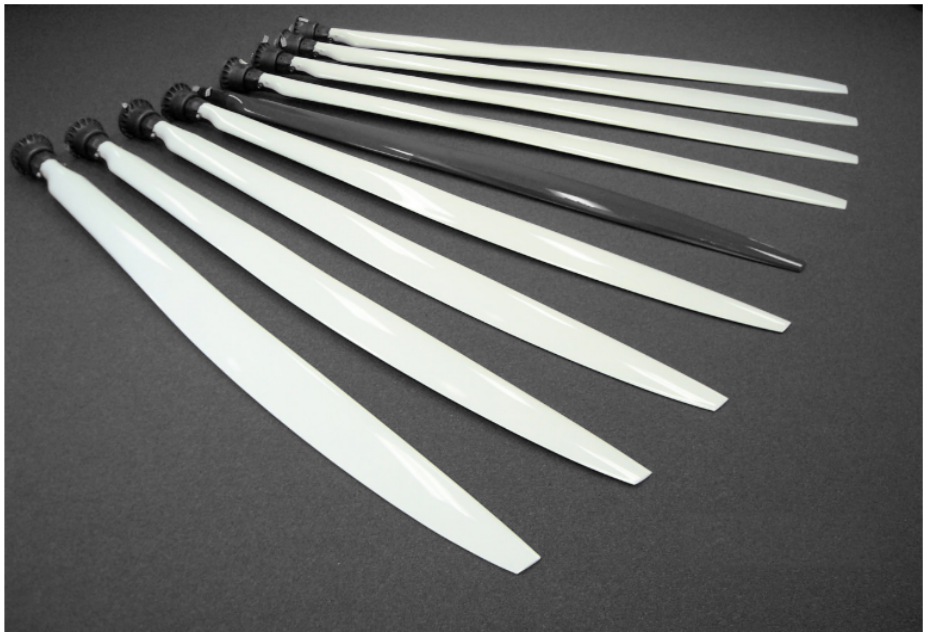

Figure 2.6: Sikorsky X2TD blades

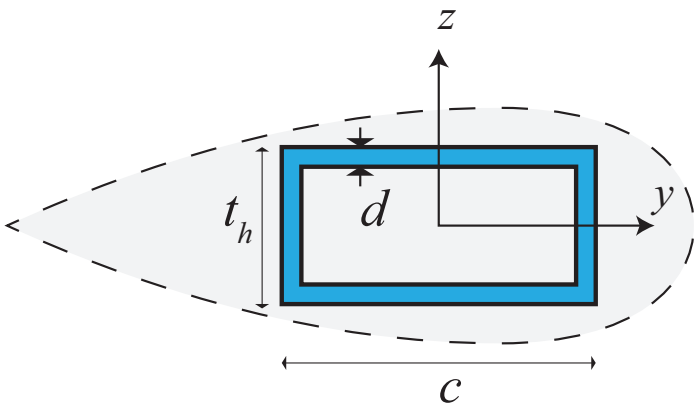

Figure 2.7: Blade cross section modeled as a hollow rectangle

The blade cross section is modeled as a hollow rectangular section shown in Fig. 2.7. The width of the cross section is assumed to be proportional to the chord c of the airfoil at a given spanwise location. The height of the cross section is proportional to the thickness t_h of the airfoil. The thickness d of the wall is assumed to be small compared to the chord and thickness of the airfoil. Therefore, the theory of bending and torsion in thin-walled sections can be applied (Chp. 5, [135]).

$$d << t_h, c \tag{2.21}$$

Based on these assumptions, the mass distribution m/m_o, mass moment of inertia distribution I_m/I_{m_o}, bending stiffness distribution EI/EI_o and torsional stiffness GJ/GJ_o are evaluated. The subscript 'o' refers to the blade properties at the root of the blade $x = 0$.

2.3.1.1 Cross sectional properties

The mass per unit length of the blade is:

$$m = \int_A \rho_b \mathrm{d}A = \rho_b A = 2\rho_b(c + t_h)d \tag{2.22}$$

The mass distribution over the span of the blade is proportional to the area of the cross section.

$$\frac{m}{m_o} = \frac{c + t_h}{c_o + t_{h_o}} \tag{2.23}$$

The geometrical area moments of inertia about the centroid of the rectangle are:

$$I_y = \int_A z^2 \mathrm{d}A = \frac{dt_h^2}{6}(t_h + 3c) \tag{2.24}$$

$$I_z = \int_A y^2 \mathrm{d}A = \frac{dc^2}{6}(c + 3t_h) \tag{2.25}$$

The mass moments of inertia are proportional to the area moments of inertia of the cross section.

$$I_{m_y} = \int_A \rho_b z^2 \mathrm{d}A = \rho_b I_y \tag{2.26}$$

$$I_{m_z} = \int_A y^2 \mathrm{d}A = \rho_b I_z \tag{2.27}$$

Assuming isotropic elastic properties, the bending stiffnesses are also proportional to the area moments of inertia:

$$\frac{I_{m_y}}{I_{m_{yo}}} = \frac{EI_y}{EI_{y_o}} = \left(\frac{t_h + 3c}{t_{ho} + 3c_o}\right)\left(\frac{t_h}{t_{ho}}\right)^2 \tag{2.28}$$

$$\frac{I_{m_z}}{I_{m_{zo}}} = \frac{EI_z}{EI_{z_o}} = \left(\frac{c + 3t_h}{c_o + 3t_{ho}}\right)\left(\frac{c}{c_o}\right)^2 \tag{2.29}$$

From the perpendicular axis theorem, the mass moment of inertia about the blade axis $\boldsymbol{x}_b$ is:

$$I_{m_x} = I_{m_y} + I_{m_z} \tag{2.30}$$

Therefore:

$$\frac{I_{m_x}}{I_{m_{xo}}} = \left(\frac{c + t_o}{c_o + t_{ho}}\right)^3 \tag{2.31}$$

The torsional stiffness constant J can be derived analytically for a thin-walled closed section in the shape of a rectangle:

$$J = \frac{4(\text{enclosed area})^2}{\dfrac{\text{perimeter}}{\text{wall thickness}}} = \frac{2dc^2t_h^2}{c + t_h} \tag{2.32}$$

Under the assumption of constant elastic properties, the torsional stiffness distribution is:

$$\frac{GJ}{GJ_o} = \left(\frac{c}{c_o}\right)^2 \left(\frac{t_h}{t_{ho}}\right)^2 \left(\frac{c_o + t_{ho}}{c + t_h}\right) \tag{2.33}$$

Note that the centroid and shear center of a hollow rectangular section are coincident at the geometric center of the rectangle. The center of mass and aerodynamic center may be shifted from the center of the rectangular cross section. The blade equations of motion derived in Ref. 129 assume non-zero offset values for the center of mass and aerodynamic center from the elastic axis. However, due to the unavailability of the blade data, the center of mass, elastic center, aerodynamic center, and area centroid are all assumed to be located at the QC of the airfoil in this study.

2.3.1.2 Effect of blade twist

The cross section of the blade is rotated about the blade feathering axis $\boldsymbol{x}_b$ due to the built-in twist and the control input pitch angle. The geometrical pitch angle θ at a point on the blade varies with spanwise location x and azimuth ψ is:

$$\theta(x) = \theta_{tw}(x) + \theta_0 + \theta_{1c}\cos\psi + \theta_{1s}\sin\psi \tag{2.34}$$

The structural dynamics equations are written in the undeformed blade coordinate system. Therefore, the bending stiffness terms are transformed from the twisted blade coordinate system to the undeformed blade coordinate system:

$$\overline{EI}_y = EI_y\cos^2\theta + EI_z\sin^2\theta \tag{2.35}$$

$$\overline{EI}_z = EI_y\sin^2\theta + EI_z\cos^2\theta \tag{2.36}$$

$$\overline{EI}_{(y-z)_1} = (EI_y - EI_z)\cos\theta\sin\theta \tag{2.37}$$

$$\overline{EI}_{(y-z)_2} = (EI_y - EI_z)(\cos^2\theta - \sin^2\theta) \tag{2.38}$$

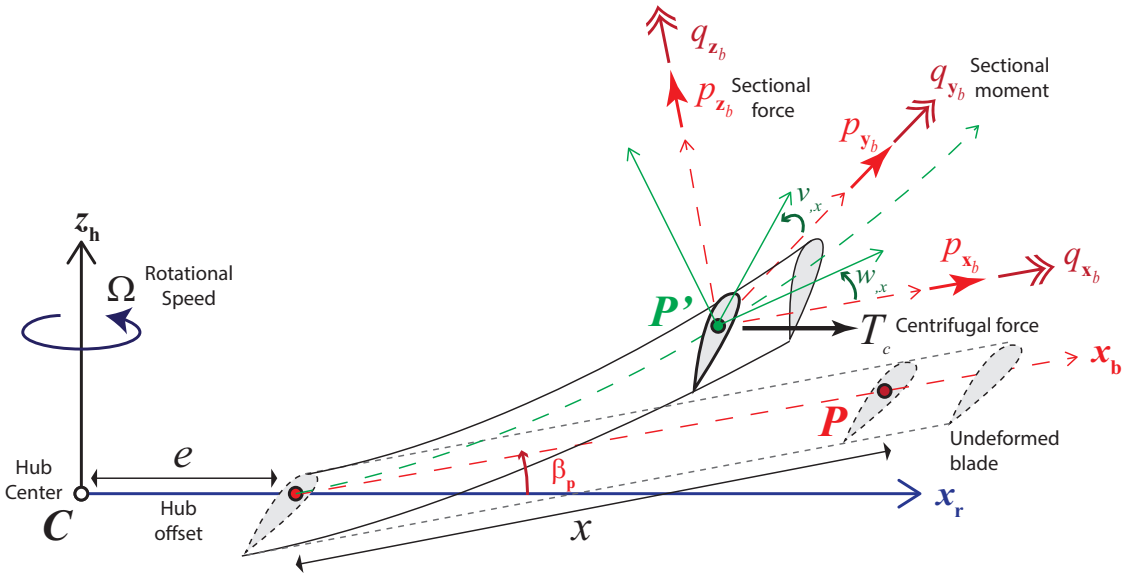

Figure 2.8: Loads acting on deformed blade cross section

Similarly, the mass moments of inertia are transformed to the undeformed blade coordinate system. Note that the structural twist ϕ is included for the inertial terms.

$$\overline{I}_{m_y} = I_{m_y}\cos^2(\theta+\phi) + I_{m_z}\sin^2(\theta+\phi) \tag{2.39}$$

$$\overline{I}_{m_z} = I_{m_y}\sin^2(\theta+\phi) + I_{m_z}\cos^2(\theta+\phi) \tag{2.40}$$

$$\overline{I}_{m_{(y-z)_1}} = (I_{m_y} - I_{m_z})\cos(\theta+\phi)\sin(\theta+\phi) \tag{2.41}$$

$$\overline{I}_{m_{(y-z)_2}} = (I_{m_y} - I_{m_z})\left[\cos^2(\theta+\phi) - \sin^2(\theta+\phi)\right] \tag{2.42}$$

2.3.2 Blade loads

The loads acting at a blade section are illustrated in Fig. 2.8. The force per unit span acting at a blade section is represented by $\boldsymbol{p}$. The moment per unit span acting at a blade section is represented by $\boldsymbol{q}$. The sectional loads consist of aerodynamic and inertial loads.

$$\boldsymbol{p} = \boldsymbol{p}^A + \boldsymbol{p}^I \tag{2.43}$$

$$\boldsymbol{q} = \boldsymbol{q}^A + \boldsymbol{q}^I \tag{2.44}$$

The loads are defined component wise in the undeformed blade coordinate system.

$$\boldsymbol{p} = p_{x_b}\widehat{\boldsymbol{i}}_b + p_{y_b}\widehat{\boldsymbol{j}}_b + p_{z_b}\widehat{\boldsymbol{k}}_b \tag{2.45}$$

$$\boldsymbol{q} = q_{x_b}\widehat{\boldsymbol{i}}_b + q_{y_b}\widehat{\boldsymbol{j}}_b + q_{z_b}\widehat{\boldsymbol{k}}_b \tag{2.46}$$

2.3.2.1 Inertial loads

The blade kinematics are derived in Appendix A. A point located at $\boldsymbol{r}$ on the blade cross section experiences an acceleration $\boldsymbol{a}_r$. The inertial loads acting at a blade cross section are obtained by integrating the product of the blade mass density ρ_b and acceleration over the area.

$$\boldsymbol{p}^I = -\int_A \rho_b \boldsymbol{a}_r \mathrm{d}A \tag{2.47}$$

$$\boldsymbol{q}^I = -\int_A (\boldsymbol{r} - \boldsymbol{P}) \times \rho_b \boldsymbol{a}_r \mathrm{d}A \tag{2.48}$$

The full expression for the acceleration $\boldsymbol{a}_r$ in the undeformed blade coordinate system is provided in Appendix A. The inertial force acting at a blade section is:

$$p^I_{x_r} = m[\Omega^2(x + e + u - \beta w) + 2\Omega\dot{v} + \beta\ddot{w} - \ddot{u}] \tag{2.49}$$

$$p^I_{y_r} = -m[\ddot{v} - \Omega^2 v + 2\Omega(\dot{u} - \beta_p\dot{w})] \tag{2.50}$$

$$p^I_{z_r} = -m(\beta\ddot{u} + \ddot{w}) \tag{2.51}$$

These forces are transformed to the undeformed blade coordinate system assuming the precone angle β_p is small:

$$p^I_{x_b} = p^I_{x_r} + \beta_p p^I_{z_r} \tag{2.52}$$

$$p^I_{y_b} = p^I_{y_r} \tag{2.53}$$

$$p^I_{z_b} = p^I_{z_r} - \beta_p p^I_{x_r} \tag{2.54}$$

The inertial moment acting at a blade section is:

$$\begin{aligned} q^I_{x_r} &= -I_{m_x}(\ddot{\theta}+\ddot{\phi}) + 2\overline{I}_{m_y}\Omega[(\dot{\theta}+\dot{\phi})v_{,x} - \dot{w}_{,x}] \\ &\quad +\overline{I}_{m_z}[2\dot{v}_{,x}\dot{w}_{,x} + v_{,x}\ddot{w}_{,x} + (w_{,x}+\beta_p)(\Omega^2 v_{,x} + \ddot{v}_{,x})] \\ &\quad +\overline{I}_{m_{(y-z)_2}}\Omega[\Omega + 2\dot{v}_{,x} + 2(w_{,x}+\beta_p)(\dot{\theta}+\dot{\phi})] \qquad (2.55) \\ q^I_{y_r} &= -I_{m_x}v_{,x}(\ddot{\theta}+\ddot{\phi}) + \overline{I}_{m_y}[\ddot{w}_{,x} - \Omega^2(w_{,x}+\beta_p) - 2\dot{v}_{,x}(\dot{\theta}+\dot{\phi})] \\ &\quad +\overline{I}_{m_{(y-z)_2}}[v_{,x}\Omega^2 - \ddot{v}_{,x} - 2\dot{w}_{,x}(\dot{\theta}+\dot{\phi})] \qquad (2.56) \\ q^I_{z_r} &= -I_{m_x}(w_{,x}+\beta_p)(\ddot{\theta}+\ddot{\phi}) - \overline{I}_{m_z}[\ddot{v}_{,x} + 2\dot{w}_{,x}(\dot{\theta}+\dot{\phi})] \\ &\quad +\overline{I}_{m_{(y-z)_2}}[\ddot{w}_{,x} - 2(\dot{v}_{,x}+\Omega)(\dot{\theta}+\dot{\phi})] \qquad (2.57) \end{aligned}$$

The inertial moments are transformed to the undeformed blade coordinate system using the following relations:

$$\begin{aligned} q^I_{x_b} &= q^I_{x_r} + \beta_p q^I_{z_r} \qquad (2.58) \\ q^I_{y_b} &= q^I_{y_r} \qquad (2.59) \\ q^I_{z_b} &= q^I_{z_r} - \beta_p q^I_{x_r} \qquad (2.60) \end{aligned}$$

Note that for the clockwise rotating blade, the sign of the moment vector changes.

$$(\boldsymbol{q}^I)^* = -\boldsymbol{q}^I \qquad (2.61)$$

2.3.2.2 Centrifugal force

The tension along the blade axis $\boldsymbol{x}_b$ is obtained from the inertial force $p^I_{x_b}$. When integrated, the tension is equal to the centrifugal force at a blade section:

$$T_c = \Omega^2 \int_x^l m(x+e)\mathrm{d}x \qquad (2.62)$$

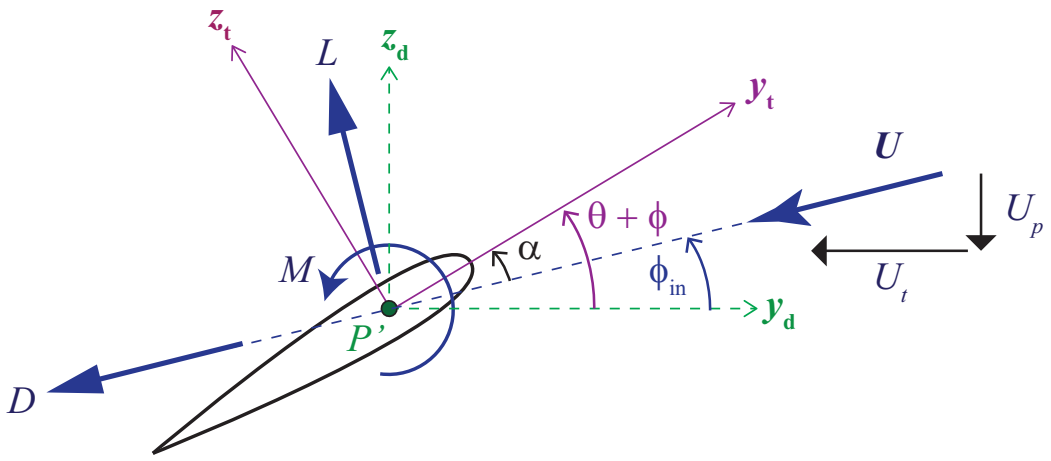

Figure 2.9: Aerodynamic loads on a blade cross section

The mass distribution of the X2TD blade varies non-linearly. Therefore, numerical integration is used to determine the centrifugal force at a point on the blade. The centrifugal force always acts in the direction of the rotating axis $\boldsymbol{x}_b$.

$$\boldsymbol{T}_c = T_c \widehat{\boldsymbol{i}}_b \tag{2.63}$$

2.3.2.3 Aerodynamic loads

The sectional lift, drag and moment are calculated using the sectional coefficients.

$$\mathcal{L} = \frac{1}{2}\rho U^2 c C_l \tag{2.64}$$

$$\mathcal{D} = \frac{1}{2}\rho U^2 c C_d \tag{2.65}$$

$$\mathcal{M} = \frac{1}{2}\rho U^2 c^2 C_m \tag{2.66}$$

The relative air speed $\boldsymbol{U}$ consists of a perpendicular and tangential component to the $\boldsymbol{y}_d$ axis as shown in Fig. 2.9.

$$\boldsymbol{U} = -U_t \widehat{\boldsymbol{j}}_d - U_p \widehat{\boldsymbol{k}}_d \tag{2.67}$$

The induced inflow angle ϕ_{in} is defined as:

$$\phi_{in} = \tan^{-1}\left(\frac{U_p}{U_t}\right) \tag{2.68}$$

The angle of attack of the airfoil is defined as:

$$\alpha = \theta + \phi - \phi_{in} \tag{2.69}$$

The sectional lift acts perpendicular to the relative air velocity experienced by the blade section. The sectional drag acts in the direction of the relative air velocity. The sectional moment acts along the deformed blade axis $\boldsymbol{x}_d$. Therefore, these loads can be transformed to the deflected blade coordinate system:

$$\boldsymbol{p}^A = -\left(\mathcal{D}\cos\phi_{\text{in}} + \mathcal{L}\sin\phi_{\text{in}}\right)\widehat{\boldsymbol{j}}_d + \left(\mathcal{L}\cos\phi_{\text{in}} - \mathcal{D}\sin\phi_{\text{in}}\right)\widehat{\boldsymbol{k}}_d \tag{2.70}$$

$$\boldsymbol{q}^A = \mathcal{M}\widehat{\boldsymbol{i}}_d \tag{2.71}$$

Under the assumption of small slopes, the aerodynamic loads can be transformed to the undeformed blade coordinate system:

$$p^A_{x_b} = \mathcal{L}\left(v_{,x}\sin\phi_{\text{in}} - w_{,x}\cos\phi_{\text{in}}\right) + \mathcal{D}\left(v_{,x}\cos\phi_{\text{in}} + w_{,x}\sin\phi_{\text{in}}\right) \tag{2.72}$$

$$p^A_{y_b} = -\mathcal{L}\sin\phi_{\text{in}} - \mathcal{D}\cos\phi_{\text{in}} \tag{2.73}$$

$$p^A_{z_b} = \mathcal{L}\left(\cos\phi_{\text{in}} + v_{,x}w_{,x}\sin\phi_{\text{in}}\right) + \mathcal{D}\left(v_{,x}w_{,x}\cos\phi_{\text{in}} - \sin\phi_{\text{in}}\right) \tag{2.74}$$

$$q^A_{x_b} = \mathcal{M} \tag{2.75}$$

$$q^A_{y_b} = v_{,x}\mathcal{M} \tag{2.76}$$

$$q^A_{z_b} = w_{,x}\mathcal{M} \tag{2.77}$$

Note that for the clockwise rotating blade, the sign of the moment vector changes.

$$(\boldsymbol{q}^A)^* = -\mathcal{M}\widehat{\boldsymbol{i}}_d^* \tag{2.78}$$

2.3.3 Equations of motion

The equations of motion of the blade are obtained from Ref. 129. The equations are a set of consistently derived non-linear partial differential equations (PDE) describing the coupled flap-lag-torsion dynamics of an isolated rotor blade.

Flap equation

$$\begin{aligned} -\left[\overline{EI}_y w_{,xx} - \overline{EI}_{(y-z)_1}(v_{,xx} + 2\phi w_{,xx}) - \overline{EI}_{(y-z)_2}\phi v_{,xx}\right]_{,xx} & \\ +(GJ\phi_{,x}v_{,xx})_{,x} + (w_{,x}T_c)_{,x} - (v_{,x}q_{x_b})_{,x} + q_{y_b,x} + p_{z_b} &= 0 \end{aligned} \tag{2.79}$$

Lag equation

$$\begin{aligned} -\left[\overline{EI}_z v_{,xx} - \overline{EI}_{(y-z)_1}(w_{,xx} - 2\phi v_{,xx}) - \overline{EI}_{(y-z)_2}\phi w_{,xx}\right]_{,xx} & \\ -(GJ\phi_{,x}w_{,xx})_{,x} + (v_{,x}T_c)_{,x} + (w_{,x}q_{x_b})_{,x} - q_{z_b,x} + p_{y_b} &= 0 \end{aligned} \tag{2.80}$$

Torsion equation

$$\begin{aligned} \left[GJ(\phi_{,x} - v_{,x}w_{,xx})\right]_{,x} - \left[\overline{EI}_{(y-z)_1}(v_{,xx}^2 - w_{,xx}^2) - \overline{EI}_{(y-z)_2}v_{,xx}w_{,xx}\right] & \\ +q_{x_b} + v_{,x}q_{y_b} + w_{,x}q_{z_b} &= 0 \end{aligned} \tag{2.81}$$

In a coaxial rotor, there are two sets of the equations of motion, one set for the upper rotor blade and one set for the lower rotor blade. Equations 2.79-2.81 are derived for a counter-clockwise rotating blade. For a clockwise rotating blade, the sign of the

spanwise moments is flipped.

$$q^*_{x_b} = -q_{x_b} \tag{2.82}$$

$$q^*_{y_b} = -q_{y_b} \tag{2.83}$$

$$q^*_{z_b} = -q_{z_b} \tag{2.84}$$

However, due to the change in sign in Eqns. 2.61 and 2.78, the overall equations of motion are unchanged. Therefore, the code implementation for the clockwise and counter-clockwise rotating blade equations of motion is identical.

2.3.4 Galerkin method

The system of PDEs (Eqns. 2.79-2.81) is transformed to a system of non-linear ODEs using the Galerkin method. The transformation removes the spatial dependence on x. The flap (w) and lag (v) deflections, and elastic twist (ϕ) are represented using uncoupled rotating mode shapes of the blade.

$$w \approx \widetilde{w}(x,t) = \sum_{i=1}^{n_F} a_{F_i}(t) W_i(x) \tag{2.85}$$

$$v \approx \widetilde{v}(x,t) = \sum_{i=1}^{n_L} a_{L_i}(t) V_i(x) \tag{2.86}$$

$$\phi \approx \widetilde{\phi}(x,t) = \sum_{i=1}^{n_T} a_{T_i}(t) \Phi_i(x) \tag{2.87}$$

The symbol "$\sim$" indicates that these are approximate representations of the exact deformations due to the limited number of modes n_F, n_L, n_T. The uncoupled rotating mode shapes W_i, V_i and Φ_i are generated using the first nine exact modes of a non-rotating uniform beam. Details of the frequency and mode shape calculations are provided in Appendix B.

2.3.4.1 Axial deformation

The blade is assumed to be inextensible. Therefore, the axial displacement at a spanwise location x is:

$$u(x) = -\frac{1}{2}\int_0^x \left(v_{,x}^2 + w_{,x}^2\right) \mathrm{d}x' \tag{2.88}$$

The approximation of the axial displacement is a non-linear function of the flap and lag generalized degrees coefficients. The integral can be simplified to:

$$\widetilde{u}(x,t) = \sum_{i=1}^{n_L}\sum_{j=1}^{n_L} a_{L_i}(t)a_{L_j}(t)\widetilde{U}_{L_{ij}}(x) + \sum_{i=1}^{n_F}\sum_{j=1}^{n_F} a_{F_i}(t)a_{F_j}(t)\widetilde{U}_{F_{ij}}(x) \tag{2.89}$$

where the approximate rotating axial displacement functions are defined using the rotating flap and lag modes of the blade:

$$\widetilde{U}_{F_{ij}}(x) = -\frac{1}{2}\int_0^x W_{i,x}(x')W_{j,x}(x')\mathrm{d}x' \tag{2.90}$$

$$\widetilde{U}_{L_{ij}}(x) = -\frac{1}{2}\int_0^x V_{i,x}(x')V_{j,x}(x')\mathrm{d}x' \tag{2.91}$$

The time derivatives of the axial terms are:

$$\dot{\widetilde{u}} = \sum_{i=1}^{n_L}\sum_{j=1}^{n_L} \left(\dot{a}_{L_i}a_{L_j} + a_{L_i}\dot{a}_{L_j}\right)\widetilde{U}_{L_{ij}} + \sum_{i=1}^{n_F}\sum_{j=1}^{n_F} \left(\dot{a}_{F_i}a_{F_j} + a_{F_i}\dot{a}_{F_j}\right)\widetilde{U}_{F_{ij}} \tag{2.92}$$

$$\begin{aligned}\ddot{\widetilde{u}} &= \sum_{i=1}^{n_L}\sum_{j=1}^{n_L} \left(\ddot{a}_{L_i}a_{L_j} + 2\dot{a}_{L_i}\dot{a}_{L_j} + a_{L_i}\ddot{a}_{L_j}\right)\widetilde{U}_{L_{ij}} \\ &\quad + \sum_{i=1}^{n_F}\sum_{j=1}^{n_F} \left(\ddot{a}_{F_i}a_{F_j} + 2\dot{a}_{F_i}\dot{a}_{F_j} + a_{F_i}\ddot{a}_{F_j}\right)\widetilde{U}_{F_{ij}}\end{aligned} \tag{2.93}$$

These definitions of the approximate axial displacement, velocity and acceleration are computationally advantageous because the integrals in the approximate rotating axial deformation functions $\widetilde{U}_F$ and $\widetilde{U}_L$ need to be computed only once (at the pre-

processing stage). During the simulations, only products of the flap and lag degrees of freedom are required to determine the axial motion of the blade.

2.3.4.2 Structural state vector

The participation coefficients a_{F_i}, a_{L_i} and a_{T_i} represent the generalized degrees of freedom of the flexible blade. Therefore, the total number of degrees of freedom of the blade are:

$$n_{\text{dof}} = n_F + n_L + n_T \tag{2.94}$$

The generalized structural degrees of freedom vector of a blade is defined to be:

$$\boldsymbol{a} = \left\{a_{F_1}, \cdots, a_{F_{n_F}}, a_{L_1}, \cdots, a_{L_{n_L}}, a_{T_1}, \cdots, a_{T_{n_T}}, \right\}^T \tag{2.95}$$

The structural state vector of the blade is defined using the generalized degree of freedom vector $\boldsymbol{a}$, and its time derivative $\dot{\boldsymbol{a}}$:

$$\boldsymbol{X}_s = \{\boldsymbol{a}^T, \dot{\boldsymbol{a}}^T\}^T \tag{2.96}$$

For a coaxial rotor, the structural state vector combines the upper and lower rotor blade generalized degrees of freedom:

$$(\boldsymbol{X}_s)_{\text{coaxial}} = \{\boldsymbol{a}_u^T, \boldsymbol{a}_l^T, \dot{\boldsymbol{a}}_u^T, \dot{\boldsymbol{a}}_l^T\} \tag{2.97}$$

2.3.4.3 Error residuals

The approximate representation of the structural deformation (Eqns. 2.85 - 2.87) are substituted in the equations of motion (Eqns. 2.79 - 2.81). The right hand sides of the equations are no longer identically zero because the solution is approximate. According to the Galerkin method, these equations are multiplied by each mode shape

in the approximation, and integrated over the span of the blade.

$$\begin{aligned}
\epsilon_{F_i} &= \int_0^l \Big[-\Big\{ \overline{EI}_y \widetilde{w}_{,xx} - \overline{EI}_{(y-z)_1}(\widetilde{v}_{,xx} + 2\widetilde{\phi}\widetilde{w}_{,xx}) - \overline{EI}_{(y-z)_2}\widetilde{\phi}\widetilde{v}_{,xx} \Big\} W_{i,xx} \\
&\quad - \Big\{ GJ\widetilde{\phi}_{,x}\widetilde{v}_{,xx} + \widetilde{w}_{,x}T - \widetilde{v}_{,x}q_{x_b} + q_{y_b} \Big\} W_{i,x} + p_{z_b} W_i \Big] \, \mathrm{d}x \qquad (2.98) \\
\epsilon_{L_i} &= \int_0^l \Big[-\Big\{ \overline{EI}_z \widetilde{v}_{,xx} - \overline{EI}_{(y-z)_1}(\widetilde{w}_{,xx} - 2\widetilde{\phi}\widetilde{v}_{,xx}) - \overline{EI}_{(y-z)_2}\widetilde{\phi}\widetilde{w}_{,xx} \Big\} V_{i,xx} \\
&\quad - \Big\{ -GJ\widetilde{\phi}_{,x}\widetilde{w}_{,xx} + \widetilde{v}_{,x}T_c + \widetilde{w}_{,x}q_{x_b} - q_{z_b} \Big\} V_{i,x} + p_{y_b} V_i \Big] \, \mathrm{d}x \qquad (2.99) \\
\epsilon_{T_i} &= \int_0^l \Big[-GJ(\widetilde{\phi}_{,x} - \widetilde{v}_{,x}\widetilde{w}_{,xx})\Phi_{i,x} + \big\{ -\overline{EI}_{(y-z)_1}(\widetilde{v}^2_{,xx} - \widetilde{w}^2_{,xx}) \\
&\quad + \overline{EI}_{(y-z)_2}\widetilde{v}_{,xx}\widetilde{w}_{,xx} + q_{x_b} + \widetilde{v}_{,x}q_{y_b} + \widetilde{w}_{,x}q_{z_b} \big\} \Phi_i \Big] \, \mathrm{d}x \qquad (2.100)
\end{aligned}$$

The residual vector is defined:

$$\boldsymbol{\epsilon} = \left\{ \epsilon_{F_1}, \cdots, \epsilon_{F_{n_F}}, \epsilon_{L_1}, \cdots, \epsilon_{L_{n_L}}, \epsilon_{T_1}, \cdots, \epsilon_{T_{n_T}}, \right\}^T \qquad (2.101)$$

The generalized degrees of freedom are obtained by setting the integrals to zero. Equations 2.98 - 2.100 can be written in compact form as:

$$\boldsymbol{\epsilon}(\boldsymbol{a}, \dot{\boldsymbol{a}}, \ddot{\boldsymbol{a}}) = 0 \qquad (2.102)$$

The residual of the equations can be separated into three components that depend on the elastic, inertial and aerodynamic terms respectively.

Elastic terms

$$\begin{aligned}
\epsilon^E_{F_i} &= \int_0^l \Big[-\Big\{ \overline{EI}_y \widetilde{w}_{,xx} - \overline{EI}_{(y-z)_1}(\widetilde{v}_{,xx} + 2\widetilde{\phi}\widetilde{w}_{,xx}) - \overline{EI}_{(y-z)_2}\widetilde{\phi}\widetilde{v}_{,xx} \Big\} W_{i,xx} \\
&\quad - \Big\{ GJ\widetilde{\phi}_{,x}\widetilde{v}_{,xx} + \widetilde{w}_{,x}T_c \Big\} W_{i,x} \Big] \, \mathrm{d}x \qquad (2.103) \\
\epsilon^E_{L_i} &= \int_0^l \Big[-\Big\{ \overline{EI}_z \widetilde{v}_{,xx} - \overline{EI}_{(y-z)_1}(\widetilde{w}_{,xx} - 2\widetilde{\phi}\widetilde{v}_{,xx}) - \overline{EI}_{(y-z)_2}\widetilde{\phi}\widetilde{w}_{,xx} \Big\} V_{i,xx} \\
&\quad - \Big\{ GJ\widetilde{\phi}_{,x}\widetilde{w}_{,xx} + \widetilde{v}_{,x}T_c \Big\} V_{i,x} \Big] \, \mathrm{d}x \qquad (2.104) \\
\epsilon^E_{T_i} &= \int_0^l \Big[-GJ(\widetilde{\phi}_{,x} - \widetilde{v}_{,x}\widetilde{w}_{,xx})\Phi_{i,x} + \big\{ -\overline{EI}_{(y-z)_1}(\widetilde{v}^2_{,xx} - \widetilde{w}^2_{,xx}) \\
&\quad + \overline{EI}_{(y-z)_2}\widetilde{v}_{,xx}\widetilde{w}_{,xx} \big\} \Phi_i \Big] \, \mathrm{d}x \qquad (2.105)
\end{aligned}$$

It is evident that the elastic terms of the residual are independent of the time derivative terms. Therefore:

$$\boldsymbol{\epsilon}^E \equiv \boldsymbol{\epsilon}^E(\boldsymbol{a}) \qquad (2.106)$$

Inertial terms

$$\begin{aligned}
\epsilon^I_{F_i} &= \int_0^l \left[\left(\widetilde{v}_{,x} q^I_{x_b} - q^I_{y_b} \right) W_{i,x} + p^I_{z_b} W_i \right] \mathrm{d}x \qquad (2.107) \\
\epsilon^I_{L_i} &= \int_0^l \left[\left(q^I_{z_b} - \widetilde{w}_{,x} q^I_{x_b} \right) V_{i,x} + p^I_{y_b} V_i \right] \mathrm{d}x \qquad (2.108) \\
\epsilon^I_{T_i} &= \int_0^l \left[q^I_{x_b} + \widetilde{v}_{,x} q^I_{y_b} + \widetilde{w}_{,x} q^I_{z_b} \right] \Phi_i \mathrm{d}x \qquad (2.109)
\end{aligned}$$

Analytical expressions for the inertial loads $\boldsymbol{p}^I_b$ and $\boldsymbol{q}^I_b$ are derived in Eqns. 2.52 - 2.54 and Eqns. 2.58 - 2.60. The inertial terms of the residual depend on both the first and second time derivatives of the generalized degrees of freedom. Therefore:

$$\boldsymbol{\epsilon}^I \equiv \boldsymbol{\epsilon}^I(\boldsymbol{a}, \dot{\boldsymbol{a}}, \ddot{\boldsymbol{a}}) \qquad (2.110)$$

Aerodynamic terms

$$\epsilon^A_{F_i} = \int_0^l \left[\left(\widetilde{v}_{,x} q^A_{x_b} - q^A_{y_b}\right) W_{i,x} + p^A_{z_b} W_i\right] \mathrm{d}x \tag{2.111}$$

$$\epsilon^A_{L_i} = \int_0^l \left[\left(q^A_{z_b} - \widetilde{w}_{,x} q^A_{x_b}\right) V_{i,x} + p^A_{y_b} V_i\right] \mathrm{d}x \tag{2.112}$$

$$\epsilon^A_{T_i} = \int_0^l \left[q^A_{x_b} + \widetilde{v}_{,x} q^A_{y_b} + \widetilde{w}_{,x} q^A_{z_b}\right] \Phi_i \mathrm{d}x \tag{2.113}$$

The attached and separated flow aerodynamic forces $\boldsymbol{p}^A_b$ and moments $\boldsymbol{q}^A_b$ over the entire spans of both blades are combined in the vectors $\boldsymbol{F}_a$ and $\boldsymbol{F}_d$ respectively. The aerodynamic loads are implicitly dependent on the blade motion and wake induced velocities.

$$\boldsymbol{\epsilon}^A \equiv \boldsymbol{\epsilon}^A(\boldsymbol{a}, \boldsymbol{F}_a, \boldsymbol{F}_d) \tag{2.114}$$

2.3.4.4 Separation of variables

The solution for the blade modes are obtained by setting the residual vector equal to zero.

$$\boldsymbol{\epsilon} = \boldsymbol{\epsilon}^E(\boldsymbol{a}) + \boldsymbol{\epsilon}^I(\boldsymbol{a}, \dot{\boldsymbol{a}}, \ddot{\boldsymbol{a}}) + \boldsymbol{\epsilon}^A(\boldsymbol{a}, \boldsymbol{F}_a, \boldsymbol{F}_d) = \boldsymbol{0} \tag{2.115}$$

The inertial term of the residual vector is expanded using Taylor series to get:

$$\boldsymbol{\epsilon}^E(\boldsymbol{a}) + \underbrace{\boldsymbol{\epsilon}^I(\boldsymbol{a}, \dot{\boldsymbol{a}}, \boldsymbol{0}) + \left[\frac{\partial \boldsymbol{\epsilon}^I}{\partial \ddot{\boldsymbol{a}}}(\boldsymbol{a}, \dot{\boldsymbol{a}}, \boldsymbol{0})\right] \ddot{\boldsymbol{a}}}_{\text{Taylor series expansion about } \ddot{\boldsymbol{a}}=0} + \boldsymbol{\epsilon}^A(\boldsymbol{a}, \boldsymbol{F}_a, \boldsymbol{F}_d) = \boldsymbol{0} \tag{2.116}$$

The equations are rewritten to obtain the second derivative of the generalized degree of freedom.

$$\ddot{\boldsymbol{a}} = -\left[\frac{\partial \boldsymbol{\epsilon}^I}{\partial \ddot{\boldsymbol{a}}}(\boldsymbol{a}, \dot{\boldsymbol{a}}, \boldsymbol{0})\right]^{-1} \left\{\boldsymbol{\epsilon}^E(\boldsymbol{a}) + \boldsymbol{\epsilon}^I(\boldsymbol{a}, \dot{\boldsymbol{a}}, \boldsymbol{0}) + \boldsymbol{\epsilon}^A(\boldsymbol{a}, \boldsymbol{F}_a, \boldsymbol{F}_d)\right\} \tag{2.117}$$

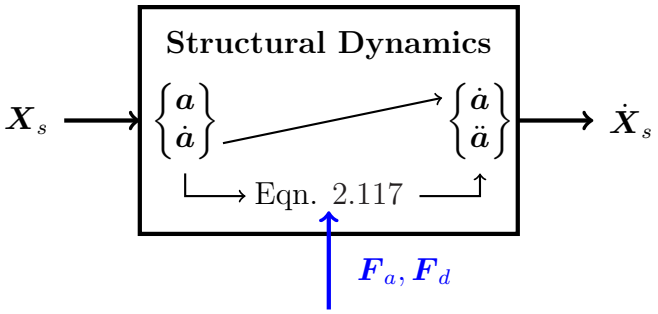

Figure 2.10: Structural dynamics module

The jacobian matrix $\left[\dfrac{\partial \boldsymbol{\epsilon}^I}{\partial \ddot{\boldsymbol{a}}}\right]$ is calculated analytically from Eqns. 2.52 - 2.54 and 2.58 - 2.60. The detailed expressions are provided in Appendix C.

Therefore, the structural dynamics module can be represented using the diagram shown in Fig. 2.10. The second time derivative $\ddot{\boldsymbol{a}}$ is obtained from Eqn. 2.117, for a given input of the generalized degrees of freedom vector $\boldsymbol{a}$, its first time derivative $\dot{\boldsymbol{a}}$, and aerodynamic loads $\boldsymbol{F}_a, \boldsymbol{F}_d$. The loads $\boldsymbol{F}_a, \boldsymbol{F}_d$ are calculated using the aerodynamics loads module described in detail in the next chapter.

CHAPTER 3

Reduced Order Modeling of Unsteady Aerodynamic Loads

In coaxial rotors, the rotor wake and blade loads are tightly coupled. Thus, both must be evaluated accurately. The accurate calculation of unsteady airfoil loads is also essential for vibration prediction, control and aeroelastic analysis. As noted in the literature survey, most coaxial comprehensive analyses use table look-up of static airfoil properties to compute spanwise blade loads. The tables are either based on experimental data, or obtained through CFD RANS computations.

The table look-up is often combined with FVW for rotor wake modeling in comprehensive analysis codes such as CAMRAD II, RCAS and UMARC. In FVW methods, the Weissinger-L lifting-line theory is a common approach to represent the rotor blade in the free wake [136, 137]. In lifting-line theory, the blade geometry is represented using vortex filaments along the quarter chord line of the blade. A higher-order version of the vortex filament lifting-line theory is the Unsteady Vortex Lattice Method (UVLM). In UVLM, the complex curved surface geometry of the blades is approximated with small vortex panels [138, 139]. The UVLM approach was combined with VVPM for coaxial rotors in Refs. 140 and 141. The blade surface geometry can also be represented using source/doublet panels instead of vortex panels. The source/-doublet panel method was combined with FVW [142] and with VVPM [143]. In Ref.

97, the combined source/doublet panel method and VVPM was applied to a X2TD like coaxial rotor in forward flight.

Conventional approaches for calculating blade loads have several disadvantages [128]. Table look-up, lifting-line and panel methods are quasi-steady approaches, therefore they may not capture loads accurately in the highly unsteady flow-field of a coaxial rotor. Lifting-line and panel methods are based on potential flow, therefore viscous drag can only be incorporated using empirical methods. Panel methods are suitable for capturing the complex blade geometry with thickness and sweep. However, the computational time and memory requirements increase at $\geq \mathcal{O}(N^2)$ for N panels. In addition, at high angles of attack, the flow does not remain attached to the surface of the panels. Therefore, boundary layer and flow separation models are required.

Therefore, unsteady aerodynamic models that can incorporate arbitrary motion are required for accurate rotary-wing aeroelastic analysis [144]. The generalized motion $\boldsymbol{h}$ of a blade cross section is obtained from the 3D blade motion represented with the structural degrees of freedom, the free-stream velocity, and the inflow distribution over the blades. The lift, moment, and drag coefficients for a cross section are combined into the generalized load vector $\boldsymbol{f}$.

$$\boldsymbol{f} = \begin{Bmatrix} C_l \\ C_m \\ C_d \end{Bmatrix} \tag{3.1}$$

The aerodynamic loads consist of attached flow and separated flow loads.

$$\boldsymbol{f} = \boldsymbol{f}_a + \boldsymbol{f}_d \tag{3.2}$$

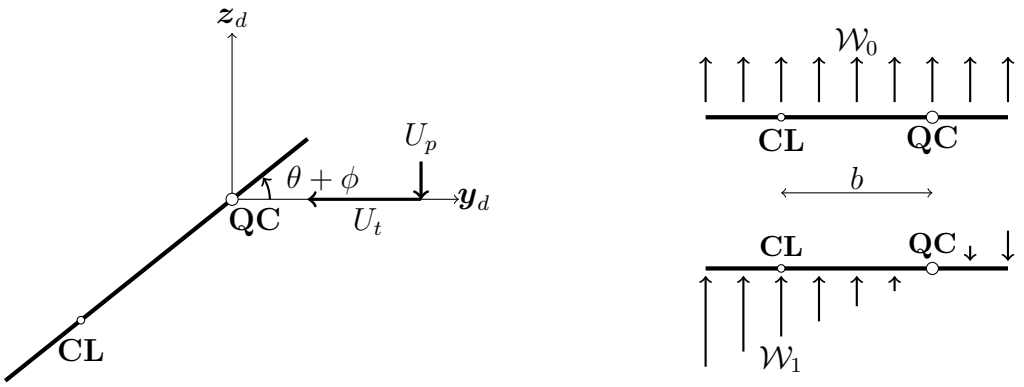

(a) Pitch and plunge motion

(b) Generalized velocities

Figure 3.1: Transformation of arbitrary airfoil motion to generalized motions

The attached flow aerodynamic loads $\boldsymbol{f}_a$ are calculated using the CFD-RFA approach [145]. The separated flow loads $\boldsymbol{f}_d$ are calculated using the ONERA-DS model. The ROMs are described in detail in this chapter.

3.1 Generalized airfoil motion

A 2D unsteady aerodynamic loads ROM for rotary-wing applications needs to accurately model the response to arbitrary airfoil motion in an unsteady freestream. In classical aeroelasticity, the airfoil motion is described using simple harmonic pitching and plunging motions [146]. The pitch and plunge motion can be transformed to a set of orthogonal normal velocity distributions. The linear combination of these generalized velocities ($\mathcal{W}_0$ and $\mathcal{W}_1$) completely describe the boundary conditions at the airfoil surface due to arbitrary pitching and plunging motion of the airfoil in an unsteady freestream. This set of generalized velocities is selected because it is directly applicable for both the CFD-RFA and ONERA-DS models used in this study.

3.1.1 Rotational transformation

The velocity of the air with respect to the blade cross section is the relative air velocity $\boldsymbol{U}$. The transformation from the relative air velocity $\boldsymbol{U}$ to the generalized velocities is shown in Fig. 3.1. The generalized airfoil velocities are equivalent to the magnitudes of the normal velocity at the collocation point (CL) i.e. the point located at $3/4^{\text{th}}$ chords from the leading edge.

$$\mathcal{W}_0 = U_t \sin(\theta + \phi) - U_p \cos(\theta + \phi) \tag{3.3}$$

$$\mathcal{W}_1 = b\left(\dot{\theta} + \dot{\phi}\right) \tag{3.4}$$

The generalized velocities are combined into a single generalized motion vector $\boldsymbol{h}$:

$$\boldsymbol{h} = \begin{Bmatrix} \mathcal{W}_0 \\ \mathcal{W}_1 \end{Bmatrix} \tag{3.5}$$

The generalized accelerations are:

$$\dot{\mathcal{W}}_0 = \left[\dot{U}_t - U_p\left(\dot{\theta} + \dot{\phi}\right)\right]\sin(\theta + \phi) + \left[U_t\left(\dot{\theta} + \dot{\phi}\right) - \dot{U}_p\right]\cos(\theta + \phi) \tag{3.6}$$

$$\dot{\mathcal{W}}_1 = b\left(\ddot{\theta} + \ddot{\phi}\right) \tag{3.7}$$

The generalized accelerations are combined in the $\dot{\boldsymbol{h}}$ vector:

$$\dot{\boldsymbol{h}} = \begin{Bmatrix} \dot{\mathcal{W}}_0 \\ \dot{\mathcal{W}}_1 \end{Bmatrix} \tag{3.8}$$

In previous implementations of generalized motion calculations [134, 147–150], the blade pitch angles $(\theta + \phi)$ are assumed to be small such that:

$$\sin(\theta + \phi) \approx \theta + \phi \tag{3.9}$$

$$\cos(\theta + \phi) \approx 1 \tag{3.10}$$

However, the Sikorsky X2TD blades have a non-linear built-in twist distribution, and the geometric pitch angle θ may be large during simulations. Therefore, the small angle assumption is ignored for the generalized motion calculations.

3.1.2 Separation of terms

The generalized motion $\boldsymbol{h}$ of the airfoil depends on the local relative air velocity $\boldsymbol{U}$ on the airfoil. The local relative air velocity can be separated into *kinematic velocity* $\boldsymbol{U}^K$ and *induced velocity* $\boldsymbol{U}^J$ components.

$$\boldsymbol{U} = \underbrace{\boldsymbol{U}_\Omega + \boldsymbol{U}_\infty + \boldsymbol{U}_S}_{\text{kinematic: } \boldsymbol{U}^K} + \underbrace{\boldsymbol{U}_B + \boldsymbol{U}_W}_{\text{induced: } \boldsymbol{U}^J} \tag{3.11}$$

The local velocity due to rotation $\boldsymbol{U}_\Omega$, free stream $\boldsymbol{U}_\infty$, and structural deformation $\boldsymbol{U}_S$ are termed as kinematic velocities since they can be completely determined by the geometric motion of the blade. The induced velocity consists of velocity induced by the blade bound circulation $\boldsymbol{U}_B$, and velocity induced by the rotor wake $\boldsymbol{U}_W$, which are determined by the blade aerodynamic model and the wake model respectively.

3.1.2.1 Kinematic velocities

The relative air velocity at the deformed point on the blade due to blade rotation is:

$$\boldsymbol{U}_\Omega = -\left(\Omega \hat{\boldsymbol{k}}_h\right) \times (\boldsymbol{P}' - \boldsymbol{C}) \tag{3.12}$$

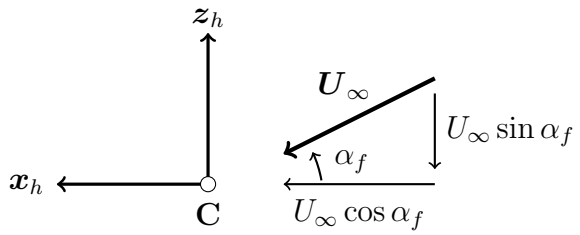

Figure 3.2: Relative velocity due to free-stream

Figure 3.2 illustrates the free-stream velocity experienced by the rotor due to the fuselage forward speed.

$$\boldsymbol{U}_\infty = U_\infty \left(\cos \alpha_f \ \hat{\boldsymbol{i}}_h - \sin \alpha_f \ \hat{\boldsymbol{k}}_h \right) \tag{3.13}$$

The angle between the hub fixed $\boldsymbol{x}_h$ axis and the net free-stream velocity is the fuselage tilt angle α_f. The advance ratio is:

$$\mu = \frac{U_\infty \cos \alpha_f}{\Omega R} \tag{3.14}$$

The relative velocity due to the structural deformation consists of two parts: the rate of change of structural displacements, and the angular velocity due to rate of change of slopes.

$$\boldsymbol{U}_S = - \left(\dot{u} \hat{\boldsymbol{i}}_b + \dot{v} \hat{\boldsymbol{j}}_b + \dot{w} \hat{\boldsymbol{k}}_b \right) - \left(-\dot{w}_{,x} \hat{\boldsymbol{j}}_b + \dot{v}_{,x} \hat{\boldsymbol{k}}_b \right) \times (\boldsymbol{P}' - \boldsymbol{P}) \tag{3.15}$$

The velocities in Eqns. 3.12, 3.13 and 3.15 are combined into tangential and perpendicular components to the $\boldsymbol{y}_d$ axis:

$$U_t^K = \dot{v} + \Omega(x + e + u + v v_{,x} - w\beta_p) + U_\infty \cos \alpha_f \left(\sin \psi + v_{,x} \cos \psi \right) \tag{3.16}$$

$$U_p^K = \dot{w} + U_\infty \sin \alpha_f + \left(U_\infty \cos \alpha_f \cos \psi + \Omega v \right) \left(w_{,x} + \beta_p \right) \tag{3.17}$$

The relative accelerations are:

$$\dot{U}_t^K = \ddot{v} + \Omega(\dot{u} + \dot{v}v_{,x} + v\dot{v}_{,x} - \dot{w}\beta_p) + U_\infty \cos\alpha_f \left[(\Omega + \dot{v}_{,x})\cos\psi - \Omega v_{,x}\sin\psi\right] \quad (3.18)$$

$$\dot{U}_p^K = \ddot{w} + \Omega\left(\dot{v} - U_\infty \cos\alpha_f \sin\psi\right)\left(w_{,x} + \beta_p\right) + \dot{w}_{,x}\left(U_\infty \cos\alpha_f \cos\psi + \Omega v\right) \quad (3.19)$$

Therefore, the expressions for the kinematic velocities and accelerations are a function of the structural state vector and its rates.

$$\boldsymbol{U}^K \equiv \boldsymbol{U}^K(\boldsymbol{X}_s) \quad (3.20)$$

$$\dot{\boldsymbol{U}}^K \equiv \boldsymbol{U}^K(\boldsymbol{X}_s, \dot{\boldsymbol{X}}_s) \quad (3.21)$$

3.1.2.2 Induced velocities

The velocity induced by the blade bound circulation $\boldsymbol{U}_B$ and the wake $\boldsymbol{U}_W$ depend on the radial and azimuthal location on the blade. The blade induced velocity $\boldsymbol{U}_B$ is a 3D effect which captures the influence of the bound circulation distributed over all blades on the surrounding blade sections. The bound circulation induced velocity $\boldsymbol{U}_B$ is determined from the vortex filament representation of the blade, a quantity derived later in this chapter. The wake induced velocity is determined from the VVPM described in Chapter 4.

The tangential and perpendicular components of the relative air velocity are calculated using dot products with the local blade deflected axis system.

$$U_t^J = -(\boldsymbol{U}_B + \boldsymbol{U}_W)\cdot\hat{\boldsymbol{j}}_d \quad (3.22)$$

$$U_p^J = -(\boldsymbol{U}_B + \boldsymbol{U}_W)\cdot\hat{\boldsymbol{k}}_d \quad (3.23)$$

The relative accelerations are obtained using the cross products with the angular rate:

$$\dot{U}_t^J = -\left[\left(-\dot{w}_{,x}\hat{\boldsymbol{j}}_b + \dot{v}_{,x}\hat{\boldsymbol{k}}_b + \Omega\hat{\boldsymbol{k}}_h\right) \times (\boldsymbol{U}_B + \boldsymbol{U}_W)\right] \cdot \hat{\boldsymbol{j}}_d \tag{3.24}$$

$$\dot{U}_p^J = -\left[\left(-\dot{w}_{,x}\hat{\boldsymbol{j}}_b + \dot{v}_{,x}\hat{\boldsymbol{k}}_b + \Omega\hat{\boldsymbol{k}}_h\right) \times (\boldsymbol{U}_B + \boldsymbol{U}_W)\right] \cdot \hat{\boldsymbol{k}}_d \tag{3.25}$$

Note that the $\dot{\boldsymbol{U}}_B$ and $\dot{\boldsymbol{U}}_W$ terms are ignored. This is based on the assumption that induced velocity at a point in the flow field does not change significantly during the time scales representative of the blade structural dynamics.

3.2 Rational function approximation for attached flow loads

The oscillatory response data from unsteady aerodynamic models can be used to generate state space representations known as rational function approximation (RFA) based ROMs [151, 152]. A time domain unsteady RFA accounting for unsteady free-stream and compressibility effects in rotary-wing applications was first developed in Ref. 147. A 2D doublet-lattice method was used to generate oscillatory aerodynamic loading on an airfoil/trailing-edge flap combination over a range of reduced frequencies. Subsequently, the RFA approach was used to convert frequency domain aerodynamic loads into time domain. This approach offers improved accuracy compared to the quasi-steady lifting-line method, and improved computational efficiency compared to CFD. The Doublet-Lattice based Rational Function Approximation (DL-RFA) was incorporated into the comprehensive rotorcraft simulation code Active VIbration and NOise Reduction (AVINOR). The code has been extensively used for performance enhancement, active vibration and noise control studies [149, 153, 154]. In Ref. 140, the DL-RFA approach was compared with UVLM for coaxial rotors in hover.

The DL-RFA method is based on potential flow theory. Therefore, it cannot predict viscous drag. The doublet-lattice calculation is based on the oscillations of a flat plate, therefore the curved surface of an airfoil is ignored. These limitations are overcome by using a compressible unsteady RANS CFD solver to generate the frequency domain unsteady aerodynamic loads. The CFD-RFA is a 2D unsteady ROM that is computationally inexpensive and includes viscous effects. Vibration control studies using AVINOR have shown that the CFD-RFA can reproduce CFD data at a fraction of the cost [134, 145, 155]. In contrast to DL-RFA, CFD-RFA predicts the unsteady drag coefficient and includes unsteady viscous effects on the airfoil lift and moment.

3.2.1 CFD based rational function approximation

The schematic in Fig. 3.3 describes the process of constructing the CFD-RFA ROM. The generalized load response to the various generalized motions is generated in time domain using CFD++, an unsteady RANS code [156]. The one equation Spalart-Allmaras turbulence model is employed in the simulations. The database consists of the amplitude, phase and frequency of the lift, moment and drag coefficients, at various Mach numbers, mean angles of attack and frequencies of oscillation. Thus, the database spans the entire range of operating conditions for the particular rotor configuration [145]. The calculation of the CFD database is a one time computational expense for a particular airfoil, and does not impact the run time of the CFD-RFA calculations.

The time domain results are transformed into state space such that the relation between the generalized forces and the generalized motions is represented by a transfer function. The transfer function $[\boldsymbol{\mathcal{Q}}]$ is in the form of Rogers approximation [151],

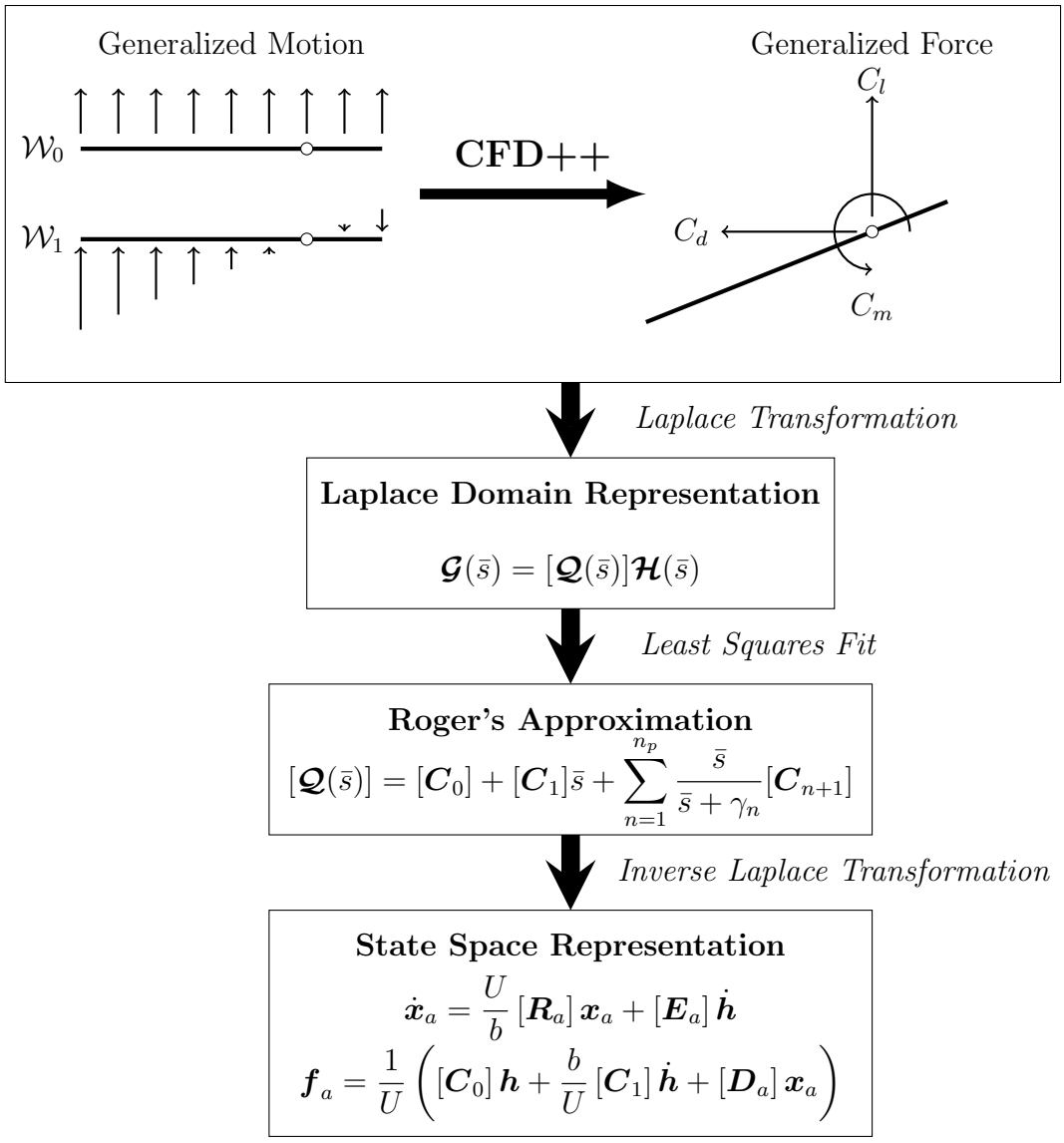

Figure 3.3: Schematic of CFD-RFA model

resulting in a RFA.

$$[\boldsymbol{\mathcal{Q}}(\bar{s})] = [\boldsymbol{C}_0] + [\boldsymbol{C}_1]\bar{s} + \sum_{n=1}^{n_p} \frac{\bar{s}}{\bar{s} + \gamma_n}[\boldsymbol{C}_{n+1}] \tag{3.26}$$

A state space model for the loads $\boldsymbol{f}_a$ and aerodynamic states $\boldsymbol{x}_a$ is generated by transforming the equations to time domain:

$$\dot{\boldsymbol{x}}_a = \frac{U}{b}[\boldsymbol{R}_a]\boldsymbol{x}_a + [\boldsymbol{E}_a]\dot{\boldsymbol{h}} \tag{3.27}$$

$$\boldsymbol{f}_a = \frac{1}{U}\left([\boldsymbol{C}_0]\boldsymbol{h} + \frac{b}{U}[\boldsymbol{C}_1]\dot{\boldsymbol{h}} + [\boldsymbol{D}_a]\boldsymbol{x}_a\right) \tag{3.28}$$

where,

$$[\boldsymbol{R}_a] = -\begin{bmatrix} \gamma_1[\boldsymbol{I}]_{3\times3} & 0 & \cdots & 0 \\ 0 & \gamma_2[\boldsymbol{I}]_{3\times3} & \ddots & \vdots \\ \vdots & \ddots & \ddots & 0 \\ 0 & \cdots & 0 & \gamma_{n_p}[\boldsymbol{I}]_{3\times3} \end{bmatrix}_{3n_p\times3n_p} \tag{3.29}$$

$$[\boldsymbol{E}_a] = \begin{bmatrix} [\boldsymbol{C}_2]_{3\times2} \\ \vdots \\ [\boldsymbol{C}_{n_p+1}]_{3\times2} \end{bmatrix}_{3n_p\times2} \tag{3.30}$$

$$[\boldsymbol{D}_a] = \begin{bmatrix} [\boldsymbol{I}]_{3\times3} & \cdots & [\boldsymbol{I}]_{3\times3} \end{bmatrix}_{3\times3n_p} \tag{3.31}$$

In the CFD-RFA, the coefficient matrices $[\boldsymbol{C}_k], k = 1\cdots n_p$ for each airfoil segment are calculated for the local Mach number M_c and angle of attack α. The coefficient matrices are interpolated from the CFD database using the piecewise cubic hermite interpolating polynomial (PCHIP) method for both variables M_c and α. The 2D interpolation scheme is implemented in an efficient manner using the GNU Scientific Library (GSL) [157].

3.2.2 Physical interpretation of RFA coefficients

The RFA coefficients can be related to airfoil characteristics such as the lift curve slope C_{l_α}. The relationship can be determined using the following approach. Assume that the airfoil is undergoing harmonic pitch oscillations at a frequency ω in a steady freestream U:

$$\alpha = \alpha_0 e^{i\omega t} \tag{3.32}$$

The generalized motion can be written in terms of the free stream and angle of attack:

$$\boldsymbol{h} = \begin{Bmatrix} U\alpha \\ b\dot{\alpha} \end{Bmatrix} = \begin{Bmatrix} U \\ \mathrm{i}\omega b \end{Bmatrix} \alpha_0 e^{\mathrm{i}\omega t} \tag{3.33}$$

The rate of change in generalized motion becomes:

$$\dot{\boldsymbol{h}} = \begin{Bmatrix} U\dot{\alpha} \\ b\ddot{\alpha} \end{Bmatrix} = \begin{Bmatrix} U \\ \mathrm{i}\omega b \end{Bmatrix} \mathrm{i}\omega\alpha_0 e^{\mathrm{i}\omega t} \tag{3.34}$$

Let the solution for the aerodynamic states $\boldsymbol{x}_a$ be of the same form:

$$\boldsymbol{x}_a = \boldsymbol{x}_0 e^{\mathrm{i}\omega t} \tag{3.35}$$

The constant $\boldsymbol{x}_0$ can be determined using Eqn. 3.27:

$$\boldsymbol{x}_0 = [\boldsymbol{A}_a]^{-1}[\boldsymbol{E}_a] \begin{Bmatrix} U \\ \mathrm{i}\omega b \end{Bmatrix} \left(\frac{b}{U}\right) \mathrm{i}\omega\alpha_0 \tag{3.36}$$

where

$$[\boldsymbol{A}_a] = \mathrm{i}k[\boldsymbol{I}] - [\boldsymbol{R}_a] \tag{3.37}$$

and the reduced frequency k is defined as

$$k = \frac{\omega b}{U} \tag{3.38}$$

Therefore, from Eqn. 3.35 the solution to the aerodynamic state vector is:

$$\boldsymbol{x}_a = \frac{b}{U}[\boldsymbol{A}]_a^{-1}[\boldsymbol{E}_a] \begin{Bmatrix} U\dot{\alpha} \\ b\ddot{\alpha} \end{Bmatrix} \tag{3.39}$$

Substituting the solution in Eqn. 3.28

$$\boldsymbol{f} = [\boldsymbol{C}_0] \begin{Bmatrix} \alpha \\ \dot{\bar{\alpha}} \end{Bmatrix} + ([\boldsymbol{C}_1] + [\boldsymbol{D}_a][\boldsymbol{A}_a]^{-1}[\boldsymbol{E}_a]) \begin{Bmatrix} \dot{\bar{\alpha}} \\ \ddot{\bar{\alpha}} \end{Bmatrix} \tag{3.40}$$

where the non-dimensional time is defined to be:

$$\bar{t} = \frac{Ut}{b} \tag{3.41}$$

The non-dimensional time derivatives of angle of attack are:

$$\dot{\bar{\alpha}} = \left(\frac{b}{U}\right)\dot{\alpha} \tag{3.42}$$

$$\ddot{\bar{\alpha}} = \left(\frac{b}{U}\right)^2 \ddot{\alpha} \tag{3.43}$$

Therefore, derivatives with respect to the pitch angle, rate and acceleration can be obtained.

$$\frac{\partial \boldsymbol{f}_a}{\partial \alpha} = [\boldsymbol{C}_0] \begin{Bmatrix} 1 \\ 0 \end{Bmatrix} \tag{3.44}$$

$$\frac{\partial \boldsymbol{f}_a}{\partial \dot{\bar{\alpha}}} = [\boldsymbol{C}_0] \begin{Bmatrix} 0 \\ 1 \end{Bmatrix} + \left([\boldsymbol{C}_1] + [\boldsymbol{D}_a][\boldsymbol{A}_a]^{-1}[\boldsymbol{E}_a] \right) \begin{Bmatrix} 1 \\ 0 \end{Bmatrix} \tag{3.45}$$

$$\frac{\partial \boldsymbol{f}_a}{\partial \ddot{\bar{\alpha}}} = \left([\boldsymbol{C}_1] + [\boldsymbol{D}_a][\boldsymbol{A}_a]^{-1}[\boldsymbol{E}_a] \right) \begin{Bmatrix} 0 \\ 1 \end{Bmatrix} \tag{3.46}$$

For static conditions, the reduced frequency is zero ($k = 0$). Therefore the matrix $[\boldsymbol{A}]_a$ simplifies to:

$$[\boldsymbol{A}_a] = -[\boldsymbol{R}_a] \tag{3.47}$$

Therefore we can simplify the following expression:

$$[\boldsymbol{D}_a][\boldsymbol{A}_a]^{-1}[\boldsymbol{E}_a] = \frac{1}{\gamma_1}[\boldsymbol{C}_2] + \cdots + \frac{1}{\gamma_{n_p}}[\boldsymbol{C}_{n_p+1}] = \sum_{i=1}^{n_p} \frac{1}{\gamma_i}[\boldsymbol{C}_{i+1}] \tag{3.48}$$

The derivatives with respect to angle of attack are:

$$C_{l_\alpha} = [\boldsymbol{C}_0]_{0,0} \tag{3.49}$$

$$C_{m_\alpha} = [\boldsymbol{C}_0]_{1,0} \tag{3.50}$$

$$C_{d_\alpha} = [\boldsymbol{C}_0]_{2,0} \tag{3.51}$$

The derivatives with respect to the rate of angle of attack are:

$$C_{l_{\dot{\tilde{\alpha}}}} = [\boldsymbol{C}_0]_{0,1} + [\boldsymbol{C}_1]_{0,0} + \sum_{i=1}^{n_p} \frac{1}{\gamma_i} [\boldsymbol{C}_{i+1}]_{0,0} \tag{3.52}$$

$$C_{m_{\dot{\tilde{\alpha}}}} = [\boldsymbol{C}_0]_{1,1} + [\boldsymbol{C}_1]_{1,0} + \sum_{i=1}^{n_p} \frac{1}{\gamma_i} [\boldsymbol{C}_{i+1}]_{1,0} \tag{3.53}$$

$$C_{d_{\dot{\tilde{\alpha}}}} = [\boldsymbol{C}_0]_{2,1} + [\boldsymbol{C}_1]_{2,0} + \sum_{i=1}^{n_p} \frac{1}{\gamma_i} [\boldsymbol{C}_{i+1}]_{2,0} \tag{3.54}$$

Similarly, the derivatives with respect to the acceleration of angle of attack are:

$$C_{l_{\ddot{\tilde{\alpha}}}} = [\boldsymbol{C}_1]_{0,1} + \sum_{i=1}^{n_p} \frac{1}{\gamma_i} [\boldsymbol{C}_{i+1}]_{0,1} \tag{3.55}$$

$$C_{m_{\ddot{\tilde{\alpha}}}} = [\boldsymbol{C}_1]_{1,1} + \sum_{i=1}^{n_p} \frac{1}{\gamma_i} [\boldsymbol{C}_{i+1}]_{1,1} \tag{3.56}$$

$$C_{d_{\ddot{\tilde{\alpha}}}} = [\boldsymbol{C}_1]_{2,1} + \sum_{i=1}^{n_p} \frac{1}{\gamma_i} [\boldsymbol{C}_{i+1}]_{2,1} \tag{3.57}$$

Comparison of lift curve slope

The lift curve slope C_{l_α} is plotted with respect to angle of attack at different Mach numbers in Fig. 3.4. The CFD-RFA results are plotted with solid lines, whereas the DL-RFA results are plotted with dashed lines. The trends are consistent with known NACA0012 characteristics. At low subsonic speeds ($M_c < 0.3$), the lift curve slope is approximately $C_{l_\alpha} \approx 2\pi$ which is the potential flow lift curve slope for a flat plate airfoil. For the DL-RFA, the slope increases with Mach number according to the Prandtl-Glauert Mach correction:

$$C_{l_\alpha}(M_c) = \frac{C_{l_\alpha}(M_c = 0)}{\sqrt{1 - M_c^2}} \tag{3.58}$$

However, the CFD-RFA lift curve slope has a non-linear variation with angle of attack and Mach number. At low Mach numbers ($M_c < 0.3$), the lift curve slope does not

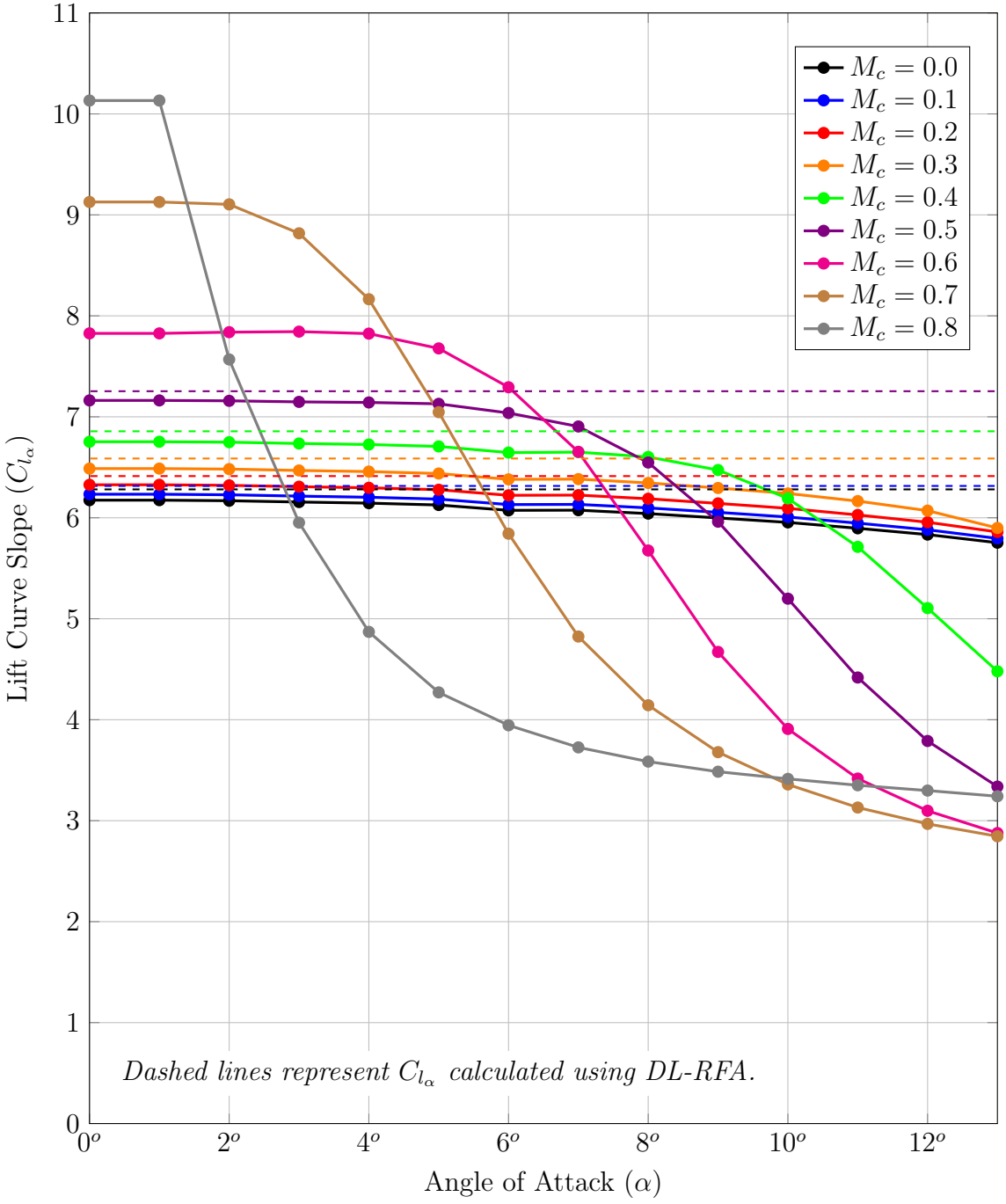

Figure 3.4: Lift curve slope C_{l_α} of a NACA0012 airfoil calculated using CFD-RFA.

vary significantly with angle of attack. This is consistent with linear potential flow theory for a flat plate. However the CFD-RFA lift curve slope decreases with increase in angle of attack in compressible and transonic flow ($M_c > 0.3$). This non-linear behavior due to the airfoil thickness and viscosity is not captured by the DL-RFA method. Therefore, the DL-RFA over-predicts lift at high angles of attack. Hence, the CFD-RFA is a superior method and appropriate for coaxial rotor unsteady load calculations.

Comparison of moment curve slope

The variation of the moment coefficient slope C_{m_α} with the Mach number and mean angle of attack is plotted in Fig. 3.5. At subsonic speeds ($M_c < 0.3$) The moment coefficient slope is positive with a gradual increase with angle of attack. Note that the pitching moment slope C_{m_α} may become negative at some combinations of Mach numbers and angles of attack. In Fig. 3.6, the moment curve slope obtained from the CFD-RFA of the NACA0012 airfoil at $\alpha = 0^o$ is plotted with respect to the Mach number. The moment curve slope is positive and increases with Mach number. However, at $M_c = 0.75$ there is a sharp decrease, and the moment curve slope becomes negative $C_{m_\alpha} < 0$. This is an aerodynamic control reversal effect. Experimental studies indicate that the moment curve slope of a NACA0012 airfoil is zero at $M_c = 0.76$ at $Re = 3 \times 10^6$ [158]. The slope is positive for $M_c = 0.74$ and negative for $M_c = 0.8$. Therefore the moment slope sign reversal calculated using CFD-RFA is validated by experimental results.

Hence, the physical interpretation of the CFD-RFA coefficients can be used for comparisons with static airfoil characteristics and experimental data.

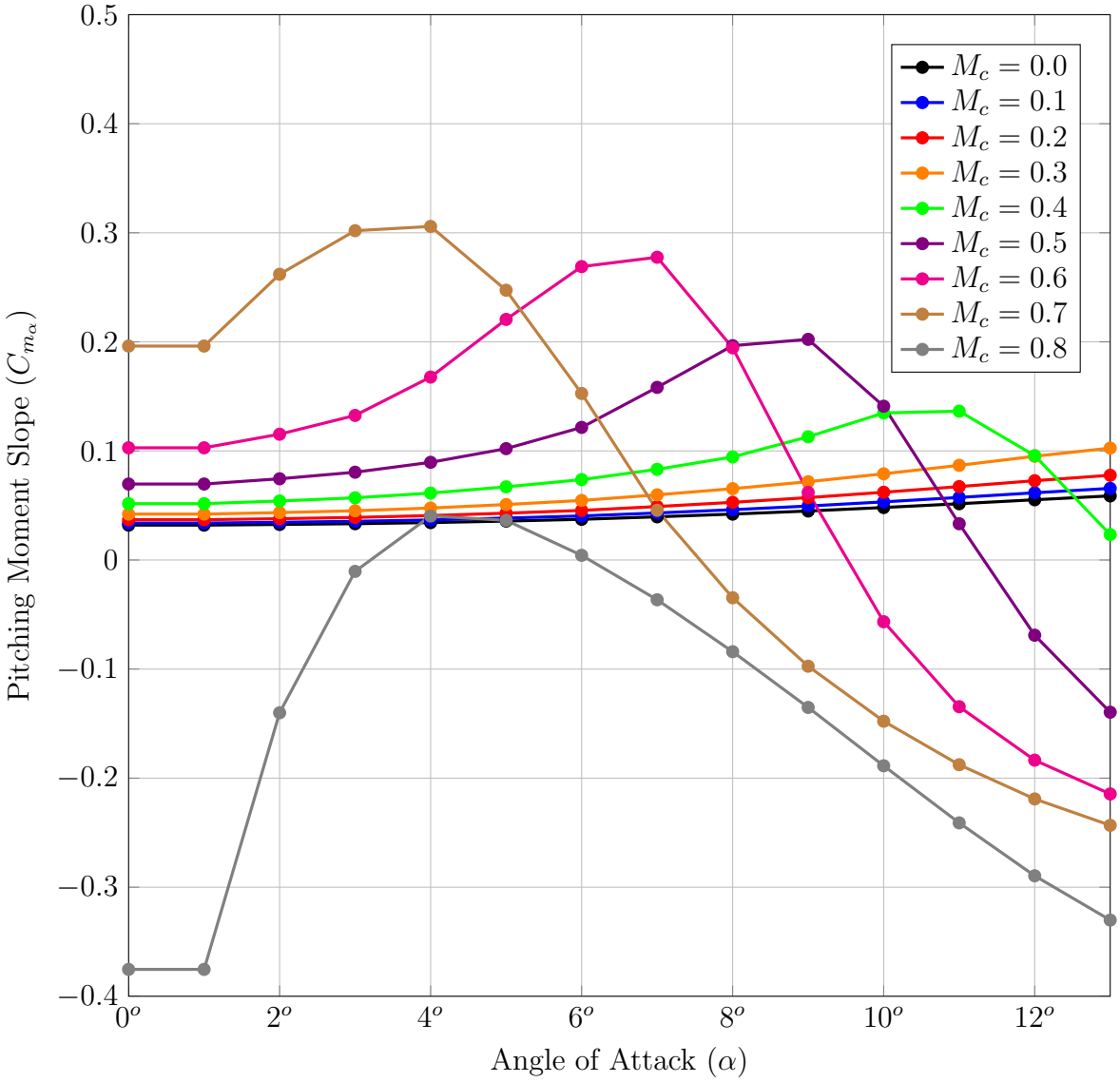

Figure 3.5: Moment curve slope C_{m_α} of a NACA0012 airfoil calculated using CFD-RFA.

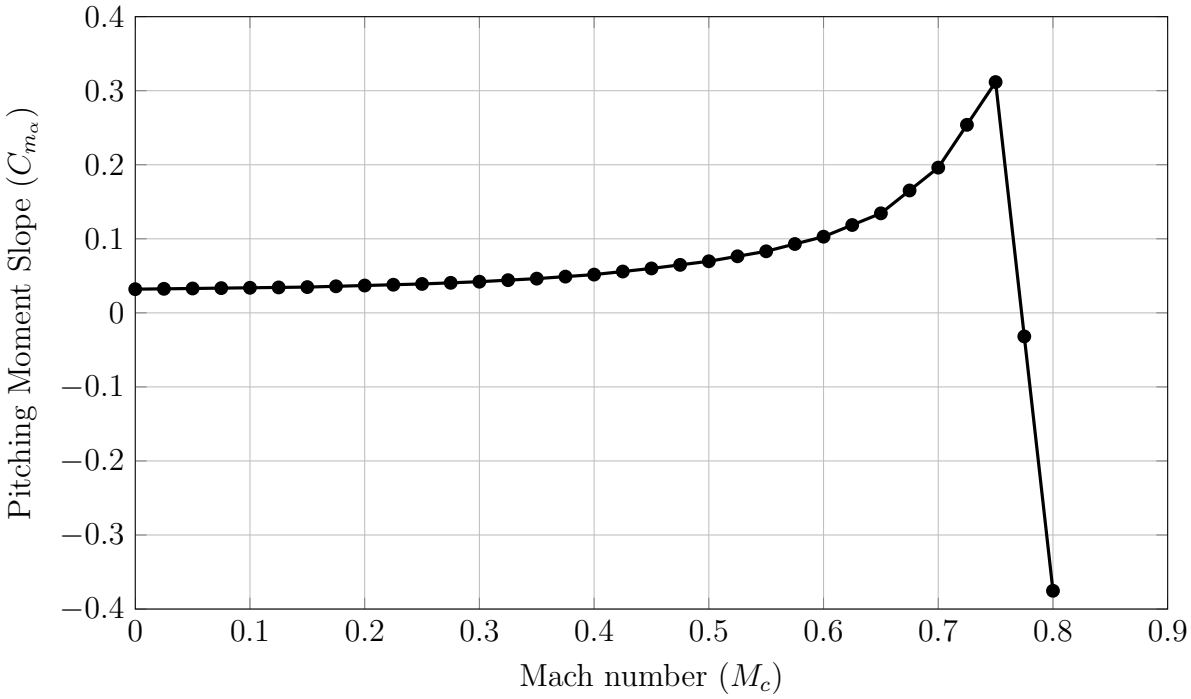

Figure 3.6: Moment Curve Slope C_{m_α} at $\alpha = 0^o$ from CFD-RFA coefficients.

3.2.3 Circulatory and non-circulatory Lift

The lift coefficient of an airfoil can be separated into circulatory and non-circulatory components:

$$C_l = \underbrace{C_l^C}_{\text{circulatory}} + \underbrace{C_l^{NC}}_{\text{non-circulatory}} \tag{3.59}$$

The circulation on the airfoil is obtained from the circulatory lift:

$$\Gamma_a = bUC_l^C \tag{3.60}$$

The circulation is defined as the contour integral of the fluid velocity over a closed path in the plane [138]. From the Kelvin-Stokes theorem, the circulation is equivalent

to the net vorticity enclosed in the contour.

$$\Gamma = \oint \boldsymbol{v} \cdot \mathrm{d}\boldsymbol{s} = \iint \boldsymbol{\omega} \cdot \hat{\boldsymbol{n}} \mathrm{d}A \tag{3.61}$$

Therefore, the circulation is only a function of the flow velocity $\boldsymbol{v}$ distribution over the airfoil. The flow velocity is a resultant of the boundary conditions generated by the generalized velocities $\mathcal{W}_0$ and $\mathcal{W}_1$. Hence, the circulatory lift is independent of time derivatives of the velocity $\dot{\mathcal{W}}_0$ and $\dot{\mathcal{W}}_1$. Based on this definition, the generalized force vector $\boldsymbol{f}_a$ can be split into two terms which depend on the generalized velocity and accelerations respectively:

$$\boldsymbol{f}_a = \underbrace{\frac{1}{U}\left[\boldsymbol{C}_0\right]\boldsymbol{h} + \frac{1}{U}\left[\boldsymbol{D}_a\right]\boldsymbol{x}_a}_{\text{Depends on } \mathcal{W}_0, \mathcal{W}_1} + \underbrace{\frac{1}{U}\left[\boldsymbol{C}_1\right]\frac{b}{U}\dot{\boldsymbol{h}}}_{\text{Depends on } \dot{\mathcal{W}}_0, \dot{\mathcal{W}}_1} \tag{3.62}$$

Therefore, the circulatory lift coefficient for an RFA model is:

$$C_l^C(\boldsymbol{h}) = \begin{Bmatrix} 1 \\ 0 \\ 0 \end{Bmatrix}^T \left(\frac{1}{U}\left[\boldsymbol{C}_0\right]\boldsymbol{h} + \frac{1}{U}\left[\boldsymbol{D}_a\right]\boldsymbol{x}_a\right) \tag{3.63}$$

This approach of separating circulatory and non-circulatory lift based on the generalized motion dependence is consistent with Theodorsen's theory [159]. The non-circulatory and circulatory components of lift in Theodorsen's theory are:

$$C_l^C(\boldsymbol{h}) = \frac{2\pi}{U}\left[\mathcal{W}_0 + \left(\frac{1}{2} - a\right)\mathcal{W}_1\right] C(k) \tag{3.64}$$

$$C_l^{NC}(\dot{\boldsymbol{h}}) = \frac{\pi}{U}\left(\frac{b}{U}\right)\left(\dot{\mathcal{W}}_0 - a\dot{\mathcal{W}}_1\right) \tag{3.65}$$

It is evident from Theodorsen's theory that the circulatory lift C_l^C is independent of the generalized acceleration vector $\dot{\boldsymbol{h}}$. Comparison with Greenberg's theory reveals

the same result [160]. Note that both Theodorsen's theory and Greenberg's theory assume incompressibility, whereas the CFD-RFA is applicable to compressible flow. However, the definition of circulation is independent of the fluid density. Therefore, this approach of computing circulatory lift from an RFA method is justified.

3.2.4 Verification study

The NACA0012 airfoil is used for the current calculations and verified with previous work [134, 145]. The Reynolds number was fixed at $Re = 2.1 \times 10^6$ for CFD simulations. The database spans angles of attack in the range $\alpha = 0^o$ to $\alpha = 13^o$, and Mach numbers from 0 to 0.8. The NACA0012 airfoil is symmetric, therefore the airfoil response at negative angles of attack is the same as the airfoil response at positive angles of attack with the appropriate change in sign. Lift and moment act in the opposite direction at negative angles of attack, whereas drag does not change sign. The mesh refinement study and optimization of the pole placement in the CFD-RFA is described in detail in Ref. 134.

In Fig. 3.7, the CFD-RFA model is compared with DL-RFA for a NACA0012 airfoil. The airfoil oscillates around a mean angle of attack of $\alpha = 5^o$, with an oscillation amplitude of $\alpha_0 = 1^o$ and reduced frequency of $k = 0.064$. The Mach number is $M_c = 0.6$. Both models use a $n_p = 5$ pole approximation. The Runge-Kutta fourth order scheme and a non-dimensional time step of $\Delta\bar{t} = 0.25$ is used. The results are compared with CFD++ calculations in Refs. 145 and 134. The reduced frequency reported in the two references have a typographical error. The authors of Refs. 134 and 145 verified that the correct reduced frequency is $k = 0.064$ and not $k = 0.062$.

The CFD-RFA predicts a lower maximum lift coefficient when compared to the DL-RFA as shown in Fig. 3.7a. The magnitude of lift is reduced in the CFD-RFA

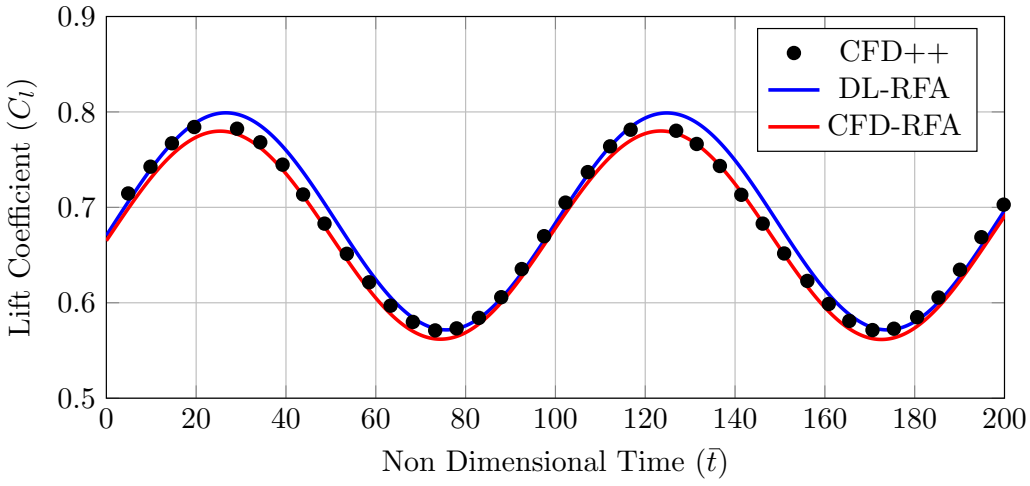

(a) Lift Coefficient

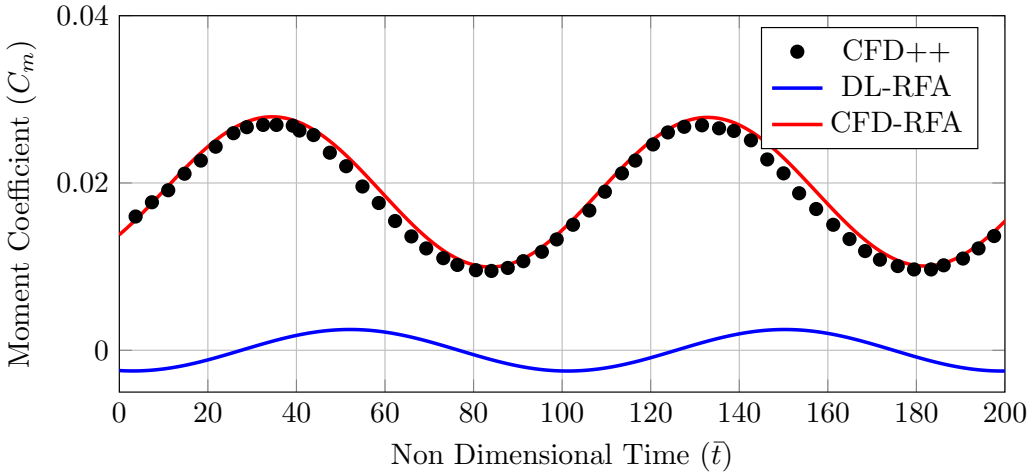

(b) Moment Coefficient

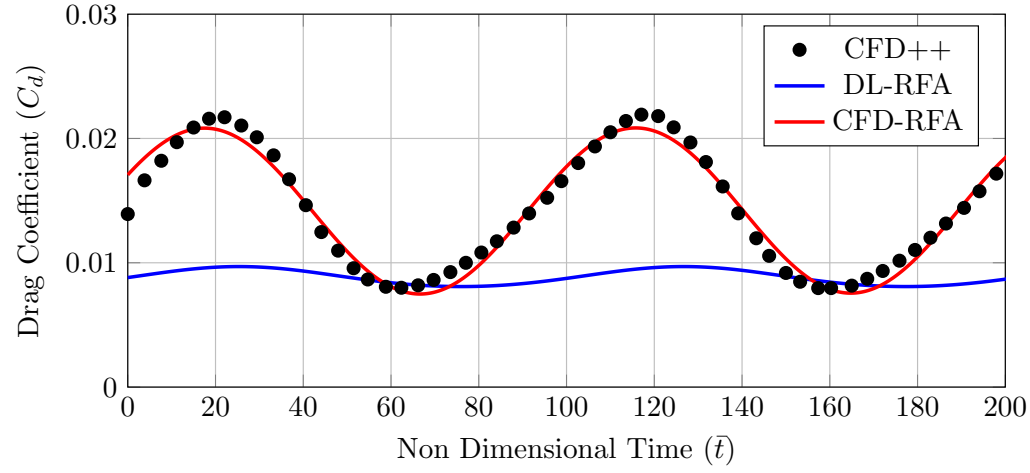

(c) Drag Coefficient

Figure 3.7: Comparison of DL-RFA and CFD-RFA models for sinusoidally pitching NACA0012 airfoil

due to the inclusion of the airfoil shape, whereas the DL-RFA result is based on the assumption that the airfoil is represented by a flat plate. The CFD-RFA calculations capture the CFD++ results better than the DL-RFA method. The DL-RFA lift coefficient overshoots the lift peak compared to the CFD-RFA and CFD++ results. There is significant difference between the airfoil pitching moment calculated using the CFD-RFA and DL-RFA method in Fig. 3.7b. The DL-RFA predicts a zero mean pitching moment. The CFD-RFA captures the CFD++ results showing a non zero mean pitching moment combined with larger oscillation amplitude compared to DL-RFA. The difference between the methods indicates that using an accurate aerodynamic load model is important.

The CFD-RFA drag is compared with a quasisteady approximation of drag in Fig. 3.7c. The drag coefficient was approximated as a quadratic function of the angle of attack using experimental data from Ref. 161:

$$C_d = 0.007 + 0.264\alpha^2 \tag{3.66}$$

The CFD-RFA model predicts a larger magnitude and variation of drag, compared to a simple quasisteady drag model. The CFD-RFA method captures the CFD++ drag prediction, with a maximum error of approximately 5%. The mean value of drag predicted by CFD-RFA is approximately 60% greater than that using the quasisteady value. The magnitude of the oscillations calculated with CFD-RFA is nearly 6.7 times the magnitude of the oscillations calculated with the quasisteady approximation. The differences in Fig. 3.7c illustrate the shortcomings of using inviscid, incompressible and quasisteady drag assumptions for calculations of unsteady loads.

3.3 Dynamic stall model for separated flow loads

In high speed flight, sections of the retreating blade encounter low Mach numbers and high angles of attack close to stall. The periodic separation and reattachment of the flow to the airfoil is accompanied by large changes in sectional loads known as dynamic stall (DS). The DS phenomenon severely limits helicopter performance by generating excessive torsional oscillations on the blade that produce unacceptable vibratory loads on pitch links. There are no closed-form solutions capable of modeling DS, and CFD cannot model this phenomenon in a reliable manner. Two semi-empirical models are in widespread use for calculating DS loads, the ONERA-DS model [162] and the Leishman-Beddoes DS model [163].

3.3.1 Physical description of dynamic stall

A detailed physical description of DS is presented in Ref. 13. The principal characteristic of DS is the formation and shedding of a vortex over the leading edge of the airfoil [164]. Figure 3.8 illustrates the DS process.

(a) Figure 3.8a illustrates the beginning of DS. As the angle of attack increases beyond the static stall angle, the boundary layer over the upper layer of the airfoil thickens. Due to the positive pitch rate $\dot{\alpha} > 0$ of the airfoil, there is a reduction in the adverse pressure gradient in the boundary layer and the flow remains attached. This causes *delay in flow separation*.

(b) As the angle of attack increases, a leading edge vortex or a separation bubble forms over the leading edge of the airfoil as shown in Fig. 3.8b. This vortex provides additional lift over the airfoil, known as *lift overshoot*. The additional lift increases the effective lift curve slope and maximum lift of the airfoil beyond static limits.

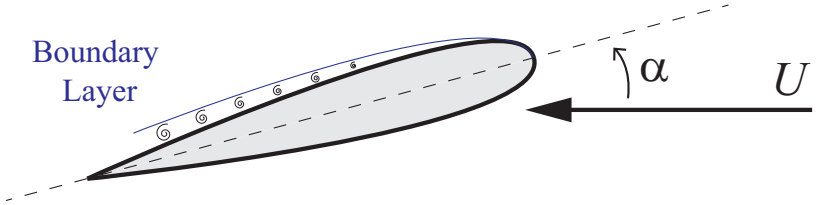

(a) Flow reversal in boundary layer

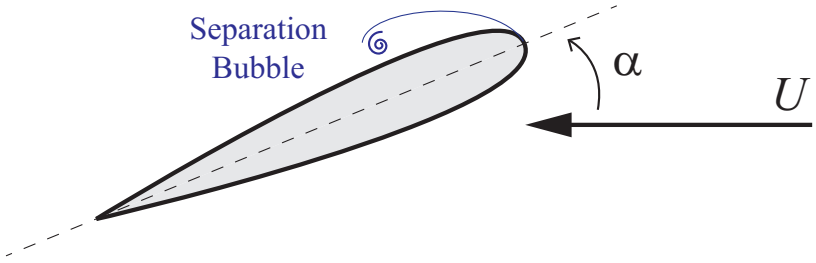

(b) Leading edge vortex formation

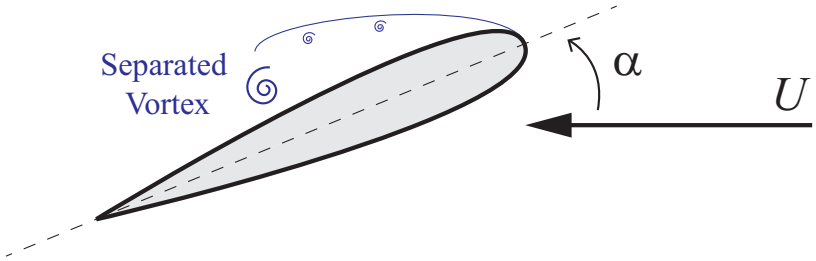

(c) Vortex separates from surface and moves over airfoil

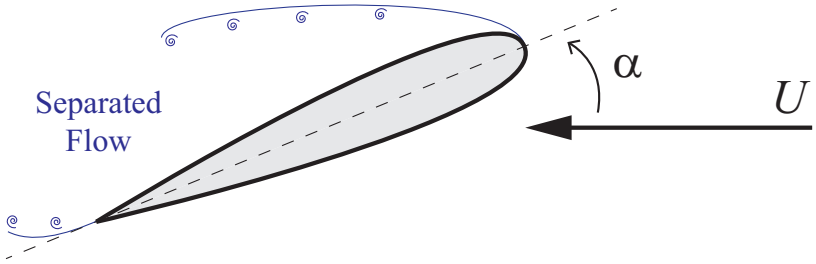

(d) Fully separated flow

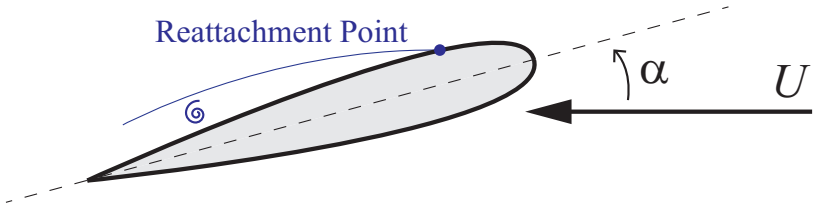

(e) Flow reattaches at point aft of leading edge

Figure 3.8: Physical description of dynamic stall

(c) The leading edge vortex separates from the surface of the airfoil and travels downstream over the upper surface of the airfoil as shown in Fig. 3.8c. The center of pressure moves aft of the airfoil and results in a large nose-down pitching moment. This is known as *moment stall*.

(d) Finally, the vortex passes over the trailing edge and into the shed wake of the airfoil in Fig. 3.8d. This causes a loss of lift known as *lift stall*. The flow completely separates over the upper surface of the airfoil. This flow state is similar to the static stall state found under steady conditions at the same angle of attack. This results in loss of lift, peak pressure drag, and maximum nose-down pitching moment.

(e) When the angle of attack decreases below the static stall angle, there is a time lag as the flow reorganizes from a fully separated state to conditions suitable for reattachment. The flow reattaches from the front to back over the airfoil as shown in Fig. 3.8e. Viscous effects have little influence on reattachment [13].

Therefore, the DS process is highly nonlinear and characterized by the presence of hysteresis.

3.3.2 Formulation of ONERA dynamic stall model

In this dissertation, DS airfoil loads are modeled using a modified version of the ONERA-DS model [162] used extensively in comprehensive rotorcraft codes [154, 165, 166]. The modified ONERA-DS model [167] is used in the current study.

The ONERA-DS model is based on a system of second order ODEs for the unsteady lift, moment and drag produced on a 2D airfoil. The differential equations are written in terms of circulation variables Γ_d^k, where the superscript k stands for lift,

moment and drag.

$$\ddot{\Gamma}_d^k + a_d^k \left(\frac{U}{b}\right) \dot{\Gamma}_d^k + r_d^k \left(\frac{U}{b}\right)^2 \left[\Gamma_d^k + bU\Delta C_d^k\right] + e_d^k U \dot{W}_0 = 0 \tag{3.67}$$

The parameter ΔC_d represents the net change in the load coefficient in static stall. The DS circulation states are rearranged into state space form:

$$\dot{\boldsymbol{x}}_d = [\boldsymbol{R}_d]\boldsymbol{x}_d + [\boldsymbol{E}_d]\dot{\boldsymbol{h}} + \boldsymbol{g}_d \tag{3.68}$$

$$\boldsymbol{f}_d = [\boldsymbol{D}_d]\boldsymbol{x}_d \tag{3.69}$$

where,

$$\boldsymbol{x}_d = \left\{\Gamma_d^{\mathcal{L}},\ \ \Gamma_d^{\mathcal{M}},\ \ \Gamma_d^{\mathcal{D}},\ \ \dot{\Gamma}_d^{\mathcal{L}},\ \ \dot{\Gamma}_d^{\mathcal{M}},\ \ \dot{\Gamma}_d^{\mathcal{D}}\right\}^T \tag{3.70}$$

$$[\boldsymbol{R}_d] = \begin{bmatrix} [\boldsymbol{0}]_{3\times3} & [\boldsymbol{I}]_{3\times3} \\ -\left(\frac{U}{b}\right)^2 \begin{bmatrix} r_d^{\mathcal{L}} & 0 & 0 \\ 0 & r_d^{\mathcal{M}} & 0 \\ 0 & 0 & r_d^{\mathcal{D}} \end{bmatrix} & -\left(\frac{U}{b}\right) \begin{bmatrix} a_d^{\mathcal{L}} & 0 & 0 \\ 0 & a_d^{\mathcal{M}} & 0 \\ 0 & 0 & a_d^{\mathcal{D}} \end{bmatrix} \end{bmatrix} \tag{3.71}$$

$$[\boldsymbol{E}_d] = -U \begin{bmatrix} [\boldsymbol{0}]_{3\times1} & [\boldsymbol{0}]_{3\times1} \\ \left\{e_d^{\mathcal{L}},\ \ e_d^{\mathcal{M}},\ \ e_d^{\mathcal{D}}\right\}^T & [\boldsymbol{0}]_{3\times1} \end{bmatrix} \tag{3.72}$$

$$\boldsymbol{g}_d = -\left(\frac{U^3}{b^2}\right) \left\{0,\ \ 0,\ \ 0,\ \ r_d^{\mathcal{L}}\Delta C_d^{\mathcal{L}},\ \ r_d^{\mathcal{M}}\Delta C_d^{\mathcal{M}},\ \ r_d^{\mathcal{D}}\Delta C_d^{\mathcal{D}}\right\}^T \tag{3.73}$$

$$[\boldsymbol{D}_d] = \frac{1}{bU} \begin{bmatrix} [\boldsymbol{I}]_{3\times3} & [\boldsymbol{0}]_{3\times3} \end{bmatrix} \tag{3.74}$$

The parameters a_d, r_d, e_d are calculated based on empirical relations presented in Ref.

162:

$$a_d^k = a_{d_0}^k + a_{d_2}^k (\Delta C_d^{\mathcal{L}})^2 \tag{3.75}$$

$$r_d^k = \left[r_{d_0}^k + r_{d_2}^k (\Delta C_d^{\mathcal{L}})^2 \right]^2 \tag{3.76}$$

$$e_d^k = e_{d_2}^k (\Delta C_d^{\mathcal{L}})^2 \tag{3.77}$$

3.3.3 Time delay in ONERA dynamic stall model

Flow separation and reattachment in DS is a hysteresis process. The DS begins when the angle of attack exceeds the critical value.

$$\alpha > \alpha_{cr} = 13^o (1 - M_c^2) \tag{3.78}$$

A time lag is introduced to delay flow separation. The non-dimensional time $\bar{t}$ represents the number of semi-chords traveled by the airfoil in time t. Note that the magnitude of the relative velocity U changes with time, therefore the non-dimensional time is an integral quantity.

$$\bar{t} = \frac{1}{b} \int_0^t U \mathrm{d}t' \tag{3.79}$$

The equations for the change in load coefficients ΔC_d are:

$$\Delta C_d^{\mathcal{L}} = \begin{cases} 0 & , \quad \bar{t} \le \tau_d^{\mathcal{L}} \\ (p_{d_0} - p_{d_1}) \Delta\alpha_d - K_d^{\mathcal{L}} \left[\exp\left(h_d^{\mathcal{L}} \Delta\alpha_d \right) - 1 \right] & , \quad \bar{t} > \tau_d^{\mathcal{L}} \end{cases} \tag{3.80}$$

$$\Delta C_d^{\mathcal{M}} = \begin{cases} 0 & , \quad \bar{t} \le \tau_d^{\mathcal{M}} \\ K_d^{\mathcal{M}} \left[\exp\left(h_d^{\mathcal{M}} (\Delta\alpha_d - 0.22) \right) - 1 \right] & , \quad \bar{t} > \tau_d^{\mathcal{M}} \end{cases} \tag{3.81}$$

$$\Delta C_d^{\mathcal{D}} = \begin{cases} 0 & , \quad \bar{t} \le \tau_d^{\mathcal{D}} \\ K_d^{\mathcal{D}} \left(1 - \left| \dfrac{\alpha_{d_0} - \alpha}{\alpha_{d_0} - \alpha_{cr}} \right|^{h_d^{\mathcal{D}}} \right) & , \quad \bar{t} > \tau_d^{\mathcal{D}} \end{cases} \tag{3.82}$$

Table 3.1: Parameters used in modified ONERA-DS model

Symbol	**Lift**	**Drag**	**Moment**
a_{d_0}	0.2	0.25	0.2
a_{d_2}	0.2	0.1	0.2
e_{d_2}	-0.05	0.01	0.01
h_d	$-0.5 + (1.5 - M_c)M_c^2$	$\left(\frac{\alpha_{d_0} - \alpha}{\alpha_{d_1} - \alpha_{cr}}\right)$	$-0.4 - 0.21\tan^{-1}[22(0.45 - M_c)]$
K_d	$0.7(1 - M_c)$	-0.292	$-0.11 - 0.19\exp[-40(M_c - 0.6)^2]$
p_{d_0}	$0.1\sqrt{1 - M_c^2}$	-	-
p_{d_1}	$0.1M_c^4$	-	-
r_{d_0}	0.3	0.2	0.25
r_{d_2}	0.2	0.2	0.1
τ_d	8	2	2

Table 3.2: Angles used in modified ONERA-DS model

Angle	**Value**
α_{d_0}	25^o
α_{d_1}	$18^o - 2^o\tan^{-1}(4M_c)$
$\Delta\alpha_d$	$\frac{180}{\pi}(\alpha - \alpha_{cr})$

The time delays τ_d for lift, drag and moment used in this study are presented in Table 3.1. Note that the time delay for lift is greater than the time delay for moment and drag, to represent the lag between the leading edge vortex formation (Fig. 3.8b) and full separation (Fig. 3.8d). The parameters used in the load coefficient equations are provided in Tables 3.1 and 3.2.

When the angle of attack decreases below the critical angle of attack α_{cr}, the change in load coefficients due to static stall ΔC_d^k are zero. When $\Delta C_d^k = 0$, the circulation states Γ_d^k and DS loads $\boldsymbol{f}_d$ decrease to zero with time due to Eqn. 3.67. This time response of the differential equations represents the delay in reattachment.

3.4 Reverse flow

In forward flight, a circular region near the hub experiences *reverse flow*, i.e. the relative air moves from the TE to the LE of the airfoil. In reverse flow, the airfoil effectively acts like a bluff body in an unsteady free-stream. In typical sharp TE airfoils, reverse flow generates excessive vortex shedding at the LE, and is accompanied by increased drag [168–171].

The reverse flow region extends from the hub center to in-board blade sections as determined by the equation:

$$\mu + \frac{r}{R} \sin \psi < 0 \tag{3.83}$$

The advance ratio μ determines the diameter of the reverse flow region. The reverse flow region for a high speed helicopter such as the Sikorsky X2TD can be very large because the advance ratios are high ($\mu \approx 0.85$). Due to the slowed rotor, the rotor RPM is reduced, and the advance ratio μ increases. To alleviate vortex shedding in reverse flow, the inner region of the rotor blades use blunt TE or *double-ended* airfoils [46].

A common approach for modeling reverse flow in rotorcraft comprehensive analysis codes is to augment look-up tables with static lift, drag and moment coefficients for an airfoil in reverse flow computed using RANS CFD. A recent study modified the source/doublet panel approach such that the Kutta condition was applied at the LE instead of the TE in reverse flow [97].

In this dissertation, advance ratios of $\mu \leq 0.5$ are considered. The local dynamic pressure is small in the reverse flow region, as shown in Fig. 3.9. The dynamic pressure over the rotor is normalized with respect to the dynamic pressure at the blade

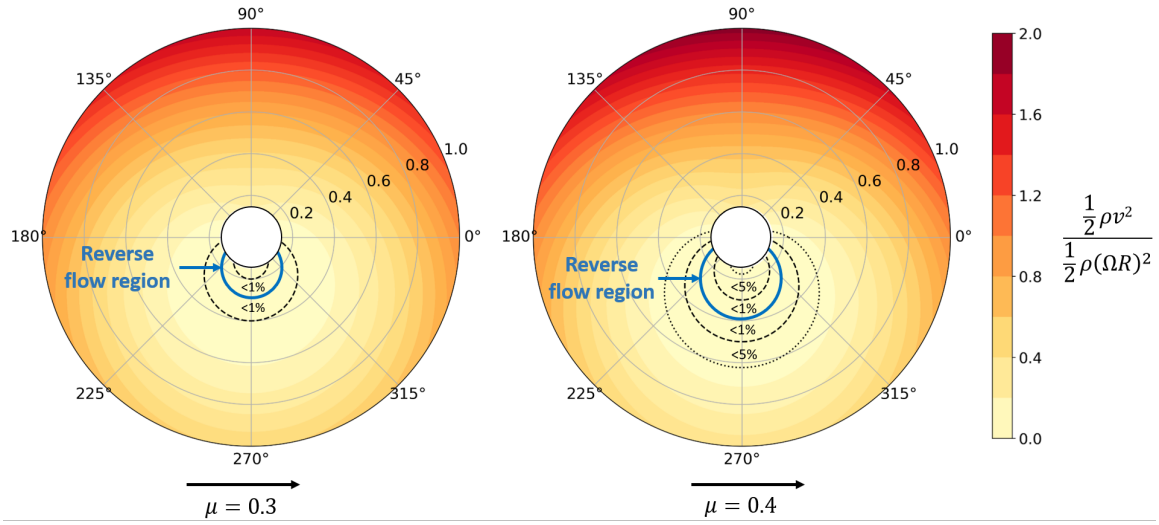

Figure 3.9: Dynamic pressure over counter-clockwise rotor in forward flight

tip in hover. The boundary of the reverse flow region is denoted with a blue line. A portion of the reverse flow region lies within the hub offset region, therefore no loads are generated there. The dynamic pressure inside the reverse flow region at $\mu = 0.3$ is less than 1% of the dynamic pressure at the blade tip (region between the two dashed lines). The reverse flow region at $\mu = 0.4$ has dynamic pressure which is less than 5% of the dynamic pressure at the blade tip. Therefore, the aerodynamic loads are small compared to the rest of the rotor.

In addition, the loads in the reverse flow region are adjacent to the blade root, therefore the effect on the bending and torsional moment at the root is small. Hence, the lift and moment in the reverse flow region are set to zero in our analysis. The drag is obtained from the CFD-RFA model. The generalized loads from the DS model are set to zero in reverse flow.

$$\boldsymbol{f} = \begin{cases} \left\{ \begin{array}{ccc} 0, & 0, & (C_d)_{\text{CFD-RFA}} \end{array} \right\}^T & , \quad U_t \leq 0 \\ \boldsymbol{f}_a + \boldsymbol{f}_d & , \quad U_t > 0 \end{cases} \tag{3.84}$$

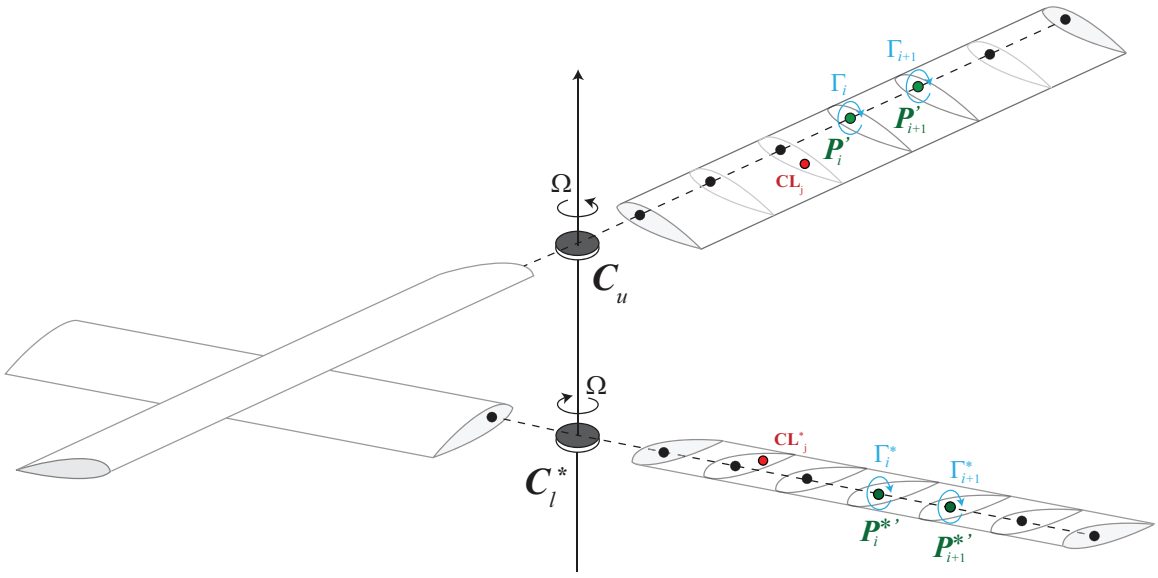

Figure 3.10: Spanwise blade aerodynamic model for a coaxial rotor

3.5 Spanwise blade aerodynamic modeling

The CFD-RFA and ONERA-DS models determine cross sectional unsteady aerodynamic loads due to the generalized motion of the airfoil. The coaxial rotor blades are represented with multiple blade cross sections as shown in Fig. 3.10. Each blade is discretized into n_s cross sections. The upper and lower rotor each have N_b blades.

3.5.1 Combined aerodynamic states

The aerodynamic states of each blade section are assembled in the combined aerodynamic state vector. The subscripts $n = 1, \cdots, n_s$ represent the blade section index of each blade.

$$\boldsymbol{X}_a = \left\{ \left\{ \begin{array}{c} (\boldsymbol{x}_a)_1 \\ \vdots \\ (\boldsymbol{x}_a)_{n_s} \end{array} \right\}^T_u , \left\{ \begin{array}{c} (\boldsymbol{x}_a)_1 \\ \vdots \\ (\boldsymbol{x}_a)_{n_s} \end{array} \right\}^T_l \right\}^T \tag{3.85}$$

$$\boldsymbol{X}_d = \left\{ \left\{ \begin{Bmatrix} (\boldsymbol{x}_d)_1 \\ \vdots \\ (\boldsymbol{x}_d)_{n_s} \end{Bmatrix}^T_u , \begin{Bmatrix} (\boldsymbol{x}_d)_1 \\ \vdots \\ (\boldsymbol{x}_d)_{n_s} \end{Bmatrix}^T_l \right\}^T \tag{3.86}$$

Similarly, the bound circulation over the blades are combined into the attached flow and separated flow circulation vectors:

$$\boldsymbol{G}_a = \left\{ \left\{ \begin{Bmatrix} (\Gamma_a)_1 \\ \vdots \\ (\Gamma_a)_{n_s} \end{Bmatrix}^T_u , \begin{Bmatrix} (\Gamma_a)_1 \\ \vdots \\ (\Gamma_a)_{n_s} \end{Bmatrix}^T_l \right\}^T \tag{3.87}$$

$$\boldsymbol{G}_d = \left\{ \left\{ \begin{Bmatrix} (\Gamma_d^{\mathcal{L}})_1 \\ \vdots \\ (\Gamma_d^{\mathcal{L}})_{n_s} \end{Bmatrix}^T_u , \begin{Bmatrix} (\Gamma_d^{\mathcal{L}})_1 \\ \vdots \\ (\Gamma_d^{\mathcal{L}})_{n_s} \end{Bmatrix}^T_l \right\}^T \tag{3.88}$$

The sectional lift, moment and drag coefficients in attached flow $\boldsymbol{f}_a$ and separated flow $\boldsymbol{f}_d$ are scaled appropriately to determine the sectional forces $\boldsymbol{p}_a^A, \boldsymbol{p}_d^A$ and moments $\boldsymbol{q}_a^A, \boldsymbol{q}_d^A$ in the blade undeformed coordinate system, as discussed in Section 2.3.2.3. Therefore, the combined blade attached and separated force vectors are.

$$\boldsymbol{F}_a = \left\{ \left\{ \begin{Bmatrix} (\boldsymbol{p}_a^A)_1 \\ \vdots \\ (\boldsymbol{p}_a^A)_{n_s} \end{Bmatrix}^T_u , \begin{Bmatrix} (\boldsymbol{q}_a^A)_1 \\ \vdots \\ (\boldsymbol{q}_a^A)_{n_s} \end{Bmatrix}^T_u , \begin{Bmatrix} (\boldsymbol{p}_a^A)_1 \\ \vdots \\ (\boldsymbol{p}_a^A)_{n_s} \end{Bmatrix}^T_l \begin{Bmatrix} (\boldsymbol{q}_a^A)_1 \\ \vdots \\ (\boldsymbol{q}_a^A)_{n_s} \end{Bmatrix}^T_l \right\}^T \tag{3.89}$$

$$\boldsymbol{F}_d = \left\{ \left\{ \begin{Bmatrix} (\boldsymbol{p}_d^A)_1 \\ \vdots \\ (\boldsymbol{p}_d^A)_{n_s} \end{Bmatrix}^T_u , \begin{Bmatrix} (\boldsymbol{q}_d^A)_1 \\ \vdots \\ (\boldsymbol{q}_d^A)_{n_s} \end{Bmatrix}^T_u , \begin{Bmatrix} (\boldsymbol{p}_d^A)_1 \\ \vdots \\ (\boldsymbol{p}_d^A)_{n_s} \end{Bmatrix}^T_l \begin{Bmatrix} (\boldsymbol{q}_d^A)_1 \\ \vdots \\ (\boldsymbol{q}_d^A)_{n_s} \end{Bmatrix}^T_l \right\}^T \tag{3.90}$$

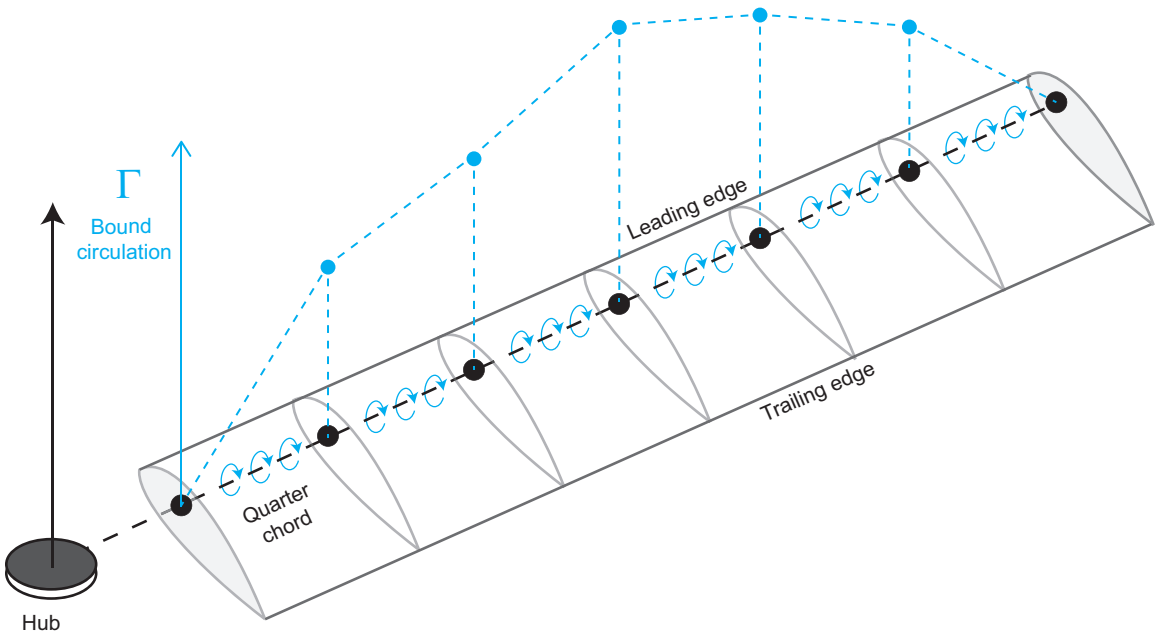

Figure 3.11: Bound circulation distribution over blade

3.5.2 Blade bound circulation

As noted in Section 3.1.2.2, the relative air velocity over the airfoil consists of velocity induced by the blade bound circulation $\boldsymbol{U}_B$. The net circulation of the airfoil consists of the attached flow and separated flow circulation.

$$\Gamma = \Gamma_a + \Gamma_d^{\mathcal{L}} \tag{3.91}$$

The bound circulation is located at the QC of the airfoil. Therefore, for a rotor blade, the bound circulation is represented as a vortex line located at the QC i.e. the elastic axis of the blade. The bound circulation varies linearly between points placed along the quarter chord line of the blade, shown in Fig. 3.11. The circulation at the root and tip of the blade is zero.

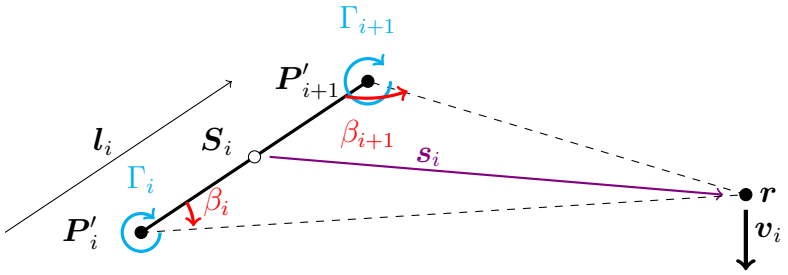

Figure 3.12: Velocity induced by bound circulation over a blade segment

3.5.2.1 Velocity induced by vortex filament

The velocity induced by the blade at a point is calculated using the Biot-Savart law. The induced velocity depends on the distances between the blade sections measured along the deformed blade. A representative vortex filament between two consecutive deformed points on the blade is shown in Fig. 3.12.

The bound circulation varies linearly between the points $\boldsymbol{P}'_i$ and $\boldsymbol{P}'_{i+1}$. The vector connecting the two points is $\boldsymbol{l}_i$.

$$\boldsymbol{l}_i = \boldsymbol{P}'_{i+1} - \boldsymbol{P}'_i \tag{3.92}$$

Note that for a clockwise rotating blade, the vector $\boldsymbol{l}_i^*$ is in the opposite direction.

$$\boldsymbol{l}_i^* = \boldsymbol{P}_i'^* - \boldsymbol{P}_{i+1}'^* \tag{3.93}$$

The length of the blade segment l_i, and the unit vector $\hat{\boldsymbol{l}}_i$ associated with $\boldsymbol{l}_i$ are:

$$l_i = |\boldsymbol{l}_i| \tag{3.94}$$

$$\widehat{\boldsymbol{l}}_i = \frac{\boldsymbol{l}_i}{l_i} \tag{3.95}$$

The point $\boldsymbol{S}_i$ is the closest point to the target location $\boldsymbol{r}$ which lies along the line

passing through the two points. The vector between the point $\boldsymbol{S}_i$ and $\boldsymbol{r}$ is $\boldsymbol{s}_i$.

$$\boldsymbol{s}_i = \boldsymbol{r} - \boldsymbol{S}_i \tag{3.96}$$

The distance s_i, and the unit vector $\hat{\boldsymbol{s}}_i$ associated with $\boldsymbol{s}_i$ are:

$$s_i = |\boldsymbol{s}_i| \tag{3.97}$$

$$\widehat{\boldsymbol{s}}_i = \frac{\boldsymbol{s}_i}{s_i} \tag{3.98}$$

We define two bound circulation terms for each blade segment representing the bound circulation at the point $\boldsymbol{S}_i$, and the change in bound circulation over the segment.

$$\Gamma_i^0 = \frac{\Gamma_i \left|\boldsymbol{P}'_{i+1} - \boldsymbol{S}_i\right| + \Gamma_{i+1} \left|\boldsymbol{S}_i - \boldsymbol{P}'_i\right|}{l_i^2} \tag{3.99}$$

$$\Gamma_i^1 = \frac{\Gamma_{i+1} - \Gamma_i}{l_i} \tag{3.100}$$

The velocity induced by the blade segment at a point $\boldsymbol{r}$ is:

$$\boldsymbol{v}_{B_i}(\boldsymbol{r}) = \frac{\widehat{\boldsymbol{l}}_i \times \widehat{\boldsymbol{s}}_i}{4\pi s_i} \left[l_i \Gamma_i^0 (\cos\beta_i + \cos\beta_{i+1}) + s_i \Gamma_i^1 (\sin\beta_i - \sin\beta_{i+1})\right] \tag{3.101}$$

Note that a blade segment can not induce velocity on itself. Therefore, when computing blade induced velocities at $\boldsymbol{CL}_i$ and $\boldsymbol{CL}_{i+1}$, the circulations Γ_i and Γ_{i+1} are set to zero respectively. The expressions are simplified to:

$$\boldsymbol{v}_{B_i}(\boldsymbol{CL}_i) = -\frac{\Gamma_{i+1}}{4\pi l_i}(1 - \sin\beta_{i+1})\hat{\boldsymbol{k}}_{t_i} \tag{3.102}$$

$$\boldsymbol{v}_{B_i}(\boldsymbol{CL}_{i+1}) = -\frac{\Gamma_i}{4\pi l_{i+1}}(1 - \sin\beta_i)\hat{\boldsymbol{k}}_{t_{i+1}} \tag{3.103}$$

3.5.2.2 Total velocity induced by all lifting surfaces

The net relative velocity $\boldsymbol{U}_B$ is the summation of the velocities induced by all the blade segments of all blades of both rotors.

$$\boldsymbol{U}_B(\boldsymbol{CL}_j) = \sum_{i=1}^{N_f} \boldsymbol{v}_{B_i}(\boldsymbol{CL}_j) \tag{3.104}$$

Therefore, the velocities at all the CLs of the coaxial rotor are combined into a single vector $\boldsymbol{V}_B$.

$$\boldsymbol{V}_B = \left\{ \begin{array}{cccc} \boldsymbol{U}_B^T(\boldsymbol{CL}_1), & \cdots, & \boldsymbol{U}_B^T(\boldsymbol{CL}_{N_s}) \end{array} \right\}^T \tag{3.105}$$

From Eqn. 3.101, it is evident that the velocity depends on the blade bound circulation, the position of the blade QCs and CLs. Therefore,

$$\boldsymbol{V}_B \equiv \boldsymbol{V}_B(\boldsymbol{X}_s, \boldsymbol{G}_a, \boldsymbol{G_d}) \tag{3.106}$$

3.6 Aerodynamic loads module

The inner construction of the aerodynamics module is illustrated in Fig. 3.13. The dashed box inside the module represents the computations that take place at each blade section. The green color in the figure indicates terms associated with the generalized motion. The blue color indicates terms associated with generalized aerodynamic loads. The red color indicates terms associated with bound circulation.

The **Generalized motion** block represents the equations presented in Section 3.1. The relative velocities due to the blade kinematics, wake induced velocity, and bound circulation induced velocity are used to determine the generalized motion vector $\boldsymbol{h}$ and its rate $\dot{\boldsymbol{h}}$.

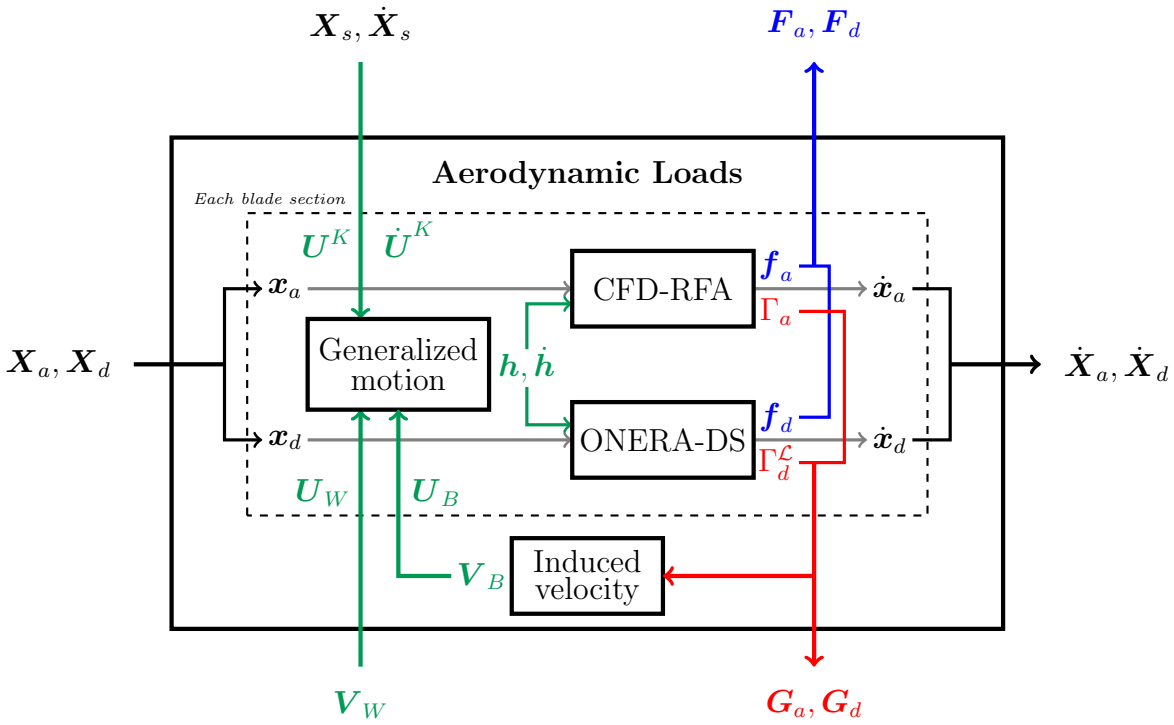

Figure 3.13: Aerodynamic loads module

The **CFD-RFA** block represents the equations provided in Section 3.2. The **ONERA-DS** block represents the equations given in Section 3.3. The two modules use the aerodynamic states $\boldsymbol{x}_a$ and $\boldsymbol{x}_d$ respectively to determine their rates $\dot{\boldsymbol{x}}_a$ and $\dot{\boldsymbol{x}}_d$. The generalized forces $\boldsymbol{f}_a$ and $\boldsymbol{f}_d$ are combined to obtain the forces acting over all the blade in the vectors $\boldsymbol{F}_a$ and $\boldsymbol{F}_d$ respectively. The bound circulation Γ_a and Γ_d over each blade section are combined in the coaxial rotor circulation vectors $\boldsymbol{G}_a$ and $\boldsymbol{G}_d$ each.

The blade circulations are used to determine the bound circulation induced velocities $\boldsymbol{V}_B$ in the **Induced velocity** block using equations described in 3.1.2.2. Figure 3.13 shows the interdependence of the bound circulation vectors $\boldsymbol{G}_a$ and $\boldsymbol{G}_d$, with the bound circulation induced velocity vector $\boldsymbol{V}_B$. The bound circulation induced velocity determines the blade loads, and hence the bound circulation. The equations

that represent this loop are solved simultaneously using Powell's Hybrid method [172] implemented in the GSL [157].

Therefore, the aerodynamics module computes the rate of change of the aerodynamic states $\boldsymbol{X}_a$ and $\boldsymbol{X}_d$, given the structural state vectors $\boldsymbol{X}_s, \dot{\boldsymbol{X}}_s$, and the wake induced velocity vector $\boldsymbol{V}_W$. The next chapter describes the VVPM and the calculation of wake induced velocities $\boldsymbol{V}_W$.

CHAPTER 4

Rotor Wake Modeling using Viscous Vortex Particle Method

The VVPM is a type of free wake analysis where the wake vorticity is represented by vortex particles. The free wake method for rotor wake modeling is a Lagrangian approach i.e. it does not require grids, and vortex structures can be resolved over long distances. Conventional free wake methods use vortex filaments for modeling the rotor wake. Vortex filaments with a finite core radius are suitable for capturing the rolled-up tip vorticity of SMR blades. In most SMR FVW analyses, the near wake region is modeled as a rigid vortex sheet that extends $30^o - 60^o$ azimuth behind a blade [59, 133]. However, due to the proximity of the upper and lower rotors in coaxial configurations, there is significant interaction between the near wake and blades. Therefore, the rigid vortex sheet assumption may not capture the distortion in the near wake due to blade-wake interactions. Furthermore, the vortex sheet must be retained for a larger azimuthal duration to capture the interactions of the near wake with both rotors. Vortex particles are generated over the complete span of the blade and therefore, are a more accurate representation of a vorticity sheet behind a blade when compared to a single vortex filament for tip vorticity and a rigid near wake sheet. Therefore, the VVPM is a more general approach for modeling the 3D wake shed from the rotor blade when compared to a vortex filament based free wake method.

Vortex particles differ from vortex filaments in two main aspects [173]. First, the core radius of vortex filaments changes due to diffusion whereas vortex particles have a fixed core shape and size. The vorticity associated with each vortex particle changes due to vortex stretching and viscous diffusion as determined from the VVPM formulation. Second, vortex filaments must remain connected to each other, whereas vortex particles convect independently. Therefore, a flow-field represented by vortex particles is not guaranteed to remain divergence-free, i.e. the continuity of vorticity is not necessarily preserved. Hence, relaxation schemes such as particle merging and vorticity redistribution are applied [86].

A suitably discretized vortex filament approach can be made equivalent to a VPM for inviscid vorticity fields, if at each time step, vortex filaments are reconstructed using finite differences and interpolation [88]. These techniques are not usually implemented in FVW models used in rotorcraft research. In viscous flows, points in neighboring vortex filaments exchange vorticity through diffusion. However, diffusion can only be modeled with empirical techniques in filament methods [88]. On the other hand, VVPM accounts for diffusion using the Particle Strength Exchange (PSE) method. The PSE is naturally suited for a vortex particle representation of the vorticity. The limiting assumptions in the validity of PSE are a) the choice of kernel for the particle, and b) the resolution of the flow-field.

Thus, radial and azimuthal changes in a complex wake system can be captured in detail using a sufficient number of vortex particles. Therefore, VVPM is suitable for calculating coaxial rotor wake structures and it can provide higher fidelity when compared to simplified vortex filament free wake analyses. Furthermore, the VVPM provides results that are sufficiently accurate when compared to CFD [97]. Studies

such as Refs. 80 and 174 indicate that VVPM is well suited for capturing non-linear flow dynamics of LE vortex formations during stall. Thus, the VVPM is an efficient method for evaluating coaxial rotor interactions in high speed flight, including DS effects. Separated flow has been modeled with vortex particles [79, 175] in applications such as flapping wings [176, 177] and wind turbines [178]. Unsteady DS loads on rotary wing vehicles have been studied extensively, however models for the separated wake structure associated with DS have not been considered in published literature.

This chapter presents the formulation of the VVPM and its application to rotor wake simulations. There are several unique contributions presented in this chapter. Analytical expressions are derived for vortex particle interactions with rotor blades modeled with vortex filaments. Several corrections in the original formulation of VVPM in Ref. 179 are also presented. A generalized vortex particle generation process in attached and separated flow is described.

4.1 Formulation

Vortex particle methods for modeling fluid dynamics are based on solving the Lagrangian description of a discretized vorticity field [86, 88]. Reference 86 is a comprehensive study of singular and regularized vortex particles, and includes viscous diffusion by redistribution of particle strengths. The VVPM does not require grid generation and it has been applied to coaxial rotors by coupling with CFD or lifting line models for blade loads [93, 94, 180]. The VVPM has been described in detail in many publications [86, 88, 92–94, 140, 143, 179–181]. The formulation presented in this chapter follows Refs. 86 and 179 with some corrections.

4.1.1 Vorticity - velocity equation

The vorticity in a flow-field is defined as the curl of the velocity:

$$\boldsymbol{\omega} = \nabla \times \boldsymbol{v} \tag{4.1}$$

Therefore, the divergence of the vorticity field is zero:

$$\nabla \cdot \boldsymbol{\omega} = \nabla \cdot (\nabla \times \boldsymbol{v}) = 0 \tag{4.2}$$

The Navier-Stokes equations in the Eulerian frame are:

$$\frac{\partial \boldsymbol{v}}{\partial t} + \boldsymbol{v} \cdot \nabla \boldsymbol{v} = -\frac{\nabla P}{\rho} + \nu \nabla^2 \boldsymbol{v} \tag{4.3}$$

The flow is assumed to be incompressible. This assumption is valid for flow away from lifting surfaces. In this dissertation, compressibility effects are included in the calculation of aerodynamic loads over the lifting surface, described in detail in Chapter 3. However, the rotor wake vorticity is considered sufficiently separated from the blades for the incompressibility condition to be valid.

The curl operator is applied to Eqn. 4.3 to obtain the vorticity-velocity equation in the Lagrangian frame:

$$\frac{\mathrm{D}\boldsymbol{\omega}}{\mathrm{D}t} = \underbrace{\boldsymbol{\omega} \cdot \nabla \boldsymbol{v}}_{\text{vortex stretching}} + \underbrace{\nu \nabla^2 \boldsymbol{\omega}}_{\text{viscous diffusion}} \tag{4.4}$$

The vorticity-velocity equation has two terms: *vortex stretching* and *viscous diffusion*.

4.1.2 Vortex particle representation

The vorticity in the flow-field is represented using vortex particles. Vortex particles are also known as *vortex sticks*, *vortex blobs*, or *vortons* in literature [173]. Each particle is associated with a vorticity strength $\boldsymbol{\alpha}_p$ (= vorticity $\times$ volume) and located at a position $\boldsymbol{r}_p$. Each vortex particle can be thought of as a small section of a vortex tube (= circulation $\times$ length). However, vortex particles are independent compared to vortex filaments. The motion of vortex filaments is restricted because each end-point is shared with a neighboring vortex filament. Therefore, vortex filaments must move as a combined entity i.e. as a chain.

The smoothed vorticity at a point $\boldsymbol{x}$ at time t is:

$$\boldsymbol{\omega}_\sigma(\boldsymbol{x},t) = \sum_{i=1}^{N_p} \boldsymbol{\alpha}_{p_i}(t)\zeta_\sigma(|\boldsymbol{x}-\boldsymbol{x}_{p_i}|) \tag{4.5}$$

where $\zeta_\sigma(s)$ is the *regularization function* that represents the distribution of vorticity in the vicinity of the vortex particle. The regularization parameter σ is also known as the *smoothing radius*. The smoothing radius is different from the core radius associated with a vortex filament. In conventional FVW models, the vortex filament represents the rolled up tip vorticity of a rotor blade. Viscosity is modeled with a diffusion rate equation that changes the core radius of the filament as a function of time. In contrast, the vortex particle smoothing radius remains invariant in the simulation. The vortex particle smoothing radius is closely related to the resolution of the flow-field. The VVPM can be shown to converge to the solution of the Navier-Stokes equations as the smoothing radius decreases and the number of particles increases.

Due to the discretization as vortex particles, the vorticity field is no longer guar-

anteed to be divergence free.

$$\nabla \cdot \boldsymbol{\omega}_\sigma(\boldsymbol{x}, t) = \sum_{i=1}^{N} \boldsymbol{\alpha}_{p_i}(t) \left[\nabla \cdot \zeta_\sigma(|\boldsymbol{x} - \boldsymbol{x}_{p_i}|)\right] \neq 0 \tag{4.6}$$

This problem is addressed using particle redistribution schemes presented later in this chapter.

The regularized velocity field induced by the vortex particles is:

$$\boldsymbol{v}_\sigma(\boldsymbol{x}, t) = \sum_{i=1}^{N_p} \boldsymbol{K}_\sigma(\boldsymbol{x} - \boldsymbol{x}_{p_i}) \times \boldsymbol{\alpha}_{p_i}(t) \tag{4.7}$$

where $\boldsymbol{K}_\sigma$ is the Biot - Savart kernel :

$$\boldsymbol{K}_\sigma(\boldsymbol{x}) = -\frac{q_\sigma(|\boldsymbol{x}|)}{|\boldsymbol{x}|^3}\boldsymbol{x} \tag{4.8}$$

A particle cannot induce velocity on itself. Therefore, the velocity of a vortex particle due to the rest of the particles in the wake is:

$$\boldsymbol{v}_\sigma(\boldsymbol{x}_i) = \sum_{\substack{j=1 \\ i \neq j}}^{N_p} \boldsymbol{K}_\sigma(\boldsymbol{x}_{p_{ij}}) \times \boldsymbol{\alpha}_{p_j} \tag{4.9}$$

where the displacement between two vortex particles i and j is defined to be:

$$\boldsymbol{x}_{p_{ij}} = \boldsymbol{x}_{p_i} - \boldsymbol{x}_{p_j} \tag{4.10}$$

The distance between two particles is the absolute value of the displacement.

$$x_{p_{ij}} = \left|\boldsymbol{x}_{p_i} - \boldsymbol{x}_{p_j}\right| \tag{4.11}$$

The rate of change of the vorticity strength is obtained from the vorticity-velocity

equation (Eqn. 4.4), and therefore consists of vortex stretching and viscous diffusion terms.

$$\frac{\mathrm{d}\boldsymbol{\alpha_{p_i}}}{\mathrm{d}t} = \left(\frac{\mathrm{d}\boldsymbol{\alpha_{p_i}}}{\mathrm{d}t}\right)_{\substack{\text{vortex}\\\text{stretching}}} + \left(\frac{\mathrm{d}\boldsymbol{\alpha_{p_i}}}{\mathrm{d}t}\right)_{\substack{\text{viscous}\\\text{diffusion}}} \tag{4.12}$$

4.1.2.1 Vortex stretching

There are three approaches for computing the vortex stretching term [86].

$$\left(\frac{\mathrm{d}\boldsymbol{\alpha_{p_i}}}{\mathrm{d}t}\right)_{\substack{\text{vortex}\\\text{stretching}}} = \begin{cases} \boldsymbol{\alpha}_{p_i} \cdot \nabla \boldsymbol{v}_{\sigma_i} & \text{Classical scheme} \\ \boldsymbol{\alpha}_{p_i} \cdot \nabla^{\mathrm{T}} \boldsymbol{v}_{\sigma_i} & \text{Transpose scheme} \\ \frac{1}{2}\boldsymbol{\alpha}_{p_i} \cdot \left(\nabla \boldsymbol{v}_{\sigma_i} + \nabla^{\mathrm{T}} \boldsymbol{v}_{\sigma_i}\right) & \text{Mixed scheme} \end{cases} \tag{4.13}$$

The first approach is the *classical scheme*:

$$\boldsymbol{\alpha}_{p_i} \cdot \nabla \boldsymbol{v}_{\sigma_i} = \sum_{j=1}^{N_p} \left[\frac{q_\sigma(x_{p_{ij}})}{x_{p_{ij}}^3} (\boldsymbol{\alpha}_{p_j} \times \boldsymbol{\alpha}_{p_i}) + (\boldsymbol{\alpha}_{p_i} \cdot \boldsymbol{x}_{p_{ij}})(\boldsymbol{\alpha}_{p_j} \times \boldsymbol{x}_{p_{ij}}) F_\sigma(x_{p_{ij}}) \right] \tag{4.14}$$

where F_σ is the vortex stretching regularization function. The second approach is the *transpose scheme*:

$$\boldsymbol{\alpha}_{p_i} \cdot \nabla^{\mathrm{T}} \boldsymbol{v}_{\sigma_i} = \sum_{j=1}^{N_p} \left[\frac{q_\sigma(x_{p_{ij}})}{x_{p_{ij}}^3} (\boldsymbol{\alpha}_{p_i} \times \boldsymbol{\alpha}_{p_j}) + \{\boldsymbol{x}_{p_{ij}} \cdot (\boldsymbol{\alpha}_{p_i} \times \boldsymbol{\alpha}_{p_j})\} \boldsymbol{x}_{p_{ij}} F_\sigma(x_{p_{ij}}) \right] \tag{4.15}$$

The third approach is the *mixed scheme*:

$$\begin{aligned} \frac{1}{2}\boldsymbol{\alpha}_{p_i} \cdot \left(\nabla \boldsymbol{v}_{\sigma_i} + \nabla^{\mathrm{T}} \boldsymbol{v}_{\sigma_i}\right) &= \frac{1}{2} \sum_{j=1}^{N_p} \big[(\boldsymbol{\alpha}_{p_i} \cdot \boldsymbol{x}_{p_{ij}})(\boldsymbol{\alpha}_{p_j} \times \boldsymbol{x}_{p_{ij}}) \\ &\quad + \{\boldsymbol{x}_{p_{ij}} \cdot (\boldsymbol{\alpha}_{p_i} \times \boldsymbol{\alpha}_{p_j})\} \boldsymbol{x}_{p_{ij}} \big] F_\sigma(x_{p_{ij}}) \end{aligned} \tag{4.16}$$

The three schemes are equivalent **if** the particle vorticity field is equal to the curl of the velocity field.

$$\boldsymbol{\omega}_\sigma(\boldsymbol{x}) = \nabla \times \boldsymbol{v}_\sigma(\boldsymbol{x}) \tag{4.17}$$

$$\Rightarrow \sum_{i=1}^{N_p} \boldsymbol{\alpha}_{p_i}(t)\zeta_\sigma(\boldsymbol{x}-\boldsymbol{x}_{p_i}) = \nabla \times \left[\sum_{i=1}^{N_p} \boldsymbol{K}_\sigma(\boldsymbol{x}-\boldsymbol{x}_i) \times \boldsymbol{\alpha}_{p_i}(t)\right] \tag{4.18}$$

Due to the non-zero divergence of the regularized vorticity field, Eqn. 4.18 is not guaranteed to be satisfied. Therefore, the three forms of the vorticity stretching term are not equivalent in a regularized vorticity field.

The mixed scheme is computationally efficient due to the symmetry of the deformation tensor $\left(\nabla + \nabla^T\right)$. However, the transpose scheme is best suited for 3D flows. Unlike the classical or mixed schemes, the transpose scheme conserves the total vorticity in the field [86]. Therefore, the transpose scheme is used in the current study.

4.1.2.2 Viscous diffusion

The viscous diffusion term is calculated using the Particle Strength Exchange (PSE) [86, 182]. In PSE, the Laplacian operator in Eqn. 4.4 is approximated with an integral operator. The integral operator transforms to a summation over the particles:

$$\left(\frac{\mathrm{d}\boldsymbol{\alpha}_{\boldsymbol{p_i}}}{\mathrm{d}t}\right)_{\substack{\text{viscous}\\ \text{diffusion}}} = \nu\nabla^2(\mathcal{V}\boldsymbol{\omega}_{\sigma_i}) = \frac{2\nu}{\sigma^2}\sum_{j=1}^{N_p}(\mathcal{V}_{p_i}\boldsymbol{\alpha}_{p_j} - \mathcal{V}_{p_j}\boldsymbol{\alpha}_{p_i})\eta_\sigma(x_{p_{ij}}) \tag{4.19}$$

The viscous diffusion interaction between two particles ensures that the increase in vorticity of one particle is equal to the decrease in vorticity strength of the other.

$$\left[(\mathcal{V}_{p_i}\boldsymbol{\alpha}_{p_j} - \mathcal{V}_{p_j}\boldsymbol{\alpha}_{p_i})\eta_\sigma(x_{p_{ij}})\right] = -\left[(\mathcal{V}_{p_j}\boldsymbol{\alpha}_{p_i} - \mathcal{V}_{p_i}\boldsymbol{\alpha}_{p_j})\eta_\sigma(x_{p_{ji}})\right] \tag{4.20}$$

Therefore, this method is called Particle Strength Exchange. The viscous interactions depend on the volume of each particle $\mathcal{V}_p$ and the distance x_p between them. The function $\eta_\sigma(s)$ is a smoothed approximation of the kernel for the heat equation. The Gaussian kernel is used in this study.

$$\eta_\sigma(s) = \frac{1}{(2\pi)^{3/2}\sigma^3} \mathrm{e}^{-s^2/2\sigma^2} \tag{4.21}$$

4.1.2.3 Regularization functions

There are several choices for the regularization function $\zeta_\sigma(s)$ available for the VVPM. In an ideal vortex particle representation, there are an infinite number of vortex particles in the flow-field, the smoothing radius σ is zero, and therefore, the regularization function $\zeta_\sigma(s)$ is the 3D Dirac delta function $\delta(s)$.

In this study, the Gaussian kernel is selected because it is consistent with the choice of kernel function $\eta_\sigma(s)$ used in PSE. The vorticity regularization function is:

$$\zeta_\sigma(s) = \frac{1}{(2\pi)^{3/2}\sigma^3} \mathrm{e}^{-s^2/2\sigma^2} \tag{4.22}$$

The regularized kernel of the Biot - Savart function is related to the vorticity regularization function with the following equation:

$$\frac{1}{s^2}\frac{\partial q_\sigma(s)}{\partial s} = \zeta_\sigma(s) \tag{4.23}$$

Therefore, the regularized kernel of the Biot - Savart function for a Gaussian vorticity regularization function is:

$$\frac{q_\sigma(s)}{s^3} = \frac{1}{4\pi s^3}\mathrm{erf}\left(\frac{s}{\sqrt{2}\sigma}\right) - \frac{1}{(2\pi)^{3/2}\sigma s^2}\mathrm{e}^{-s^2/2\sigma^2} \tag{4.24}$$

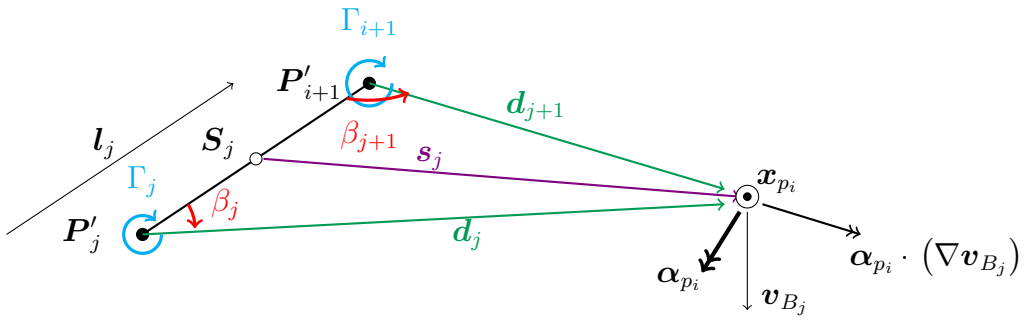

Figure 4.1: Vortex filament - vortex particle interaction

The regularization function for the vortex stretching term is defined as:

$$F_\sigma(s) = \frac{1}{s}\frac{\partial}{\partial s}\left(\frac{q_\sigma(s)}{s^3}\right) = \frac{1}{s^2}\left[\zeta_\sigma(s) - 3\frac{q_\sigma(s)}{s^3}\right] \tag{4.25}$$

4.1.3 Vortex filament - vortex particle interaction

The rotor blades are represented using vortex filaments described in Section 3.5.2. Therefore, the blade-wake interactions in VVPM are governed by vortex filament - vortex particle interactions. Vortex filaments affect both the velocity and rate of change of vorticity strength of vortex particles, as shown in Fig. 4.1.

4.1.3.1 Induced velocity due to vortex filaments

The velocity induced by a vortex filament at a vortex particle is derived using Biot-Savart law (Eqn. 3.101):

$$\boldsymbol{v}_{B_j}(\boldsymbol{x}_{p_i}) = \frac{\widehat{\boldsymbol{l}}_j \times \widehat{\boldsymbol{s}}_{ij}}{4\pi s_{ij}}\left[l_j\Gamma_j^0(\cos\beta_j + \cos\beta_{j+1}) + s_{ij}\Gamma_j^1(\sin\beta_j - \sin\beta_{j+1})\right] \tag{4.26}$$

where

$$\boldsymbol{s}_{ij} = \boldsymbol{x}_{p_i} - \boldsymbol{S}_{ij} \tag{4.27}$$

The point $\boldsymbol{S}_j$ is the point on a line along the vortex filament j that is closest to the vortex particle at $\boldsymbol{x}_{p_i}$. Therefore, the total velocity induced by the blade bound

circulation on each vortex particle is:

$$\boldsymbol{v}_B(\boldsymbol{x}_{p_i}) = \frac{1}{4\pi}\sum_{j=1}^{N_f}\left(\frac{\widehat{\boldsymbol{l}}_j \times \widehat{\boldsymbol{s}}_{ij}}{s_{ij}}\right)\left[l_j\Gamma_j^0(\cos\beta_j + \cos\beta_{j+1}) + s_{ij}\Gamma_j^1(\sin\beta_j - \sin\beta_{j+1})\right] \tag{4.28}$$

4.1.3.2 Vortex stretching due to vortex filaments

The velocity field induced by vortex filaments has a complex spatial distribution due to the deformed geometry of the blades and non-linear blade circulation distribution. Therefore, the vorticity strength of each vortex particle is subject to vortex stretching effects due to the blade bound circulation. The vorticity stretching effect is determined using the following equation:

$$\left(\frac{\mathrm{d}\boldsymbol{\alpha}_{\boldsymbol{p_i}}}{\mathrm{d}t}\right)_{\substack{\text{bound}\\ \text{circulation}}} = \boldsymbol{\alpha}_{p_i}\cdot\nabla\boldsymbol{v}_B \tag{4.29}$$

The vortex stretching effect on a particle i due to a linearly varying circulation distribution over a vortex filament j is:

$$\begin{aligned}
\boldsymbol{\alpha}_{p_i}\cdot(\boldsymbol{\nabla}\boldsymbol{v}_{B_j}) \;=\; & \frac{1}{4\pi s_{ij}^2}\Big[\left\{l_i\Gamma_j^0(\cos\beta_j + \cos\beta_{j+1}) + s_{ij}\Gamma_j^1(\sin\beta_j - \sin\beta_{j+1})\right\}(\hat{\boldsymbol{l}}_j \times \boldsymbol{\alpha}_i) \\
& + \boldsymbol{\alpha}_i\cdot(\widehat{\boldsymbol{l}}_j \times \widehat{\boldsymbol{s}}_{ij})\Big\{\left(l_i\Gamma_j^0(\sin\beta_j - \sin\beta_{j+1}) - s_{ij}\Gamma_j^1(\cos\beta_j + \cos\beta_{j+1})\right)\widehat{\boldsymbol{l}}_j \\
& - \left(2l_i\Gamma_j^0(\cos\beta_j + \cos\beta_{j+1}) - s_{ij}\Gamma_j^1(\sin\beta_j - \sin\beta_{j+1})\right)\widehat{\boldsymbol{s}}_j \\
& - \left(l_i\Gamma_j^0\sin\beta_j - s_{ij}\Gamma_j^1\cos\beta_j\right)\cos\beta_j\widehat{\boldsymbol{d}}_j \\
& - \left(l_i\Gamma_{j+1}^0\sin\beta_{j+1} + s_{ij}\Gamma_j^1\cos\beta_{j+1}\right)\cos\beta_{j+1}\widehat{\boldsymbol{d}}_{j+1}\Big\}\Big]
\end{aligned} \tag{4.30}$$

Therefore, the net vortex stretching effect due to the bound circulation distribution over the entire rotor system is obtained by summing over all the vortex filaments.

$$\boldsymbol{\alpha}_{p_i}\cdot\nabla\boldsymbol{v}_B = \sum_{j=1}^{N_f}\boldsymbol{\alpha}_{p_i}\cdot(\boldsymbol{\nabla}\boldsymbol{v}_{B_j}) \tag{4.31}$$

Note that Eqn. 4.30 has not been presented previously in literature. Therefore, it is likely that other VVPM studies have (incorrectly) ignored this effect in their formulation.

4.1.4 Governing equations

The vortex particles move due to the combination of free-stream velocity, the velocity induced by the bound circulation, and the velocity induced by the vortex particles. The vorticity strength changes with time because of vortex stretching effects due to particle-particle and particle-filament interactions, and due to viscous diffusion effects. Therefore, the combined governing equations of VVPM are:

$$\frac{\mathrm{d}\boldsymbol{x}_{p_i}}{\mathrm{d}t} = \underbrace{\boldsymbol{v}_\infty}_{\text{free-stream}} + \underbrace{\boldsymbol{v}_\sigma(\boldsymbol{x}_{p_i})}_{\text{Eqn. 4.9}} + \underbrace{\boldsymbol{v}_B(\boldsymbol{x}_{p_i})}_{\text{Eqn. 4.28}} \tag{4.32}$$

$$\frac{\mathrm{d}\boldsymbol{\alpha}_{p_i}}{\mathrm{d}t} = \underbrace{\boldsymbol{\alpha}_{p_i} \cdot \nabla^{\mathrm{T}} \boldsymbol{v}_\sigma(\boldsymbol{x}_{p_i})}_{\text{Eqn. 4.15}} + \underbrace{\boldsymbol{\alpha}_{p_i} \cdot \boldsymbol{\nabla} \boldsymbol{v}_B(\boldsymbol{x}_{p_i})}_{\text{Eqn. 4.31}} + \underbrace{\nu \nabla^2(\mathcal{V}\boldsymbol{\omega}_{\sigma_i})}_{\text{Eqn. 4.19}} \tag{4.33}$$

Equations 4.32 and 4.33 govern the evolution of vortex particles in a rotor wake. There are N_p vortex particles, and both equations require summations over the rest of the $(N_p - 1)$ vortex particles. Therefore, the total number of computations required at each time step is $\mathcal{O}(N_p^2)$.

4.2 Convergence of the Viscous Vortex Particle Method

The convergence of the VVPM has been discussed extensively in previous research [88, 183–185]. In the regularized vortex particle description of the flow-field, the error norms for the vorticity $\boldsymbol{\omega}_\sigma$ and velocity $\boldsymbol{v}_\sigma$ fields go to zero as the number of particles N_p increases, and the smoothing radius σ decreases subject to the constraint that

neighboring vortex particles overlap.

$$\frac{d_p}{\sigma} < 1 \tag{4.34}$$

where d_p is the typical distance between neighboring particles. To satisfy this requirement, *particle splitting* and *particle merging* are applied as relaxation schemes.

The major challenge in VVPM is that as time evolves the particle vorticity field $\boldsymbol{\omega}_\sigma$ does not remain divergence-free (Eqn. 4.6). In contrast, vortex filament based FVW methods guarantee a divergence-free flow-field. Therefore, relaxation schemes are required to ensure that vortex particle distribution retains a good representation of the vorticity field. Viscous diffusion implemented using PSE also helps maintain a divergence-free flow-field [86].

4.2.1 Particle splitting

The particle splitting algorithm is applied to ensure that the vorticity field is well discretized at all times. The criteria for particle splitting is based on Ref. 86. The particle is split if its strength increases to twice of its original strength.

$$|\boldsymbol{\alpha}_{p_i}(t)| \geq 2|\boldsymbol{\alpha}_{p_i}(t_0)| \tag{4.35}$$

Two new particles are placed along the direction of the original vorticity.

$$\boldsymbol{x}_{p_{\text{split}}} = \boldsymbol{x}_{p_i} \pm \frac{1}{4}\sigma_i \left(\frac{\boldsymbol{\alpha}_{p_i}}{|\boldsymbol{\alpha}_{p_i}|} \right) \tag{4.36}$$

Their new vorticity strength is equally divided between the two new particles:

$$\boldsymbol{\alpha}_{p_{\text{split}}} = \frac{1}{2}\boldsymbol{\alpha}_{p_i} \tag{4.37}$$

4.2.2 Particle merging

In particle merging, vortex particles that are in close proximity are replaced with a single vortex particle. Merging helps maintain a uniform distribution of vortex particles in the flow-field. In addition, the reduced number of particles decreases the computational requirements.

There are two criteria that particles have to satisfy for merging [94]. The first criterion is that the separation between the particles is smaller than a prescribed value.

$$\left|\boldsymbol{x}_{p_i} - \boldsymbol{x}_{p_j}\right| < \frac{1}{8}(\sigma_i + \sigma_j) \tag{4.38}$$

The second criterion is that particle strengths need to be nearly aligned with each other.

$$1 - \frac{\boldsymbol{\alpha}_i \cdot \boldsymbol{\alpha}_j}{|\boldsymbol{\alpha}_i||\boldsymbol{\alpha}_j|} \geq 10^{-4} \tag{4.39}$$

The new position of the merged particle is at the vorticity strength weighted average of the positions of the original particles.

$$\boldsymbol{x}_{p_{\text{merge}}} = \frac{|\boldsymbol{\alpha}_{p_i}|\boldsymbol{x}_{p_i} + |\boldsymbol{\alpha}_{p_j}|\boldsymbol{x}_{p_j}}{|\boldsymbol{\alpha}_{p_i}| + |\boldsymbol{\alpha}_{p_j}|} \tag{4.40}$$

The new strength is the sum of the strengths of the old particles.

$$\boldsymbol{\alpha}_{p_{\text{merge}}} = \boldsymbol{\alpha}_{p_i} + \boldsymbol{\alpha}_{p_j} \tag{4.41}$$

4.2.3 Flow-field diagnostics

There are several diagnostic quantities defined for a VVPM vorticity field which help determine when to apply a relaxation scheme. There are two types of diagnostics for a vortex particle field: *linear* and *quadratic*. Note that in a rotor wake system,

vortex particles are continuously generated from the blades. Therefore, the invariant diagnostic terms are not strictly valid for rotor wakes modeled using VVPM. However, diagnostics are useful for verification studies.

4.2.3.1 Linear diagnostics

There are three linear diagnostics in the VVPM: *total vorticity*, *linear impulse* and *angular impulse*. These diagnostics are linear in terms of vorticity strength $\boldsymbol{\alpha}_p$.

Total vorticity

The total vorticity $\boldsymbol{\Omega}$ for vortex particles is:

$$\boldsymbol{\Omega} = \sum_{i=1}^{N_p} \boldsymbol{\alpha}_{p_i} \tag{4.42}$$

The total vorticity is conserved with the transpose scheme for vortex stretching (Eqn. 4.15) [186]. Viscous diffusion implemented using PSE also conserves total vorticity (Eqn. 4.20).

$$\frac{\mathrm{d}\boldsymbol{\Omega}}{\mathrm{d}t} = 0 \tag{4.43}$$

Linear impulse

The linear impulse $\boldsymbol{I}$ for a system of vortex particles is:

$$\boldsymbol{I} = \frac{1}{2} \sum_{i=1}^{N_p} (\boldsymbol{x}_{p_i} \times \boldsymbol{\alpha}_{p_i}) \tag{4.44}$$

The linear impulse $\boldsymbol{I}$ is *nearly* conserved by all schemes (Eqn. 4.13) as long as the regularized particle vorticity field remains a good representation of a divergence-free field [179].

$$\frac{\mathrm{d}\boldsymbol{I}}{\mathrm{d}t} \to 0 \tag{4.45}$$

The term *nearly* is used because the proof requires an integral over an *unbounded* volume of the flow-field:

$$\int_{\infty} (\boldsymbol{\omega} \times \boldsymbol{v}) \, \mathrm{d}\mathcal{V} \to 0 \tag{4.46}$$

The unbounded volume integral is zero for a physical flow-field without any vorticity sources.

Angular impulse

The angular impulse $\boldsymbol{I}$ for a system of vortex particles is:

$$\boldsymbol{A} = \frac{1}{3} \sum_{i=1}^{N_p} \boldsymbol{x}_{p_i} \times (\boldsymbol{x}_{p_i} \times \boldsymbol{\alpha}_{p_i}) \tag{4.47}$$

The angular impulse $\boldsymbol{A}$ is not generally conserved, however numerical computations in Ref. 179 indicate that the $\left(\frac{\mathrm{d}\boldsymbol{A}}{\mathrm{d}t} \right)$ remains small when the vorticity field is divergence-free.

4.2.3.2 Quadratic diagnostics

There are three quadratic diagnostics that are relevant for the VVPM analysis presented in this thesis: helicity $\mathcal{H}$, kinetic energy E and enstrophy $\mathcal{E}$. Each quadratic diagnostic can be evaluated in three forms: singular, semi-regularized (with subscript σ) and twice-regularized (with subscript $\sigma\sigma$).

In the singular form of quadratic diagnostics, the vortex particles are represented with the 3D Dirac delta function $\delta(s)$ instead of the regularized kernel $\zeta_\sigma(s)$. In the twice-regularized form of quadratic diagnostics, both terms in the quadratic product are regularized. Twice-regularized quadratic diagnostics are difficult to evaluate analytically, and in general, cannot be derived in closed-form. In the semi-regularized quadratic form, only one of the terms in the quadratic product is regularized. Semi-

regularized quadratic diagnostics can be evaluated in closed-form with certain choices of the regularization function $\zeta_\sigma(s)$.

Helicity

The helicity $\mathcal{H}$ measures the net linkage of vortex lines. Helicity is not a conserved quantity in viscous flows because vortex lines can reconnect in VVPM. The helicity $\mathcal{H}$ in singular form is:

$$\mathcal{H} = \int (\boldsymbol{\omega} \cdot \boldsymbol{v}) \mathrm{d}\mathcal{V} = \frac{1}{4\pi} \sum_{\substack{i=1 \\ j=1}}^{N_p} \frac{1}{x_{p_{ij}}^3} \left[\boldsymbol{x}_{p_{ij}} \cdot (\boldsymbol{\alpha}_{p_i} \times \boldsymbol{\alpha}_{p_j}) \right] \tag{4.48}$$

The semi-regularized helicity is:

$$\mathcal{H}_\sigma = \int (\boldsymbol{\omega} \cdot \boldsymbol{v}_\sigma) \mathrm{d}\mathcal{V} = \sum_{i,j=1}^{N_p} \frac{q(\boldsymbol{x}_{p_{ij}})}{x_{p_{ij}}^{\boxed{3}}} \left[\boldsymbol{x}_{p_{ij}} \cdot (\boldsymbol{\alpha}_{p_i} \times \boldsymbol{\alpha}_{p_j}) \right] \tag{4.49}$$

Note that the exponent '3' (boxed in Eqn. 4.49) is missing in the original derivation presented in Eqn. 128 of Ref. 86.

Kinetic Energy

The kinetic energy E in singular form is:

$$E = \frac{1}{2} \int (\boldsymbol{v} \cdot \boldsymbol{v}) \mathrm{d}\mathcal{V} \tag{4.50}$$

$$= \frac{1}{16\pi} \sum_{\substack{i,j=1 \\ i \neq j}}^{N_p} \frac{1}{x_{p_{ij}}^3} \left[x_{p_{ij}}^2 \boldsymbol{\alpha}_{p_i} \cdot \boldsymbol{\alpha}_{p_j} + \left(\boldsymbol{x}_{p_{ij}} \cdot \boldsymbol{\alpha}_{p_i} \right) \left(\boldsymbol{x}_{p_{ij}} \cdot \boldsymbol{\alpha}_{p_j} \right) \right] \tag{4.51}$$

The $i = j$ term is removed to avoid the singularity due to the self-induced velocity of a particle. The semi-regularized kinetic energy E_σ cannot be evaluated analytically for the Gaussian kernel. However, it can be evaluated for the high-order algebraic

smoothing kernel:

$$E_\sigma = \frac{1}{2}\int (\boldsymbol{v}\cdot\boldsymbol{v}_\sigma)\mathrm{d}\mathcal{V} \tag{4.52}$$

$$= \frac{1}{16\pi}\sum_{\substack{i,j=1\\ i\neq j}}^{N_p} \frac{(x_{p_{ij}}^2+2\sigma^2)\boldsymbol{\alpha}_{p_i}\cdot\boldsymbol{\alpha}_{p_j} + \left(\boldsymbol{x}_{p_{ij}}\cdot\boldsymbol{\alpha}_{p_i}\right)\left(\boldsymbol{x}_{p_{ij}}\cdot\boldsymbol{\alpha}_{p_j}\right)}{(\sigma^2+x_{p_{ij}}^2)^{3/2}} \tag{4.53}$$

where the high-order algebraic smoothing kernel is:

$$\zeta_\sigma(s) = \frac{1}{4\pi\sigma^3}\frac{15/2}{(s^2+\sigma^2)^{7/2}} \tag{4.54}$$

The kinetic energy E is not conserved in viscous unbounded flows. However, the rate of change of kinetic energy is related to the viscosity and *enstrophy* of the flow-field.

$$\frac{\mathrm{d}E}{\mathrm{d}t} = -\nu\mathcal{E} \tag{4.55}$$

Enstrophy

The enstrophy of a flow-field is defined as the volume integral of the dot product of vorticity with itself.

$$\mathcal{E} = \int (\boldsymbol{\omega}\cdot\boldsymbol{\omega})\mathrm{d}\mathcal{V} \tag{4.56}$$

The enstrophy of a flow-field in singular form cannot be evaluated because the integral of the square of a delta function is undefined. The semi-regularized enstrophy is:

$$\mathcal{E}_\sigma = \int (\boldsymbol{\omega}\cdot\boldsymbol{\omega}_\sigma)\mathrm{d}\mathcal{V} \tag{4.57}$$

$$= \frac{1}{8\pi}\sum_{i,j=1}^{N_p}\frac{\sigma^3}{(x_{p_{ij}}^2+\sigma^2)^{9/2}}\Big[(x_{p_{ij}}^2+\sigma^2)(2x_{p_{ij}}^4+7\sigma^2x_{p_{ij}}^2+20\sigma^4)\boldsymbol{\alpha}_{p_i}\cdot\boldsymbol{\alpha}_{p_j} - 3(4x_{p_{ij}}^4+18\sigma^2x_{p_{ij}}^2+7\sigma^4)(\boldsymbol{x}_{p_{ij}}\cdot\boldsymbol{\alpha}_{p_i})(\boldsymbol{x}_{p_{ij}}\cdot\boldsymbol{\alpha}_{p_j})\Big] \tag{4.58}$$

Therefore, the vortex particle self-enstrophy becomes:

$$(\mathcal{E}_\sigma)_i = \frac{5\left|\boldsymbol{\alpha}_{p_i}\right|^2}{2\pi\sigma^3} \tag{4.59}$$

Equation 4.58 is a correction to the original formulation of the semi-regularized enstrophy derived in Eqn. 139 of Ref. 86, and Eqn. G.48 of Ref. 179. The incorrect expression was dimensionally inconsistent and had different magnitudes and signs of coefficients. The self enstrophy is doubled according to the new expression. This correction was verified in personal communications with the author of Refs. 86 and 179.

Enstrophy is not conserved in viscous and inviscid flows because of vortex stretching. However, the rate of change of kinetic energy can be compared with the enstrophy in the flow-field using Eqn. 4.55. Therefore, in numerical simulations, Eqn. 4.55 can be used to verify the correct implementation of the VVPM.

4.2.4 Verification study

The expressions derived in Sections 4.1 and 4.2 were verified for a thin vortex ring. The test case was selected from Section 3.5.5 of Ref. 179. A vortex ring is a torus defined by a ring radius R_0, core radius r_c and circulation strength Γ_v. A polar coordinate system (r_v, θ_v) is used for points in the cross-section of the vortex ring.

4.2.4.1 Exact solution

The vorticity field of the cross-section of a thin isolated vortex ring is represented with a Gaussian core circulation distribution:

$$\boldsymbol{\omega}(r_v, \theta_v) = \frac{\Gamma_v}{2\pi r_c^2}\left(1 + \frac{r_v}{R_0}\cos\theta_v\right)\mathrm{e}^{-r_v^2/2r_c^2} \tag{4.60}$$

Table 4.1: Vortex ring parameters

Vortex ring radius	R_0	1.0
Circulation	Γ_v	1.0
Core radius	r_c	0.10
Discretization core radius	r_0	0.35
Time step	Δt	0.025
Reynolds number	Re	400
Kinematic viscosity	ν	2.50×10^{-3}

Table 4.2: Analytical calculations for vortex ring

Ring speed	U_R	0.27672
Enstrophy	$\mathcal{E}$	50.75
Rate of Kinetic Energy	$\frac{\mathrm{d}E}{\mathrm{d}t}$	-0.126875

The exact enstrophy based on this vorticity field is:

$$\mathcal{E} = \frac{\Gamma_v^2 R_0}{2r_c^2}\left(1 + \frac{3}{2}\frac{r_c^2}{R_0^2}\right) \tag{4.61}$$

The vortex ring translates at a speed U_R:

$$U_R = \frac{\Gamma_v}{4\pi R_0}\left[\log\left(\frac{8R_0}{r_c}\right) - 0.9045935\right] \tag{4.62}$$

The vortex ring parameters are tabulated in Table 4.1. The Reynolds number Re for a vortex ring is:

$$Re = \frac{\Gamma_v}{\nu} \tag{4.63}$$

The exact analytical enstrophy, speed and rate of change of kinetic energy for the vortex ring are calculated in Table 4.2. The exact values are compared with the numerical results to verify the VVPM calculations.

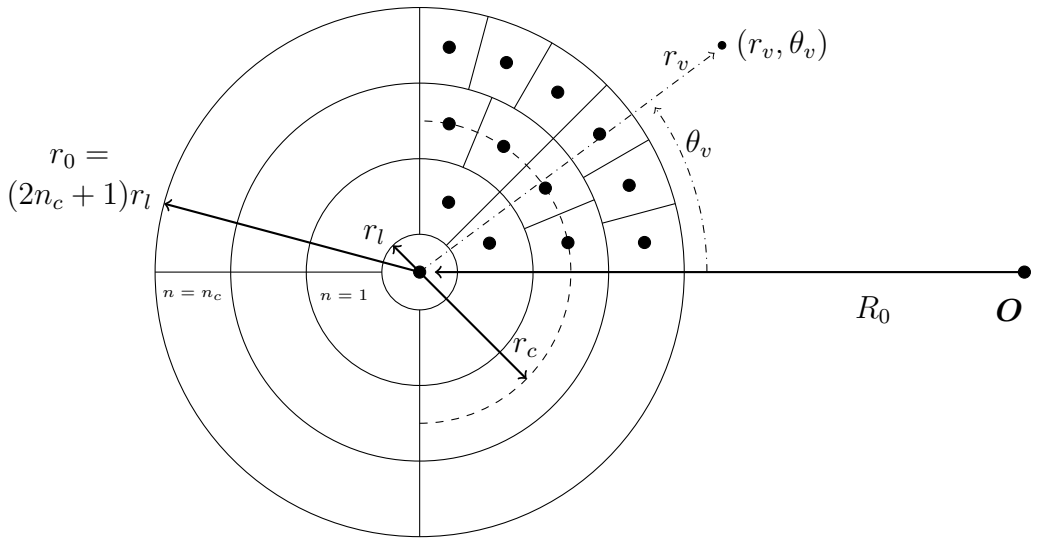

Figure 4.2: Vortex tube core discretization

4.2.4.2 Vortex ring discretization

The vortex ring is discretized with vortex particles using the Knio-Ghoniem scheme described in Ref. 187. The core of the vortex ring is divided into $n_c + 1$ layers as shown in Fig. 4.2. The maximum discretization core radius of r_o is used to define the vortex particle representation of the vortex ring core. The thickness of each layer in the vortex core is $2r_l$. A particle in the vortex core is located at a radial distance $\overline{r}_i$.

$$r_l = \frac{r_0}{2n_c + 1} \tag{4.64}$$

$$\overline{r}_i = 2ir_l \quad , \quad i > 0 \tag{4.65}$$

The vortex ring is divided into n_ψ azimuthal segments. The volume associated with a vortex particle in the i^{th} layer of the cross-section is:

$$\mathcal{V}_{p_i} = \left(\frac{2\pi}{n_\psi}\right)(2r_l)\left[(\theta_{v_2} - \theta_{v_1})R_0\overline{r}_i + (\sin\theta_{v_2} - \sin\theta_{v_1})\left(\frac{r_l^2 + 3\overline{r}_i^2}{3}\right)\right] \tag{4.66}$$

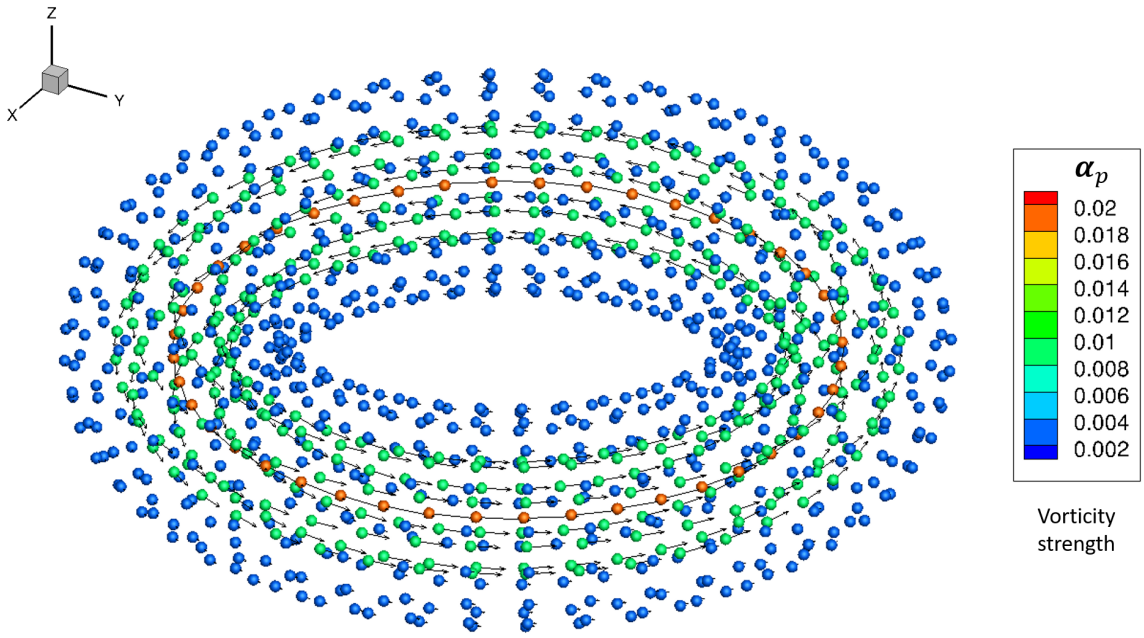

Figure 4.3: Three layer vortex particle representation of a vortex ring

The vortex particle strength is calculated by solving a linear system of equations that satisfy the vorticity field distribution in Eqn. 4.60:

$$\begin{Bmatrix} \boldsymbol{\omega}_\sigma(\boldsymbol{x}_{p_1}) \\ \vdots \\ \boldsymbol{\omega}_\sigma(\boldsymbol{x}_{p_{N_p}}) \end{Bmatrix} = \begin{bmatrix} \zeta_\sigma\left(\boldsymbol{x}_{p_{1,1}}\right) & \cdots & \zeta_\sigma\left(\boldsymbol{x}_{p_{1,N_p}}\right) \\ \vdots & \ddots & \vdots \\ \zeta_\sigma\left(\boldsymbol{x}_{p_{N_p,1}}\right) & \cdots & \zeta_\sigma\left(\boldsymbol{x}_{p_{N_p,N_p}}\right) \end{bmatrix} \begin{Bmatrix} \boldsymbol{\alpha}_{p_1} \\ \vdots \\ \boldsymbol{\alpha}_{p_{N_p}} \end{Bmatrix} \tag{4.67}$$

Note that in Ref. 179, an iterative scheme is used to solve for the particle strengths. Therefore, there are some differences in the results compared in this verification study.

4.2.4.3 Results

The vortex ring results were calculated for three different number of core layers: $n_c = 4$, $n_c = 5$ and $n_c = 6$ in Tables 4.3 - 4.5 respectively. An example of the vortex particle representation is shown in Fig. 4.3. Three layers are shown for clarity. Each vortex particle is represented by a sphere centered at $\boldsymbol{x}_p$, and an arrow in the direction of the vorticity strength $\boldsymbol{\alpha}_p$. The length of the arrow and the color of the sphere

indicate the magnitude of the vorticity strength of the vortex particle. The strongest particles are at the center of the vortex ring, denoted by an orange-red color. The second layer has weaker vorticity strength and is colored light green. The outermost layer has the weakest vorticity strength, and is denoted in blue.

In Tables 4.3 - 4.5, the linear impulse $|I|$ is less than that obtained from Ref. 179 for all three cases. The kinetic energy $E_{\sigma,f}$ assuming a divergence-free field is calculated using Eqn. 119 of Ref. 86. The difference between the kinetic energies is less than one percent $|E_\sigma - E_{\sigma,f}| < 1\%$ indicating that the field is nearly divergence free. Therefore, the vortex particle representation of the flow-field is excellent.

The ring translation speed and the rate of change of kinetic energy due to viscous diffusion are comparable to the analytical (Table 4.2) and reported results (Ref. 179). The rate of change of kinetic energy is calculated using a second order finite-difference approach:

$$\frac{\mathrm{d}\widetilde{E}}{\mathrm{d}t}(0) = \frac{-E_\sigma(2\Delta t) + 4E_\sigma(\Delta t) - 3E_\sigma(0)}{2\Delta t} \tag{4.68}$$

The semi-regularized enstrophy is calculated using Eqn. 4.58. Note that enstrophy calculated in Ref. 86 uses the *incorrect derivation*, as described in Section 4.2.3.2. The enstrophy is compared with the divergence-free approximation from Eqn. 132 of Ref. 86. The error is $|\varepsilon| < 1.6\%$ for all three cases. Therefore, the negligible error between the divergence-free approximation and actual semi-regularized enstrophy indicates the vortex particle representation of the flow-field is excellent.

The vortex ring results presented in this section compare well with those in Ref. 179, therefore the VVPM implemented in the dissertation is suitable for use in complex flows such as a coaxial rotor wake system.

Table 4.3: Results for a vortex ring with 4 core layers

Layers	n_c	4	
Azimuthal locations	n_ψ	80	
Smoothing radius	σ	0.10	
Diagnostic		**Result**	**Ref. 179**
Linear Impulse	$\lvert I\rvert$	3.16545	3.213919
Semi-regularized Kinetic Energy	E_σ	1.01669	1.047552
Divergence-free Kinetic Energy	$E_{\sigma,f}$	1.01677	1.047634
Ring Translation Speed	U_R	0.2496272	0.26605
Viscous diffusion	$\mathrm{d}\widetilde{E}/\mathrm{d}t$	-0.1496	-0.1276
Semi-regularized Enstrophy	$\mathcal{E}_\sigma$	61.4109	61.34640*
Divergence-free Enstrophy	$\mathcal{E}_{\sigma,f}$	60.4121	62.38420

Table 4.4: Results for a vortex ring with 5 core layers

Layers	n_c	5	
Azimuthal locations	n_ψ	100	
Smoothing radius	σ	0.0840	
Diagnostic		**Result**	**Ref. 179**
Linear Impulse	$\lvert I\rvert$	3.1785	3.215482
Semi-regularized Kinetic Energy	E_σ	1.01366	1.036491
Divergence-free Kinetic Energy	$E_{\sigma,f}$	1.01369	1.036526
Ring translation Speed	U_R	0.2510928	0.26607
Viscous diffusion	$\mathrm{d}\widetilde{E}/\mathrm{d}t$	-0.1526	-0.12684
Semi-regularized Enstrophy	$\mathcal{E}_\sigma$	58.3174	58.30524*
Divergence-free Enstrophy	$\mathcal{E}_{\sigma,f}$	57.6503	58.99072

Table 4.5: Results for a vortex ring with 6 core layers

Layers	n_c	6	
Azimuthal locations	n_ψ	117	
Smoothing radius	σ	0.0735	
Diagnostic		**Result**	**Ref. 179**
Linear Impulse	$\lvert I\rvert$	3.18646	3.218423
Semi-regularized Kinetic Energy	E_σ	1.01211	1.031477
Divergence-free Kinetic Energy	$E_{\sigma,f}$	1.01213	1.031498
Ring translation Speed	U_R	0.2519636	0.26620
Viscous diffusion	$\mathrm{d}\widetilde{E}/\mathrm{d}t$	-0.1534	-0.12687
Semi-regularized Enstrophy	$\mathcal{E}_\sigma$	56.619	56.61377*
Divergence-free Enstrophy	$\mathcal{E}_{\sigma,f}$	56.0819	57.16328

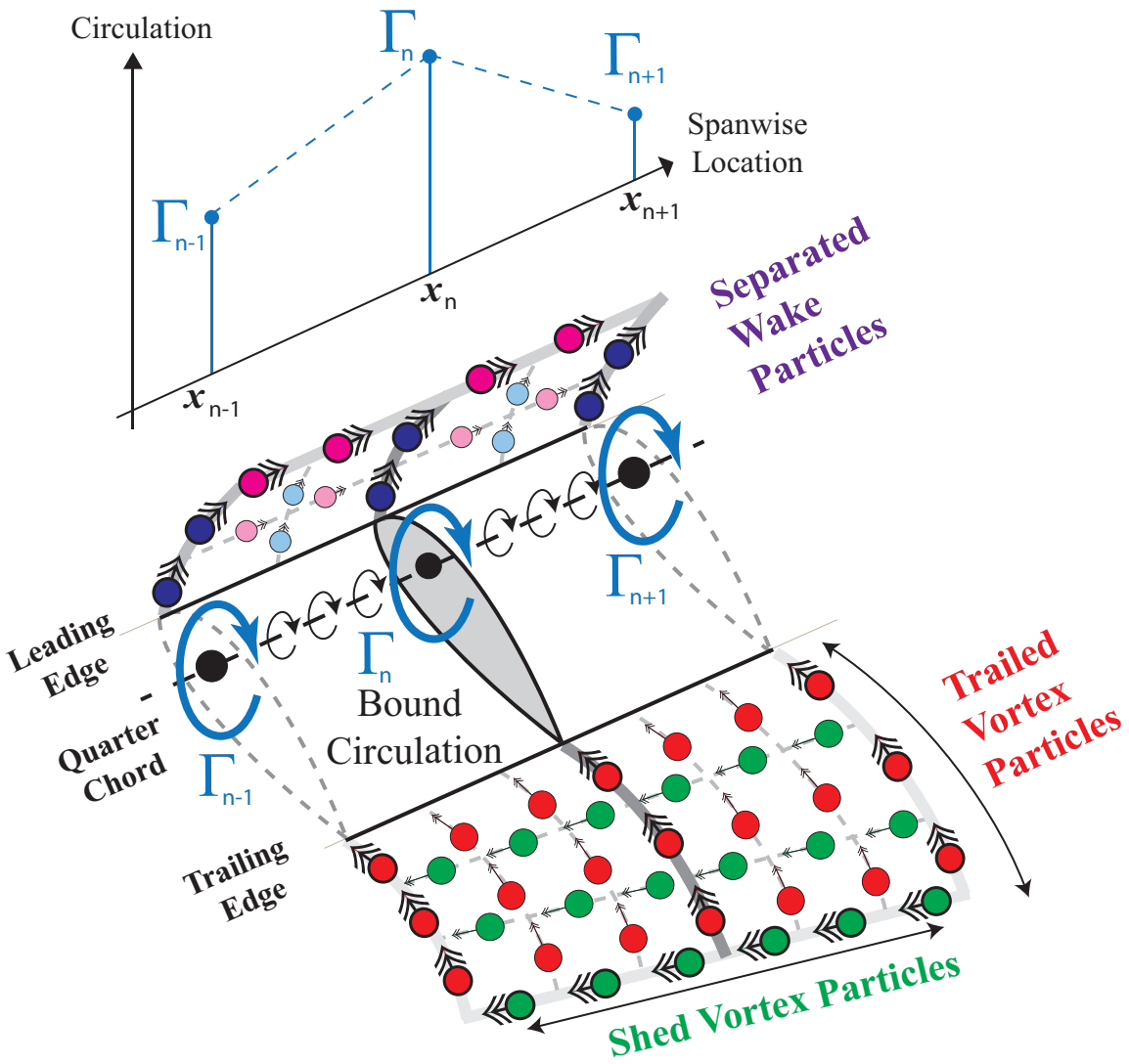

Figure 4.4: Vortex particle generation over rotor blade

4.3 Vortex particle generation

The vortex particle generation is governed by the principle of conservation of vorticity in the flow-field. The change in circulation over the blades generates new vortex particles in the flow such that the net vorticity is conserved. The particle generation process is illustrated in Fig. 4.4. In attached flow, the circulation $\boldsymbol{G}_a$ is determined using the CFD-RFA approach, to generate vortex particles from the TE of the blade [140, 141, 188]. In separated flow, the circulation $\boldsymbol{G}_d$ is determined using the ONERA-

DS model, to generate vortex particles from the LE of the blade [189].

Note that the vortex particles generated induce unsteady velocities, which may result in double counting of unsteady loads already incorporated in CFD-RFA and ONERA-DS models. The effects of this double counting are mitigated by generating shed vortex particles in the regions between quadrature points used for calculating loads, as shown in Fig. 4.4. Shed vortex particles are generated assuming a linearly varying circulation distribution between consecutive quadrature points. Therefore, loads calculated at the blade section do not include the effects of a vortex particle generated at the same location. However, the effects of the shed vorticity from the blade section is included in the overall wake. Furthermore, the CFD-RFA and ONERA-DS are 2D models that assume that shed vorticity moves downstream on a flat 2D plane, illustrated by dashed lines in Fig. 4.5. For a helicopter rotor, each blade section moves on a curved cylindrical plane, as shown in Fig. 4.5. Therefore, the separation between the shed vortex and the airfoil is on a curved plane. The offset between the flat and curved plane depends on the azimuth angle of the blade path, as shown in Fig. 4.5. Due to the deviation in the path of the shed vortex, the effects on the unsteady loads is different when compared to a 2D plane assumption.

4.3.1 Attached flow

The vorticity generated in the wake behind a moving bound circulation vortex line consists of two terms: *shed vorticity* and *trailing vorticity*. Shed vortex particles are generated at the TE of the blade section due to the time varying bound circulation $\dot{\Gamma}_a$ (denoted in green in Fig. 4.4). Trailed vortex particles are generated along the span due to the spanwise varying bound circulation over the blade $\nabla\Gamma_a$ (denoted in red in Fig. 4.4).

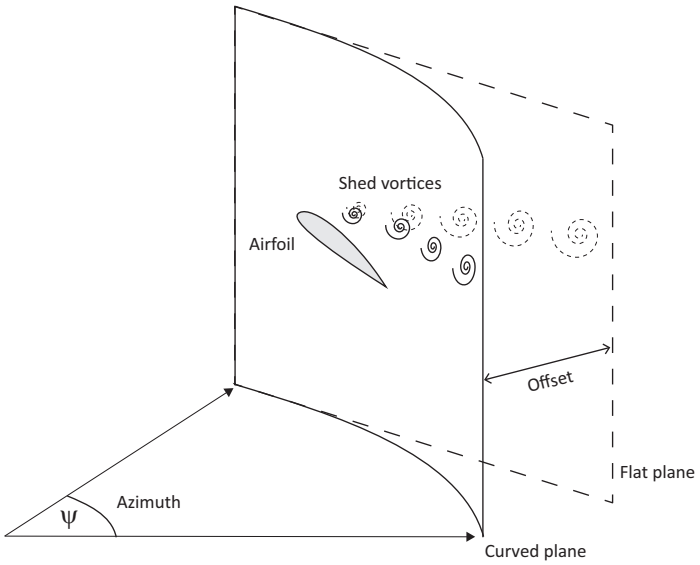

Figure 4.5: Comparison of curved and 2D path of shed wake vortices for a rotating blade section

The region swept by the blade is discretized into vortex particles based on a specified resolution h_{res}. The particle smoothing radius σ is 1.5 times the resolution h_{res} to ensure that the convergence criteria is maintained.

$$\sigma = 1.5 h_{res} \tag{4.69}$$

4.3.1.1 Trailing particles

Trailing vortex particles are generated due to the spanwise varying circulation. These vortices are perpendicular to the blade as they are shed. Figure 4.6 illustrates the discretization process for trailing particles. The TE points of a vortex filament at time t and $t - \Delta t$ form a quadrilateral. Therefore, the trailed vortex particles are not placed exactly perpendicular to the blade. However, for a small time step size, the approximation is valid.

Consider the line segment connecting the TE point i at time t and $t - \Delta t$. The line segment is uniformly divided into m_{p_i} particles. The number of the particles m_{p_i}

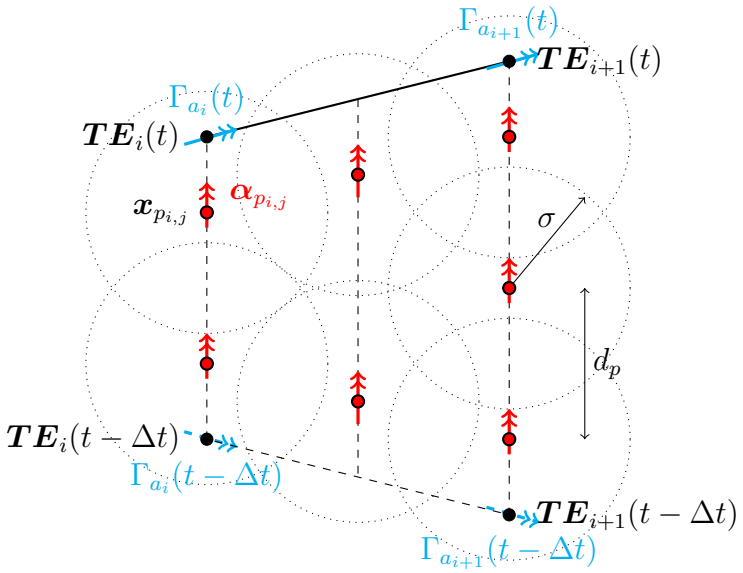

Figure 4.6: Trailing vortex particle generation

is obtained by dividing the length of the arc by the resolution h_{res}.

$$m_{p_i} = \left\lceil \frac{|\boldsymbol{TE}_i(t) - \boldsymbol{TE}_i(t-\Delta t)|}{h_{\text{res}}} \right\rceil \tag{4.70}$$

The distance d_{p_i} between particles along the line segment i is:

$$d_{p_i} = \frac{|\boldsymbol{TE}_i(t) - \boldsymbol{TE}_i(t-\Delta t)|}{m_{p_i}} \tag{4.71}$$

The position of a vortex particle j along the line segment i is:

$$\boldsymbol{x}_{p_{i,j}} = \boldsymbol{TE}_i(t-\Delta t) + \left(j - \frac{1}{2}\right)\left[\frac{\boldsymbol{TE}_i(t) - \boldsymbol{TE}_i(t-\Delta t)}{m_{p_i}}\right] \quad , \quad j = 1 \cdots m_{p_i} \tag{4.72}$$

Each particle has equal vorticity strength. The direction of the vorticity is along the line segment.

$$\boldsymbol{\alpha}_{p_{i,j}} = \left[\Gamma_{a_{i+1}}(t) - \Gamma_{a_i}(t)\right]\left[\frac{\boldsymbol{TE}_i(t) - \boldsymbol{TE}_i(t-\Delta t)}{m_{p_i}}\right] \tag{4.73}$$

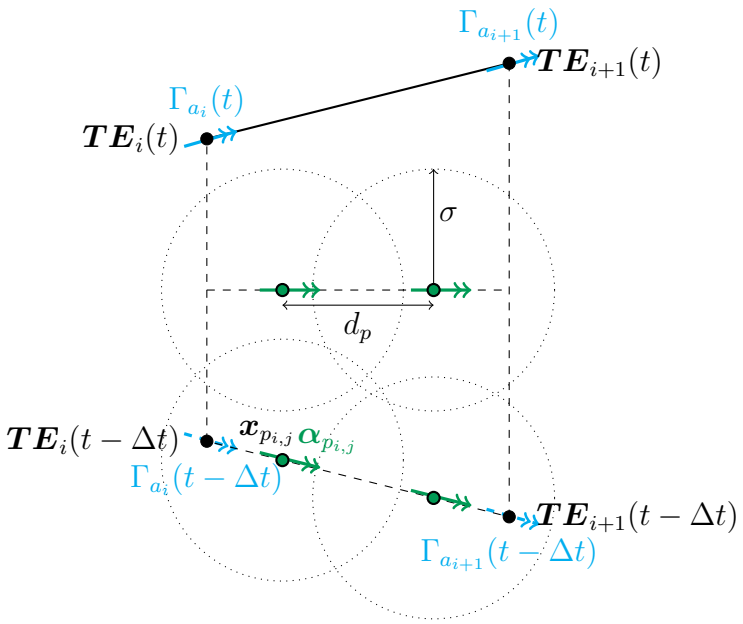

Figure 4.7: Shed vortex particle generation

Each vortex particle is also associated with a volume $\mathcal{V}_{p_{i,j}}$. The volume of fluid associated with the vortex particle is the product of the airfoil cross-section area A_i, and the distance d_{p_i}.

$$\mathcal{V}_{p_{i,j}} = A_i d_{p_i} \tag{4.74}$$

Trailing vortex particles are generated at each blade location i. Trailing vortex particles are also generated along intermediate blade locations when the distance between consecutive blade section is greater than the resolution h_{res}.

$$h_{\text{res}} < |\boldsymbol{TE}_{i+1} - \boldsymbol{TE}_i| \tag{4.75}$$

Vortex particle position and strength for intermediate blade locations are determined using linear interpolation.

4.3.1.2 Shed particles

Shed vortex particles are generated due to the time varying bound circulation. Shed vortices are parallel to the trailing edge of the blade. Figure 4.7 illustrates the discretization process for shed vortex particles. The number of shed vortex particles m_{p_i} is obtained by dividing the length of the TE vortex filament by the resolution h_{res} .

$$m_{p_i} = \left\lceil \frac{|\boldsymbol{TE}_{i+1}(t-\Delta t) - \boldsymbol{TE}_i(t-\Delta t)|}{h_{\text{res}}} \right\rceil \tag{4.76}$$

The distance between vortex particle centers is:

$$d_{p_i} = \frac{|\boldsymbol{TE}_{i+1}(t-\Delta t) - \boldsymbol{TE}_i(t-\Delta t)|}{m_{p_i}} \tag{4.77}$$

Vortex particles are placed along the line connecting the TE points at the previous time step $(t-\Delta t)$.

$$\boldsymbol{x}_{p_{i,j}} = \boldsymbol{TE}_i(t-\Delta t) + \left(j - \frac{1}{2}\right)\left[\frac{\boldsymbol{TE}_{i+1}(t-\Delta t) - \boldsymbol{TE}_i(t-\Delta t)}{m_{p_i}}\right],\ \ j = 1 \cdots m_{p_i} \tag{4.78}$$

The circulation at the point j at a time t is:

$$\Gamma_{a_{i,j}}(t) = \Gamma_{a_i}(t) + \left(j - \frac{1}{2}\right)\left[\frac{\Gamma_{a_{i+1}}(t) - \Gamma_{a_i}(t)}{m_{p_i}}\right] \quad , \quad j = 1 \cdots m_{p_i} \tag{4.79}$$

The vorticity strength of a vortex particle j along the line segment connecting the i^{th} and $(i+1)^{\text{th}}$ TE point is:

$$\boldsymbol{\alpha}_{p_{i,j}} = \left[\Gamma_{a_{i,j}}(t-\Delta t) - \Gamma_{a_{i,j}}(t)\right]\left[\frac{\boldsymbol{TE}_{i+1}(t-\Delta t) - \boldsymbol{TE}_i(t-\Delta t)}{m_{p_i}}\right] \tag{4.80}$$

The volume of fluid associated with shed vortex particles is:

$$\mathcal{V}_{p_{i,j}} = \left[A_i + \left(j - \frac{1}{2} \right) \left(\frac{A_{i+1} - A_i}{m_{p_i}} \right) \right] d_{p_i} \tag{4.81}$$

Shed vortex particles are placed at intermediate locations using linear interpolation as described for the trailing vortex particle generation.

4.3.2 Separated flow

The ONERA-DS model does not describe the physical changes in the flow during DS. Experimental studies on a NACA0012 airfoil indicate that flow separation and vortex shedding are the most important characteristics of DS [164]. Therefore, the ONERA-DS model is extended to generate a separated wake during DS. This approach is based on previous work on DS modeling for airfoils [190]. The process for a 2D pitching airfoil (Fig. 4.8) consists of three stages described below:

1. The flow is attached when the angle of attack is below the critical angle of attack ($\alpha < \alpha_{cr}$), as illustrated in Fig. 4.8a. Airfoil loads and bound circulation are calculated using the CFD-RFA model. A wake associated with the time varying, attached flow bound circulation Γ_a is present behind the airfoil.

2. The DS calculation is initiated when the airfoil angle of attack exceeds the critical angle of attack ($\alpha > \alpha_{cr}$). The non dimensional time spent in stall ($\bar{t}$) starts at this instance. A leading edge bubble is formed during this period. In Fig. 4.8b, the time in stall is less than the prescribed time delay for lift ($\bar{t} < \tau_d$). The flow continues to remain attached and calculations proceed as described for Fig. 4.8a.

3. When the time in stall exceeds the time delay for lift ($\bar{t} > \tau_d$), the ONERA-DS circulation $\Gamma_d^{\mathcal{L}}$ is calculated (Fig. 4.8c). Experimental measurements indicate

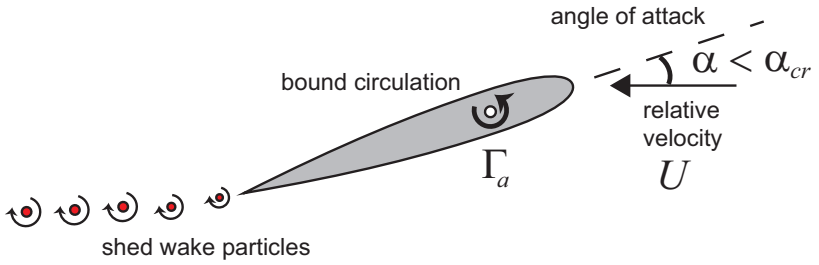

(a) Attached flow

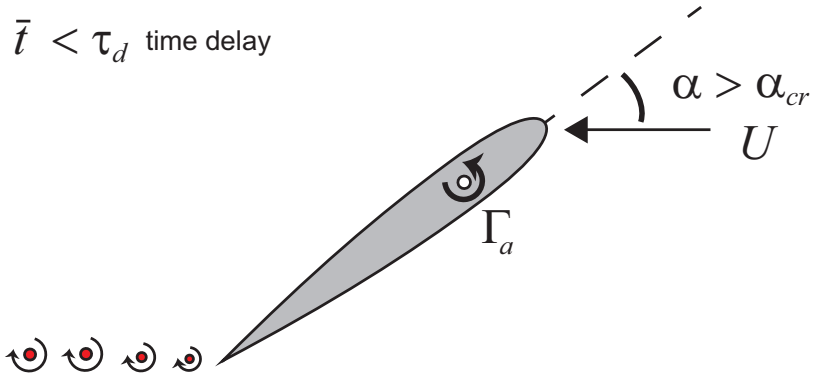

(b) Stall delay

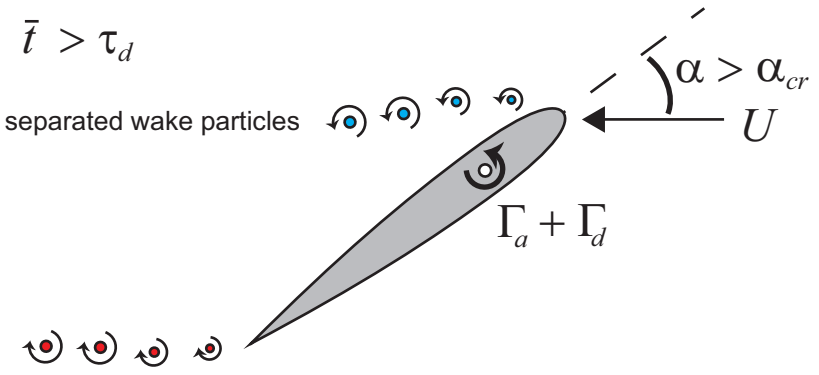

(c) Flow separation

Figure 4.8: Modeling separated wake with vortex particles during dynamic stall

that at this instance, abrupt flow separation occurs over the airfoil due to the formation of a vortex [164]. The separated flow is represented using a vortex particle generated at the LE of the airfoil. This is a reasonable assumption because experimental measurements indicate that flow separation occurs at $0.5\%c$ from the LE. The DS circulatory lift obtained from the ONERA-DS model is represented by bound circulation $\Gamma_d^{\mathcal{L}}$ at the quarter chord of the airfoil. The strength of the LE vortex particle is obtained from the rate of change in the DS bound circulation $\dot{\Gamma}_d^{\mathcal{L}}$. The vortex particle moves over the airfoil surface under the influence of the free stream velocity and the bound circulation over the airfoil. When the angle of attack decreases below the critical angle of attack ($\alpha < \alpha_{cr}$), the flow reattaches at the LE and the cycle repeats (Fig. 4.8a).

The particle generation process for a 2D airfoil is applied at each blade section experiencing DS. The vortex particle discretization is identical to the procedure described for attached flow in Section 4.3.1, with two changes: 1) $\boldsymbol{LE}$ points are used instead of $\boldsymbol{TE}$, and 2) DS circulation $\Gamma_d^{\mathcal{L}}$ is used instead of the attached flow circulation Γ_a.

Therefore, the formation of a horseshoe separated wake structure over the LE has 3D effects that are not captured by the conventional ONERA-DS loads. Radial flow effects are captured because the separated wake particles translate due to the local velocity. The separated wake vortex particles influence the flow velocities over the entire rotor, therefore the combined ONERA-DS and VVPM model is an effective 3D extension of the 2D ONERA-DS model.

The 3D effects of the separated wake modify rotor loads due to three reasons. First, the separated wake interacts directly with rotor blades that lie in its path. Second, the induced velocity due to the separated wake modifies the inflow distribution over the rotor and hence the angle of attack. The region and timing of DS on the

rotor is modified due to the change in angle of attack. Third, including the separated wake modifies the rest of the wake structure. The modified wake changes the inflow distribution over the rotor and affects the rotor loads.

4.4 Computational acceleration techniques

The VVPM is the most computationally expensive component of the aeroelastic simulations. Each particle interacts with all other particles except itself. Equations 4.9, 4.15 and 4.19 require summations over all the particles. Therefore, the kernels $\eta_\sigma(x_{p_{ij}}), \zeta_\sigma(x_{p_{ij}}), q_\sigma(x_{p_{ij}})/x^3_{p_{ij}}$ and $F_\sigma(x_{p_{ij}})$ are computed for each unique pair of particles i and j. The kernel calculations are expensive because they require evaluating the exponential function $[\exp(-s^2/2\sigma^2)]$ and the error function $[\text{erf}(s/2\sigma)]$. There are $N_p(N_p-1)/2$ unique pairs among N_p particles. Hence the computational complexity of the particle-particle interactions is $\mathcal{O}(N_p^2)$.

4.4.1 Parallelization

Modern High Performance Computing (HPC) uses parallelization to reduce computational times by distributing tasks over multiple computational threads, processors and/or Graphics Processing Units (GPU). In this dissertation, the Open Multi-Processing (OpenMP) application programming interface for shared-memory multiprocessing programming in C++ is employed.

The advantage of parallelization is shown in Fig. 4.9. The vorticity field $\boldsymbol{\omega}_\sigma(\boldsymbol{x}_p)$ due to a random distribution of N_p vortex particles in a $[1\times1\times1]$ cube was calculated with different number of parallelization threads. The vorticity strength $\boldsymbol{\alpha}_p$ of each particle was also assigned randomly. Figure 4.9 is plotted using log-log axes. For the single thread calculation (in black), as the number of particles increases, the compu-

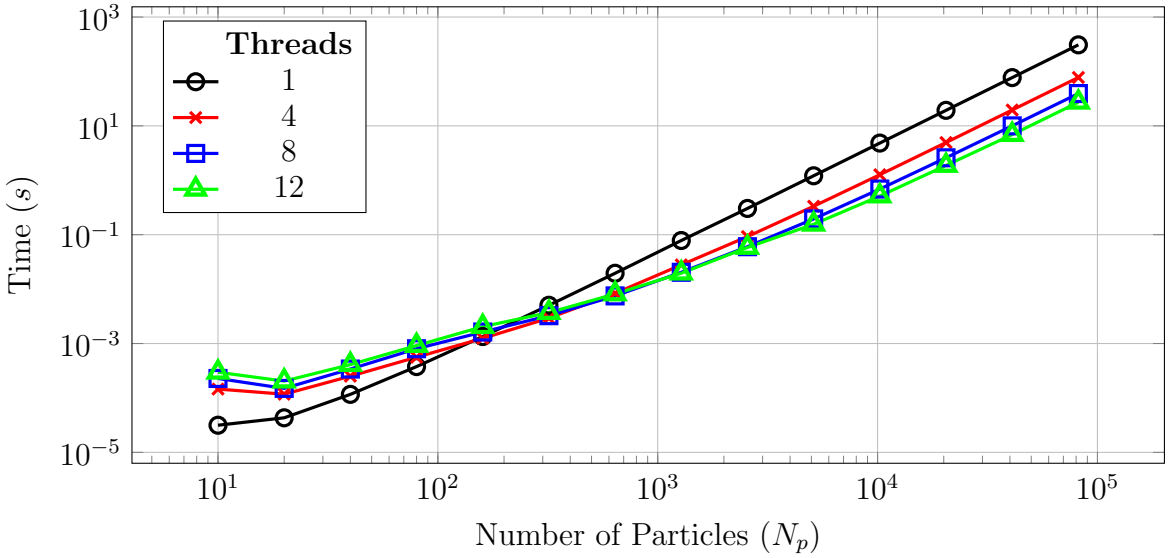

Figure 4.9: Computational times for parallelized particle interaction calculations

tational time increases linearly in the log scale. The slope of the line is approximately 2, therefore the computational time scales at $\mathcal{O}(N_p^2)$.

In Fig. 4.9, when the number of particles N_p is less than approximately 320, increasing the number of threads increases the computational time requirements compared to a single thread calculation. This is because the *overhead* costs associated with sharing memory and distributing tasks between multiple threads are greater than the computational benefit gained by parallelizing the N_p^2 calculations. However, as the number of particles increases beyond $N_p = 320$, increasing the number of threads decreases the computational time. Note that increasing the number of threads does not reduce the computational time linearly. For example, in the 12 thread calculation in Fig. 4.9, the computational time decreased by a factor of 11.35 (and not 12) compared to the single thread calculation. This difference is due to the computational overhead of parallelization, which increases with the number of threads.

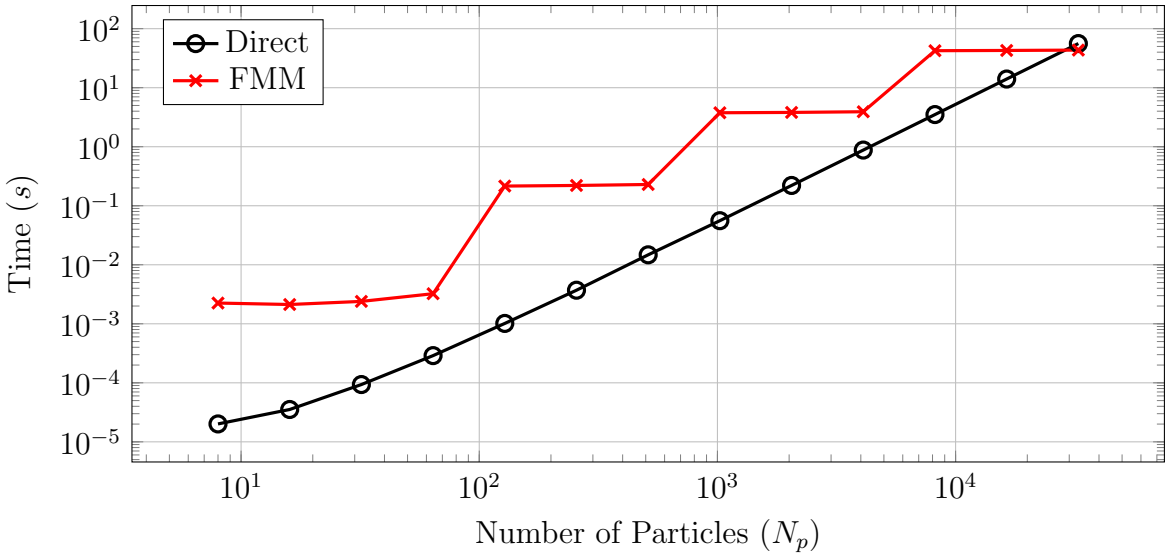

Figure 4.10: Computational times for parallelized FMM calculations

4.4.2 Fast Multipole Method

Parallelizing the direct summations reduces computational time by efficiently distributing computational power. However, the computational time still scales with $\mathcal{O}(N_p^2)$. *Fast summation methods* are mathematical algorithms that reduce the computational cost of direct summations to $\mathcal{O}(N_p^\gamma)$ (where $1 \leq \gamma < 2$), or $\mathcal{O}(N_p \log N_p)$. A well known example of a fast summation method is the Fast Fourier Transform (FFT). The Fast Multipole Method (FMM) reduces the cost of computing all pairwise interactions in a system of N_p particles to $\mathcal{O}(N_p)$. The FMM is considered to be one of the top 10 algorithms of the 20$^{\text{th}}$ century by the Society for Industrial and Applied Mathematics (SIAM). The FMM is used in CHARM [191], RCAS [93, 94, 192] and other rotor/propeller wake analyses [85] .

A detailed description and formulation of FMM is available in Refs. 193 and 194. The main idea behind the algorithm is the *divide-and-conquer strategy*. The particles are divided into clusters. The influence of each particle in a cluster is calculated at the

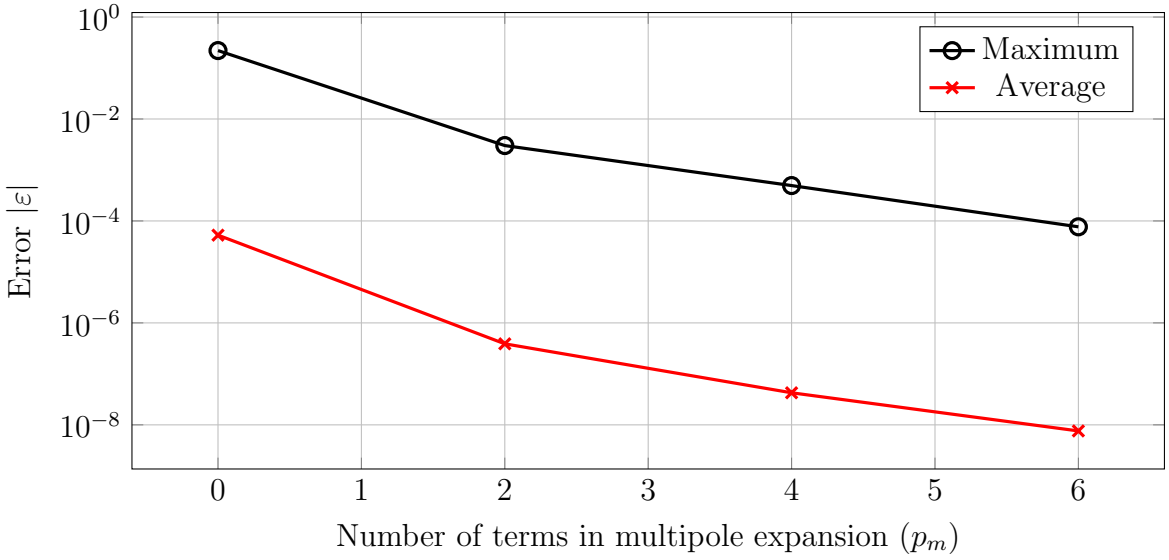

Figure 4.11: Error estimates in parallelized FMM calculations

center of the cluster in the form of *multipole moments*. The influence of all particles at a point is approximated by the direct interaction of particles in its neighborhood, summed with the multipole expansions of clusters that are well separated from the point. Therefore, the summation over N_p particles is reduced to a summation over N_c clusters and the number of terms p_m in the multipole expansion. Increasing the number of expansion terms p_m decreases the error in the approximation. An adaptive procedure is applied to divide the domain into appropriate sized clusters.

The computational time for velocity calculations of randomly distributed vortex particles is plotted in Fig. 4.10. The FMM summation and multipole evaluations were parallelized with 12 threads. The FMM is computationally expensive compared to the direct summation for less than $N_p \leq 32768$ particles. Note, that the time required for FMM computations increases in a step-wise way, instead of uniformly like the direct summation method. This is because the FMM computational time is determined by the number of cluster interactions instead of particle interactions. At each "step" in Fig. 4.10, the number of clusters required is increasing. The number

of clusters is determined by the maximum number of particles per cluster. As the number of particles increase, more clusters are added only when the particle limit is exceeded. Therefore, in the flat portions of the steps in Fig. 4.10, the number of clusters is not changing but the number of particles is increasing within them.

The error in FMM velocity calculations compared to the direct summation is shown in Fig. 4.11. The errors were calculated for a system of $N_p = 32768$ particles. As the number of terms in the multiple expansion increase, both the maximum and average error decrease. The maximum error is four orders of magnitude greater than the average error. Note, that the FMM is only slightly faster than the direct summation for $N_p = 32768$ particles (Fig. 4.10). However, the error can be as high as 10^{-4}. As the system of particles evolves with time, the errors accumulate and the wake system may not have the same structure as that with the direct summation calculations. Therefore, the FMM does not have a significant advantage for the wake calculations presented in this dissertation.

4.4.3 Fast Gauss Transform

The Fast Gauss Transform (FGT) is a fast summation method that evaluates the sum of N_p Gaussian functions at each point in $\mathcal{O}(N_p)$ time [195, 196]. The FGT is based on a divide-and-conquer strategy, combined with the manipulation of Hermite expansions and Taylor series. The FGT is closely related to the FMM. The FGT is applicable for VVPM computations when the Gaussian kernel is used for the regularization functions $\zeta_\sigma(s)$ and $\eta_\sigma(s)$.

The vorticity calculations of randomly distributed vortex particles presented in Section 4.4.1 was repeated using FGT in Fig. 4.12. The improved FGT algorithm from Ref. 197 was employed in the calculations. The FGT parameters were selected

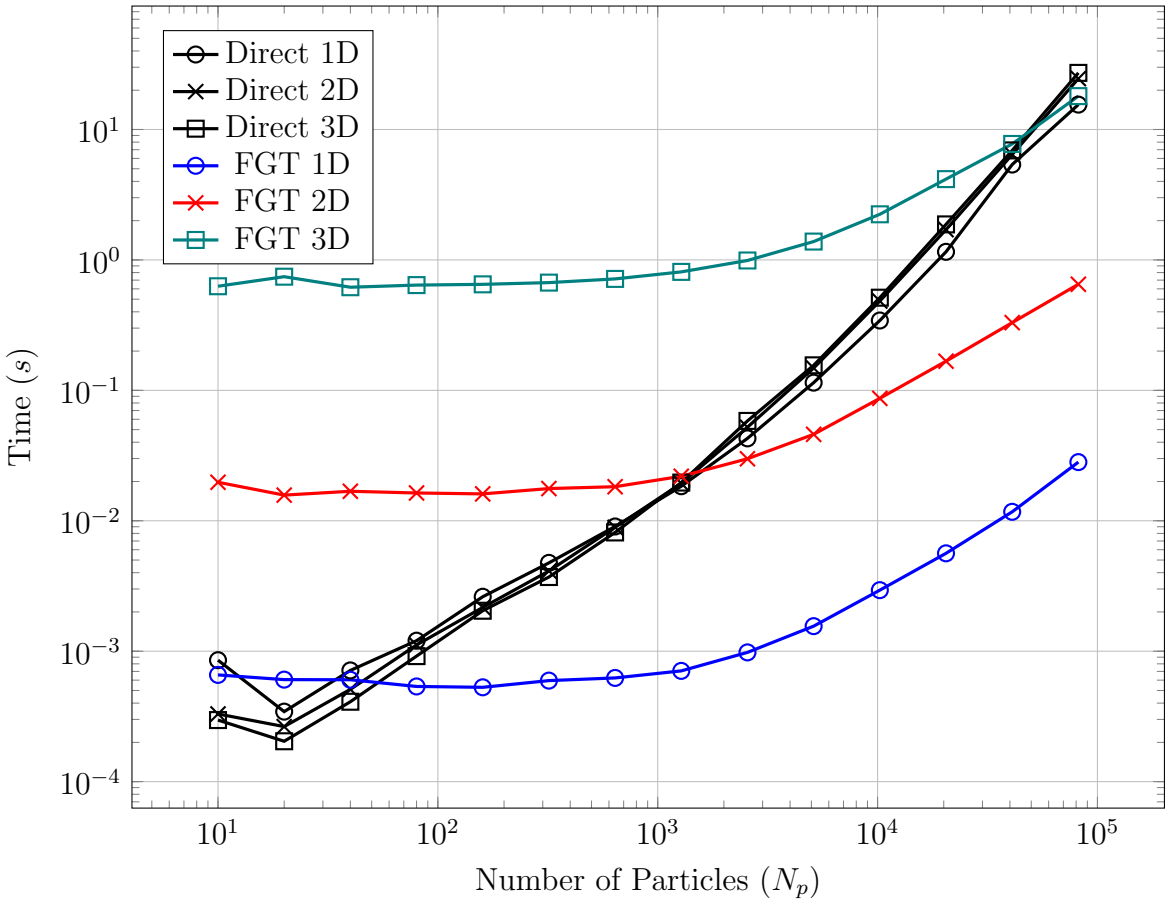

Figure 4.12: Computational times for parallelized FGT calculations

such that the error bound was $|\varepsilon| \leq 1 \times 10^{-6}$. Both the direct summation and FGT calculations were parallelized using 12 computational threads. The efficacy of the algorithm was compared for particles in 1D (distributed between $[0, 1]$ on a line), 2D (distributed inside a 1×1 square) and 3D (distributed inside a $1 \times 1 \times 1$ cube).

The 1D FGT results are plotted in blue in Fig. 4.12. The computational time remains relatively constant below 10^{-3} seconds for particles less than $N_p \leq 1280$. The direct summation calculations rapidly grow and become computationally expensive compared to FGT beyond $N_p \geq 80$ particles.

Similarly, the 2D and 3D FGT results are plotted in red and green respectively in Fig. 4.12. Note that the computational time for the FGT calculations increases by an order of magnitude with increase in dimension. The FGT calculations in 2D are faster compared to the direct summations beyond $N_p \geq 1280$ particles. The 3D FGT calculations are faster compared to the direct summations only beyond $N_p \geq 81920$ particles. This increase in computational time with increase in dimensions is referred to as the *curse of dimensionality*. Although the computational time in FGT is proportional to $\mathcal{O}(N_p)$, the proportionality constant behaves exponentially with the number of dimensions n_d.

$$t_{\text{FGT}} \propto p_m^{n_d} \cdot N_p \tag{4.82}$$

where p_m represents the number of expansion terms in FGT, and determines the maximum error bound of the calculation. In contrast, the direct summation method does not suffer from the curse of dimensionality, and scales linearly with the number of dimensions.

$$t_{\text{Direct}} \propto n_d \cdot N_p^2 \tag{4.83}$$

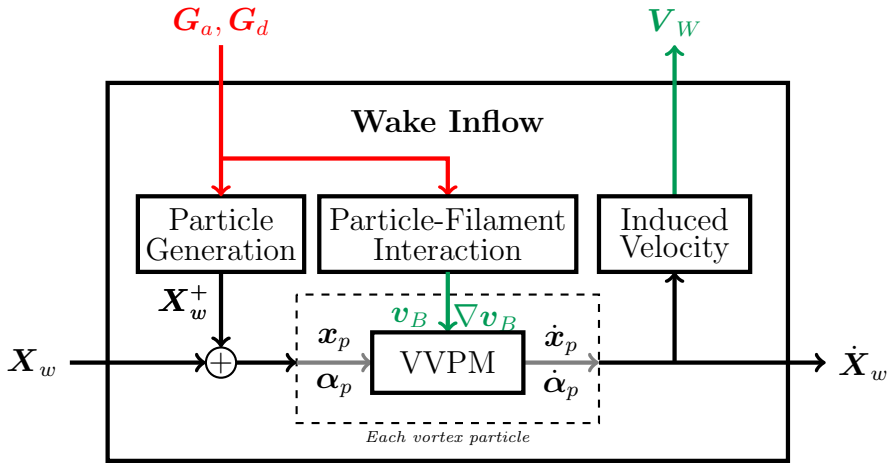

Figure 4.13: Wake inflow module

The number of particles in the coaxial rotor wake calculations are approximately $N_p \approx 2.5 \times 10^4$. For this number of particles, the 3D FGT computations are slightly expensive compared to direct summations, and also have an error of $|\varepsilon| \leq 10^{-6}$. Therefore, the FGT is not sufficiently useful for accelerating computations for the VVPM employed in this dissertation. Hence, the VVPM calculations presented in this dissertation use parallelized direct summations, and FMM and FGT are not employed.

4.5 Wake inflow module

The final wake inflow module is illustrated by Fig. 4.13. The particle positions $\boldsymbol{x}_p$ and vorticity strengths $\boldsymbol{\alpha}_p$ define the VVPM state vector $\boldsymbol{X}_w$.

$$\boldsymbol{X}_w = \left\{ \left\{ \begin{matrix} \boldsymbol{x}_{p_1} \\ \vdots \\ \boldsymbol{x}_{p_{N_p}} \end{matrix} \right\}^T , \left\{ \begin{matrix} \boldsymbol{\alpha}_{p_1} \\ \vdots \\ \boldsymbol{\alpha}_{p_{N_p}} \end{matrix} \right\}^T \right\}^T \tag{4.84}$$

In the **Particle Generation** block, the bound circulation distribution $\boldsymbol{G}_a$ and $\boldsymbol{G_d}$ are used to generate new particles in the vector $\boldsymbol{X}_w^+$, as described in Section 4.3. Particle splitting (Section 4.2.1) and merging (Section 4.2.2) are also applied at this step. Therefore, the size of the vector $\boldsymbol{X}_W$ changes at each time step.

Next, the vortex particle interactions are computed at each particle as shown in the dashed box in Fig. 4.13. The governing equations in the **VVPM** block are described in Section 4.1.4. In the **Particle-Filament Interaction** block, the vortex filament influence on the vortex particles is calculated, as described in Section 4.1.3.

In the **Induced Velocity** block in Fig. 4.13, the velocity at each CL point on the blade is calculated using Eqn. 4.32. These velocities are assembled into the vector $\boldsymbol{V}_w$:

$$\boldsymbol{V}_W = \left\{ \begin{array}{cccc} \boldsymbol{v}_\sigma(\boldsymbol{CL}_1)^T, & \cdots, & \boldsymbol{v}_\sigma(\boldsymbol{CL}_{N_c})^T \end{array} \right\}^T \tag{4.85}$$

Therefore, this chapter completes the description of the **Wake Inflow** module in the coaxial rotor aeroelastic analysis (Fig. 2.1).

CHAPTER 5

Solution of the Aeromechanical Problem

The aeromechanical formulation of the coaxial rotor system combines the structural dynamics of the counter-rotating blades, unsteady spanwise aerodynamic loads and the inflow distribution due to the wake. In this chapter, the aeromechanical formulation is used to determine the time response of the blades (Sec. 5.1). In Sec. 5.2, the blade loads are combined to calculate the total loads on the rotor hub. In Sec. 5.3, the hub loads are used to determine the control inputs required for force and moment equilibrium of the coaxial helicopter in hover and forward flight. Finally, the aeroelastic stability of the system in equilibrium is analysed in Sec. 5.4.

5.1 Time integration

The response of the coaxial rotor system is obtained by integrating the states of the system over time. Due to the modular structure of the aeroelastic formulation (Fig. 2.1), the blade dynamic response and wake evolution can be treated separately. The total blade state vector $\boldsymbol{y}$ is the combination of the structural and aerodynamic state vectors:

$$\boldsymbol{y} = \left\{ \begin{array}{ccc} \boldsymbol{X}_s^T, & \boldsymbol{X}_a^T, & \boldsymbol{X}_d^T \end{array} \right\}^T \tag{5.1}$$

The nonlinear system of equations of the structural dynamics and aerodynamic loads module are represented by the vector function $\boldsymbol{g}$:

$$\dot{\boldsymbol{y}} = \boldsymbol{g}\left(t, \boldsymbol{y}\right) \tag{5.2}$$

The time stepping is conducted in two stages. First, the rate of change of total blade states $\dot{\boldsymbol{y}}$ is calculated. During this step, the wake induced velocity vector $\boldsymbol{V}_w$ is kept constant. The aerodynamic loads $\boldsymbol{F}_a, \boldsymbol{F}_d$ and the rate of change of structural states $\dot{\boldsymbol{X}}_s$ are calculated simultaneously using an iterative solver based on Powell's conjugate direction method implemented in the GSL [157, 172]. The rate vector $\dot{\boldsymbol{y}}$ is integrated in time using the fourth-order Runge-Kutta method (RK4).

Next, the wake evolution is calculated by integrating the rate of change of the wake states $\dot{\boldsymbol{X}}_w$ in time using RK4. The blade structural and aerodynamic states are kept constant during the calculation of the new wake particle states $\boldsymbol{X}_w$.

The time-marching continues until periodic convergence of the blade states is achieved. The coaxial rotor is a nonlinear periodic system in both hover and forward flight. A coaxial rotor in hover experiences periodic loads due to the blade passage effect. The N_b blades of the upper and lower rotor pass each other $2N_b$ times during a revolution. Periodic loads are generated due to the changing induced velocity. Therefore, the periodicity of the coaxial rotor in hover is $2N_b$/rev. The time-period of the periodic system in hover is:

$$T_{\text{hover}} = \frac{\pi}{N_b \Omega} \tag{5.3}$$

In forward flight, the free-stream velocity $\boldsymbol{U}_\infty$ at a blade station varies with azimuth, therefore the system has a periodicity of 1/rev. The time-period of the periodic

system in forward flight is:

$$T_{\text{forward flight}} = \frac{2\pi}{\Omega} \tag{5.4}$$

Therefore, the nonlinear system of equations $\boldsymbol{g}$ are periodic with a time period T:

$$\boldsymbol{g}(t, \boldsymbol{y}) = \boldsymbol{g}(t + nT, \boldsymbol{y}) \quad , \quad n \in \mathbb{Z} \tag{5.5}$$

The periodic solution of the system of Eqns. 5.2 and 5.5 is represented by $\boldsymbol{y}_p(t)$. Therefore:

$$\dot{\boldsymbol{y}}_p(t) = \boldsymbol{g}\left(t, \boldsymbol{y}_p(t)\right) \tag{5.6}$$

$$\boldsymbol{y}_p(t) = \boldsymbol{y}_p(t + nT) \quad , \quad n \in \mathbb{Z} \tag{5.7}$$

5.2 Rotor hub loads

The total hub force and moment due to blade loading are obtained by integrating the distributed loads along the span of the isolated blade in the rotating frame, transforming them to the non-rotating hub fixed reference frame, and then summing the contribution of each blade at the rotor hub.

The net force and moment at the hub due to the blade are $\boldsymbol{F}_b$ and $\boldsymbol{M}_b$ respectively. The spanwise distributed force $\boldsymbol{p}$ and moment $\boldsymbol{q}$ are integrated over the blade span to calculate $\boldsymbol{F}_b$ and $\boldsymbol{M}_b$.

$$\boldsymbol{F}_b = \int_0^l \boldsymbol{p} \, \mathrm{d}x \tag{5.8}$$

$$\boldsymbol{M}_b = \int_0^l \left[\boldsymbol{q} + (\boldsymbol{P}' - \boldsymbol{C}) \times \boldsymbol{p}\right] \, \mathrm{d}x \tag{5.9}$$

The loads are numerically integrated over the blade span using the Gauss-Lobatto

quadrature [198]. The Gauss-Lobatto quadrature is used because it includes the endpoints of the domain. Including the endpoints is convenient because the blade circulation and sectional aerodynamic loads can be set to zero at the root and tip locations, thus improving the accuracy of the numerical integration.

The forces and moments from each blade are added to obtain the total loads at the rotor hub.

$$\boldsymbol{F}_h(\psi) = \sum_{i=1}^{N_b} \boldsymbol{F}_{b_i}(\psi_i) \tag{5.10}$$

$$\boldsymbol{M}_h(\psi) = \sum_{i=1}^{N_b} \boldsymbol{M}_{b_i}(\psi_i) \tag{5.11}$$

where

$$\psi_i = \psi + \frac{2\pi}{N_b}(i-1) \quad , \quad i = 1 \cdots N_b \tag{5.12}$$

Note that in hover, the blade response and loads are periodic at a frequency of $2N_b$/rev. The in-plane forces and moments are canceled out for a rotor with $N_b > 1$ identical blades. Only the vertical component of the blade force and moment are retained. Therefore, the rotor hub loads in Eqns. 5.10 and 5.11 further simplify to:

$$\boldsymbol{F}_{h,\text{hover}}(\psi) = N_b F_{b_Z}(\psi)\widehat{\boldsymbol{k}} \tag{5.13}$$

$$\boldsymbol{M}_{h,\text{hover}}(\psi) = N_b M_{b_Z}(\psi)\widehat{\boldsymbol{k}} \tag{5.14}$$

The unit vector $\widehat{\boldsymbol{k}}$ is along the $\boldsymbol{Z}$ axis of the rotor hub. The hub forces and moments are integrated over the azimuth to obtain the revolution-averaged hub loads that are

required for the trim analysis.

$$\int_0^{2\pi} \boldsymbol{F}_h(\psi)\ \mathrm{d}\psi = F_X\widehat{\boldsymbol{i}} + F_Y\widehat{\boldsymbol{j}} + F_Z\widehat{\boldsymbol{k}} \tag{5.15}$$

$$\int_0^{2\pi} \boldsymbol{M}_h(\psi)\ \mathrm{d}\psi = M_X\widehat{\boldsymbol{i}} + M_Y\widehat{\boldsymbol{j}} + M_Z\widehat{\boldsymbol{k}} \tag{5.16}$$

The $(\boldsymbol{X}, \boldsymbol{Y}, \boldsymbol{Z})$ axis system is a body-fixed counter-clockwise coordinate system centered at the helicopter center of gravity (CG). The unit vectors along the three axes are $\widehat{\boldsymbol{i}}, \widehat{\boldsymbol{j}}$ and $\widehat{\boldsymbol{k}}$. The revolution averaged hub forces are normalized with respect to the air density ρ, rotor disk area πR^2 and the square of the tip speed ΩR. The moment terms are normalized with an additional factor, the rotor radius R.

$$C_{F_i} = \frac{F_i}{\rho\pi\Omega^2 R^4} \tag{5.17}$$

$$C_{M_i} = \frac{M_i}{\rho\pi\Omega^2 R^5} \tag{5.18}$$

where $i = X, Y, Z$.

The rotor thrust coefficient C_T is the Z component of the hub force.

$$C_T = \frac{F_Z}{\rho\pi\Omega^2 R^4} = C_{F_Z} \tag{5.19}$$

5.3 Trim analysis

A helicopter in steady flight is governed by force and moment equilibrium. The aeroelastic response of a rotor can be calculated for a given control setting and flight condition. However, the operating state of the helicopter is typically provided in terms of forward speed and net gross weight. Therefore a trim calculation procedure is required which involves iterating the control settings to achieve the necessary

force and moment equilibrium [58]. The complexity of the aerodynamic, inertial and structural forces on the rotor blades is responsible for the non-linear coupling of loads and control inputs. The coupling effects are minimized by mixing of control inputs mechanically or electronically by a flight control system [59].

The helicopter pilot has four main controls: a collective lever, a cyclic control stick (that moves fore-aft and left-right) and a rudder pedal. In a conventional SMR helicopter, these controls are connected to the main rotor collective θ_0, lateral cyclic θ_{1c}, longitudinal cyclic θ_{1s} and tail rotor collective respectively. In coaxial rotor helicopters, this arrangement varies. In the Kamov coaxial helicopters, the pedal controls the differential collective, the collective lever controls the mean collective pitch of both rotors and the cyclic stick gives equal cyclic input to each rotor. In the Sikorsky X2TD, the pedal controls differential collective in low speed flight and the rudder on vertical tail fins in high speed flight [47, 49]. The pilot controls the mean collective and cyclic pitch angles, while differential cyclic inputs are provided by the Fly By Wire (FBW) and Stability Augmentation System (SAS). The X2TD has a propulsor for augmenting the forward thrust. A propulsor pitch control input is required to change the propulsor thrust. In addition, a slowed rotor system is used for improved performance in forward flight. Due to the availability of these additional control inputs, the coaxial helicopter is an *over-actuated system*.

The trim procedure for coaxial rotor helicopters requires several modifications. In hover, the collective pitch on the two contra-rotating rotors is changed individually to balance the yaw moment. Forward flight trim is more complicated. The cyclic controls need to be coupled to maintain pitch and roll moment equilibrium. The coupling is highly non-linear and changes with forward speed because of the unsteady aerodynamic interaction and aeroelastic blade response.

5.3.1 Hover

In hover, the net thrust is equal to the helicopter weight, and the net yaw moment is zero.

$$(C_{F_Z})_u + (C_{F_Z})_l = C_W \tag{5.20}$$

$$(C_{M_Z})_u + (C_{M_Z})_l = 0 \tag{5.21}$$

The helicopter weight coefficient is defined as:

$$C_W = \frac{W_f}{\rho\pi\Omega^2 R^4} \tag{5.22}$$

The thrust and torque depends on the collective pitch θ_0 of each rotor. However, the two rotors operate in different aerodynamic environments, therefore they do not generate the same loads at the same collective pitch.

There are two main approaches used for coaxial rotor trim in hover. The first approach is to fix the upper rotor collective pitch, and vary the lower rotor pitch to balance the upper rotor moment. This approach is mainly used in experimental studies such as Refs. 36 and 37. This method is convenient because experiments in Ref. 40 indicate that the upper rotor loads are insensitive to the lower rotor pitch settings.

The second approach consists of using *mixed controls*, i.e. the mean collective pitch angle and the differential collective:

$$\theta_0 = \frac{(\theta_0)_u + (\theta_0)_l}{2} \tag{5.23}$$

$$\Delta\theta_0 = \frac{(\theta_0)_u - (\theta_0)_l}{2} \tag{5.24}$$

The equivalent collective inputs to each rotor are:

$$(\theta_0)_u = \theta_0 + \Delta\theta_0 \tag{5.25}$$

$$(\theta_0)_l = \theta_0 - \Delta\theta_0 \tag{5.26}$$

Increasing the mean collective pitch increases the total thrust coefficient. Increasing the differential collective increases the upper rotor thrust and torque, and decreases lower rotor thrust and torque. This approach is used in experimental [33] and computational studies [102, 109, 115, 199].

Experimental studies indicate that the lower rotor collective pitch is greater than the upper rotor collective pitch at hover trim [37]. The upper and lower rotor interactions are maximum at hover because the entire upper rotor wake passes through the lower rotor plane. The lower rotor experiences larger inflow and therefore the angle of attack is reduced at each blade section. The lower rotor thrust and torque are both reduced compared to the upper rotor. Therefore, the collective pitch for the lower rotor needs to increase to counter the torque of the upper rotor.

5.3.2 Forward flight

There are two different trim solutions for SMR helicopters in forward flight: *propulsive/free-flight trim* and *wind tunnel* trim. In wind tunnel trim, the trim objective is lateral and longitudinal moment equilibrium. In free-flight trim, all net forces and moments about the CG are zero.

Different studies use different sets of control inputs for trimming the coaxial rotor in forward flight. In some computational studies, the cyclic inputs are equal for the upper and lower rotor [77, 115]. In the XH-59A, the control inputs were mixed using

a rotor phasing parameter Ψ [45]. The phasing parameter Ψ couples the longitudinal cyclic with differential lateral control. The modified pitch inputs are:

$$\theta_u = (\theta_0 + \Delta\theta_0) - A_1 \cos(\psi_u + \Psi) - B_1 \sin(\psi_u + \Psi) \tag{5.27}$$

$$\theta_l = (\theta_0 - \Delta\theta_0) - A_1 \cos(\psi_l + \Psi) + B_1 \sin(\psi_l + \Psi) \tag{5.28}$$

where A_1 and B_1 are the lateral and longitudinal control parameters for the XH-59A.

The most common choice of control inputs is mean and differential collective and cyclic pitch. Each rotor has independent collective, lateral cyclic and longitudinal cyclic controls. The cyclic controls are mixed into mean and differential components:

$$\theta_{1c} = \frac{(\theta_{1c})_u + (\theta_{1c})_l}{2} \tag{5.29}$$

$$\theta_{1s} = \frac{(\theta_{1s})_u + (\theta_{1s})_l}{2} \tag{5.30}$$

$$\Delta\theta_{1c} = \frac{(\theta_{1c})_u - (\theta_{1c})_l}{2} \tag{5.31}$$

$$\Delta\theta_{1s} = \frac{(\theta_{1s})_u - (\theta_{1s})_l}{2} \tag{5.32}$$

Therefore, the pitch inputs to the upper and lower rotor are:

$$\theta_u = (\theta_0 + \Delta\theta_0) + (\theta_{1c} + \Delta\theta_{1c}) \cos\psi_u + (\theta_{1s} + \Delta\theta_{1s}) \sin\psi_u \tag{5.33}$$

$$\theta_l = (\theta_0 - \Delta\theta_0) + (\theta_{1c} - \Delta\theta_{1c}) \cos\psi_l + (\theta_{1s} - \Delta\theta_{1s}) \sin\psi_l \tag{5.34}$$

The forces and moments acting on a representative coaxial rotor helicopter are shown in Fig. 5.1. The $(\boldsymbol{X}_o, \boldsymbol{Y}_o, \boldsymbol{Z}_o)$ axis system is a counter-clockwise coordinate system centered at the helicopter CG which is always aligned with the ground reference frame. Several simplifying assumptions are made due to the lack of available data for the X2TD:

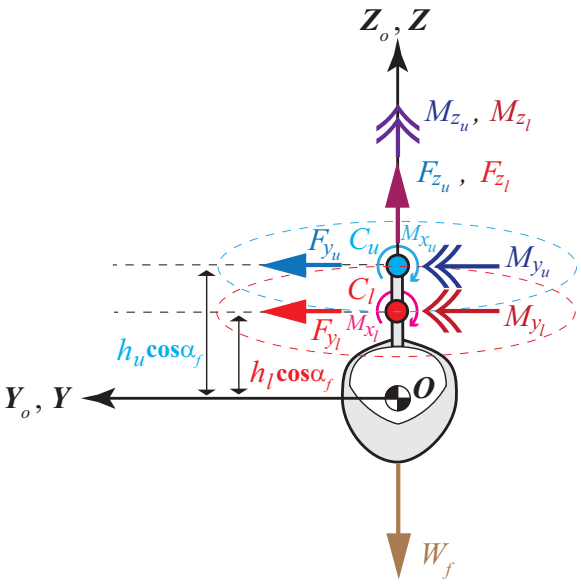

(a) $Y - Z$ Plane

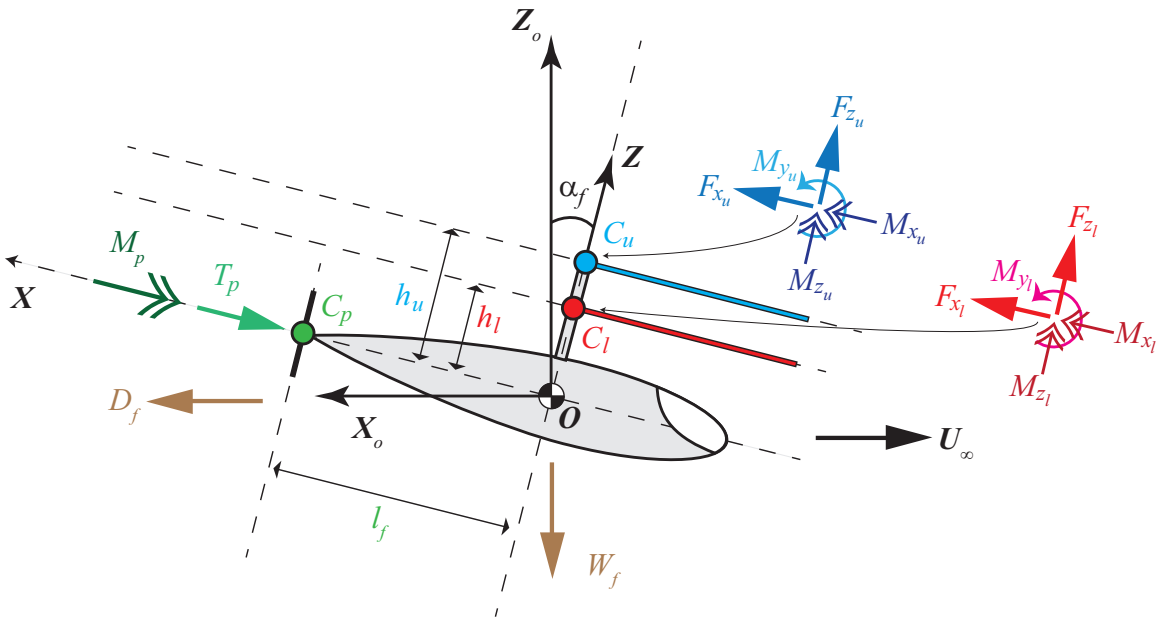

(b) $X - Z$ Plane

Figure 5.1: Forces and moments acting on a coaxial helicopter in forward flight

1. The CG is located at a point $\boldsymbol{O}$. The upper and lower rotor hubs are located at a vertical distance h_u and h_l above the CG respectively. The separation between the two hubs is h.

$$h = h_u - h_l \tag{5.35}$$

   There is no horizontal offset between the CG and the hubs.

2. The fuselage is tilted forward at an angle of α_f. Due to the lateral symmetry of the coaxial helicopter, the side-slip angle is assumed to be zero in forward flight.

3. The fuselage generates a drag force D_f opposite to the direction of flight $\boldsymbol{U}_\infty$. The fuselage pitching moment and other loads generated due to the fuselage aerodynamics are ignored. The helicopter drag force is defined as:

$$D_f = \frac{1}{2}\rho U_\infty^2 f C_{d_f} \tag{5.36}$$

   where the term fC_{d_f} is the equivalent fuselage flat plate area. The net drag coefficient of the fuselage is defined as:

$$C_{D_f} = \frac{D_f}{\rho\pi\Omega^2 R^4} = \frac{1}{2}\frac{\mu^2}{\cos^2\alpha_f}\left(\frac{fC_{d_f}}{\pi R^2}\right) \tag{5.37}$$

4. The propulsor is located at a point $\boldsymbol{C}_p$ at a horizontal distance of l_p from the CG. There is no vertical offset between the CG and the propulsor. The propulsor thrust and torque are T_p and M_p respectively.

5. Forces and moments due to the vertical and horizontal tail surfaces are ignored.

Based on these assumptions, the force and moment equilibrium equations are:

$$D_f - T_p \cos\alpha_f + (F_{X_u} + F_{X_l}) \cos\alpha_f - (F_{Z_u} + F_{Z_l}) \sin\alpha_f = 0 \quad (5.38)$$

$$F_{Y_l} + F_{Y_u} = 0 \quad (5.39)$$

$$-W_f - T_p \sin\alpha_f + (F_{X_u} + F_{X_l}) \sin\alpha_f + (F_{Z_u} + F_{Z_l}) \cos\alpha_f = 0 \quad (5.40)$$

$$(M_p + M_{X_l} + M_{X_u}) \cos\alpha_f - (M_{Z_l} + M_{Z_u}) \sin\alpha_f$$

$$-(F_{Y_l} h_l + F_{Y_u} h_u) \cos\alpha_f = 0 \quad (5.41)$$

$$M_{Y_l} + M_{Y_u} + F_{X_l} h_l + F_{X_u} h_u = 0 \quad (5.42)$$

$$(M_p + M_{X_l} + M_{X_u}) \sin\alpha_f + (M_{Z_l} + M_{Z_u}) \cos\alpha_f$$

$$-(F_{Y_l} h_l + F_{Y_u} h_u) \sin\alpha_f = 0 \quad (5.43)$$

Note that there are 7 unknown trim variables: fuselage tilt angle (α_f), mean collective and cyclic pitch inputs (θ_0, θ_{1c}, θ_{1s}), and differential collective and cyclic inputs ($\Delta\theta_0$, $\Delta\theta_{1c}$, $\Delta\theta_{1s}$). However there are only 6 equilibrium equations (Eqns. 5.38 - 5.43). In addition, the propulsor thrust T_p and torque M_p are unknown due to lack of available data.

Therefore, additional information is required to solve the forward flight trim problem. Computational studies using RCAS [127, 200] have explored different trim constraints to optimize performance, loads and vibrations on the helicopter. In Ref. 127, the pitch attitude, rotor RPM and differential lateral cyclic were fixed, while the other controls were changed. In Ref. 200, differential cyclics, propulsive thrust and RPM were set to constant values. The mean collective, lateral and longitudinal cyclic, differential collective, roll attitude and propulsive thrust were varied.

In this dissertation, two free-flight trim conditions are considered. The first assumes that the propulsor is not operating. The second assumes that the fuselage is

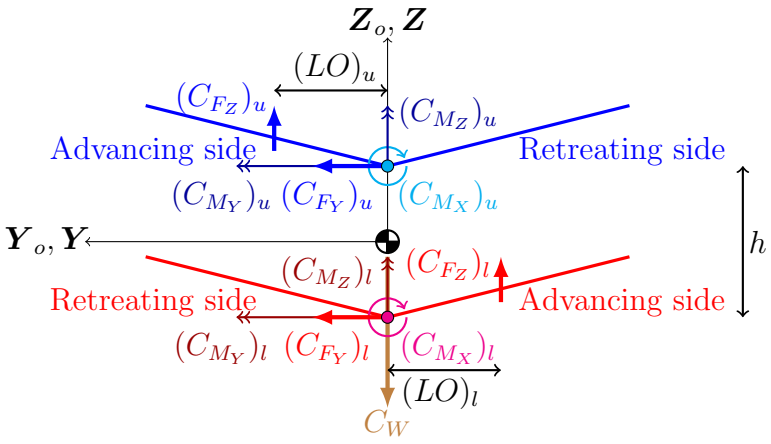

(a) Y-Z plane

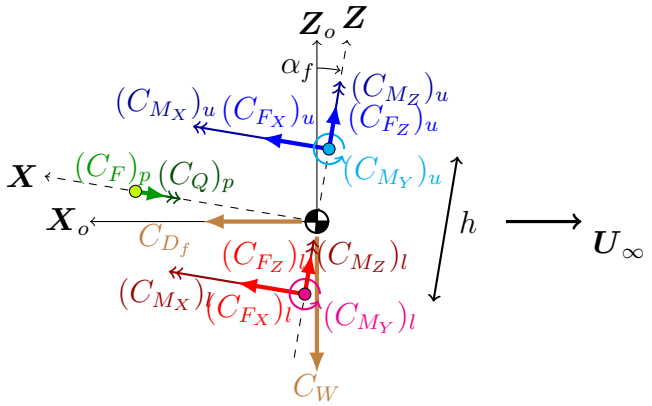

(b) X-Z plane

Figure 5.2: Simplified free body diagram of coaxial rotor without propulsor

flying at a level attitude with the propulsor providing forward thrust.

5.3.2.1 Propulsor off

With the propulsor off, the propulsor thrust and torque are zero. The CG is assumed to lie at the midpoint of the upper and lower rotor hubs, because the weight distribution of the X2TD is not available in open literature. Based on these two assumptions, a simplified free body diagram is shown in Fig. 5.2. The equations in non-dimensional

form are:

$$(C_{F_X})_u + (C_{F_X})_l = C_W \sin\alpha_f - \frac{\mu^2}{2\cos\alpha_f}\left(\frac{fC_{D_f}}{\pi R^2}\right) \tag{5.44}$$

$$(C_{F_Y})_u + (C_{F_Y})_l = 0 \tag{5.45}$$

$$(C_{F_Z})_u + (C_{F_Z})_l = C_W \cos\alpha_f + \frac{\mu^2}{2}\left(\frac{fC_{D_f}}{\pi R^2}\right)\frac{\sin\alpha_f}{\cos^2\alpha_f} \tag{5.46}$$

$$(C_{M_X})_u + (C_{M_X})_l = \frac{1}{2}\left(\frac{h}{R}\right)[(C_{F_Y})_u - (C_{F_Y})_l] \tag{5.47}$$

$$(C_{M_Y})_u + (C_{M_Y})_l = \frac{1}{2}\left(\frac{h}{R}\right)[(C_{F_X})_l - (C_{F_X})_u] \tag{5.48}$$

$$(C_{M_Z})_u + (C_{M_Z})_l = 0 \tag{5.49}$$

The seventh equation required for trim is the Lift Offset (LO) of the rotor. The non-zero roll moment of each rotor at the hub is characterized by the LO [201]. The LO for a coaxial rotor is defined as the effective lateral displacement of the net rotor thrust of each rotor from the hub center (Fig. 5.2a):

$$\text{LO} = \frac{(C_{M_X})_u - (C_{M_X})_l}{(C_{F_Z})_u + (C_{F_Z})_l} \tag{5.50}$$

The LO is positive when the net thrust of the rotor is shifted towards the advancing side. A positive LO offloads the retreating side of the rotor, and allows trim at higher speeds for a coaxial rotor. Reference 201 indicates that a higher LO increases the maximum lift capability of a medium size coaxial helicopter at the cost of greater flap bending moments. The flap bending moments increase because each rotor has a non-zero roll moment due to the LO. In Ref. 124 the effects of LO on blade tip clearance, rotor performance and vibratory loads were examined for a model coaxial rotor. Lift offsets between 0.15 and 0.4 for an advance ratio of $\mu = 0.3$ were considered optimal in Refs. 201 and 124 because the lift capability of the rotor was increased without a substantial increase in vibrations.

Therefore, the 7 equations (Eqns. 5.44 - 5.50) are used to solve for the 7 trim variables (α_f, θ_0, θ_{1c}, θ_{1s},$\Delta\theta_0$, $\Delta\theta_{1c}$, $\Delta\theta_{1s}$).

5.3.2.2 Level attitude

An advantage of the propulsor on a coaxial rotor helicopter is the ability to fly at a level attitude. The Sikorsky Raider-X is a strong contender for the FARA program because of its exceptional maneuverability which includes the ability to accelerate with a level attitude [9]. The propulsor is able to provide the forward thrust required to overcome fuselage drag, without the need to tilt the rotor.

$$\alpha_f = 0 \tag{5.51}$$

Figure 5.3 indicates the forces and moments acting on the helicopter at level attitude. The equilibrium equations are simplified to:

$$-D_f + T_p - F_{X_u} - F_{X_l} = 0 \tag{5.52}$$

$$F_{Y_l} + F_{Y_u} = 0 \tag{5.53}$$

$$-W + F_{Z_u} + F_{Z_l} = 0 \tag{5.54}$$

$$M_p + M_{X_l} + M_{X_u} - F_{Y_l}h_l - F_{Y_u}h_u = 0 \tag{5.55}$$

$$M_{Y_l} + M_{Y_u} + F_{X_l}h_l + F_{X_u}h_u = 0 \tag{5.56}$$

$$M_{Z_l} + M_{Z_u} = 0 \tag{5.57}$$

The propulsor thrust only affects the horizontal force equilibrium equation (Eqn. 5.52). We assume that the propulsor can generate sufficient thrust to counter the fuselage drag and rotor horizontal force at all times. Therefore, Eqn. 5.52 is eliminated. In addition, the propulsor torque is ignored ($M_p = 0$). The system of equations

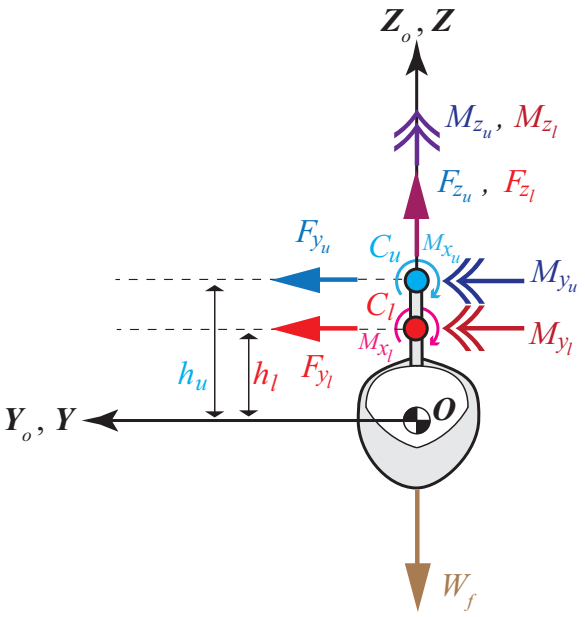

(a) $Y - Z$ Plane

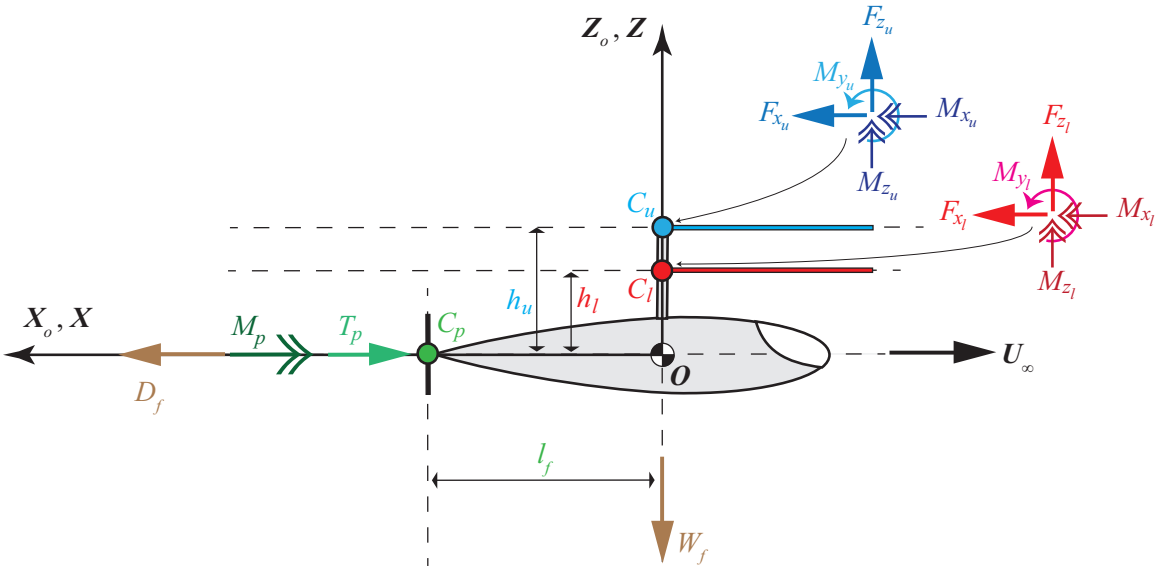

(b) $X - Z$ Plane

Figure 5.3: Forward flight trim including propulsor thrust without fuselage tilt

is simplified to:

$$
\begin{aligned}
(C_{F_Y})_u + (C_{F_Y})_l &= 0 && (5.58)\\
(C_{F_Z})_u + (C_{F_Z})_l &= C_W && (5.59)\\
(C_{M_X})_u + (C_{M_X})_l &= \frac{1}{2}\left(\frac{h}{R}\right)[(C_{F_Y})_u - (C_{F_Y})_l] && (5.60)\\
(C_{M_Y})_u + (C_{M_Y})_l &= \frac{1}{2}\left(\frac{h}{R}\right)[(C_{F_X})_l - (C_{F_X})_u] && (5.61)\\
(C_{M_Z})_u + (C_{M_Z})_l &= 0 && (5.62)
\end{aligned}
$$

Therefore, the 5 equilibrium equations (Eqns. 5.58 - 5.62) and 1 lift-offset equation (Eqn. 5.50) are sufficient to determine the 6 trim variables (θ_0, θ_{1c}, θ_{1s},$\Delta\theta_0$, $\Delta\theta_{1c}$, $\Delta\theta_{1s}$). Hence, this is an alternative scheme for forward flight trim that includes propulsor thrust and zero fuselage tilt.

5.3.2.3 Wind tunnel trim

Wind tunnel tests on coaxial rotors have been conducted in Refs. 51, 52, 202. References 51, 52 are experimental studies of the S-97 Raider and SB>1 Defiant scale-models. Limited information is provided about the wind tunnel trim procedure. In Ref. 202, the fuselage and propulsor are not included in the tests. Therefore, $T_p = M_p = 0$. The wind tunnel tests were conducted for different fixed upper rotor collective pitch (θ_0^u) and fuselage tilt (α_f) settings. Therefore, there are only 5 trim variables: lower rotor collective pitch (θ_0^l), and cyclic pitch inputs for both rotors (θ_{1c}^u, θ_{1s}^u, θ_{1c}^l, θ_{1s}^l).

Five trim equations are required to determine the pitch inputs. First, the roll moment of the upper and lower rotor are equal and opposite.

$$(C_{M_X})_u + (C_{M_X})_l = 0 \qquad (5.63)$$

The magnitude of the roll moment is determined from the LO setting.

$$(C_{M_X})_u = -(C_{M_X})_l = \frac{\text{LO}}{2}\left[(C_{F_Z})_u + (C_{F_Z})_l\right] \tag{5.64}$$

Second, the pitching moment of the upper and lower rotor are individually set to zero.

$$(C_{M_Y})_u = 0 \tag{5.65}$$

$$(C_{M_Y})_l = 0 \tag{5.66}$$

The vertical hub moments of the upper and lower rotor are equal and opposite.

$$(C_{M_Z})_u + (C_{M_Z})_l = 0 \tag{5.67}$$

Therefore, Eqns. 5.63 - 5.67 are the 5 trim equations required to determine the 5 pitch inputs in wind tunnel trim.

5.3.3 Trim solution

In many computational studies, the trim solution is obtained using simplified inflow models. Good first estimates for trim are obtained using BEMT with assumed wake inflow [59]. For example, the CFD/CSD study [109] used table look-up for blade sectional loads and inflow calculations in the trim iterations. Therefore, trim convergence was faster by avoiding the computationally expensive CFD calculations in each iteration. In FLIGHTLAB, a two-loop trim algorithm was used [94]. The inner loop included vehicle dynamics and aerodynamics using the finite state dynamic inflow model. The outer loop simulated the rotor wake using the VVPM. In this dissertation, simplified inflow models were not used. VVPM was used in each trim iteration for accuracy and consistency of results.

The hybrid Powell's method [172] in GSL [157] was applied to solve the trim equations. The residuals of the equilibrium equations were normalized so that a uniform tolerance could be applied to solve the system of non-linear equations. The residuals of the force equilibrium equations were divided by the weight coefficient C_W, and the moment equilibrium equations were divided by the ideal torque coefficient C_{q_0}.

$$C_{q_0} = \frac{C_W^{3/2}}{\sqrt{2}} \tag{5.68}$$

The tolerance δ_t for the solution of the trim equations was kept at 10^{-3}. This implies that the acceleration on the fuselage at trim convergence is < 0.001g. The LO is within $0.1\%R$ of the set value at trim. Therefore, the accuracy of the trim solution is considered adequate for the aeroelastic analysis.

5.4 Aeroelastic stability analysis

Coaxial rotors have a non-zero moment at each rotor hub due to the LO [201]. Stiff composite hingeless rotor blades are required to sustain the large root bending moments and reduce the possibility of blade strike between the rotors [124]. Furthermore, the proximity of the two rotors induces periodic blade passage loading effects and unsteady rotor wake interactions that are absent in SMR configurations.

In coaxial helicopters such as the X2TD, the rotor RPM is reduced at high speeds to prevent the drag penalty associated with the advancing blade tip Mach number. The centrifugal loads decrease and the blade mode shapes change due to reduced rotor RPM. Fluidlastic dampers have been proposed to reduce lagwise loads on a variable speed rotor [203]. Furthermore, DS induced loads can excite torsional modes of hingeless blades [204]. This combination of LO, periodic blade passage effect, un-

steady rotor wake interaction, combined with stiff hingeless blades and reduced rotor RPM, implies that the aeroelastic stability analysis of a coaxial rotor system requires special attention.

A limited number of studies have addressed the aeroelastic stability of coaxial rotors. The stability and control characteristics of the ABC rotor were studied using flight tests in Ref. 205. The study reported vehicle handling qualities but not blade dynamic response. The aeroelastic boundaries of the Kamov coaxial helicopters were presented in Ref. 206. The study noted that it was necessary to include compressibility and DS to capture blade flutter. Sikorsky studied the stability of the X2TD in forward flight using RCAS in Ref. 47. The modal damping was determined by simulating transient blade response to cyclic pulses. The lag modes were predicted to have the least damping, on the order of 1–2%. The damping did not change significantly with airspeed.

Hingeless blades are classified as stiff-in-plane or soft-in-plane based on the non-dimensional frequency of the rotating lag mode. Stiff-in-plane rotor blades have rotating lag frequencies above 1/rev whereas soft-in-plane blades have rotating lag frequencies below 1/rev. Stiff-in-plane hingeless blade rotors have received much less attention compared to soft-in-plane hingeless rotors [207, 208]. Stiff-in-plane rotors do not encounter air and ground resonance instabilities, however the coupled flap-lag-torsion stability degrades in forward flight [209]. The effect of rotor speed on the aeroelastic stability boundary of a model hingeless rotor has been studied experimentally [210]. The results indicated that the lag mode can potentially become unstable and its modal damping is sensitive to the aerodynamic conditions.

The aeroelastic stability analysis of the stiff-in-plane hingeless coaxial rotor blades

is a major contribution of this dissertation. The coaxial rotor is a periodic system in both hover and forward flight. However, no previous study has noted this property. In this study, the aeroelastic stability is analysed using a periodic system model. Furthermore, the aeroelastic coupling between different modes of the upper and lower rotor that has been ignored in previous studies is included.

5.4.1 Floquet theory

Periodic system stability is governed by Floquet theory. Numerical methods to determine the stability of non-linear periodic systems were developed for a SMR in forward flight [211, 212]. These numerical methods are also applicable to a coaxial rotor in hover and forward flight.

The stability of a periodic system is determined from the state transition matrix (STM) $[\boldsymbol{\Phi}(T,0)]$ at the end of a period T. The STM of the system is computed using the *single-pass algorithm* [211]. First, the nonlinear periodic system $\boldsymbol{g}$ is linearized about the periodic equilibrium states $\boldsymbol{y}_p$. The k^{th} column of the system matrix $[\boldsymbol{\mathcal{A}}(t)]$ is:

$$\boldsymbol{\mathcal{A}}_k(t) \approx \frac{\boldsymbol{g}\left(t, \boldsymbol{y}_p(t) + \delta_k \hat{\boldsymbol{e}}_k\right) - \boldsymbol{g}\left(t, \boldsymbol{y}_p(t)\right)}{\delta_k} \tag{5.69}$$

where $\widehat{\boldsymbol{e}}_k$ is a unit vector with its k^{th} entry equal to one and the rest zero.

$$\widehat{\boldsymbol{e}}_k = \left\{ \begin{array}{ccccccc} 0, & \cdots, & 0, & \underbrace{1,}_{k^{\text{th}}\text{ index}} & 0, & \cdots, 0 \end{array} \right\}^T \tag{5.70}$$

Note that the perturbations $\delta_k \hat{\boldsymbol{e}}_k$ are only for entries corresponding to the structural states $\boldsymbol{X}_s$ in the vector $\boldsymbol{y}$. The wake induced velocities $\boldsymbol{V}_w$ are assumed to be constant during the perturbations. We define the vector $\boldsymbol{z}_k$ such that:

$$\dot{\boldsymbol{z}}_k(t) = [\boldsymbol{\mathcal{A}}(t)]\boldsymbol{z}_k(t) \tag{5.71}$$

with the initial condition:

$$\boldsymbol{z}_k(0) = \widehat{\boldsymbol{e}}_k \tag{5.72}$$

The STM is obtained by the integration of Eqn. 5.71 over the time period T.

$$[\boldsymbol{\Phi}(T,0)] = \left[\begin{array}{cccc} \boldsymbol{z}_1(T), & \cdots, & \boldsymbol{z}_n(T) \end{array} \right] \tag{5.73}$$

The complex eigenvalues of the STM at teh end of one period $[\boldsymbol{\Phi}(T,0)]$ are denoted as *characteristic multipliers* Λ. The corresponding eigenvectors $\boldsymbol{\xi}$ represent the coupled modes of the system.

$$[\boldsymbol{\Phi}(T,0)]\boldsymbol{\xi} = \Lambda\boldsymbol{\xi} \tag{5.74}$$

The complex eigenvalues of a matrix with real entries appear in complex conjugate pairs.

$$\Lambda = \Lambda_{\mathbb{R}} \pm \mathrm{i}\Lambda_{\mathbb{I}} \tag{5.75}$$

The system is stable if the magnitude of each characteristic multipliers is less than one.

$$|\Lambda| = \sqrt{\Lambda_{\mathbb{R}}^2 + \Lambda_{\mathbb{I}}^2} < 1 \tag{5.76}$$

The *characteristic exponents* λ are related to the characteristic multipliers Λ.

$$\lambda = \zeta \pm \mathrm{i}\omega \tag{5.77}$$

The imaginary part of the characteristic exponent ω is related to the modal frequency, modified by integer multiples of the common period of the system.

$$\zeta = \frac{1}{2T}\ln\left(\Lambda_{\mathbb{R}}^2 + \Lambda_{\mathbb{I}}^2\right) \tag{5.78}$$

$$\omega = \frac{1}{T}\tan^{-1}\left(\frac{\Lambda_{\mathbb{I}}}{\Lambda_{\mathbb{R}}}\right) \pm \frac{2\pi n}{T} \quad , \quad n \in \mathbb{Z} \tag{5.79}$$

The condition for stability in Eqn. 5.76 is equivalent to:

$$\zeta < 0 \tag{5.80}$$

Therefore, the characteristic exponents λ are used to determine stability of the periodic aeroelastic systems.

5.4.2 Modal identification and coupling

The aeroelastic interactions couple the natural blade modes of a coaxial rotor system. For coaxial rotors, the identification of blade modes using frequency tracking is challenging because upper and lower rotor blades have identical natural frequencies. Several techniques have been developed to identify blade modes of SMRs in forward flight using Floquet analysis [213, 214]. Reference 215 used the dominant components of eigenvectors of the Floquet STM to identify modal damping. In the present study, the modal coupling of the coaxial rotor system is determined using a graphical method based on Ref. 215.

The characteristic multiplier Λ, i.e the eigenvalue of the STM at the end of a period $[\boldsymbol{\Phi}(T,0)]$, has a corresponding eigenvector $\boldsymbol{\xi}$. The entries in the eigenvector $\boldsymbol{\xi}$ are arranged in order of the structural state vector $\boldsymbol{X}_s$. The eigenvectors are normalized such that the l^2-norm is equal to one.

$$\sum_{i=1}^{2n_{\text{dof}}} |\xi_i|^2 = 1 \tag{5.81}$$

The absolute value of each element of the eigenvector indicates the contribution of the structural degree of freedom in the eigenvector [215]. For example, in an uncoupled eigenvector, all entries except one will be zero. However, due to the aeroelastic coupling between modes in coaxial rotors, multiple entries in the eigenvector can be

non-zero, indicating that the corresponding structural states are coupled.

The structural state vector $\boldsymbol{X}_s$ contains both the degrees of freedom $\boldsymbol{a}$ and the rates $\dot{\boldsymbol{a}}$ of the structural deformation. To simplify the identification of blade modes in the eigenvector, the entries corresponding to $\boldsymbol{a}$ and $\dot{\boldsymbol{a}}$ of each structural degree of freedom are combined in a new vector $\boldsymbol{\eta}$, defined as the *reduced eigenvector* form of $\boldsymbol{\xi}$.

$$\eta_{a_i} = \sqrt{|\xi a_i|^2 + |\xi_{\dot{a}_i}|^2} \tag{5.82}$$

Therefore, the l^2-norm of the original eigenvector $\boldsymbol{\xi}$ is preserved for the reduced eigenvector $\boldsymbol{\eta}$. Furthermore, the reduced eigenvector $\boldsymbol{\eta}$ is real. The eigenvalues Λ and eigenvectors $\boldsymbol{\xi}$ appear in pairs of complex conjugates. Therefore, the reduced eigenvector $\boldsymbol{\eta}$ is unique for each complex conjugate pair. The coupling of natural rotating modes can be examined by comparing the relative magnitude of the entries η_a in the reduced eigenvector $\boldsymbol{\eta}$.

A simple example is illustrated by Fig. 5.4. A uniform, untwisted SMR blade at zero collective pitch and zero precone is modeled with $n_F = 3$ flap modes, $n_L = 2$ lag modes, and $n_T = 1$ torsional mode. Therefore, the system has $n_{\text{dof}} = 6$ degrees of freedom. Aerodynamic loads are ignored. Therefore, the system represents free vibrations of a rotating blade.

The reduced eigenvectors $\boldsymbol{\eta}$ are arranged in columns to form a 6×6 matrix as shown in Fig. 5.4. The columns are arranged left to right in increasing order of the frequency ω of the corresponding characteristic exponent. Each cell is colored according to the magnitude of the corresponding entry $|\eta_i|$ in the eigenvector. The intensity of the color indicates the magnitude of the contribution of the mode in the eigenvector.

In this simplified example, each eigenvector represents the natural uncoupled rotating mode of the blade, therefore the reduced eigenvectors are unit vectors. Only the cells corresponding to each mode are colored, indicating that the natural modes are uncoupled. The frequencies for each eigenvector correspond to the natural frequencies of the blade. For example, in Fig. 5.4, the first cell of the first column is colored and the rest of the cells are blank, indicating that the frequency ω_1 corresponds to the first natural rotating flap mode F1. Similarly, the frequency ω_2 corresponds to the first natural rotating lag mode L1. Therefore, the frequencies and damping can be associated with each natural mode. The relative intensity of color in the cells indicates the relative contribution of each natural mode to the eigenvector and depicts the coupling strength in a graphic manner.

The method described works equally well for coaxial rotors. The frequencies and damping of the upper and lower rotor blades are similar because the blades are structurally identical. Therefore, it is difficult to specify the stability characteristics of the upper and lower rotor based on the characteristic exponents alone. The reduced eigenvector matrix helps identify which characteristic exponent corresponds to which rotor. Therefore, the coupling between different modes and rotors can be identified using this graphical method.

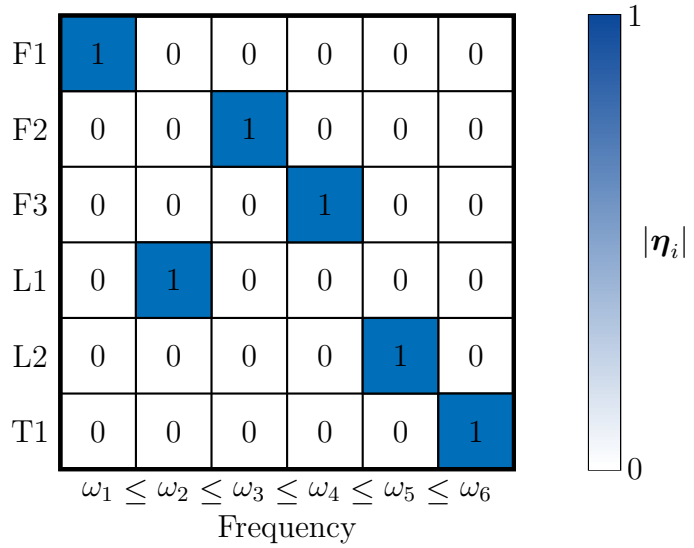

Figure 5.4: Modal identification matrix of an untwisted uniform SMR blade

CHAPTER 6

Results for a Coaxial Rotor in Hover

6.1 Validation with experiments

Table 6.1: UT Austin rotor parameters

Parameter		**Value**
Number of blades	N_b	2
Radius	R	1.016 m
Chord	c	0.076 m
Offset	e	0.122 m
Precone	β_p	3^o
Tip Speed	ΩR	152.146 m/s
Rotor Separation	h	0.14 m

Results were validated with experiments conducted on the UT Austin model rotor in hover [39]. The rotor parameters are given in Table 6.1. The blades are untwisted, and have a constant chord and thickness distribution. The calculations assume a rigid rotor, i.e. the structural deformation is ignored. The hover performance is measured in terms of the rotor thrust coefficient C_T and torque coefficient C_Q. For coaxial rotors, the thrust and torque coefficients are:

$$C_T = (C_{F_Z})_u + (C_{F_Z})_l \tag{6.1}$$

$$C_Q = |(C_{M_Z})_u| + |(C_{M_Z})_l| \tag{6.2}$$

Periodic convergence was achieved within five revolutions for both the SMR and coax-

ial rotors. The change in mean thrust and torque coefficients between the last two revolutions was less than 1%. The azimuthal step size was 12^o. SMR calculations for 6 revolutions were completed in under 5 minutes, whereas computations for coaxial rotors took 15 minutes on a desktop computer with eight Intel Xeon(R) E5440 processors. Approximately 14,400 particles were present at the end of the coaxial computations. Additional increase in the number of generated particles did not produce any significant change in the loads results.

The sensitivity of the coaxial rotor load calculations to the azimuthal step size was evaluated. The blade pitch angles were set at $\theta_0 = 10^o$. The simulations were run for 8 revolutions. For an azimuthal step size of $\Delta\psi = 6^o$, the number of particles exceeded $N_p = 550,000$ at the end of the simulation. For the azimuthal step size of $\Delta\psi = 12^o$, the number of particles at the end of the simulation was approximately $N_p = 220,000$. When comparing the two step size calculations, the error in the vertical force and moment was under 0.8% and 0.2% respectively. An examination of the vortex particle wake revealed that large number of particles were concentrated in the initial vortex shed by the blades. This region undergoes the greatest amount of vortex stretching, however it is located a distance of one rotor diameter below the blades. Therefore particles in this region have minimal effect on blade loads. In studies such as Refs. 93 and 94, particles beyond a fixed wake cutoff distance, typically the rotor diameter, are deleted for computational efficiency. The simulations presented in the validation study retain all particles to prevent any artificial wake distortion.

The comparison of the experimental data and VVPM calculations is shown in Fig. 6.1. There is excellent correlation between the calculations and experimental data. There is a small deviation from the experimental data at higher thrust coefficients for the SMR. This may be due to structural deformation effects which are ignored in the

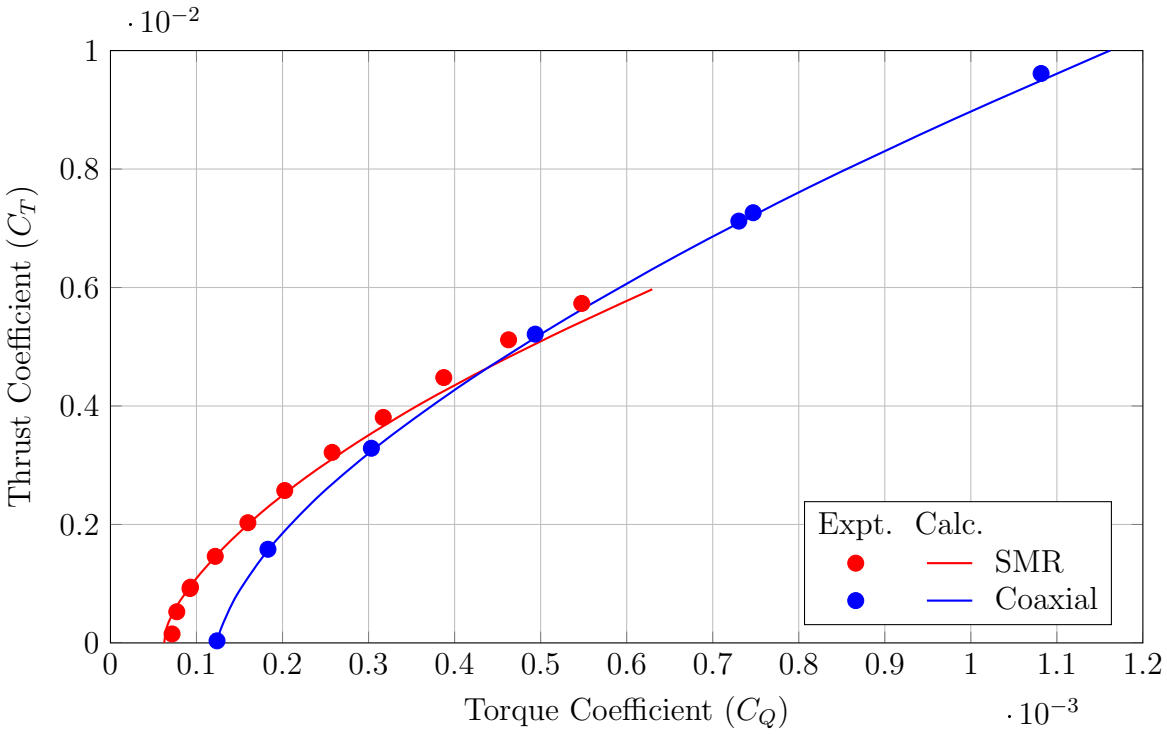

Figure 6.1: Comparison of experimental thrust and torque coefficient for SMR and coaxial rotors with VVPM calculations

validation calculations. As thrust of the SMR increases, the increased blade loading results in larger structural deformation which modifies the thrust and torque. For a coaxial rotor, the thrust of each individual rotor is decreased compared to the SMR due to the interaction effects. Therefore, even at higher total thrust, the individual blade loading is small compared to the SMR. Hence, structural deformation effects are small and do not affect the thrust and torque of the coaxial rotor.

6.2 Rotor blades resembling the Sikorsky X2TD

The results presented in this dissertation are based on a rotor resembling the X2TD. The blade geometry, mass and stiffness distribution were selected to resemble the properties of the X2TD published in open literature [46]. Table 6.2 provides the rotor properties. Figures 6.2a and 6.2b show the geometry of the X2TD blade.

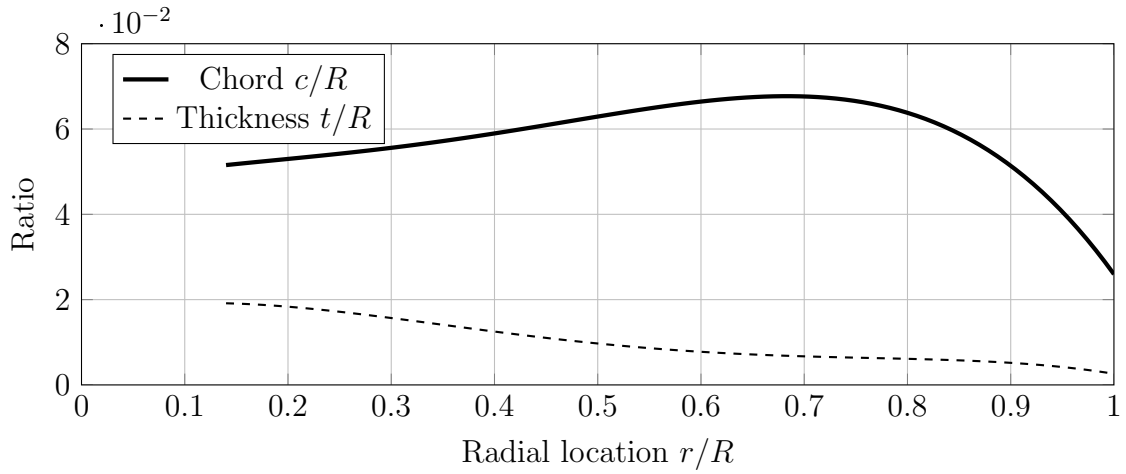

(a) Chord and thickness

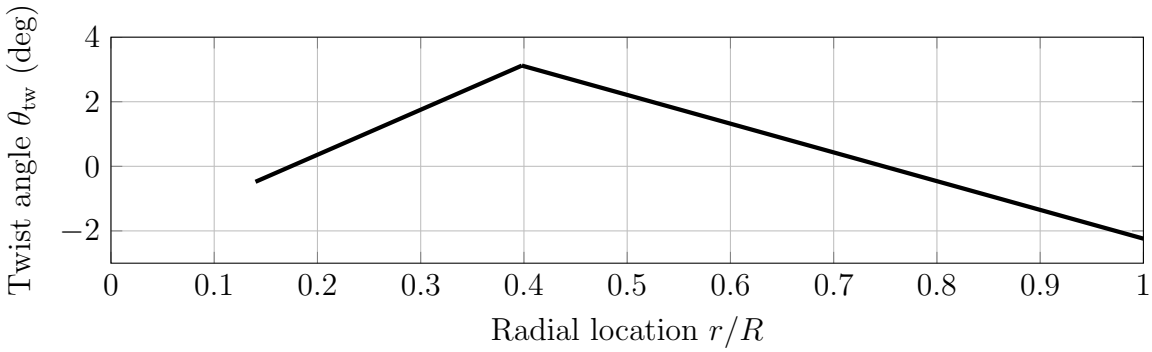

(b) Twist

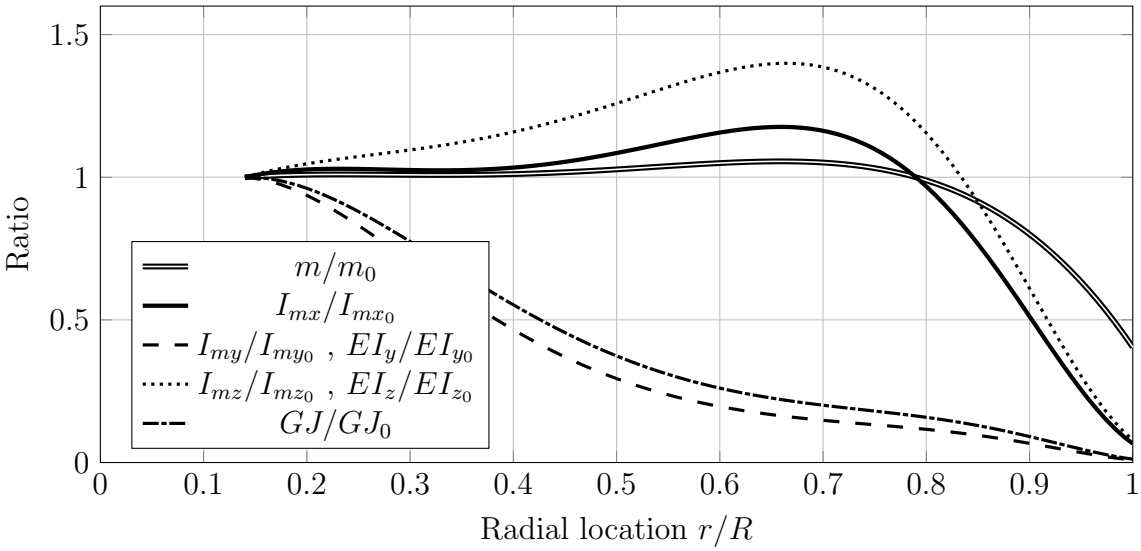

(c) Inertia and stiffness

Figure 6.2: Spanwise distribution of blade properties

Table 6.2: Parameters of model rotor resembling X2TD

Parameter	**Value**
Ω	450 RPM
β_p	3.0^o
e/R	14%
R	4.0 m
m_o	6.05 kg/m
I_{my_o}	7.4×10^{-3} kg.m
I_{mz_o}	3.3×10^{-2} kg.m
EI_{y_o}	9.24×10^4 kg.m^2
EI_{z_o}	2.25×10^5 kg.m^2
GJ_o	7.42×10^4 kg.m^2

The X2TD has composite blades, however the material properties and structural data are not available in open literature. Therefore, the material properties are assumed to be linearly elastic and homogeneous. The calculated spanwise distribution of mass and stiffness properties are illustrated in Fig. 6.2c.

The blade properties at the root are determined by matching the first flap, lag and torsion frequencies to known values provided in Ref. 47. The calculated blade frequencies at hover RPM are shown in Table 6.3. The structural model is based on 3 rotating flap modes, 2 rotating lag modes and 1 torsional mode ($n_F = 3$, $n_L = 2$, $n_T = 1$). The number of modes were selected such that all modes with natural frequencies below 10/rev were included and the rest were ignored. The Southwell plot shown in Fig. 6.3 illustrates the effect of rotor RPM on the blade natural frequencies. The blade frequencies are normalized with respect to the rotor RPM at hover Ω_0.

$$\overline{\omega} = \frac{\omega}{\Omega_0} \tag{6.3}$$

The X2TD rotor hover simulations were run for 15 revolutions to allow the wake to achieve periodic convergence. A total of approximately $N_p = 44,000$ particles

Table 6.3: Calculated rotating blade natural frequencies

Mode		Frequency (/rev)
Flap 1	$\overline{\omega}_{F1}$	1.40
Flap 2	$\overline{\omega}_{F2}$	3.89
Flap 3	$\overline{\omega}_{F3}$	8.39
Lag 1	$\overline{\omega}_{L1}$	1.54
Lag 2	$\overline{\omega}_{L2}$	9.24
Torsion 1	$\overline{\omega}_{T1}$	9.5

were used in each simulation. The visualization of the vortex particles in the wake is shown in Fig. 6.4. The upper rotor blades are shaded blue. The lower rotor blades are shaded red. The particles are represented by arrows. The arrow points is in the direction of the vorticity of each particle. The length and color of the arrow represent the magnitude of the vorticity strength $|\boldsymbol{\alpha}_p|$.

The principal feature of the coaxial rotor wake is the helical tip vortex structure emanating from the upper and lower rotor. The vortex particles collect into a wide vortex ring structure several rotor radii below the hub. In most free wake analyses, vortex particles beyond 1 rotor diameter from the hub are deleted because they have negligible effect on the rotor hub loads. However, the vortex ring is required to maintain the tip vortex helical structure near the rotor. Therefore, vortex particles were retained for 5 revolutions after which they were assumed to have dissipated.

6.3 Rotor hub loads

In Fig. 6.5, the thrust coefficient C_T of the coaxial rotor resembling the X2TD is plotted with respect to the mean collective pitch θ_0 at yaw trim. The collective pitch setting was varied between $\theta_0 = 8^o$ and $\theta_0 = 15^o$. The results in Fig. 6.5 indicate that the upper rotor thrust is always greater than the lower rotor thrust. The upper rotor shares approximately 53% - 55% of the total thrust, which is consistent with exper-

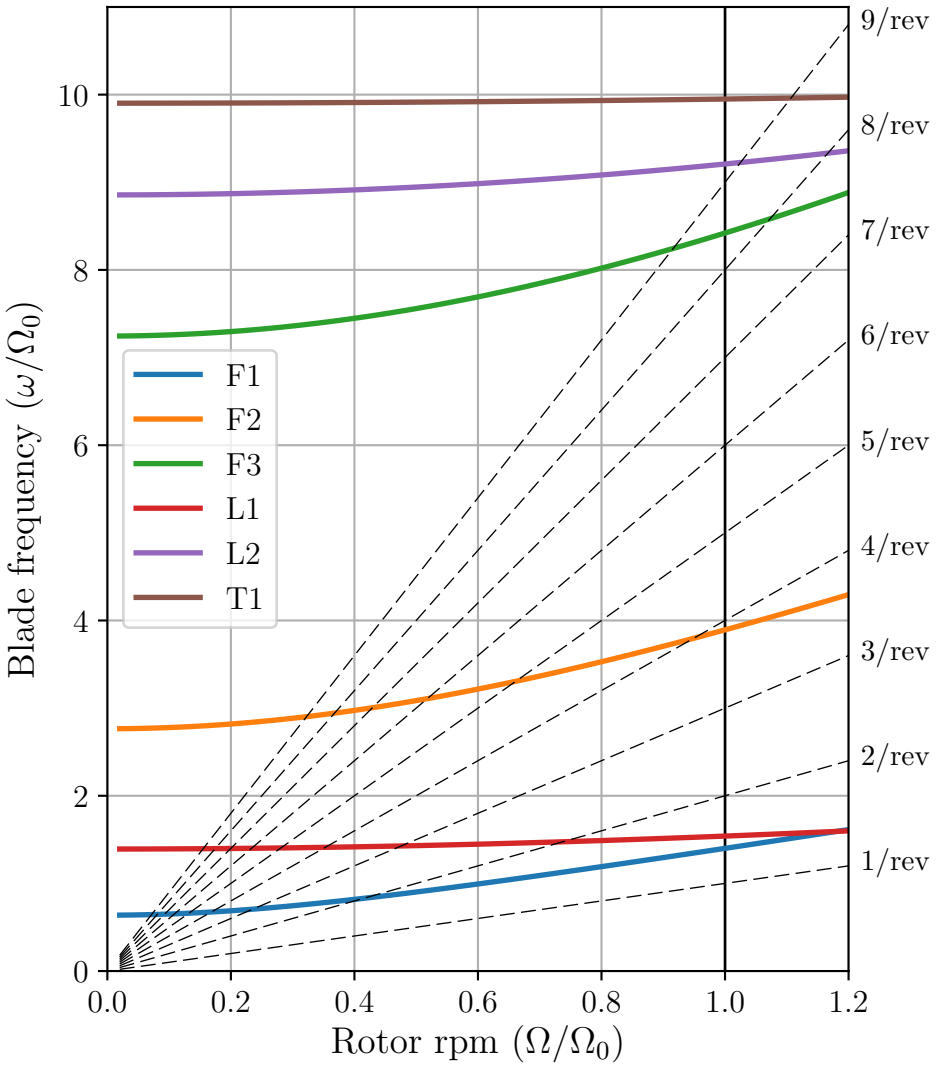

Figure 6.3: Variation of blade natural frequencies with rotor RPM, $\theta_0 = 0.0^o$

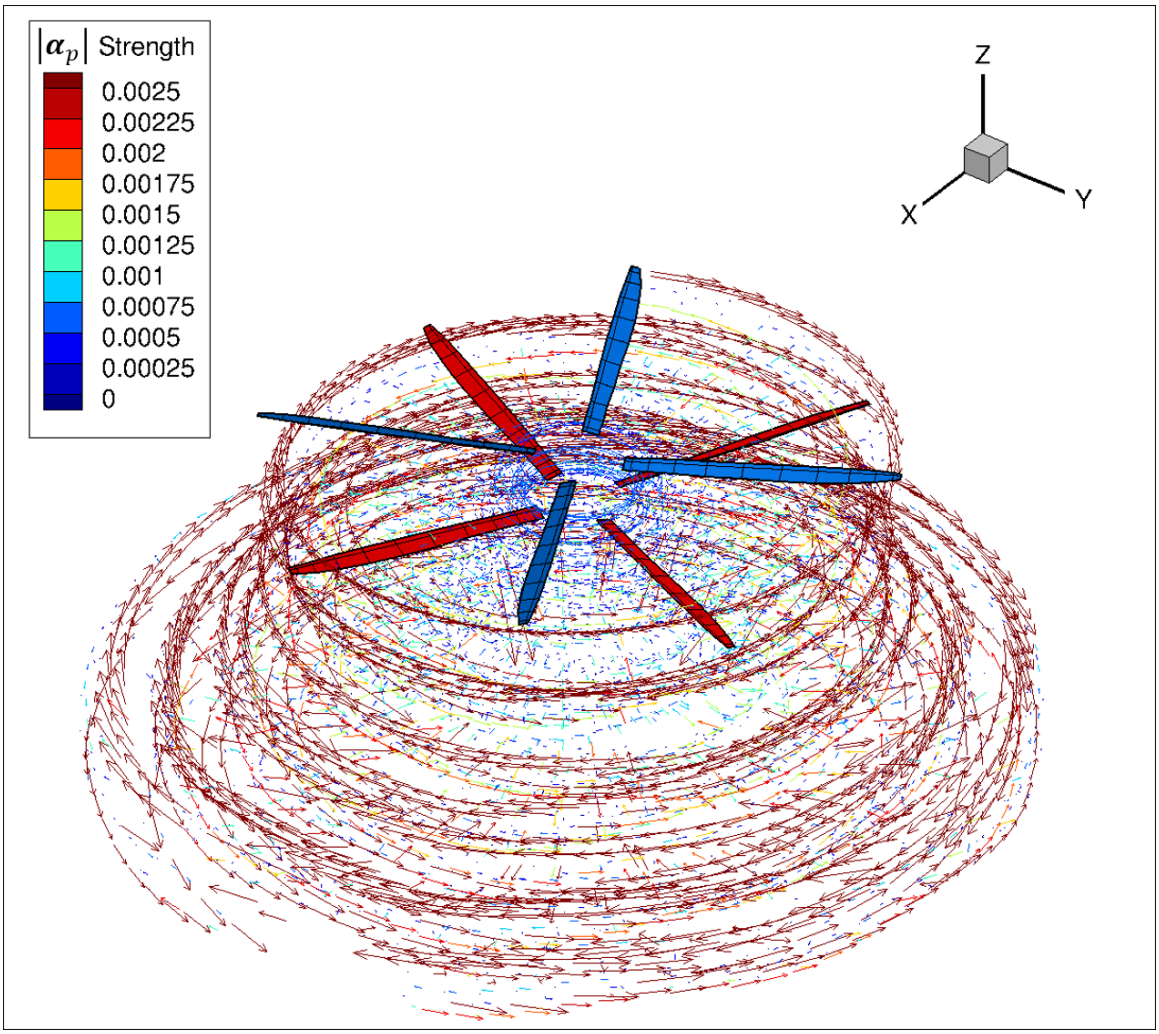

Figure 6.4: Coaxial rotor wake visualization in hover

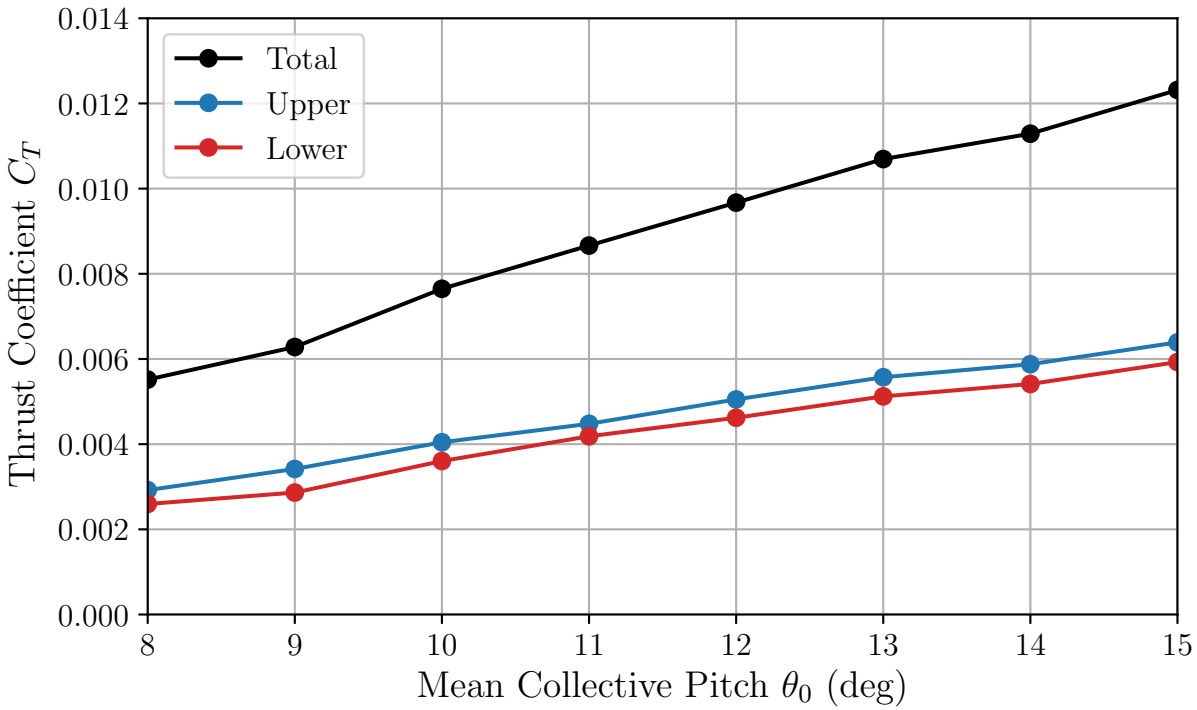

Figure 6.5: Effect of mean collective pitch on coaxial rotor thrust coefficient in hover

imental observations for other coaxial rotors [37, 122]. The thrust sharing remains nearly constant at different total thrust levels. The weight coefficient of the X2TD is $C_W = 0.01$. Therefore, hover trim is achieved at a collective pitch of approximately $\theta_0 = 12.4^o$.

The coaxial rotor thrust over a revolution is shown in Fig. 6.6. The thrust oscillates 8 times in every revolution due to the blade passage effect. Both the upper and lower rotors experience the thrust oscillations due to blade passage. The blades pass each other at every integer multiple of $\psi = 45^o$. The thrust decreases sharply when the blades cross each other, and then steadily increases till the next blade passage. The oscillations in the upper and lower rotor thrust are in phase. The peak-to-peak magnitude of the oscillation in the total thrust is nearly 20% of the mean thrust. The upper rotor thrust is greater than the lower rotor thrust indicating that the blade passage effect does not affect the upper and lower rotor identically.

In Fig. 6.7, the magnitude of the 8/rev oscillations in vertical hub force ΔC_{F_z} is plotted with respect to the mean total thrust coefficient C_T. As the thrust increases the magnitude of the oscillations increases. Note that the oscillations in the lower rotor vertical hub force are always greater than the upper rotor. Therefore, even though the lower rotor produces less mean thrust than the upper rotor, the oscillations in the lower rotor vertical hub force are greater than the upper rotor.

$$(C_{F_Z})_l < (C_{F_Z})_u \tag{6.4}$$

$$(\Delta C_{F_Z})_l > (\Delta C_{F_Z})_u \tag{6.5}$$

These differences in the rotor loads are a consequence of the inflow distribution over the coaxial rotor in hover.

6.4 Inflow distribution

The inflow distribution affects the thrust and torque of the coaxial rotor. The inflow velocity $\boldsymbol{U}^J$ is induced by the vortex particles in the wake $\boldsymbol{U}^J_W$ and the blade bound circulation $\boldsymbol{U}^J_B$. Both components have different characteristics and influence the blade loads differently.

The mean inflow (averaged over a revolution) at a radial location due to the wake and the blade bound circulation is shown in Fig. 6.8. The vertical component of the inflow U_Z is normalized with the tip speed ΩR. The mean wake induced inflow is greater than the blade bound circulation induced inflow at all collective pitch settings.

$$U^J_{W_Z} > U^J_{B_Z} \tag{6.6}$$

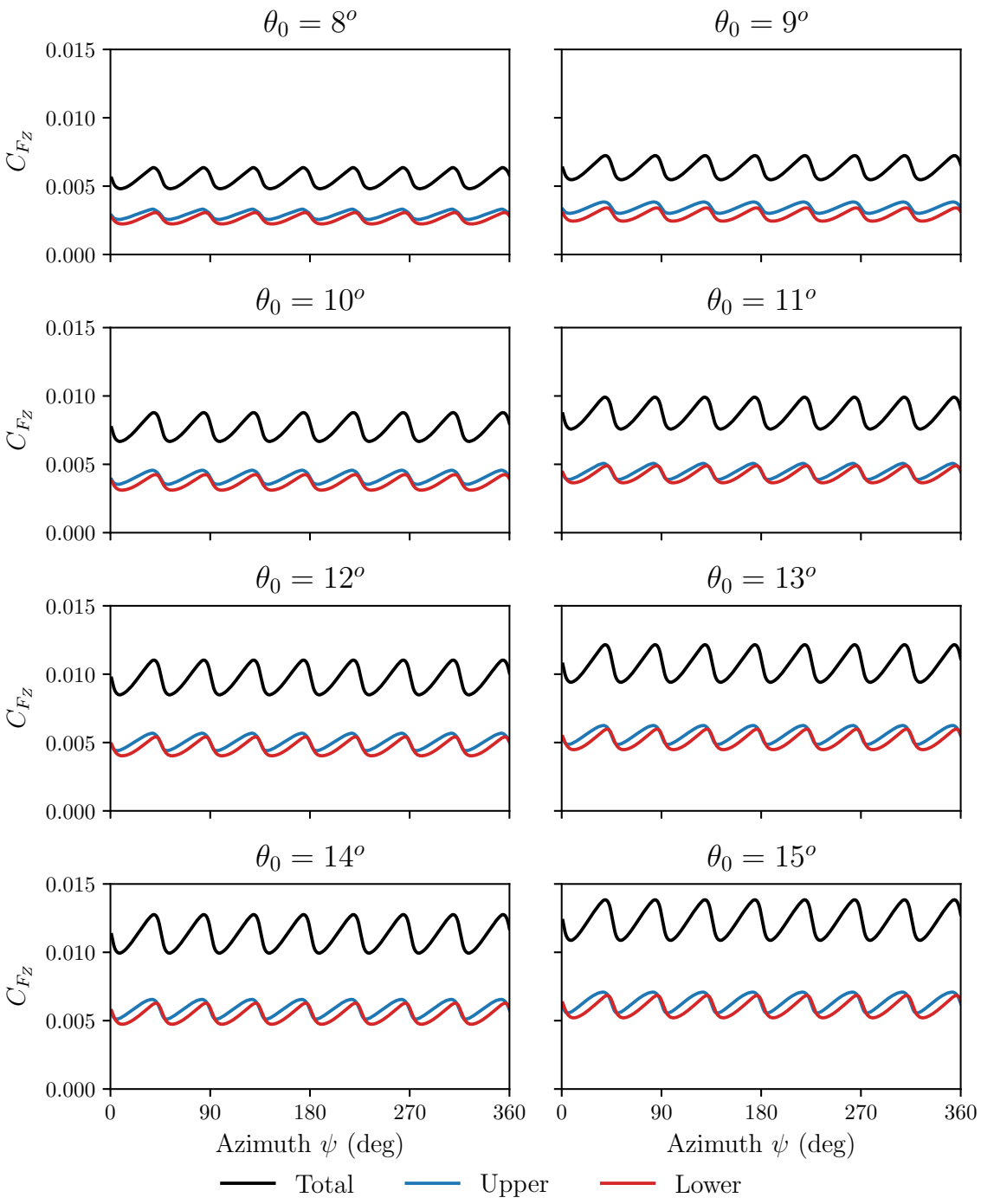

Figure 6.6: Coaxial rotor thrust in hover

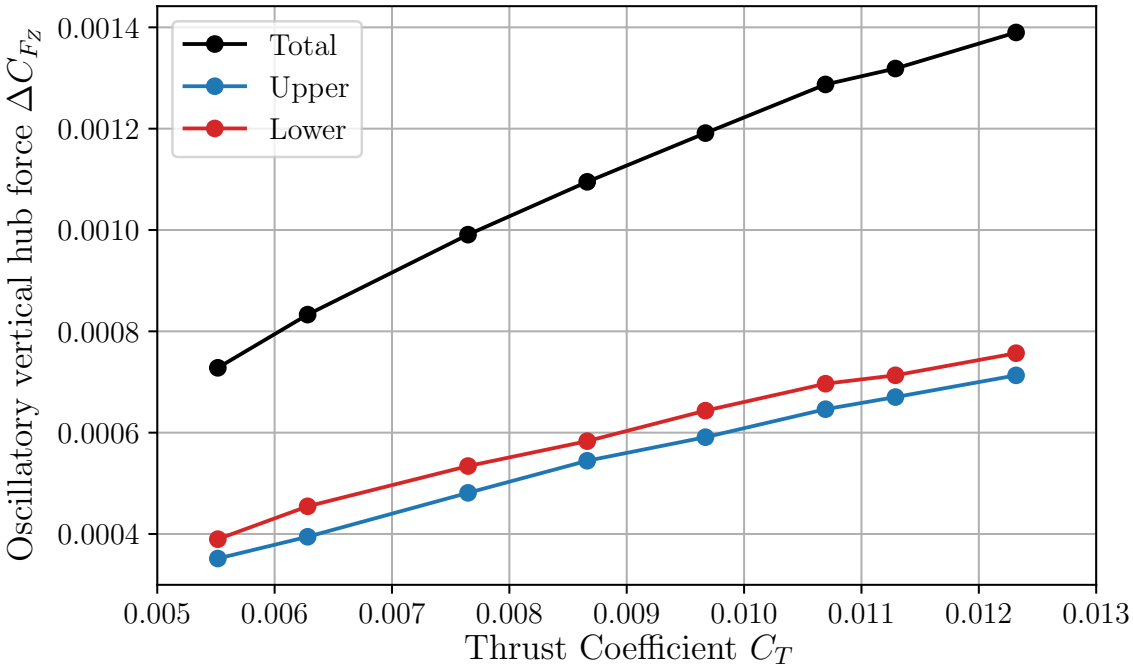

Figure 6.7: Oscillatory vertical hub force for a coaxial rotor in hover

The wake induced inflow is larger for the lower rotor compared to the upper rotor at all collective pitch settings.

$$\left(U^J_{W_Z}\right)_l > \left(U^J_{W_Z}\right)_u \tag{6.7}$$

The bound circulation induced inflow is almost the same for the two rotors. Therefore, the smaller mean thrust of the lower rotor is due to a larger wake induced inflow compared to the upper rotor. The wake induced inflow increases with increase in collective pitch. However, the blade bound circulation induced inflow does not change significantly with increase in collective pitch.

The oscillations in the vertical hub force due to the blade passage effect are caused by the oscillations in the inflow. The oscillatory wake and blade bound circulation induced inflow at a collective pitch of $\theta_0 = 12^o$ are shown in Fig. 6.9. A different color scale is used for the wake induced and bound circulation induced inflow to distinguish the two components. The intensity of the color indicates the magnitude of

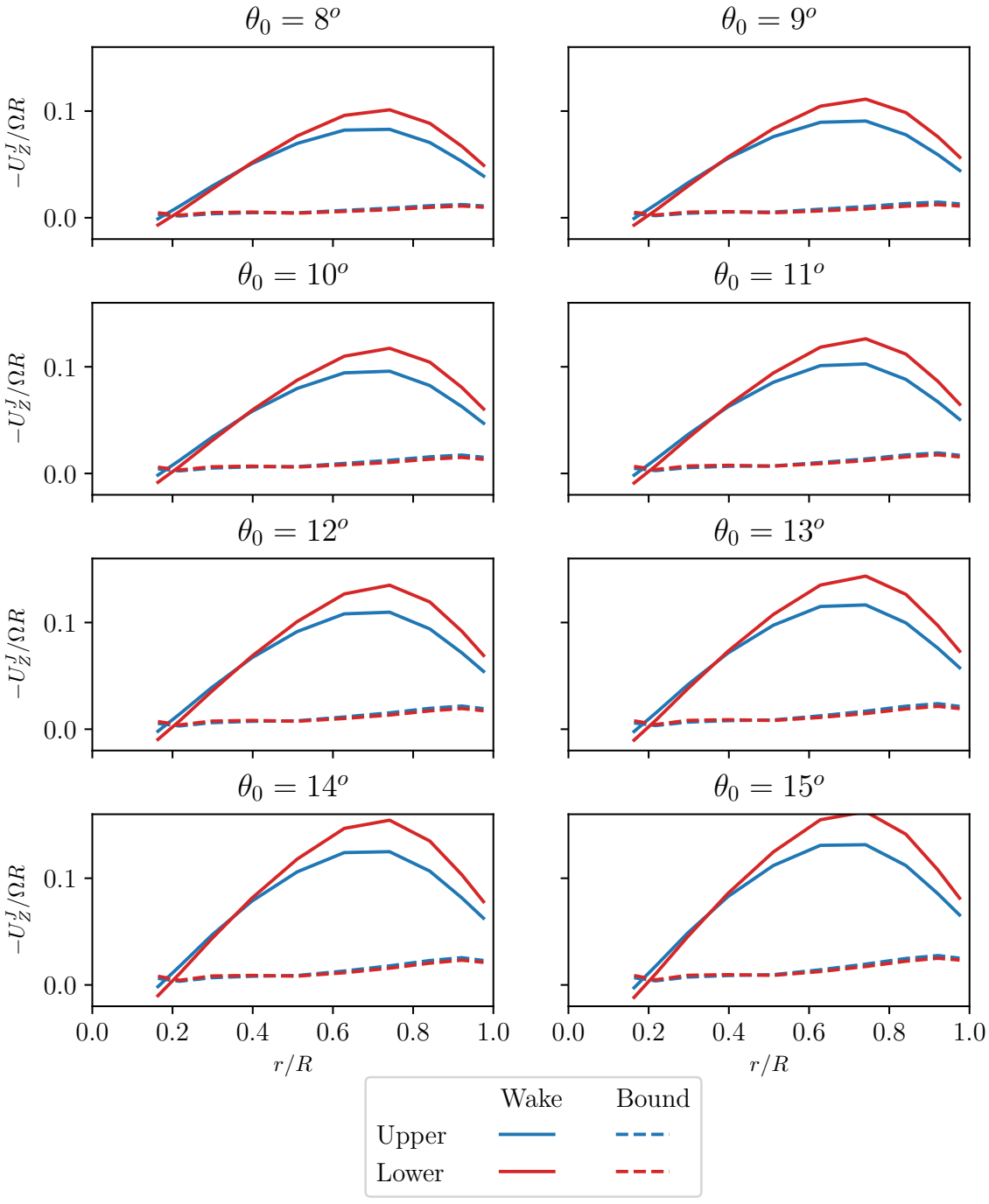

Figure 6.8: Mean coaxial rotor inflow distribution in hover

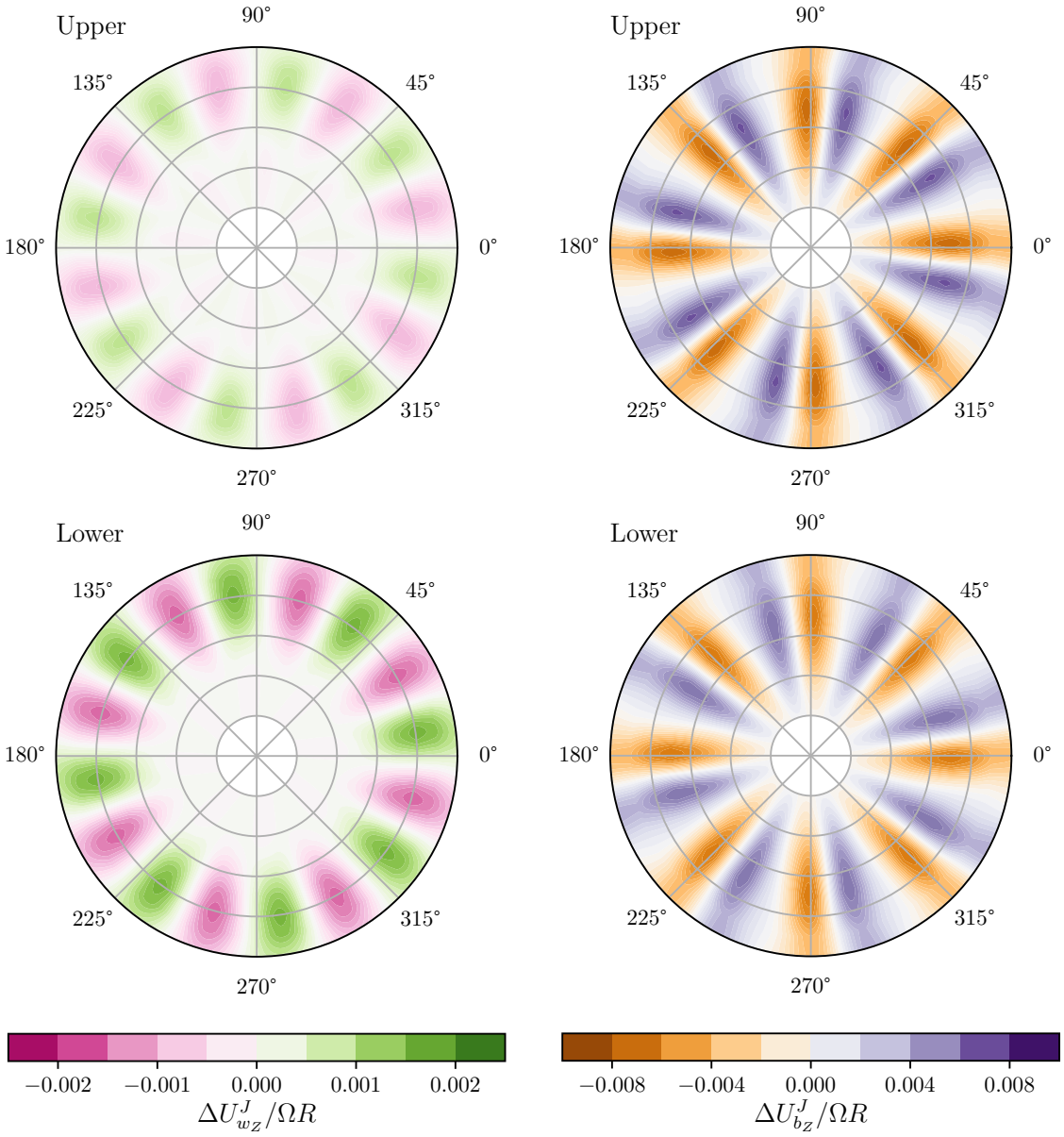

(a) Wake induced inflow $\Delta \boldsymbol{U}_W$ (b) Bound circulation induced inflow $\Delta \boldsymbol{U}_B$

Figure 6.9: Oscillatory inflow on a coaxial rotor in hover ($\theta_0 = 12^o$)

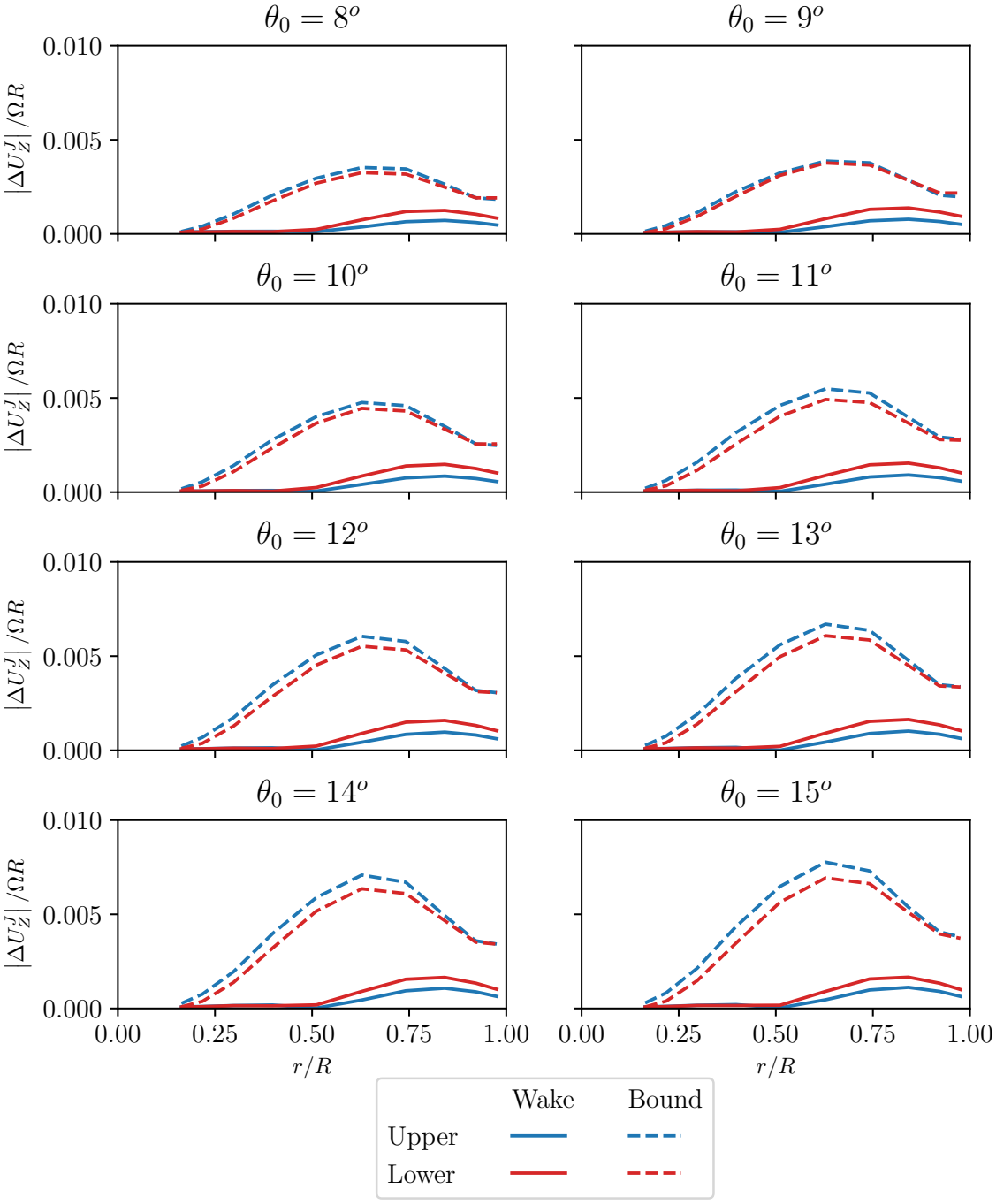

Figure 6.10: 8/rev coaxial rotor inflow distribution in hover

the oscillations. The change in induced velocity is normalized with respect to the tip speed. The inflow distribution repeats at intervals of $\Delta\psi = 45^o$, giving rise to the 8/rev oscillations in thrust. The upper and lower rotor are counter-rotating, therefore the azimuthal distribution of the inflow on the two rotors is in opposite directions.

The oscillations in the wake induced inflow $\Delta U^J_{W_Z}$ (Fig. 6.9a) are reduced by a factor of four compared to the blade bound circulation induced inflow $\Delta U^J_{B_Z}$ (Fig. 6.9b). In Fig. 6.9a, the effects of the oscillatory wake induced inflow are concentrated in the outboard region near the $80\%R$ radial location. However, in Fig. 6.9b, the oscillations are uniformly distributed over the blade. Due to the larger magnitude of oscillations and a uniform spanwise distribution, the blade bound circulation induced inflow is more effective in modifying the blade loads when compared to the wake induced inflow. Therefore, the blade passage effect in hover is primarily a result of the blade bound circulation induced inflow.

The magnitude of the 8/rev oscillations in inflow ΔU^J_Z over the blade span is shown in Fig. 6.10. The 8/rev oscillations in the inflow are an order of magnitude smaller compared to the mean inflow in Fig. 6.8. In Fig. 6.10, the oscillations in the bound circulation induced inflow are greater compared to the wake induced inflow.

$$\Delta U^J_{B_Z} > \Delta U^J_{W_Z} \tag{6.8}$$

The radial distribution of the oscillatory inflow indicates that the wake effects are negligible for the inner region of the blade $r < 50\%R$, as shown earlier in Fig. 6.9a. The oscillatory blade bound circulation induced inflow has a maximum at approximately $r = 70\%R$. The location of maximum oscillatory bound circulation induced inflow does not change with collective pitch.

At low collective pitch $\theta_0 < 10^o$, the difference in the upper and lower rotor oscillatory bound circulation induced inflow is very small. As the collective pitch increases, the oscillations in the upper rotor bound circulation induced inflow are greater than the lower rotor.

$$\left(\Delta U^J_{B_Z}\right)_u > \left(\Delta U^J_{B_Z}\right)_l \tag{6.9}$$

However, for the wake induced inflow, the effect is opposite. The lower rotor oscillatory wake induced inflow is always greater when compared to the upper rotor.

$$\left(\Delta U^J_{W_Z}\right)_l > \left(\Delta U^J_{W_Z}\right)_u \tag{6.10}$$

Therefore, the effects of the inflow distribution on the vertical hub force can be summarized as follows: First, the mean rotor thrust C_T is primarily affected by the wake induced inflow U_{W_Z}. Second, the lower rotor experiences larger wake induced inflow, and therefore the lower rotor mean thrust is smaller compared to the upper rotor. Third, the 8/rev blade passage loads are primarily caused by the oscillations in blade bound circulation inflow. Fourth, the oscillatory wake induced inflow increases the magnitude of the 8/rev loads on the lower rotor.

6.5 Aeroelastic stability analysis

6.5.1 Stability

The STM of the coaxial rotor in hover was calculated using the single-pass method with a period of $1/8^{\text{th}}$ of a revolution due to the blade passage effect. The characteristic exponents of the STM were calculated to determine system stability. In Fig.

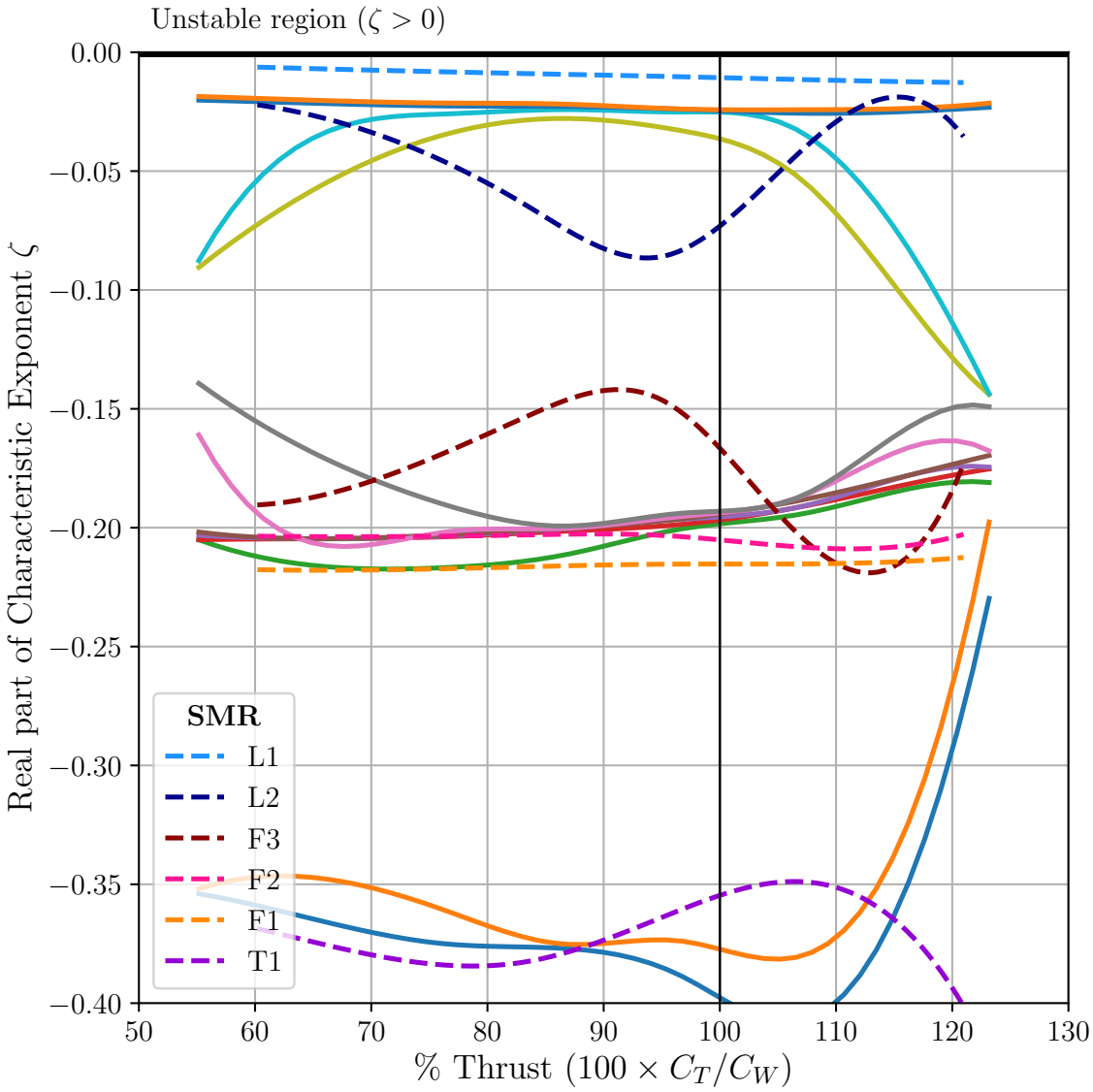

Figure 6.11: Effect of thrust on aeroelastic stability of coaxial rotor in hover

6.11, the real part of the characteristic exponent is plotted with respect to the rotor thrust. The rotor thrust is normalized with respect to the weight coefficient C_W. There are 12 characteristic exponents because the upper and lower rotor blades have 6 structural degrees of freedom each. Each characteristic exponent is plotted with a solid line of a different color. Note that the modes cannot be identified without examining the eigenvectors. All modes are stable because the real part of the characteristic exponent is negative at all thrust levels.

The stability results are compared with a SMR with same blades as used in the coaxial rotor. The SMR is axisymmetric in hover, therefore constant coefficient linear stability analysis can be applied. The thrust for the SMR is normalized with respect to half the weight of the X2 helicopter. In Fig. 6.11, the SMR results are plotted using dashed lines. The SMR modes are identified from the frequency ω i.e. the imaginary part of the eigenvalue. The first lag mode $L1$ (dashed light blue line) is the least stable. Note that the two least stable coaxial modes are located below the SMR $L1$ modes. Therefore, these are the upper and lower rotor $L1$ modes. The stability of the upper and lower rotor first lag modes is the same at all thrust levels. However, the magnitude of the real parts of the characteristic exponent of the first lag modes for a coaxial rotor are nearly double that of the SMR. Therefore, the coaxial rotor aerodynamic loads increase the damping of the first lag modes compared to the same blade in a SMR in hover.

Increasing the thrust modifies the stability margins of the blade modes. Between 75% - 105% thrust, the four least stable coaxial modes have nearly the similar stability margin. At 120% thrust, all modes other than the first two lag modes, move towards a value of $\zeta = -0.15$. This occurs because of the large collective pitch of $\theta_0 = 15.0^o$ required for 120% thrust. Increasing the collective pitch changes the flap $\overline{EI}_y$ and

lag $\overline{EI}_z$ stiffness of the blade as described in the structural model (Eqns. 2.35-2.36). Therefore, the elastic coupling between the flap and lag modes increases with collective pitch and affects the real part of the characteristic exponent. The rotor-wake interactions in a SMR are reduced compared to a coaxial rotor and a smaller collective pitch ($\theta_0 = 12^o$) is required for 120% thrust. Therefore, the elastic coupling is not significant at 120% thrust.

6.5.2 Modal coupling

The identification and coupling of modes is examined in Fig. 6.12. The reduced eigenvectors $\boldsymbol{\eta}$ of the STM are arranged in columns to form a matrix. Each eigenvector is labeled on the horizontal axis with the real part of the corresponding characteristic exponent ζ. Each horizontal row in the matrix corresponds to a particular rotating mode shape. The first six rows are the flap, lag and torsional modes of the upper rotor, and the next six rows are the same information for the lower rotor. The columns are arranged left to right in order of decreasing stability as represented by the real part of the characteristic exponent. The intensity of the color in the appropriate square is proportional to the magnitude of each entry η_i evaluated from Eqn. 5.82. In any given column in the matrix, colored squares indicate the presence of coupling and blank squares indicate lack of coupling. The intensity of the colors in a given column reflects the relative magnitude of the coupling between the appropriate modes.

In Fig. 6.12a, the reduced eigenvector matrix is presented for a collective pitch of $\theta_0 = 10^o$. For each eigenvector, multiple entries in the column are colored, indicating that the modes are coupled. The least stable modes ($\zeta = -0.021, -0.023$) are the two right most columns of the matrix. They are dominated by the first lag modes of the upper and lower rotor respectively. The first two eigenvectors ($\zeta = -0.375, -0.361$) are coupled torsion, third flap and second lag modes, for the upper and lower rotor.

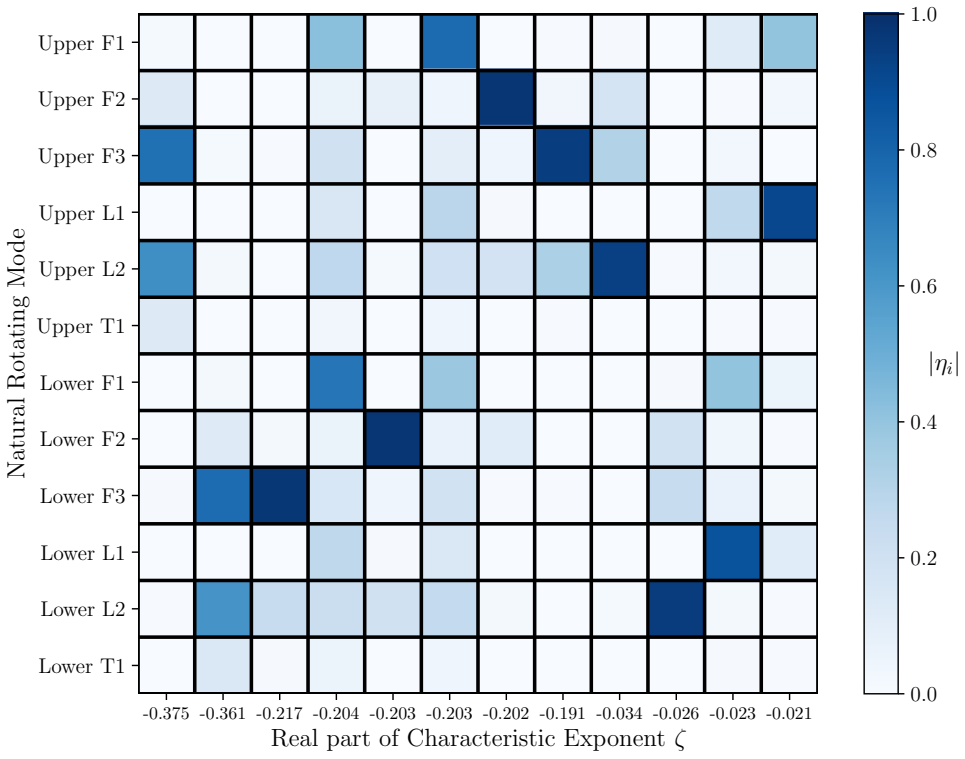

(a) $\theta_0 = 10^o$

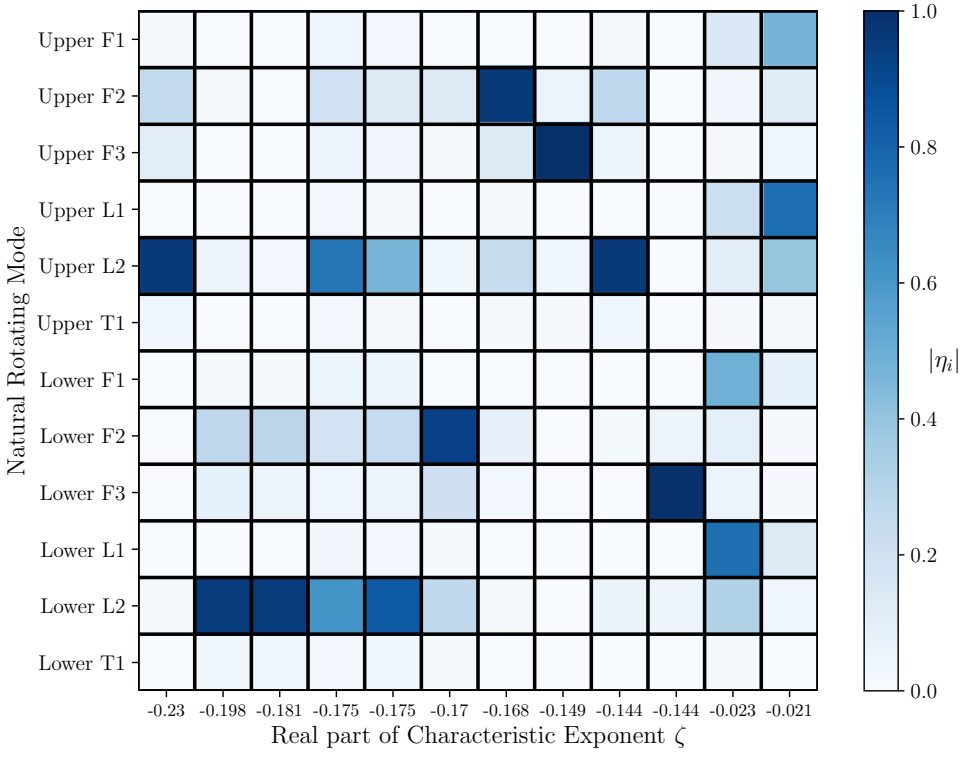

(b) $\theta_0 = 15^o$

Figure 6.12: Modal coupling for a coaxial rotor in hover

The magnitude of the real parts of the characteristic exponent among all eigenvectors that are high values are the coupled torsion - third flap - second lag modes, and these are the most stable.

The fourth and sixth eigenvectors ($\zeta = -0.204, -0.203$) in Fig. 6.12a are the coupled upper and lower rotor first flap modes. The inter-rotor coupling is interesting because it is due to aerodynamic interactions captured by the wake and blade inflow distribution. Note that the structural model of the hub is not included. Therefore there is no transfer of inertial and elastic forces between the two rotors, yet the eigenvectors indicate that the aeroelastic modes of the two rotors are coupled.

The modal coupling at the collective pitch of $\theta_0 = 15^o$ is examined in Fig. 6.12b. The real parts of the characteristic exponents of the two least stable modes ($\zeta = -0.023, -0.021$) have not changed, however the coupling between the first lag mode and first flap mode has increased. In Fig. 6.12a, the third least stable mode ($\zeta = -0.026$) is dominated by the second lag mode of the lower rotor. However, at $\theta_0 = 15^o$ in Fig. 6.12b, the third least stable mode ($\zeta = -0.026$) is dominated by the third flap mode of the lower rotor.

An interesting inter-rotor coupling is evident at $\theta_0 = 15^o$ in Fig. 6.12b. The fourth and fifth eigenvectors ($\zeta = -0.175, -0.175$) are coupled upper and lower rotor second lag modes. Due to the larger collective pitch angle, the aerodynamic lift and drag are increased at each blade section and increase the coupling between the upper and lower rotor. As mentioned previously, the inter-rotor coupling is interesting because it is purely due to aerodynamic interactions.

Therefore, increasing the collective pitch and rotor thrust changes the aeroelastic

stability and coupling of coaxial rotor blades. The first lag modes are the least stable at all levels of thrust calculated in this study. Other blade modes have a non-linear response to collective pitch, however they remain well below the stability margin.

CHAPTER 7

Results for a Coaxial Rotor in Forward flight

Forward flight results for the X2TD like coaxial rotor were calculated at advance ratios of $\mu = 0.3 - 0.5$ and a fixed LO of 0.3. The effect of LO was examined by varying it between LO = 0.2 and LO = 0.4 at fixed advance ratios of $\mu = 0.3$ and $\mu = 0.5$. The range of LO is based on previous studies [124, 201]. The forward flight results converged quickly compared to hover calculations because the wake is swept away from the rotor in forward flight as shown in Fig. 7.1. Converged periodic response was obtained in 5 revolutions. Previous studies have indicated that 2 revolutions are sufficient for converged results [123]. In forward flight, vortex particles are convected away from the rotor. Due to the large distance from the rotor, their influence on rotor loads can be considered to be negligible. Reference 93 indicates that a wake cutoff distance of 2 rotor radii from the hub is sufficient for SMR calculations. In this dissertation, a more conservative cutoff distance of 2 rotor diameters ($= 4R$) from the rotor hub is selected. Approximately $N_p = 31,000$ particles were used in each simulation. The azimuthal step size was reduced to $\Delta\psi = 3^o$ to capture the high frequency response of unsteady blade loads.

In Fig. 7.1, the wake structure is symmetric about the $\boldsymbol{X} - \boldsymbol{Z}$ plane. The strongest vortex particles (colored red) are generated from the blade tip. Weaker vortex particles (colored blue) are shed from the inner portion of the blade. However,

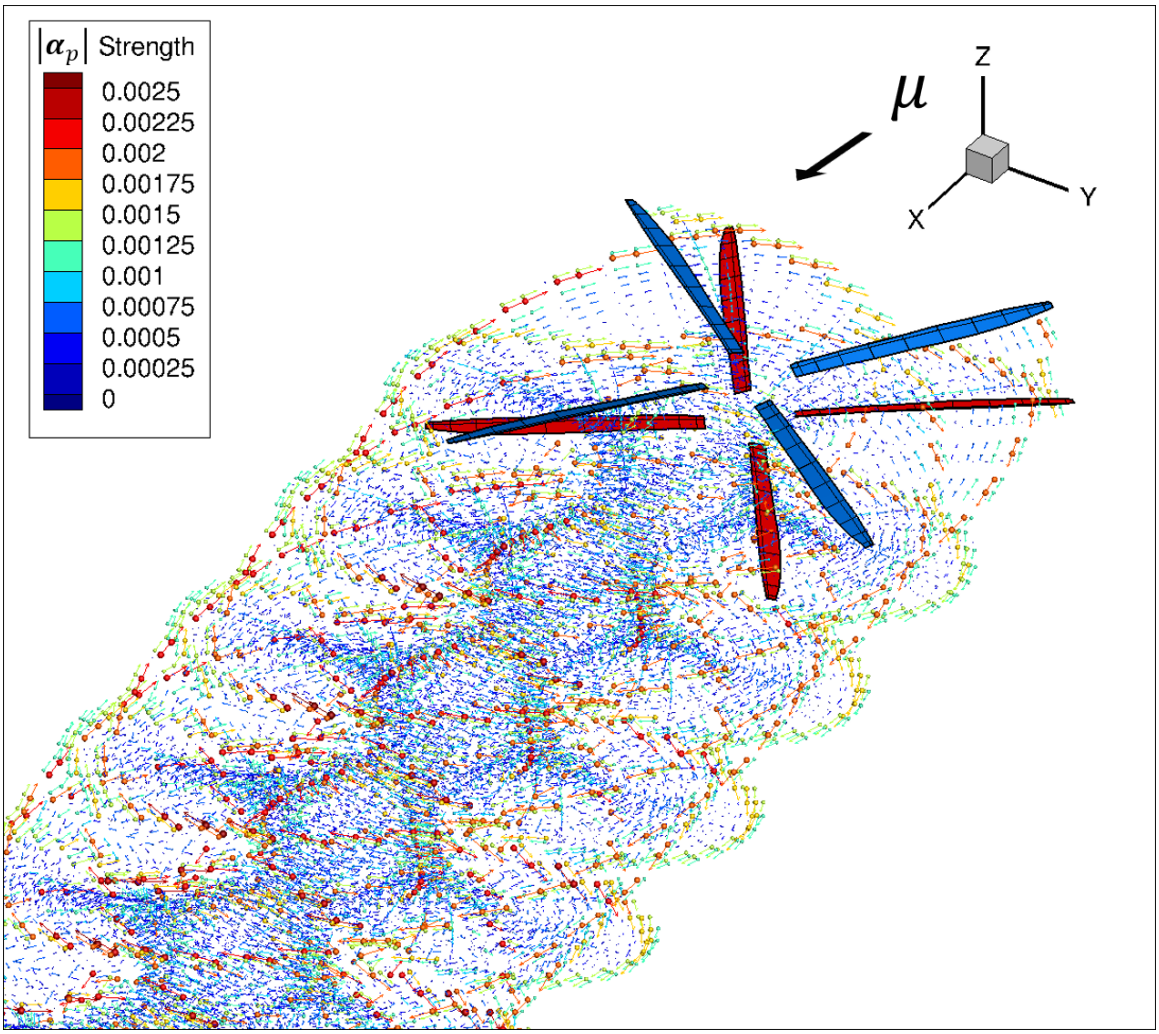

Figure 7.1: Coaxial rotor wake visualization in forward flight ($\mu = 0.4$)

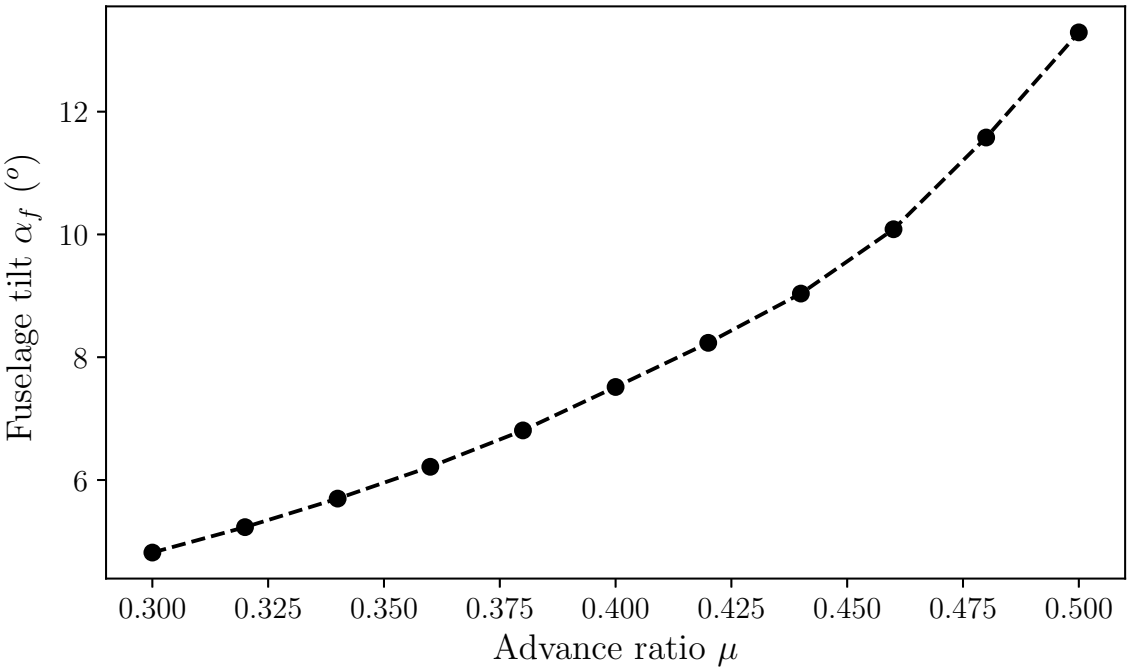

Figure 7.2: Fuselage tilt for a coaxial rotor in forward flight with propulsor off

there are some strong vortex particles that are shed near the hub due to the separated wake in DS, and high angles of attack near the reverse flow region. There are strong interactions between the vortex particles and blades in the inner region of the rotor that are difficult to discern from the wake visualization only. Therefore, the effects of the complex coaxial rotor wake structure on the trim, rotor hub loads, inflow distribution and aeroelastic stability are studied in detail in the following sections.

7.1 Trim results

The control inputs in forward flight were calculated using the propulsor off (Sec. 5.3.2.1) and level attitude (Sec. 5.3.2.2) trim procedures. The effect of advance ratio and LO are examined separately.

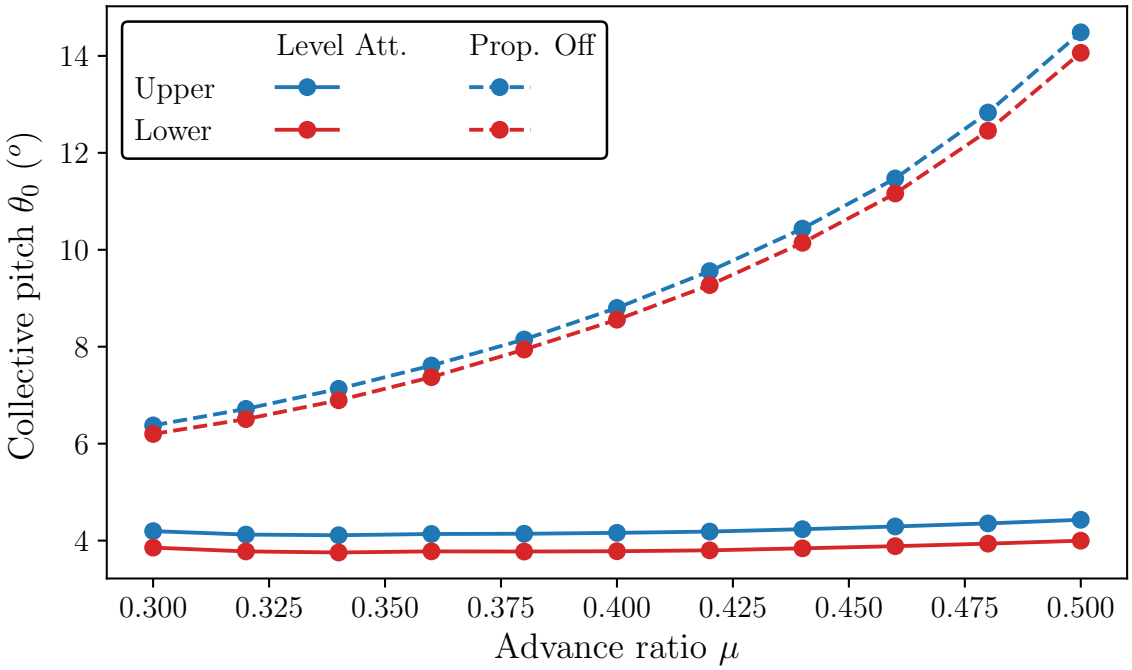

Figure 7.3: Collective pitch inputs for a coaxial rotor in forward flight

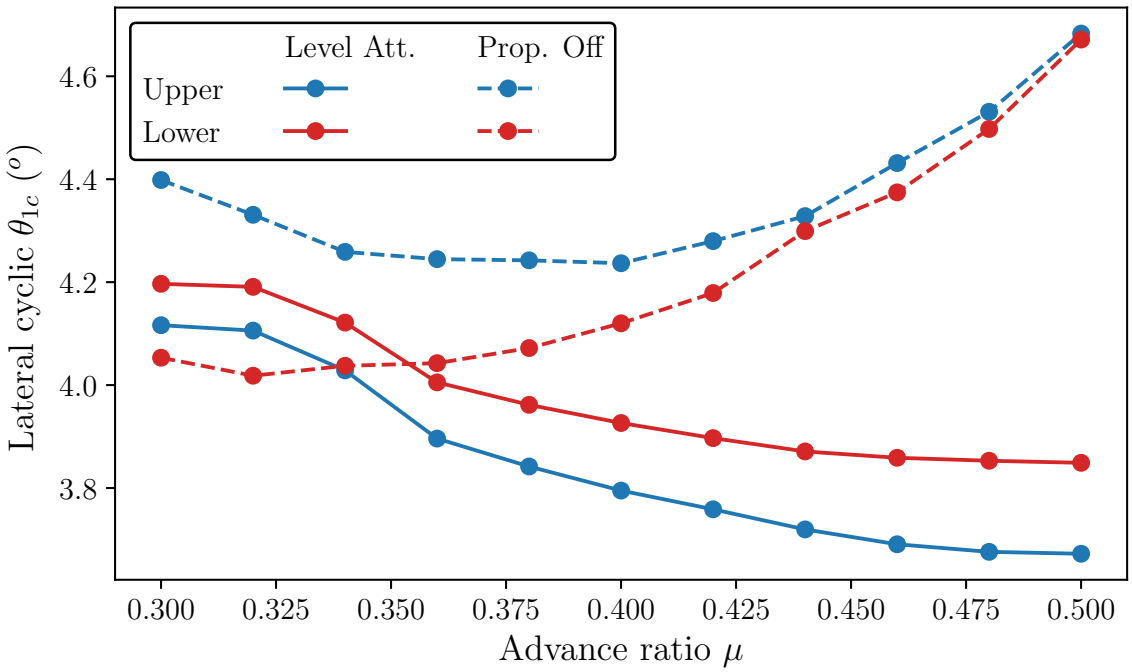

Figure 7.4: Lateral cyclic inputs for a coaxial rotor in forward flight

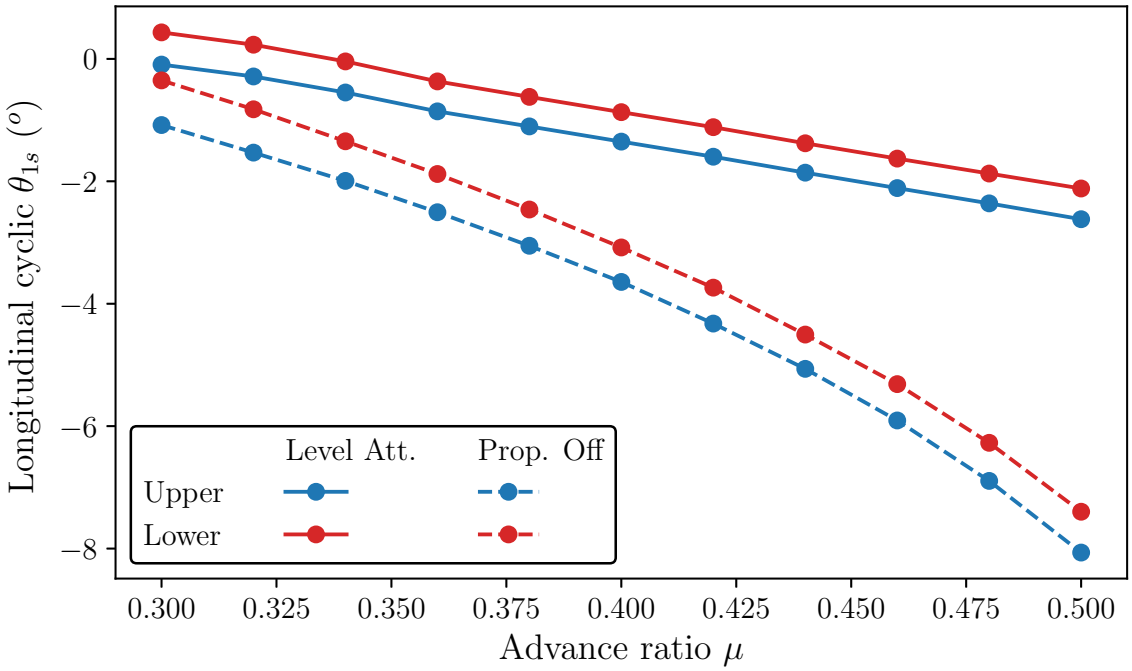

Figure 7.5: Longitudinal cyclic inputs for a coaxial rotor in forward flight

7.1.1 Effect of advance ratio

The fuselage tilt angle α_f for the propulsor off condition is shown in Fig. 7.2. The fuselage tilt increases from $\alpha_f = 5^o$ to $\alpha_f = 14^o$ as the advance ratio increases from $\mu = 0.3$ to $\mu = 0.5$. For the level attitude trim, the fuselage tilt is $\alpha_f = 0^o$.

The effect of advance ratio μ on the collective pitch θ_0 is shown in Fig. 7.3. The upper rotor collective is plotted in blue, and the lower rotor collective is plotted in red. For trim with propulsor off, the collective pitch increases with advance ratio from approximately $\theta_0 = 6^o$ to $\theta_0 = 14^o$. The collective pitch increases because the rotor thrust needs to provide both forward thrust and vertical lift. In level attitude trim, the collective pitch does not change significantly with advance ratio, and remains relatively small ($\theta_0 \approx 4^o$). For both types of trim, the upper rotor collective is greater than the lower rotor collective. Note that in hover, the lower rotor collective pitch is always greater than the upper rotor to maintain yaw trim. Therefore, in forward

flight the differential collective input $\Delta\theta_0$ changes sign.

The effect of advance ratio on the lateral cyclic is shown in Fig. 7.4. For level attitude trim, the lateral cyclic decreases from approximately $\theta_{1c} = 4.1^o - 4.2^o$ to $\theta_{1c} = 3.7^o - 3.9^o$. The lower rotor lateral cyclic is greater than the upper rotor lateral cyclic by approximately 0.1^o. For trim with propulsor off, the behavior is significantly different. The lateral cyclic increases with advance ratio by nearly 1^o. The upper rotor lateral cyclic is greater than the lower rotor cyclic by 0.4^o at $\mu = 0.3$. As the advance ratio increases, the difference between the upper and lower rotor cyclic decreases. The difference is negligible at $\mu = 0.5$. Therefore, at high speed ($\mu \geq 0.45$) with propulsor off, the differential lateral cyclic is zero ($\Delta\theta_{1c} = 0$).

The effect of advance ratio on the longitudinal cyclic is shown in Fig. 7.5. For level attitude trim, the longitudinal cyclic decreases linearly as advance ratio increases. For trim with propulsor off, the longitudinal cyclic decreases rapidly to nearly -8^o at $\mu = 0.5$. In both types of trim, the magnitude of the lower rotor longitudinal cyclic is less than the magnitude of the upper rotor longitudinal cyclic.

The differences in the cyclic control inputs indicates that the interaction between the two rotors is different when using the two different types of trim. With a tilted rotor, the coaxial wake operates very near the blades. The upper rotor wake may pass through the lower rotor tip path plane. Therefore the advance ratio has a strong effect on the rotor loads. Without fuselage tilt, the rotor-wake interaction does not change significantly with advance ratio, therefore the control pitch settings remain small.

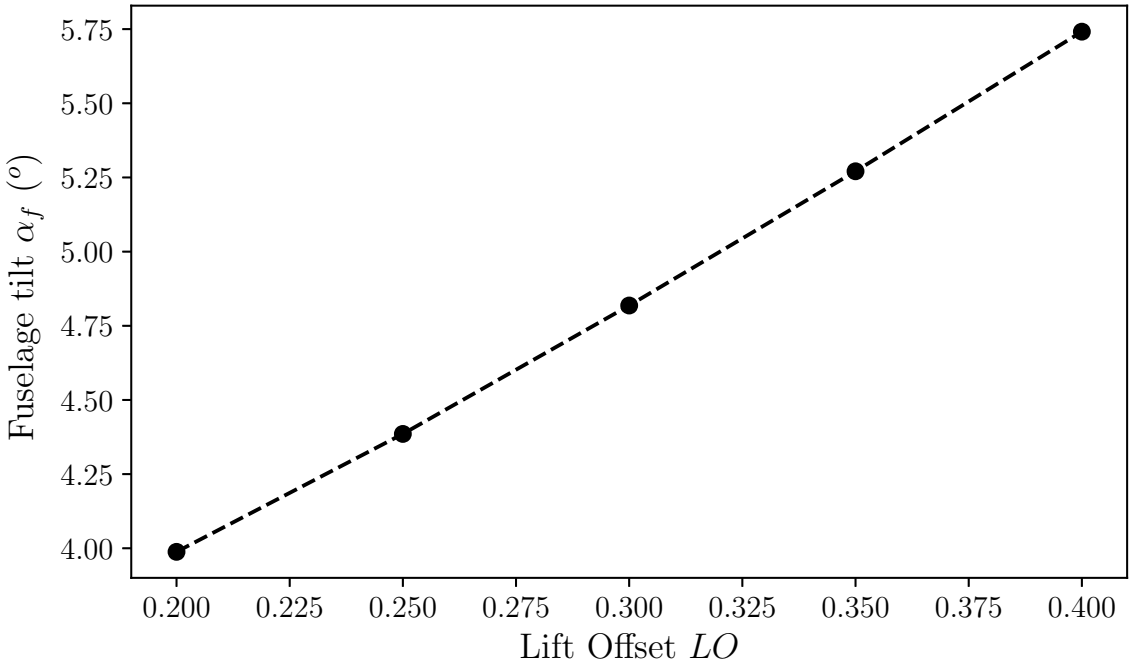

Figure 7.6: Effect of lift offset on fuselage tilt for a coaxial rotor in forward flight with propulsor off

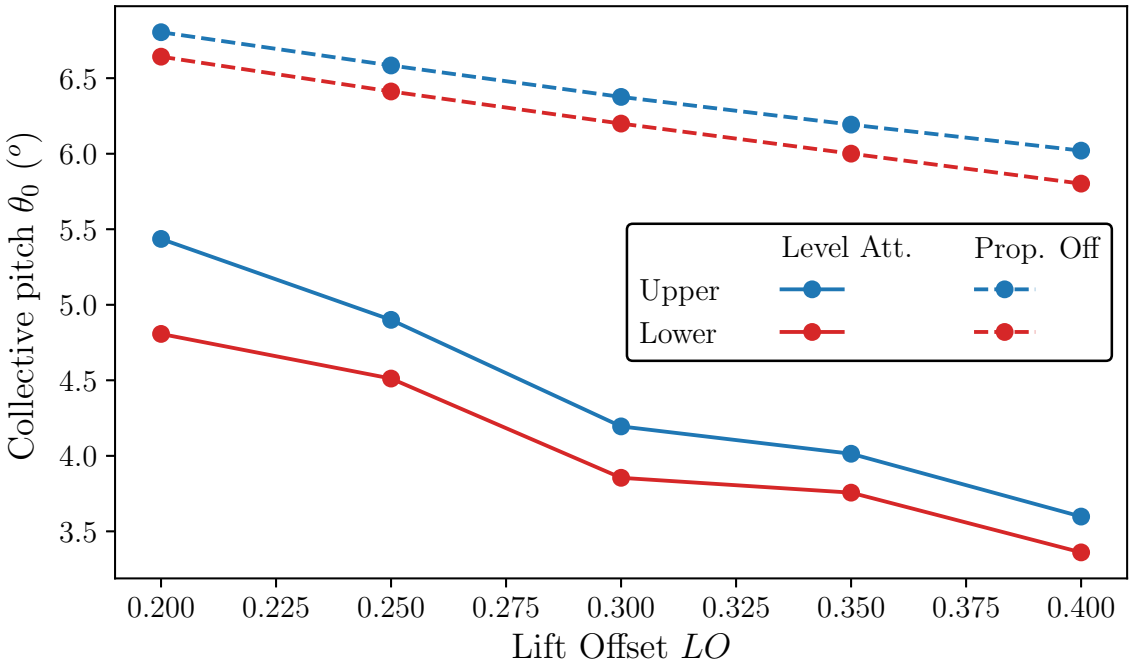

Figure 7.7: Effect of lift offset on collective pitch inputs in forward flight

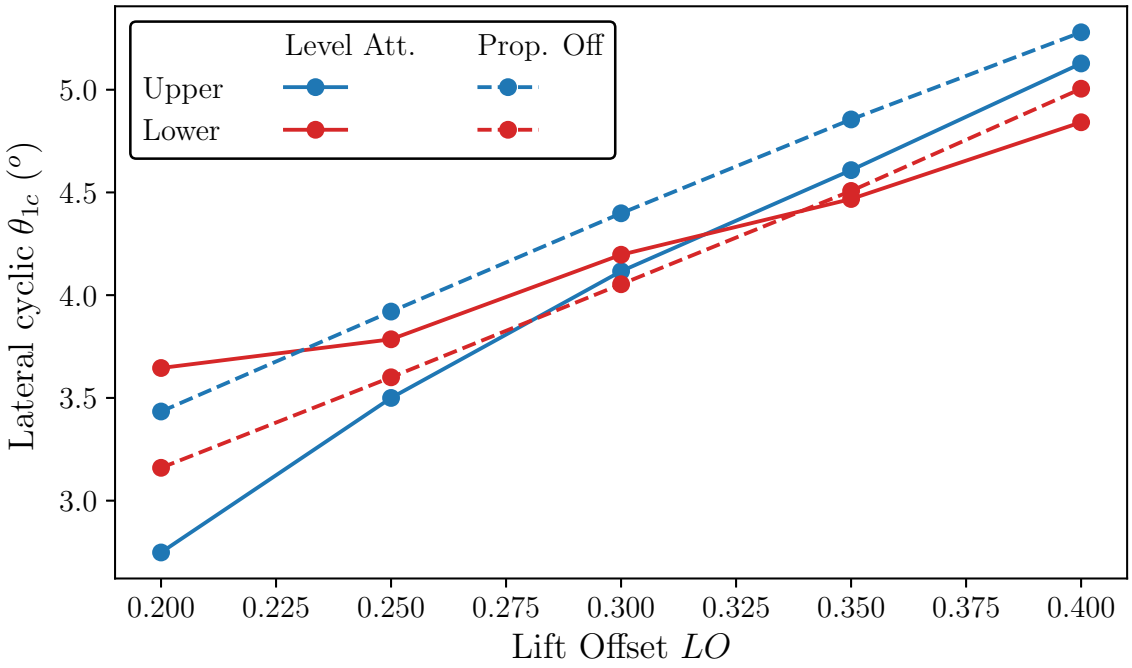

Figure 7.8: Effect of lift offset on lateral cyclic input in forward flight

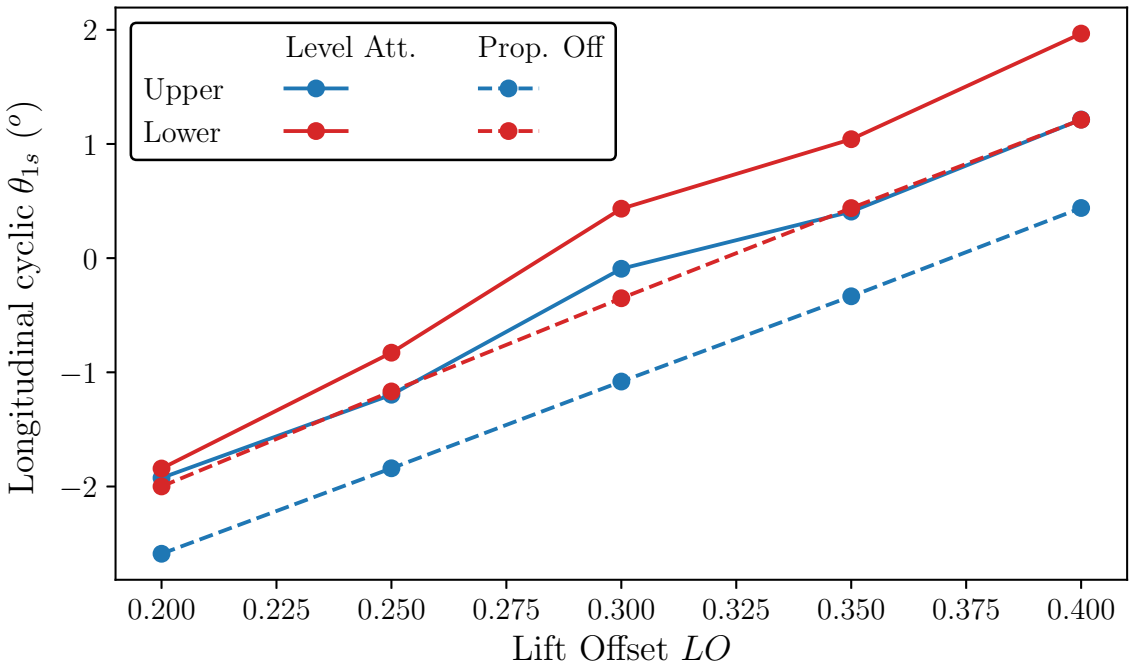

Figure 7.9: Effect of lift offset on longitudinal cyclic in forward flight

7.1.2 Effect of lift offset

The fuselage tilt angle α_f increases with increase in LO as shown in Fig. 7.6. The fuselage tilt increases from $\alpha_f = 4^o$ to $\alpha_f = 5.75^o$ at a fixed advance ratio of $\mu = 0.3$. The collective pitch requirement diminishes with increase in LO (Fig. 7.7). For trim with propulsor off, the collective pitch decreases 0.5^o from LO = 0.2 to LO = 0.4. However, in trim with level attitude, the collective pitch decreases nearly 1.5^o with increase in LO. Therefore, the effect of LO on the collective pitch is significant. As the LO increases, the center of rotor thrust moves towards the advancing side where dynamic pressures are higher. Therefore, a smaller collective blade pitch is required to maintain the same amount of thrust. Hence, the required collective pitch decreases with increased LO.

Increasing the LO increases the lateral and longitudinal cyclic requirements for both trim procedures. In Fig. 7.4, the lateral cyclic increases by nearly 1.5^o for trim with propulsor off. For level attitude trim, the lateral cyclic for the upper rotor increases by 2^o, whereas the lateral cyclic for the lower rotor increases by only 1^o. Note that at a LO of 0.2, the lower rotor lateral cyclic is greater than the upper rotor lateral cyclic, however at LO = 0.4, the upper rotor lateral cyclic is greater than the lower rotor cyclic. Therefore the differential lateral cyclic $\Delta\theta_{1c}$ changes sign at approximately LO = 0.325 at an advance ratio $\mu = 0.3$. The effect of LO on the longitudinal cyclic at $\mu = 0.3$ is shown in Fig. 7.9. The longitudinal cyclic increases by approximately 4^o with increase in LO from LO = 0.2 to LO = 0.4, for both trim procedures.

It is evident that the LO modifies the trim setting of the rotor considerably. The longitudinal cyclic θ_{1s} is most sensitive to the LO setting because it's primary effect is

to change the hub rolling moment C_{M_X}. The rest of the collective and cyclic controls are modified in order to maintain the force and moment equilibrium of the coaxial rotor.

7.2 Power requirements

The control inputs on the rotor in level attitude forward flight produce an effect on the power required as shown in Fig. 7.10. The power coefficient C_P of a coaxial rotor is related to the vertical hub moment:

$$C_P = |(C_{M_Z})_u| + |(C_{M_Z})_l| \tag{7.1}$$

Note that the power required by the propulsor is not included in the level attitude calculation. Therefore, Fig. 7.10 compares only the main rotor power requirements. In Fig. 7.10a, the power required for the coaxial rotor at level attitude remains nearly constant at $C_P = 0.00038$ with increase in advance ratio. However, with fuselage tilted and propulsor off, the power required nearly doubles from $C_P = 0.0006$ to $C_P = 0.0012$ when the advance ratio is increased from $\mu = 0.3$ to $\mu = 0.5$.

The LO has a smaller effect on the power requirement. In Fig. 7.10b, the power required for the coaxial rotor at level attitude decreases by approximately 10% with increase in LO from LO = 0.2 to LO = 0.4. However, with fuselage tilted and propulsor off, the power consumption increases by approximately only 4%.

The coaxial rotor power requirement with the propulsor off is 1.5 to 3 times the main rotor power requirement at level attitude. Therefore, the coaxial rotor system is more efficient in edgewise flight compared to a fuselage tilted flight. The propulsor is designed to produce forward thrust efficiently. Therefore, for the same amount of

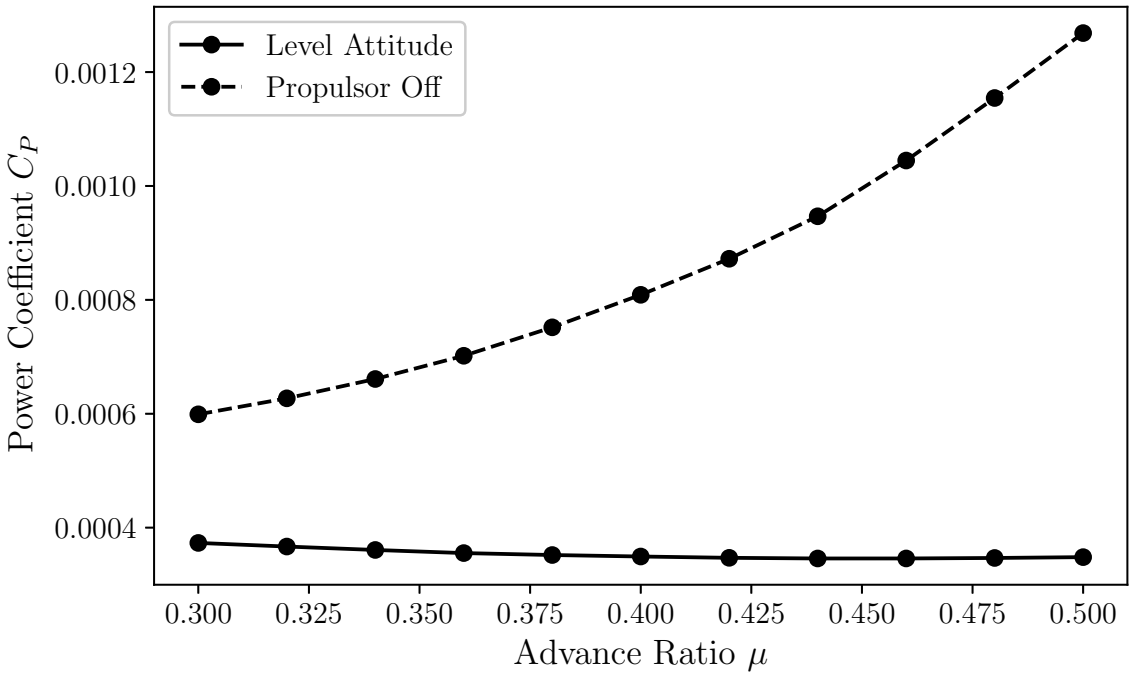

(a) Effect of advance ratio

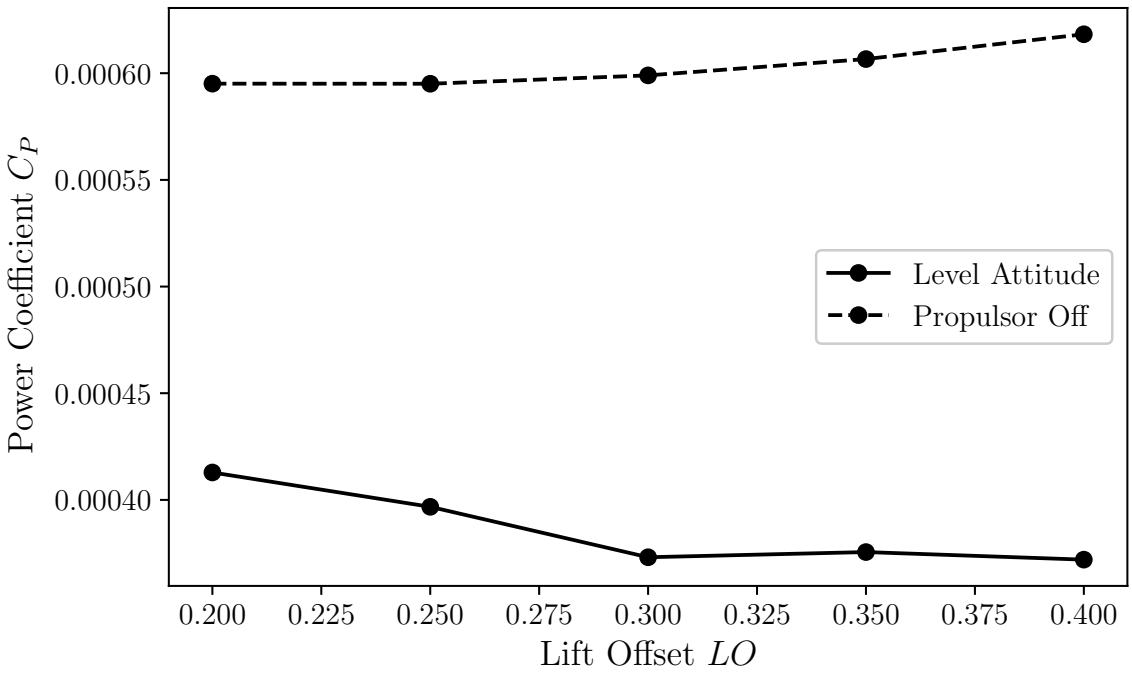

(b) Effect of lift offset

Figure 7.10: Coaxial rotor power consumption in forward flight

engine power, higher forward speeds can be achieved by flying at a level attitude with a propulsor compared to flying with fuselage tilt without a propulsor. An additional benefit is that the streamlined fuselage has reduced drag when maintaining a level attitude. However, the effect of fuselage orientation on the drag has not been included in this study.

7.3 Rotor hub loads

7.3.1 Effect of advance ratio

The loads on a coaxial rotor in forward flight are different when compared to hover. Figure 7.11 illustrates the unsteady vertical hub force on a coaxial rotor at advance ratios of $\mu = 0.3$ and $\mu = 0.5$. The results for trim with propulsor off are shown in Fig. 7.11a. At $\mu = 0.3$, there are large oscillations in the vertical hub force at a frequency of 4/rev. Increasing the advance ratio to $\mu = 0.5$, decreases the magnitude of the oscillations and increases the higher frequency components present in the loads. The higher frequency loads are due to DS effects which become evident at the higher advance ratio of $\mu = 0.5$. Furthermore, due to the fuselage tilt, the upper rotor wake passes through the lower rotor plane and increases unsteady rotor-wake interactions.

The oscillatory vertical hub force at level attitude is shown in Fig. 7.11b. At $\mu = 0.3$, the magnitude of the 4/rev oscillations increase when compared to trim with propulsor off. The 4/rev oscillations decrease when the advance ratio increases to $\mu = 0.5$. The upper and lower rotor loads are in phase for both advance ratios.

The magnitude of the 4/rev and 8/rev vibratory hub loads are shown in Fig. 7.12. The oscillatory vertical hub force ΔC_{F_Z}, roll moment ΔC_{M_X} and pitch moment ΔC_{M_Z} vibrations have the highest values, and therefore are the most important. The mag-

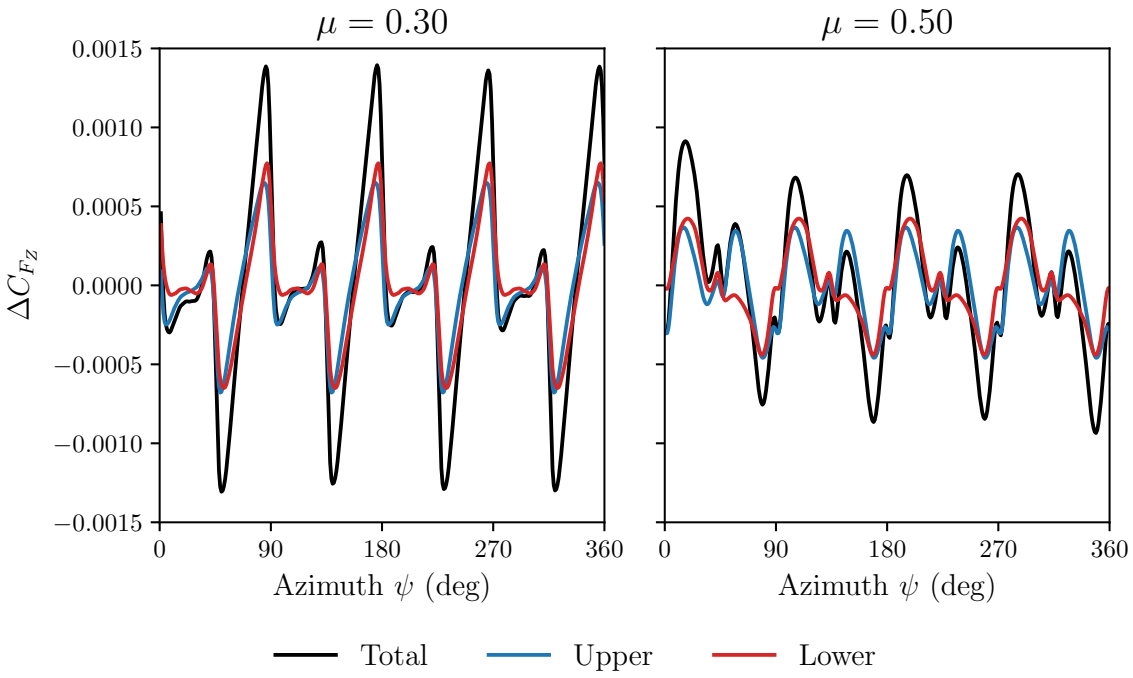

(a) Propulsor off

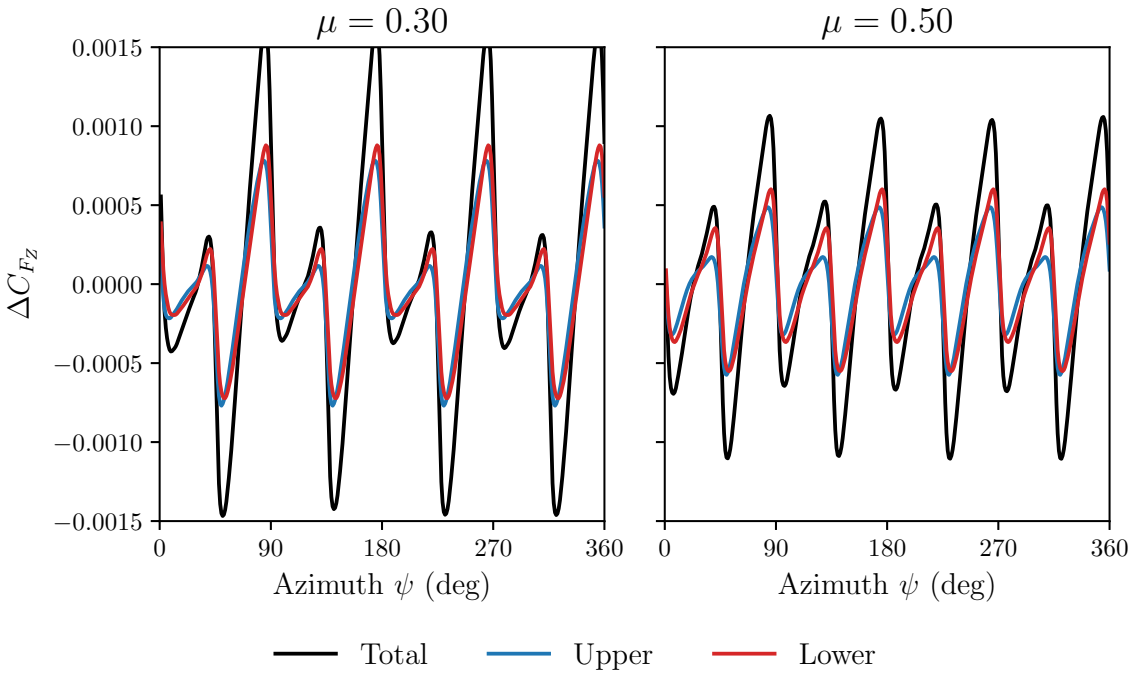

(b) Level attitude

Figure 7.11: Oscillatory vertical hub loads on a coaxial rotor in forward flight

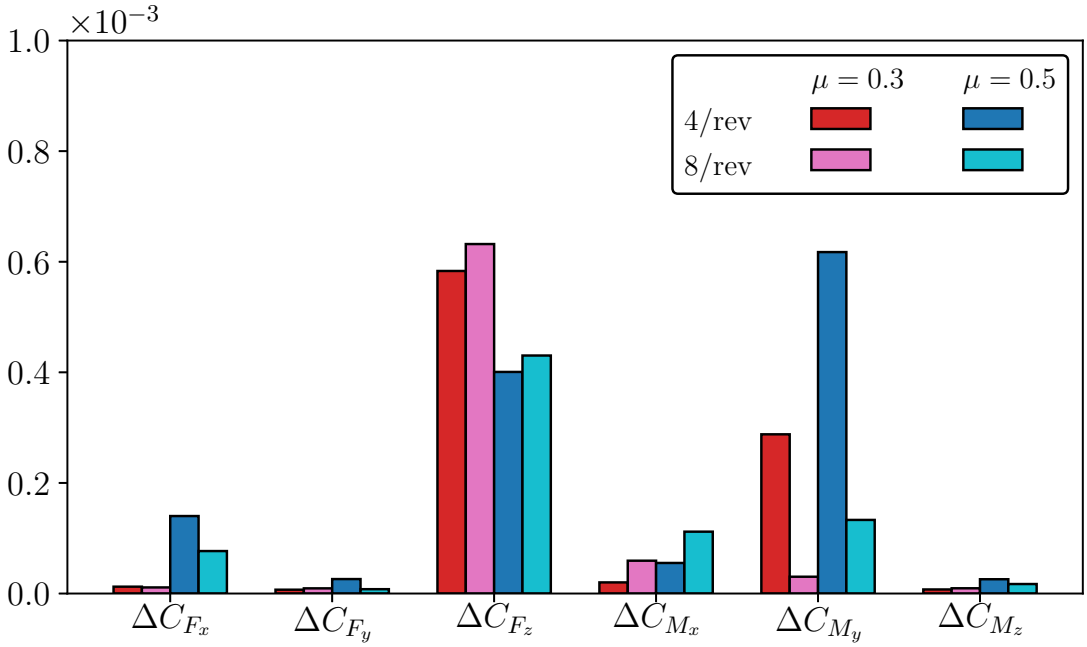

(a) Propulsor off

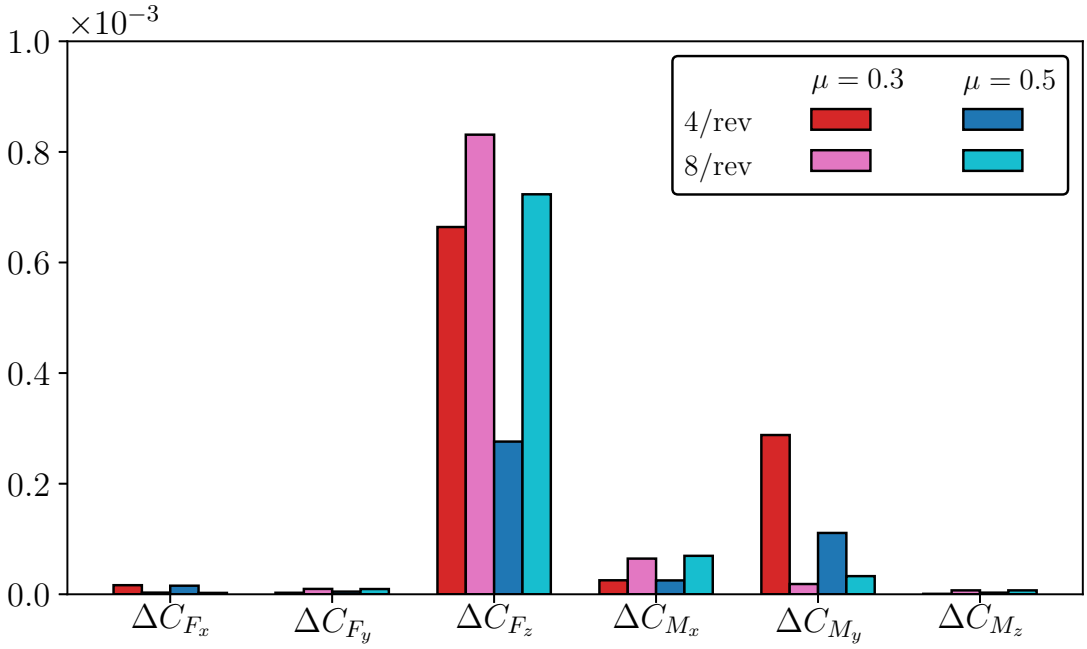

(b) Level attitude

Figure 7.12: Effect of advance ratio on coaxial rotor hub loads in forward flight

nitude of the longitudinal force ΔC_{F_Z}, lateral force ΔC_{F_Y} and yaw moment ΔC_{M_Z} are negligible by comparison.

The hub loads for trim with propulsor off are shown in Fig. 7.12a. The 8/rev vertical hub force is greater than the 4/rev component at both advance ratios. This implies that the blade passage effect is significant in forward flight. Increasing the advance ratio decreases the magnitude of both the 4/rev and 8/rev vertical hub force. However the 4/rev pitching moment nearly doubles with increase in advance ratio. With trim at level attitude in Fig. 7.12b, increasing the advance ratio has the opposite effect on the hub pitching moment. The 4/rev component of the oscillatory pitching moment are reduced by almost 50% at $\mu = 0.5$. Similarly, the 4/rev vertical hub force also decreases by nearly 50% with increase in advance ratio.

It is evident that the trim condition has a strong influence on the vibratory hub loads of a coaxial rotor in forward flight. With the propulsor off, the rotor has to provide both lift and forward thrust for the helicopter. The lift distribution has to change to increase thrust and maintain the LO in a different aerodynamic environment due to the rotor tilt and increased rotor-wake interaction. Therefore, the oscillations in the hub pitching moment increase with advance ratio. However, at level attitude, the aerodynamic environment does not change significantly with advance ratio. The rotor wake interactions decrease as the wake is swept away at a faster rate. The rotor tilt is zero. The rotor is capable of producing the lift required to counter the helicopter weight in an efficient manner. Therefore, both the oscillatory hub vertical force and pitching moment decrease.

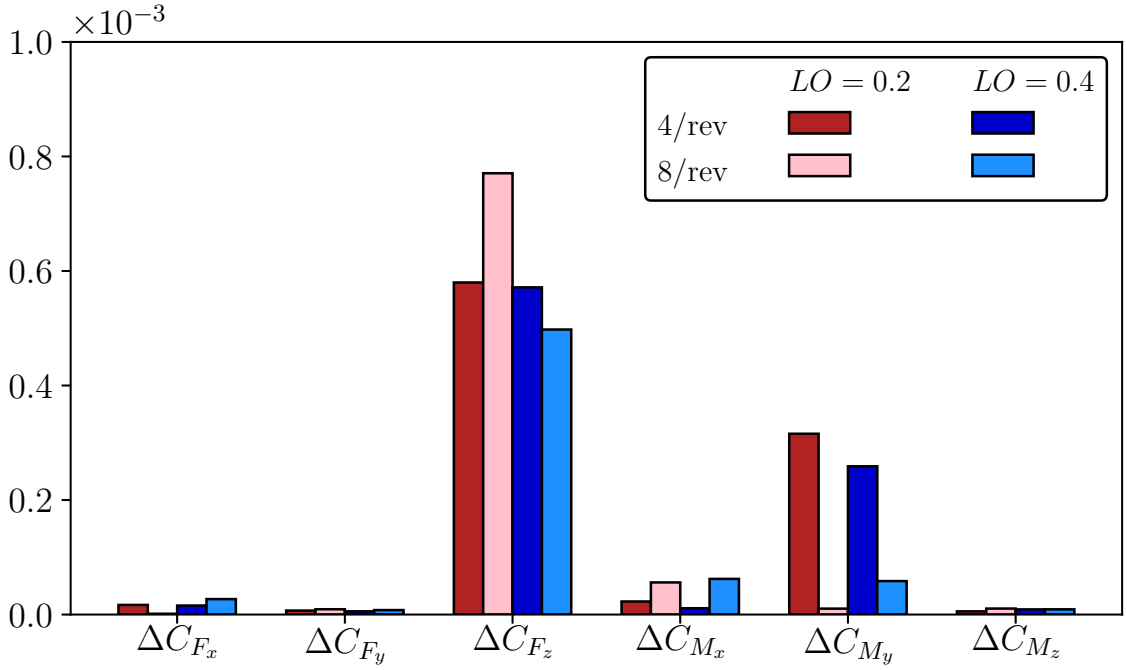

(a) Propulsor off

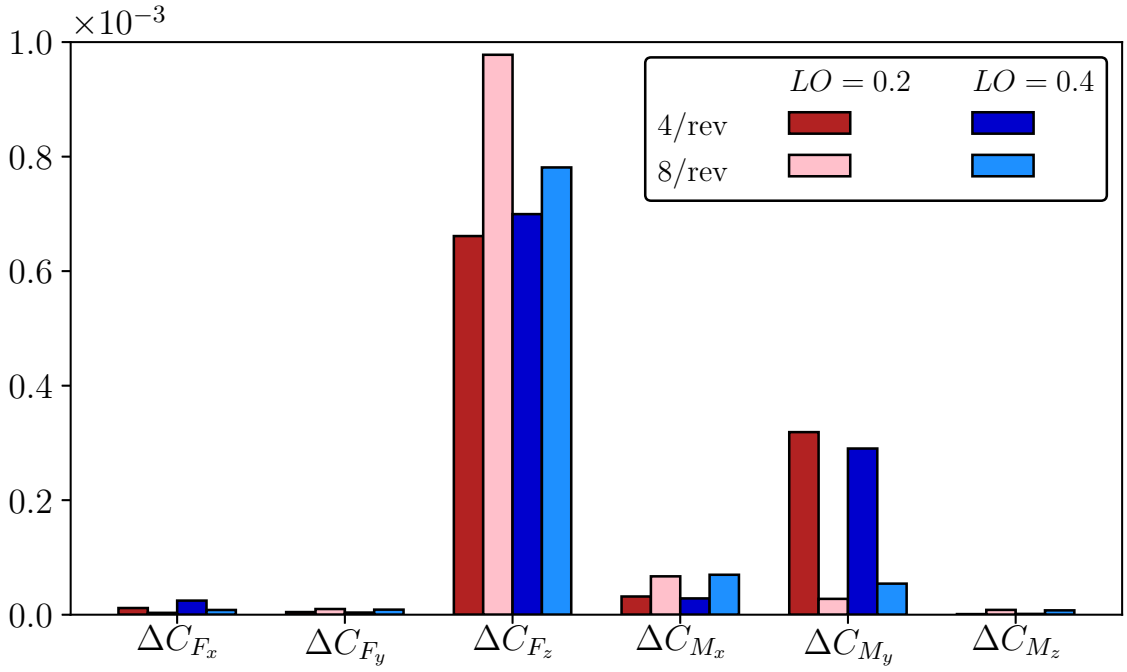

(b) Level attitude

Figure 7.13: Effect of lift offset on coaxial rotor hub loads in forward flight

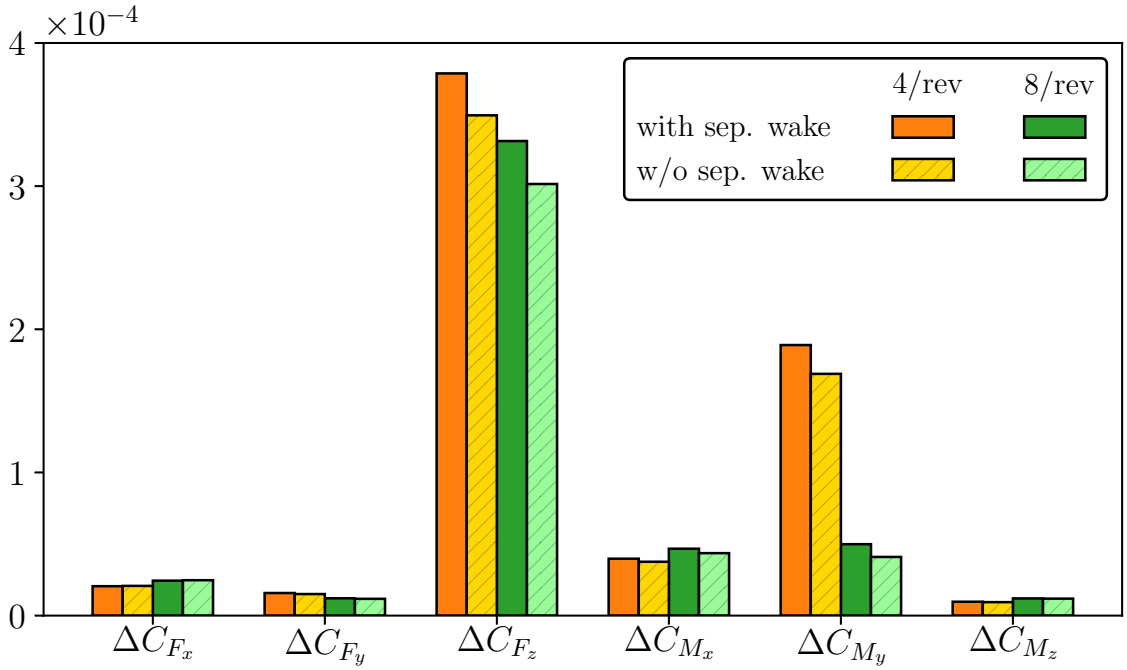

Figure 7.14: Coaxial rotor vibratory hub loads at $\mu = 0.4$

7.3.2 Effect of lift offset

The effect of LO on the rotor hub loads is shown in Fig. 7.13 for both trim procedures. Increasing the LO from LO = 0.2 and LO = 0.4 decreases the hub loads. Increasing the LO offloads the retreating side and increases the loads on the advancing side of the rotor. Therefore, the vibratory loads due to DS effects on the retreating side are reduced with increase in advance ratio.

7.3.3 Effect of separated wake

The effect of the separated wake is examined in Fig. 7.14. The hub loads were calculated for trim with propulsor off at an advance ratio of $\mu = 0.4$. The calculations were also repeated for the same trim settings without the generation of the separated wake due to DS. The vibratory hub loads for the coaxial rotor at $\mu = 0.4$ when including the separated wake are plotted in Fig. 7.14. The in-plane hub shears ΔC_{F_X}

and ΔC_{F_Y} are not influenced by the separated wake. The vertical hub shear ΔC_{F_Z} is only slightly affected by the separated wake. The 4/rev vertical hub shear increases by 8% whereas the 8/rev vertical hub shear increases by 9% with the inclusion of the separated wake. The 4/rev pitching moment ΔC_{M_Y} increases by 11% when the separated wake is included. The 8/rev pitching moment increases by approximately 18% with the influence of the separated wake. These results indicate clearly that the separated wake plays an important role in the vibratory hub loads of the coaxial rotor.

7.4 Blade sectional loads

The LO setting has a significant effect on the distribution of spanwise blade loads. Figures 7.15 and 7.16 illustrate the distribution of the normal force distribution over the upper and lower rotors at LO settings of LO = 0.2 and LO = 0.4. The normal force coefficient C_n is:

$$C_n = C_l \cos\alpha + C_d \sin\alpha \tag{7.2}$$

The normal force coefficient is multiplied by the square of the local Mach number M_c^2 to account for the varying dynamic pressure over the rotor.

In Fig. 7.15a, the LO is 0.2. The reverse flow region is denoted by grey shading. The upper and lower rotor normal force distributions are almost mirror images of each other about the $\psi = 0^o$ axis since the rotors counter-rotate. The normal force is maximum in a small region near the tip of the blade at $\psi = 90^o$ for the upper rotor, and $\psi = 270^o$ for the lower rotor. In Fig. 7.15b, the LO is increased to LO = 0.4. The normal force increases significantly in the tip region between $\psi = 45^o - 135^o$ for the upper rotor, and $\psi = 225^o - 315^o$ for the lower rotor. Therefore, the net lift is shifted towards the advancing side of each rotor.

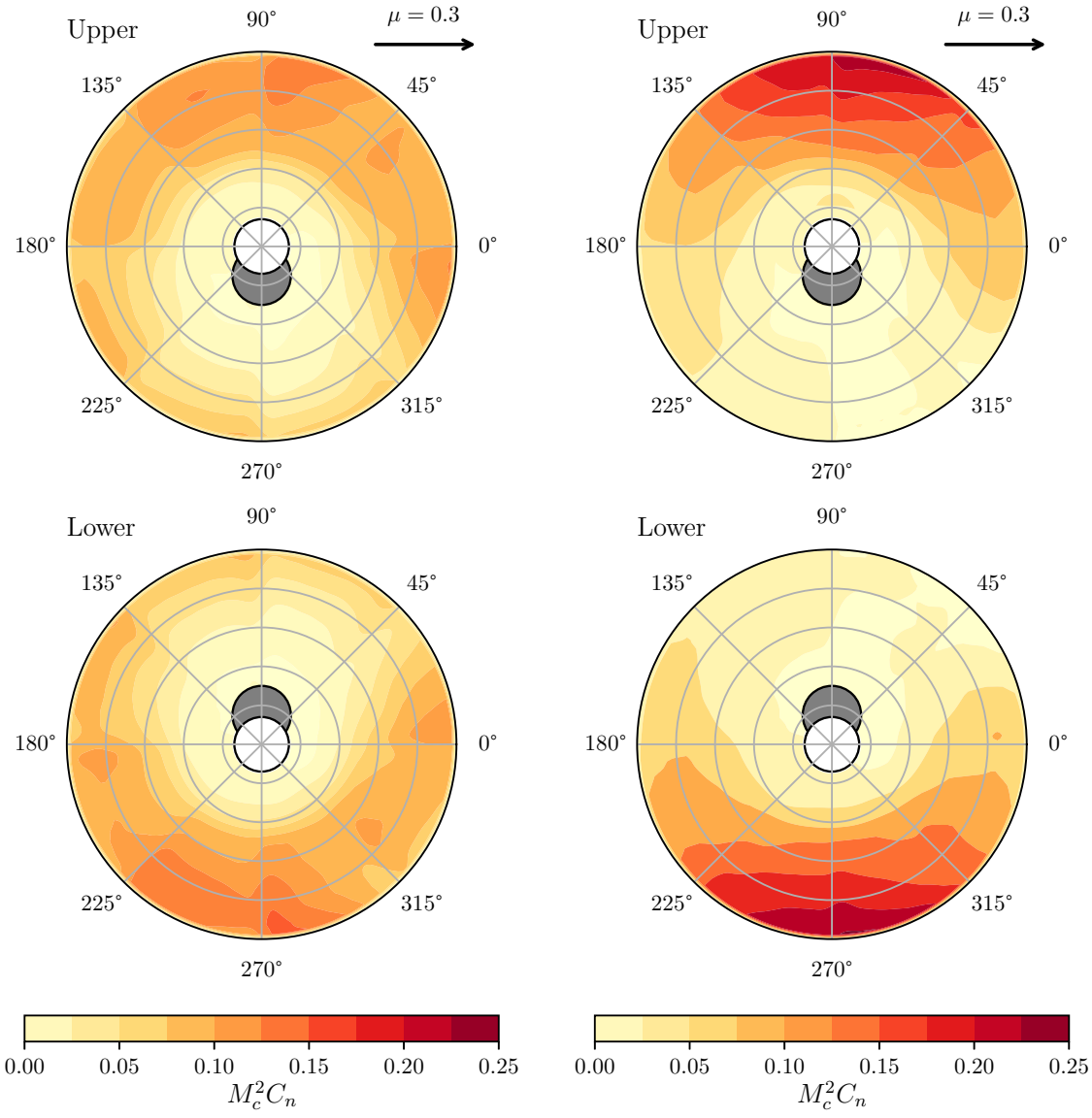

(a) LO = 0.2

(b) LO = 0.4

Figure 7.15: Sectional normal force distribution on a coaxial rotor in forward flight with propulsor off

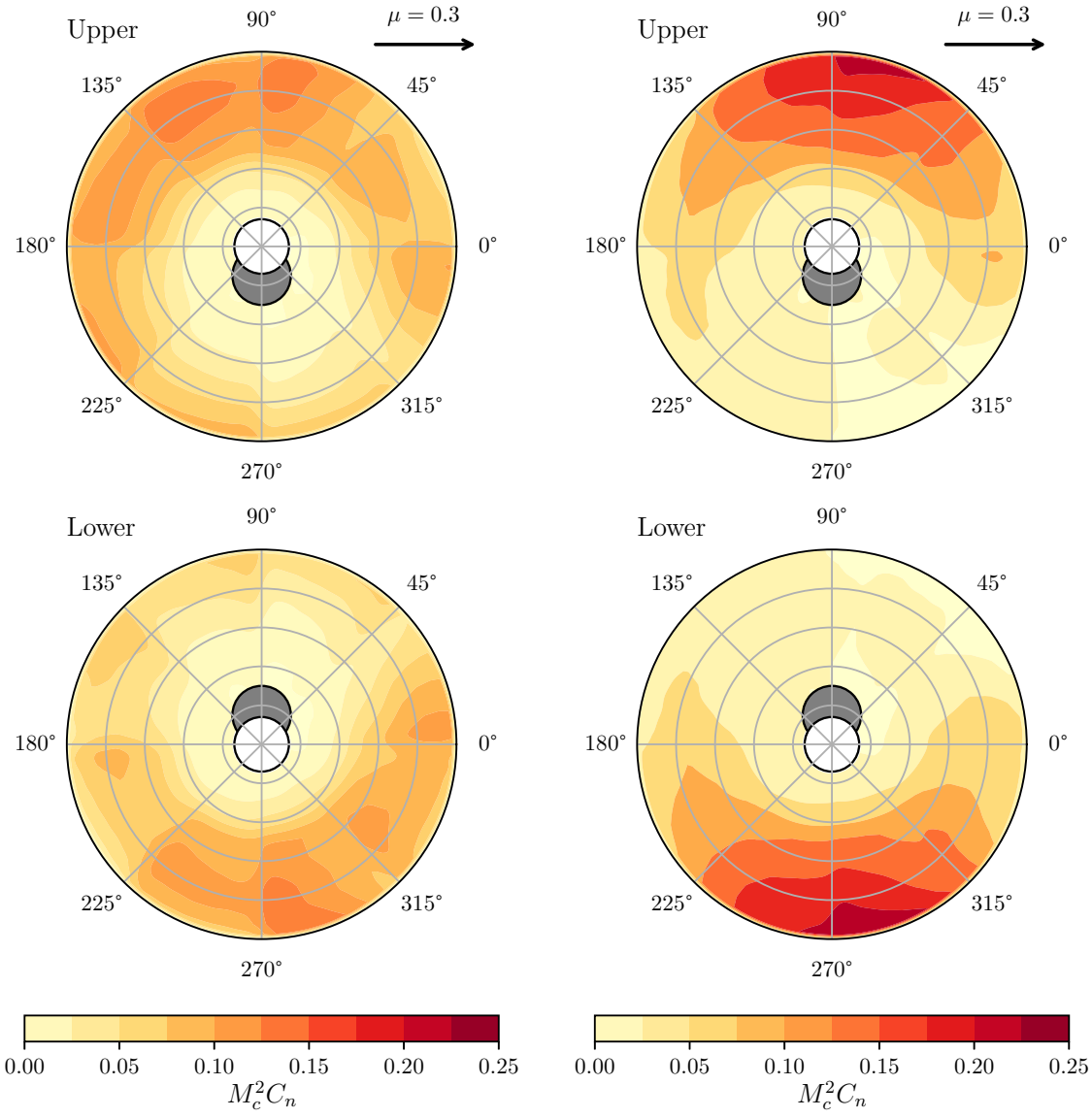

(a) LO = 0.2

(b) LO = 0.4

Figure 7.16: Sectional normal force distribution on a coaxial rotor in forward flight with level attitude

The results are similar for coaxial trim at level attitude in Fig. 7.16. In Fig. 7.16a, both the upper rotor and lower rotor have multiple regions of large normal force on the advancing sides of the rotors. For the upper rotor, one such region is located near the $\psi = 90^o$ azimuth, and another one at $\psi = 135^o$ azimuth. These regions are due to the blade passage effect in forward flight. The dynamic pressure is maximum near the $\psi = 90^o$ azimuth, therefore the blade passage loads increase. The blade passage loads are easier to identify in the level attitude trim because the rotor-wake interactions are reduced when compared to the trim with propulsor off.

7.5 Inflow distribution

The sectional load distribution on the coaxial rotor is a consequence of the induced inflow distribution U_Z^J. The inflow represents the combined effect of the wake and blade bound circulation induced velocities. The inflow distribution on the upper and lower rotors in forward flight trim with propulsor off is shown in Fig. 7.17. The inflow distributions on the upper and lower rotor are nearly mirror images of each other about the $\psi = 0^o$ axis for the counter-rotating blades. The differences between the upper and lower rotor are due to the differential collective and cyclic inputs required to trim the rotor.

In Fig. 7.17a, the advance ratio is $\mu = 0.3$. The inflow is maximum in a region near the blade tip at $\psi = 45^o$ for the upper rotor, and $\psi = 315^o$ for the lower rotor. At an advance ratio to $\mu = 0.5$ (Fig. 7.17b) the inflow distribution changes significantly. There is a region of strong upflow (shaded red) near the hub and reverse flow region. The inflow in the aft region of the rotor is reduced compared to the lower advance ratio of $\mu = 0.3$.

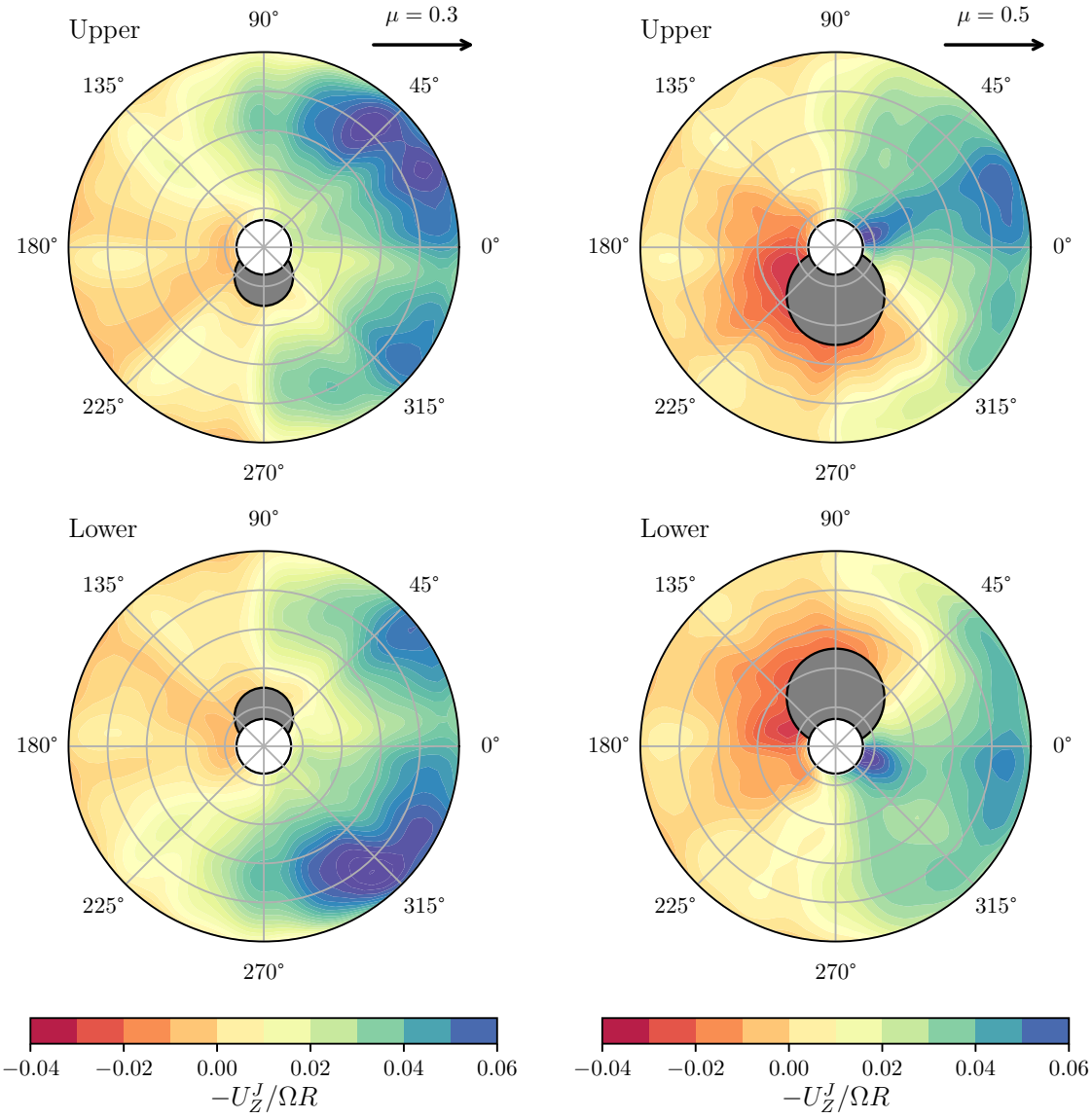

(a) $\mu = 0.3$

(b) $\mu = 0.5$

Figure 7.17: Inflow distribution on a coaxial rotor in forward flight with propulsor off

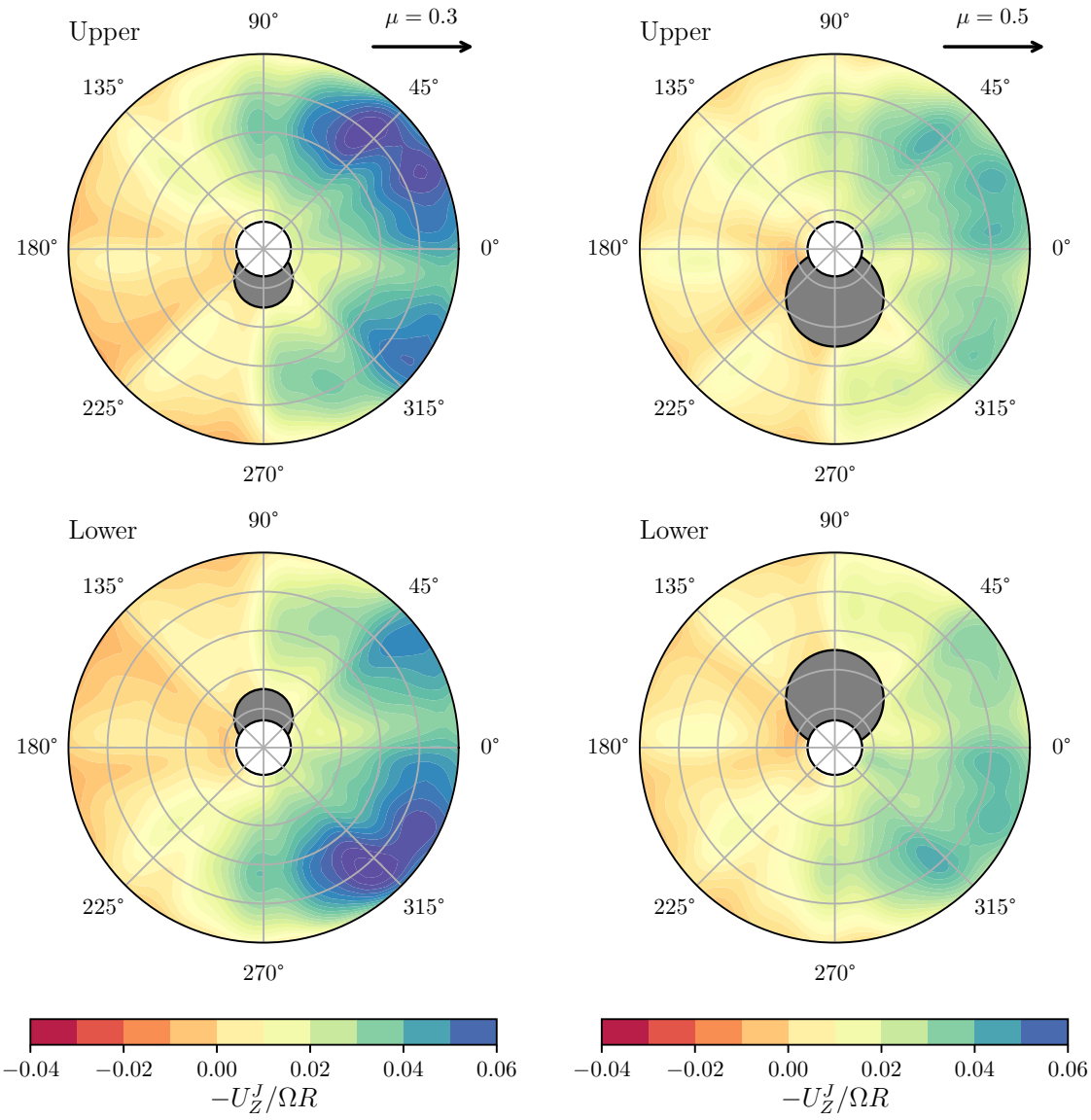

(a) $\mu = 0.3$ (b) $\mu = 0.5$

Figure 7.18: Inflow distribution on a coaxial rotor in forward flight at level attitude

The inflow distribution in forward flight trim with level attitude is shown in Fig. 7.18. The results for $\mu = 0.3$ in Fig. 7.18a are similar to the results for trim with propulsor off in Fig. 7.17a. The inflow distributions are similar because the fuselage tilt angle $\alpha_f \approx 5^o$ is small. However, at $\mu = 0.5$ in Fig. 7.18b , the inflow distribution is very different. There is no region of upflow for trim with level attitude.

This difference in the inflow distribution at $\mu = 0.5$ is determined by examining at the wake induced inflow and blade bound circulation induced inflow separately. The wake induced inflow at an advance ratio of $\mu = 0.5$ is shown in Fig. 7.19. There are significant differences between the propulsor off (Fig. 7.19a) and the level attitude (Fig. 7.19b) trim results. In Fig. 7.19a, the wake induced inflow is relatively small over the entire upper rotor. However, the lower rotor has strong regions of upflow and inflow on the retreating side. There are two regions (shaded green) at $\psi = 225^o$ and $\psi = 270^o$ near the mid span of the blade. In Fig. 7.19b, the upper and lower rotor are mirror images of each other. A strong inflow region is present at the rear of the rotor between $\psi = 315^o$ and $\psi = 45^o$. While the wake induced inflow is different for the two trim procedures, the strong region of upflow in Fig. 7.17b is not caused by the wake induced component because the wake induced inflow component in the region is small.

The bound circulation induced inflow at an advance ratio of $\mu = 0.5$ is shown in Fig. 7.20. For the case of trim with propulsor off (Fig. 7.20a), the bound circulation induced inflow is positive in the aft region of the rotor (between $\psi = 315^o - 90^o$ for the upper rotor and $\psi = 270^o - 45^o$ for the lower rotor). There is a strong region of upflow (shaded dark orange) in front of the rotor hub and reverse flow region ($\psi = 180^o$). By comparison, with the case of trim at a level attitude in Fig. 7.20b, the bound circulation induced inflow is benign over the entire rotor. Therefore, the strong region

of upflow near the hub with propulsor off is due to the bound circulation induced component of the inflow. This difference in inflow distribution is responsible for the larger magnitude of vibratory vertical hub force and pitching moments on the rotor hub at trim with propulsor off. This implies an accurate model of blade circulation and unsteady spanwise aerodynamic loads is necessary to capture the vibratory hub loads for a coaxial rotor in forward flight.

7.6 Aeroelastic stability analysis

7.6.1 Stability

The aeroelastic stability of the coaxial rotor is illustrated in Figs. 7.21 and 7.22. The STM of the periodic system is calculated using the single-pass method with a period of 1 revolution. The stability of the system is determined from the real part of characteristic exponents of the STM. There are a total of 12 modes for the coaxial rotor: 6 each for the upper and lower rotor. The 6 modes of each rotor correspond to 3 flap, 2 lag and 1 torsional mode. A different color is used for each of the 12 modes in Figs. 7.21 and 7.22.

7.6.1.1 Effect of advance ratio

The effect of advance ratio on the aeroelastic stability of the coaxial rotor modes is examined in Fig. 7.21. The real parts of the characteristic exponents are plotted with respect to the advance ratio for trim with propulsor off in Fig. 7.21a, and at level attitude trim in Fig. 7.21b. All modes are stable for both trim procedures because all points lie below the $\zeta = 0$ line.

In Fig. 7.21a, as the advance ratio increases to $\mu = 0.35$, the blue and green modes approach each other indicating that the coupling between modes is changing.

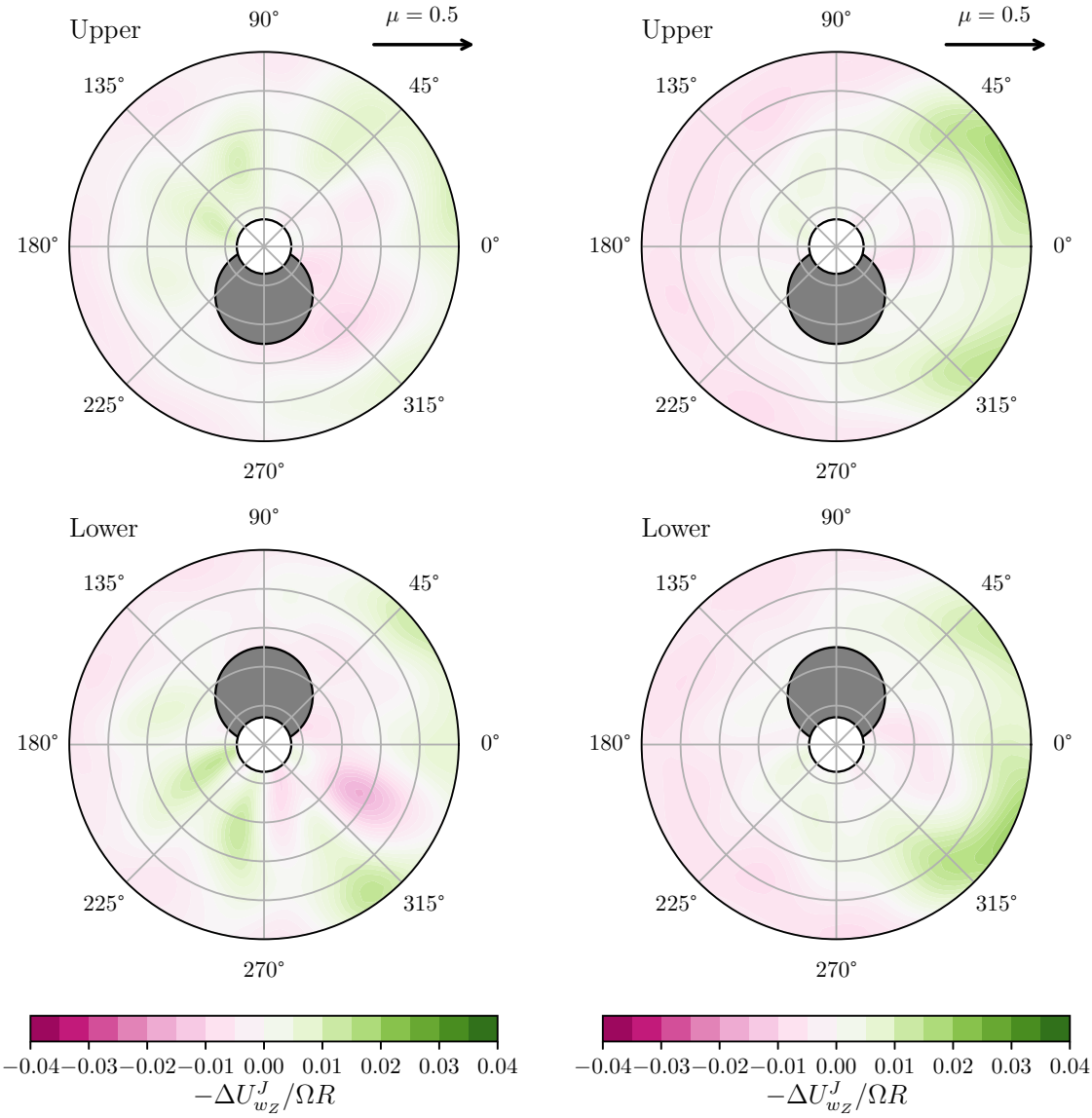

(a) Propulsor off

(b) Level attitude

Figure 7.19: Oscillatory wake induced inflow distribution on a coaxial rotor in forward flight ($\mu = 0.5$)

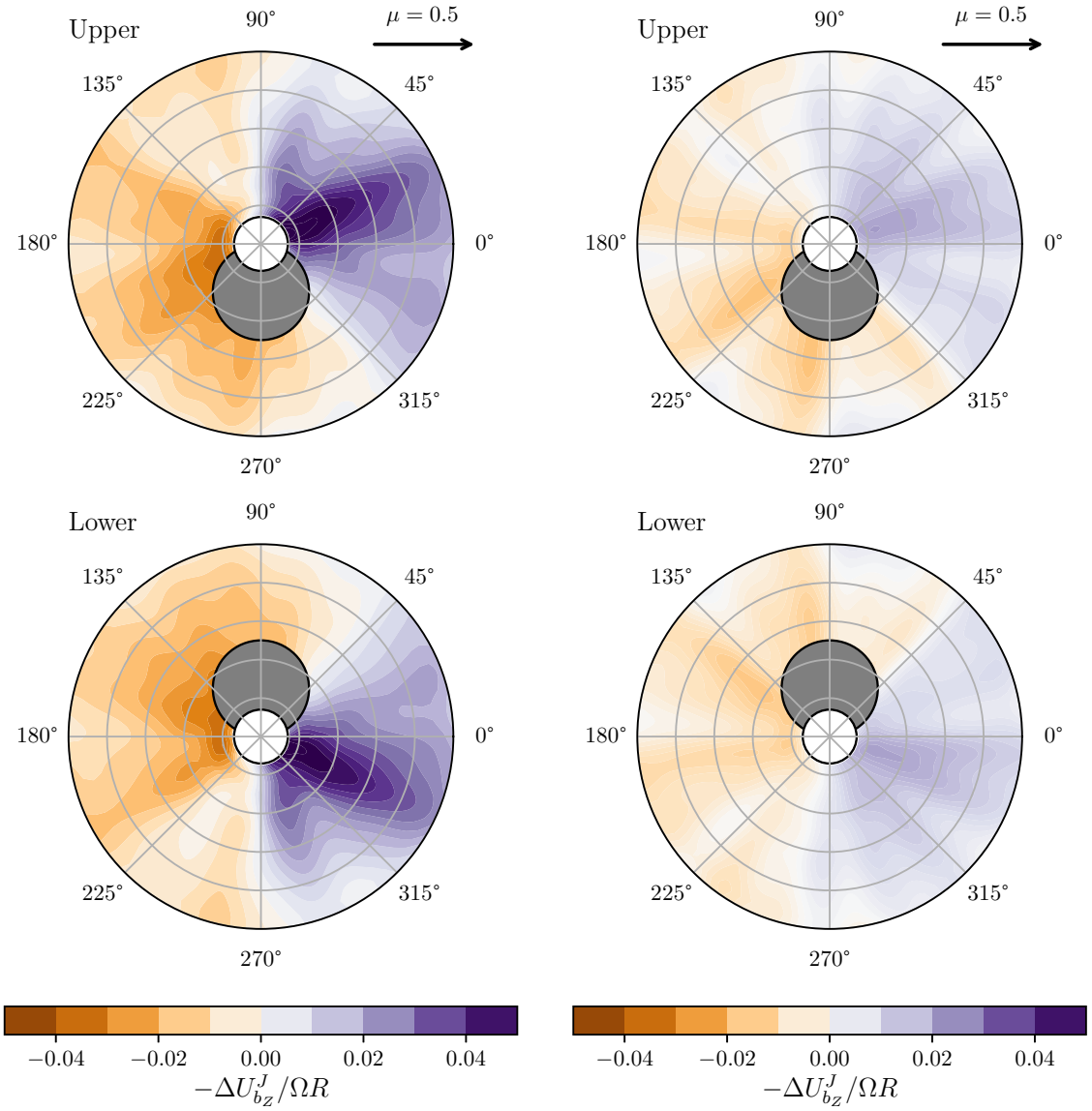

(a) Propulsor off

(b) Level attitude

Figure 7.20: Oscillatory blade bound circulation induced inflow distribution on a coaxial rotor in forward flight ($\mu = 0.5$)

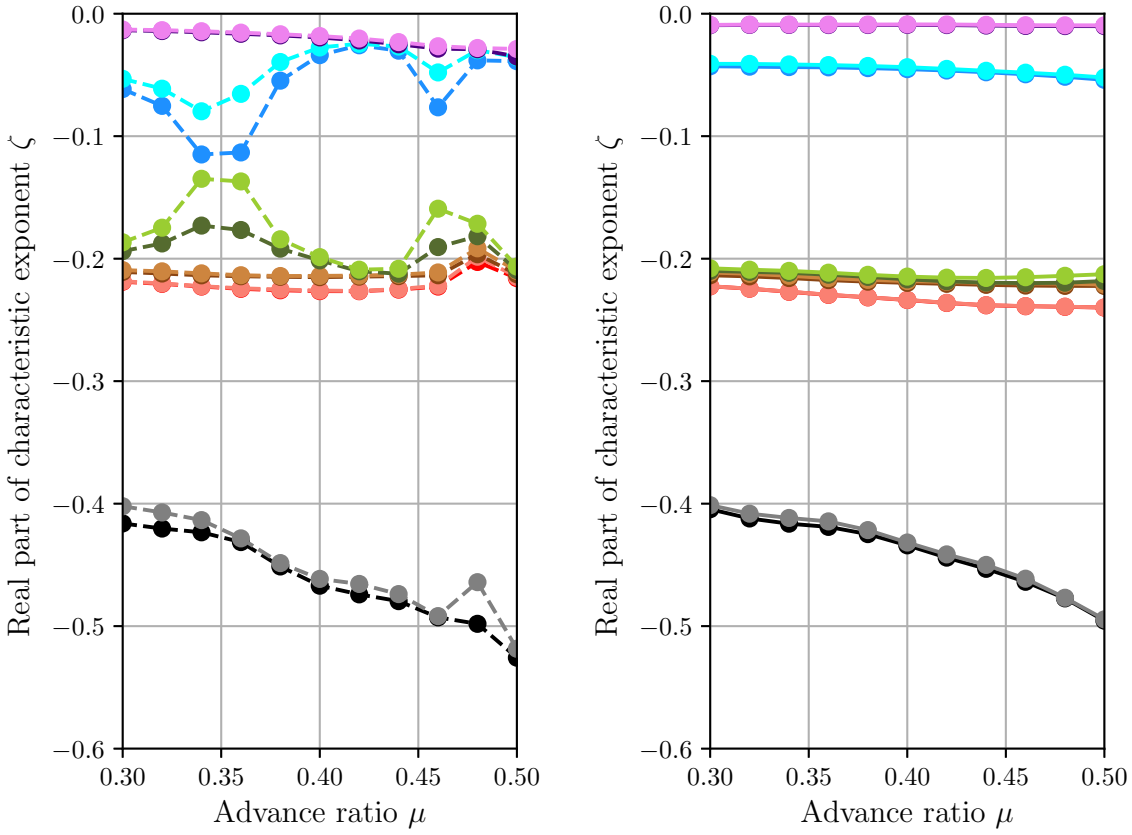

(a) Propulsor off

(b) Level attitude

Figure 7.21: Effect of advance ratio on aeroelastic stability of a trimmed coaxial rotor in forward flight (LO = 0.3)

A similar coupling occurs at $\mu = 0.46$. However, all modes remain stable. At level attitude in Fig. 7.21b, the real parts of the characteristic exponents of the coaxial rotor remain well-behaved at all advance ratios. As the advance ratio increases, the real parts of the characteristic exponents decrease gradually. Therefore, the stability of all modes increases with forward speed at level attitude trim.

The difference in aeroelastic stability due to the propulsor off and level attitude trim procedures is related to the blade collective pitch settings. As the collective pitch increases, the bending stiffness terms $\overline{EI}_y$ and $\overline{EI}_z$ change. Therefore, increasing the collective pitch changes the elastic coupling between the flap and lag modes. In the trim calculations for the collective pitch (Fig. 7.3), it was noted that with level attitude, the collective pitch remains constant at approximately $\theta_0 = 4^o$, whereas for the propulsor off condition, the collective pitch increases from $\theta_0 = 6^o$ to $\theta_0 = 14^o$ with advance ratio. Therefore, for trim with propulsor off, the large change in collective pitch with advance ratio causes significant elastic coupling.

7.6.1.2 Effect of lift offset

In Fig. 7.22, the LO is increased from LO = 0.2 to LO = 0.4 at a fixed advance ratio of $\mu = 0.3$. In Fig. 7.22a, the separation between the modes is greater when compared to 7.22b. This is due to increased rotor-wake interaction when the fuselage is tilted. The effect of the LO on the aeroelastic stability is negligible for both trim procedures.

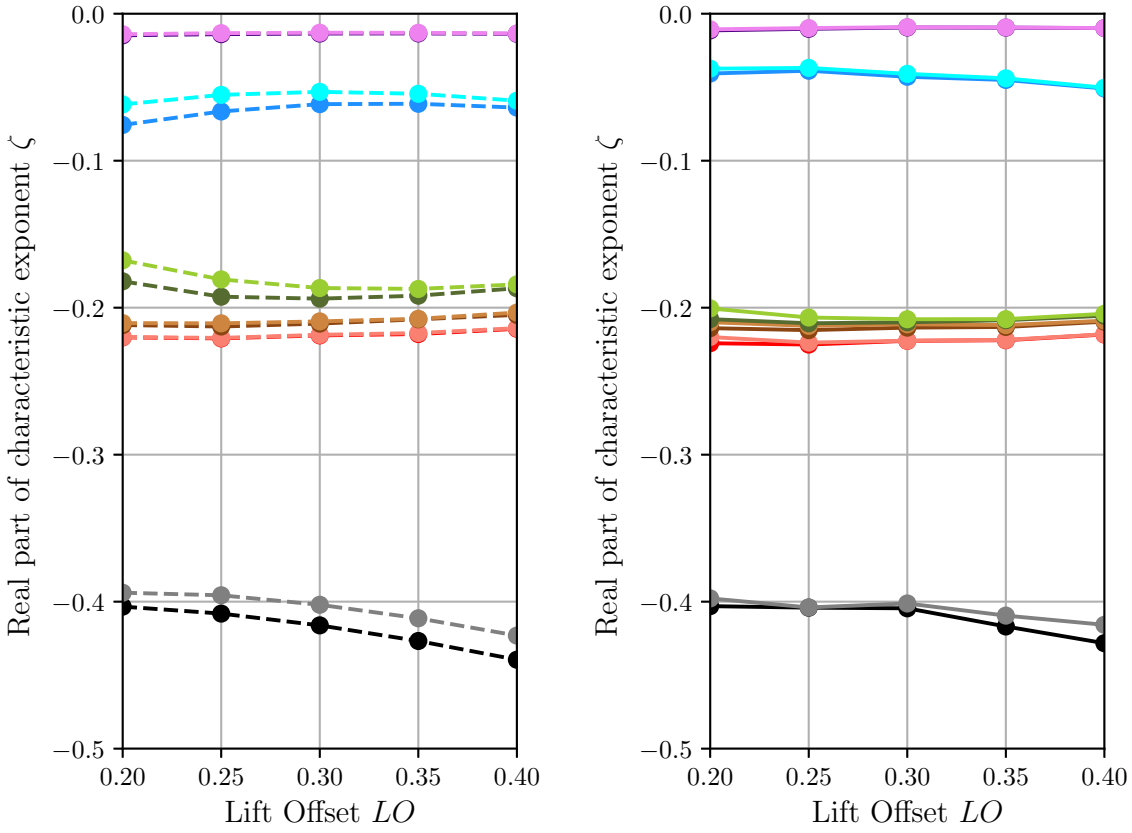

(a) Propulsor off

(b) Level attitude

Figure 7.22: Effect of lift offset on aeroelastic stability of a trimmed coaxial rotor in forward flight ($\mu = 0.3$)

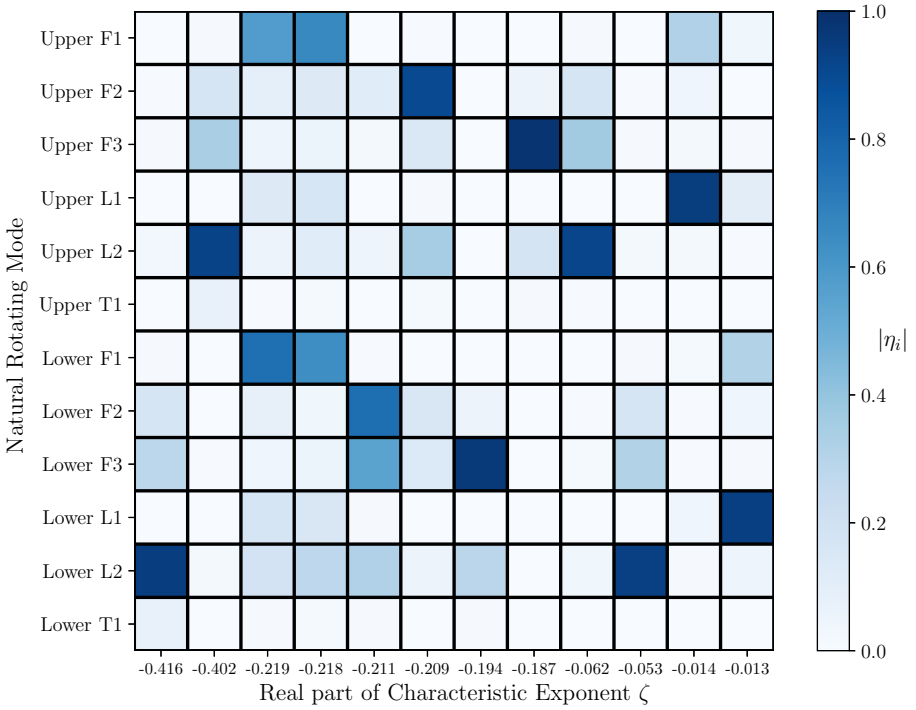

(a) $\mu = 0.3$

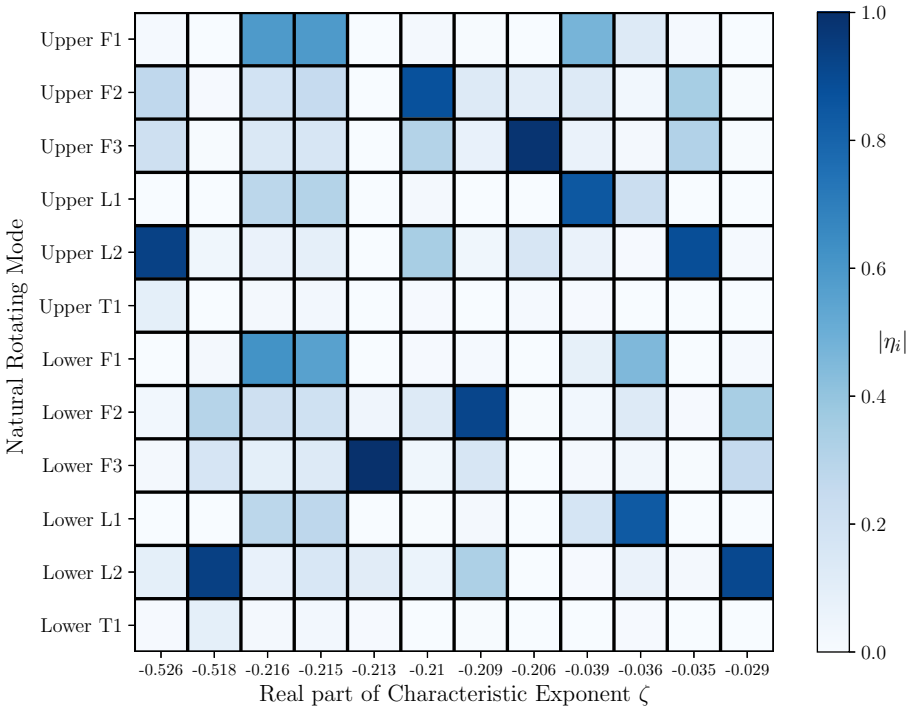

(b) $\mu = 0.5$

Figure 7.23: Effect of advance ratio on modal coupling for a coaxial rotor in forward flight with propulsor off (LO = 0.3)

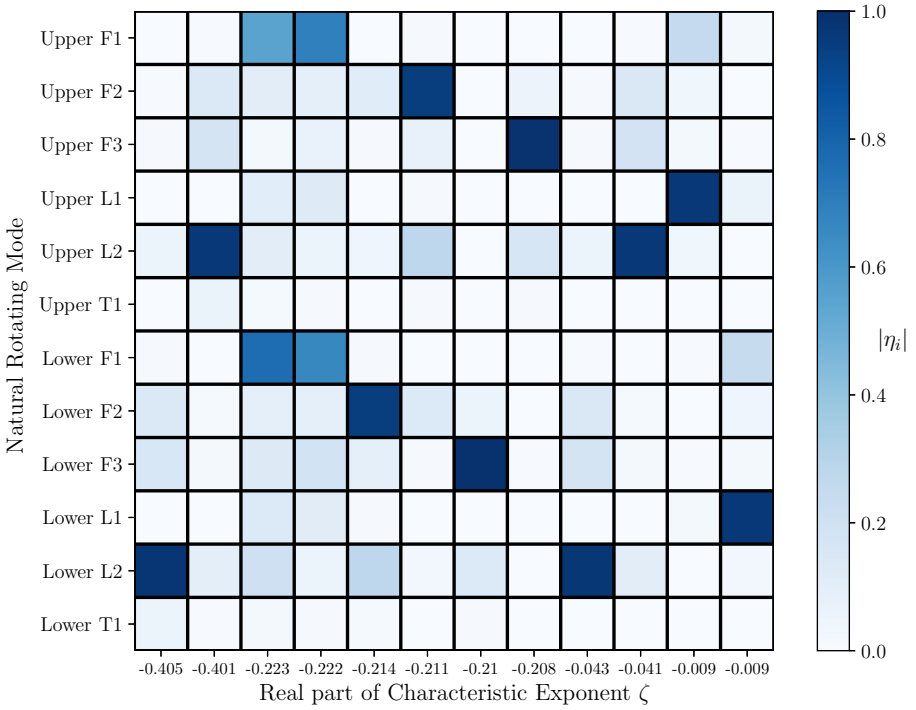

(a) $\mu = 0.3$

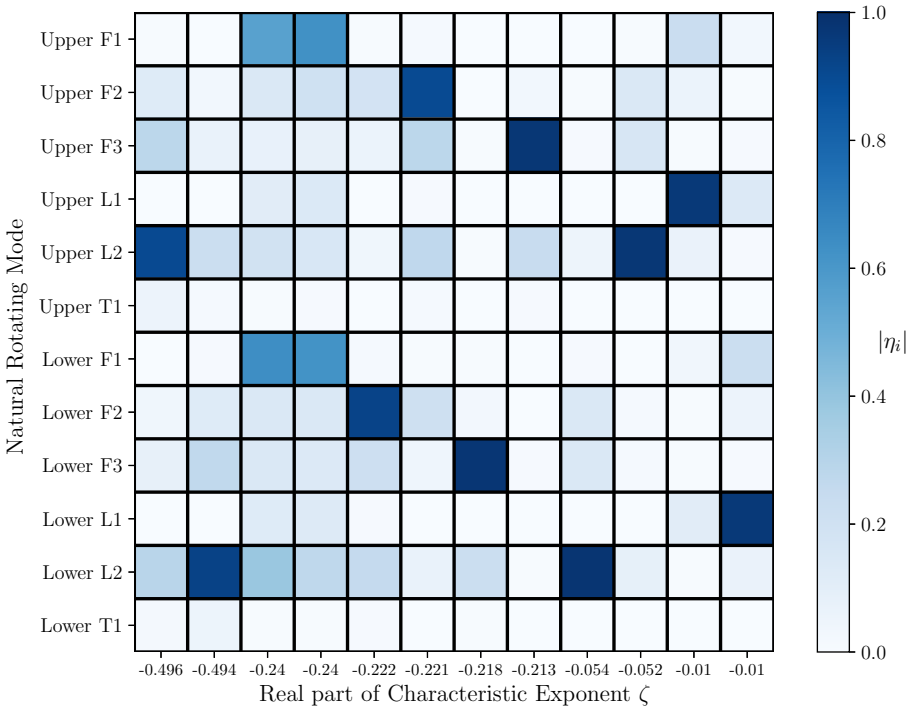

(b) $\mu = 0.5$

Figure 7.24: Effect of advance ratio on modal coupling for a coaxial rotor in forward flight at level attitude (LO = 0.3)

7.6.2 Modal coupling

7.6.2.1 Effect of advance ratio

The reduced eigenvectors for the coaxial rotor in forward flight are shown in Figs. 7.23 and 7.24. The results for trim with propulsor off are shown in Fig. 7.23. The two right most columns of the matrix in Fig. 7.23a are the two least stable modes ($\zeta = -0.013$ and $\zeta = -0.014$). The color distribution in each column indicates that the least stable mode is dominated by the lower rotor first lag mode, and the second least stable mode is dominated by the upper rotor first lag mode. Note for hover results in Fig. 6.12, the upper rotor was less stable compared to the lower rotor. The real parts of the characteristic exponents of the least stable modes in hover are $\zeta = -0.021$, whereas in forward flight the value is reduced to $\zeta = -0.013$. Therefore, forward flight at $\mu = 0.3$ with propulsor off has a lower stability margin when compared to hover. The third and fourth columns of the matrix ($\zeta = -0.219$ and $\zeta = -0.218$) are coupled first flap modes of the upper and lower rotor respectively. Therefore the inter-rotor coupling in hover persists in forward flight as well.

Increasing the advance ratio to $\mu = 0.5$ increases the stability margin. The two least stable modes in Fig. 7.23b have larger magnitudes of the real parts of the characteristic exponents ($\zeta = -0.035$ and $\zeta = -0.029$). Note that the two eigenvectors are dominated by the second lag mode of the lower and upper rotor respectively. Therefore, increasing the advance ratio changes the order of stability of the modes. This change in stability of the modes is also evident in Fig. 7.21a. The blue and violet lines representing the second lag mode and the first lag mode overlap each other at $\mu = 0.5$, indicating the stability margins of the modes is similar.

The reduced eigenvector matrices for trim at level attitude are shown in Fig. 7.24.

Increasing the advance ratio from $\mu = 0.3$ in Fig. 7.24a to $\mu = 0.5$ in Fig. 7.24b does not change the modal coupling significantly. However the stability margins increase. The two least stable modes at $\mu = 0.3$ are the first lag modes of the lower and upper rotor respectively ($\zeta = -0.009$). As the advance ratio increases to $\mu = 0.5$ in Fig. 7.24b, the magnitude of the real parts of the characteristic exponents increases to $\zeta = -0.01$.

The modal coupling does not change significantly with trim at level attitude due to the collective pitch settings. The change in collective pitch with advance ratio is negligible, therefore the elastic coupling between the flap and lag modes is not affected.

7.6.2.2 Effect of lift offset

The LO did not have a significant effect on the modal coupling for trim with propulsor off. Therefore only results for trim at level attitude are presented. In Fig. 7.25, the reduced eigenvector matrices at an advance ratio of $\mu = 0.3$ are calculated for LO settings of LO = 0.2 and LO = 0.4.

In Fig. 7.25a, the two least stable modes at LO = 0.2 are dominated by the first lag modes of the lower and upper rotor ($\zeta = -0.011$). However, at LO = 0.4 in Fig. 7.25b, the two least stable modes have a strong inter-rotor first lag mode coupling, and the stability margin is reduced ($\zeta = -0.010$).

The inter-rotor coupling of the first flap modes is also affected by the change in LO. In Fig. 7.25a, the third and fourth eigenvectors ($\zeta = -0.224$ and $\zeta = -0.220$) are dominated by the lower rotor and upper rotor first flap modes. Increasing the LO to 0.4 in Fig. 7.25b, couples the first flap and second lag modes of both rotors. In

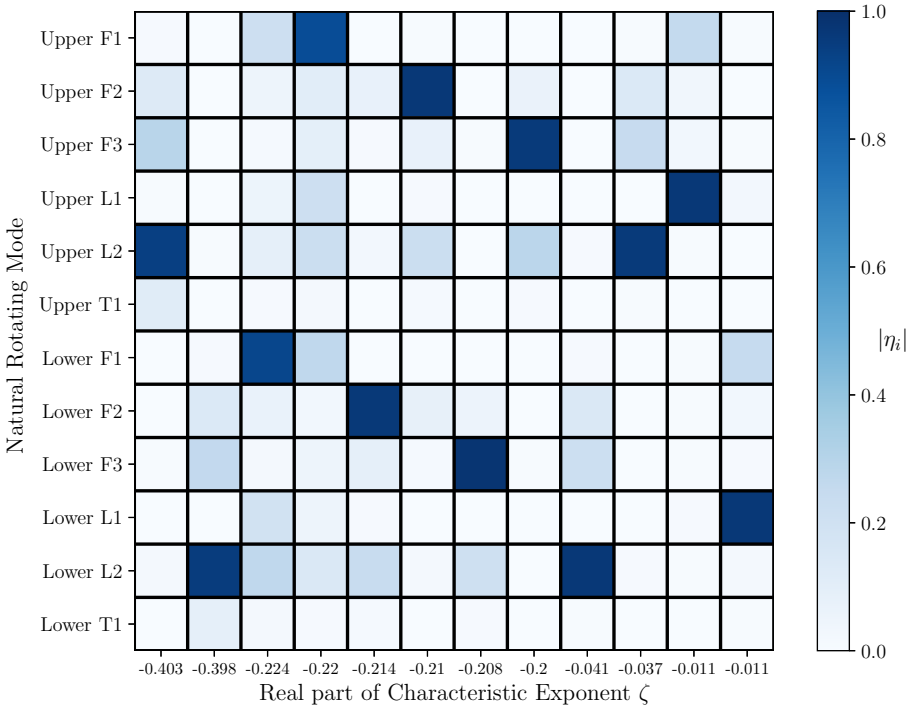

(a) LO = 0.2

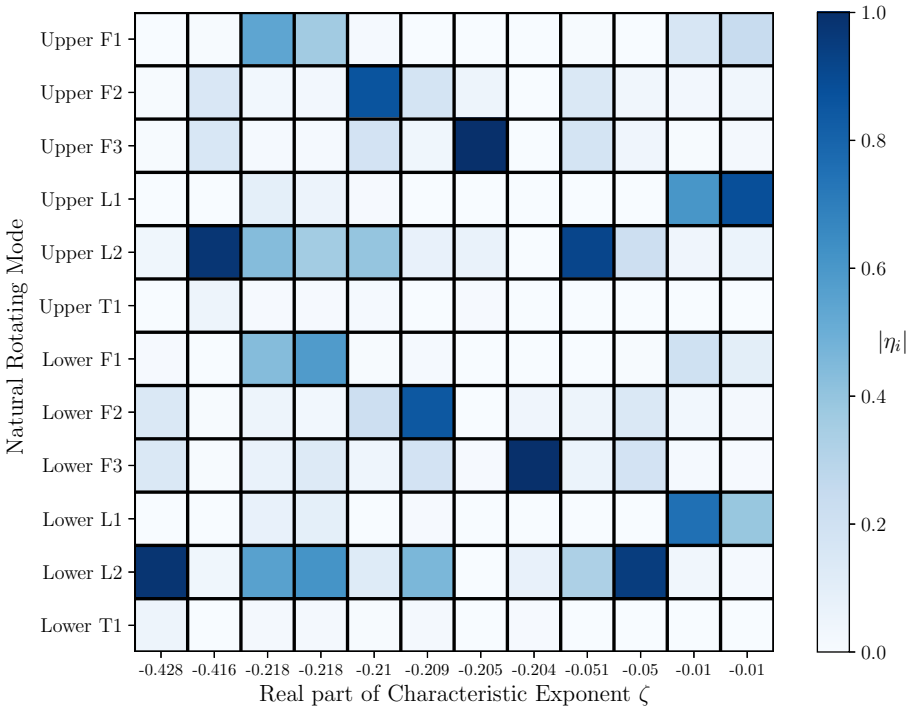

(b) LO = 0.4

Figure 7.25: Effect of lift offset on modal coupling for a coaxial rotor in forward flight at level attitude ($\mu = 0.3$)

addition, the stability margin is reduced to $\zeta = -0.218$.

Therefore, increasing the LO increases the inter-rotor coupling of the flap and lag modes of the coaxial rotor when trimmed at level attitude. Note that the inter-rotor coupling is a consequence of just the aerodynamic interactions between the two rotors because the inertial and elastic loads of the hub connecting the two rotors are not modeled in the analysis. The periodic blade passage effect combines with the high dynamic pressure on the advancing side of the rotor to produce the inter-rotor flap-lag coupling.

7.7 Rotor tip path plane

The tip path plane of the coaxial rotor at $\mu = 0.4$ is shown in Fig. 7.26. The blue and red dots represent the location of the upper and lower rotor hubs respectively. The rear and side views of the rotor clearly indicate that the blades are well separated and blade strike does not appear to be a concern. The aft view (Fig. 7.26b) indicates that the upper and lower rotor tip path planes are tilted in opposing directions. The upper rotor is tilted towards the left by an angle of 3.4^o whereas the lower rotor is tilted right by an angle of 3.5^o. Therefore, the blade tip on the retreating side of the upper rotor and the advancing side of the lower rotor ($Y/R = -1$) are closest to each other, and are separated by a distance of $9\%R$. On the other hand, the blade tip on the advancing side of the upper rotor and the retreating side of the lower rotor ($Y/R = 1$) are separated from each other by a distance of $20\%R$. The proximity of the blades affects the interaction between the bound circulation and the wake. Therefore, the interaction effects on a coaxial rotor in forward flight are not symmetric about the $\boldsymbol{X}$ axis. Therefore, the structural deformation of the stiff blades is important for accurate modeling of the aerodynamic interactions on coaxial rotors.

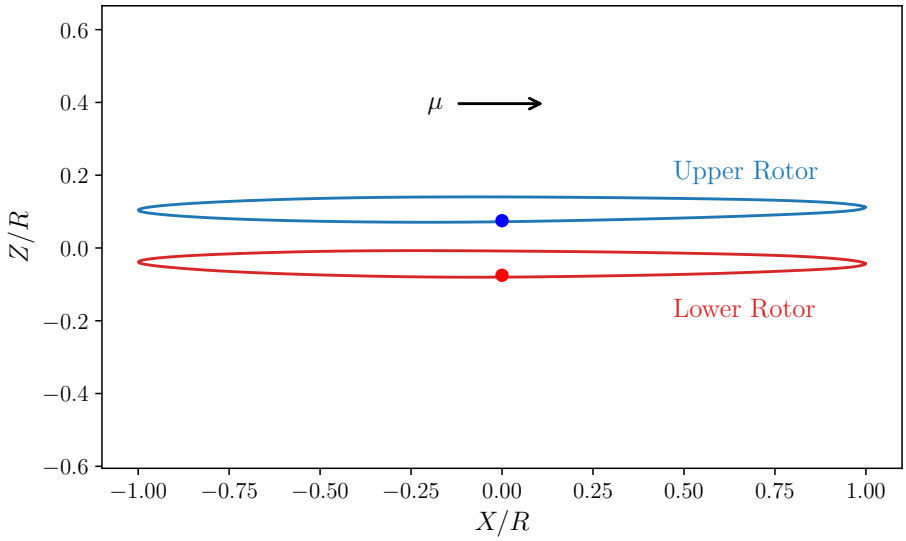

(a) Side view

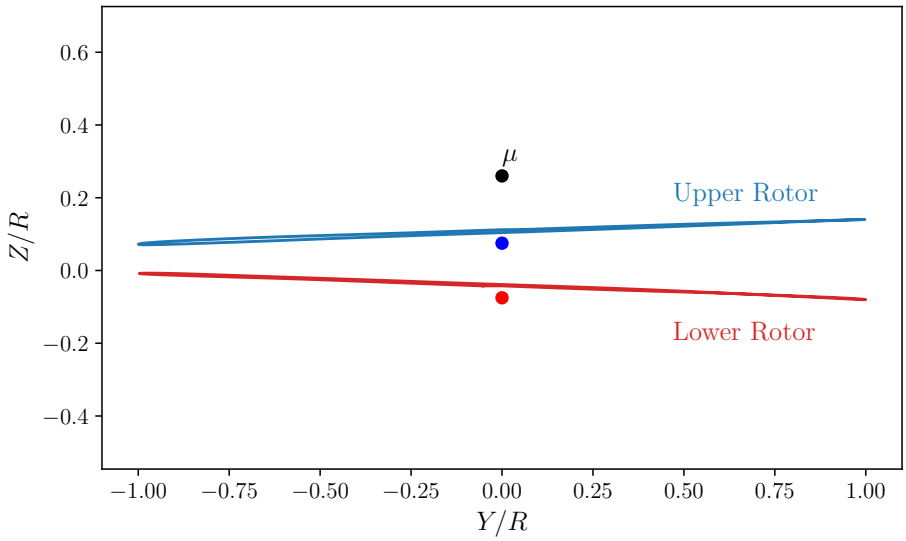

(b) Aft View

Figure 7.26: Tip path plane for the coaxial rotor at $\mu = 0.4$.

CHAPTER 8

Concluding Remarks

This dissertation is a fundamental and detailed aeromechanical analysis of a hingeless coaxial rotor in hover and forward flight. The aeroelastic formulation is tailored to overcome challenges in coaxial rotor structural, aerodynamic, and wake modeling. The computational results provide a unique and novel insight into the flow physics and aeroelastic interactions that take place in a coaxial rotor, and provide an improved physical understanding of this complex system. Thus, the work presented in this thesis makes an important contribution to the design and development of the next generation of high speed coaxial rotor helicopters.

8.1 Conclusions

The CFD-RFA model was verified with CFD results for a 2D pitching airfoil in Sec. 3.2.4. The VVPM was verified for the case of a translating vortex ring in Sec. 4.2.4. The combined CFD-RFA and VVPM models were validated with experimental data from the UT Austin SMR and coaxial rotor in Sec. 6.1. Therefore, the combined aeroelastic formulation is appropriate for the examination of full scale coaxial rotor behavior in hover and forward flight. The principal results for a coaxial rotor resembling the X2TD are summarized next:

1. In hover, the mean upper rotor thrust is greater than lower rotor thrust at all collective pitch settings in hover trim. Yaw equilibrium is enforced by using the

differential collective pitch input $\Delta\theta_0$. The wake induced inflow is larger for the lower rotor compared to the upper rotor, therefore the effective angle of attack of blade sections in the lower rotor is reduced. The effect of the mean blade induced bound circulation is negligible compared to the wake induced inflow. Therefore, the lower rotor thrust is reduced when compared to the upper rotor.

2. The coaxial rotor experiences 8/rev blade passage loads in hover. The blade passage effect is due to the periodic change in proximity of the counter-rotating upper and lower rotor blades. The changing distance between the blades influences the velocity induced by the blade bound circulation. The blade bound circulation induced velocity is the primary cause of the blade passage effect because the magnitude of the 8/rev blade bound circulation induced inflow oscillations are greater than the oscillations in wake induced inflow. The blade passage effect can only be captured by an accurate model of the blade bound circulation interactions and an accurate unsteady spanwise aerodynamic loading model.

3. The blade passage effect generates 8/rev periodic loads on both the upper and lower rotor. The oscillations in the upper and lower rotor are in phase, and combine to generate oscillatory vertical hub loads of a magnitude nearly 20% of the mean thrust on the coaxial rotor hub. Despite the mean thrust of the lower rotor being smaller when compared to the upper rotor in hover, the 8/rev oscillatory loads on the lower rotor are greater than the loads on the upper rotor. The oscillatory hub loads are higher on the lower rotor due to the oscillatory wake induced inflow. The oscillatory wake induced inflow is greater on the lower rotor compared to the upper rotor because the wake vortices are closer to the lower rotor. The oscillatory wake induced inflow is concentrated near the tip of the blade where the dynamic pressures are high. Therefore, the lower rotor

experiences larger oscillatory loads compared to the upper rotor.

4. It was found that the aeroelastic stability of the coaxial rotor in hover is governed by equations with periodic coefficients and stability has to be determined from Floquet analysis of the periodic system. The coaxial rotor modes were stable at all collective pitch settings tested $\theta_0 = 8^o - 15^o$. However, the modes exhibited non-linear behavior with changing collective pitch due to aeroelastic coupling.

5. The first lag modes of the coaxial rotors are the least stable in hover. However, the stability margin of the first lag modes is almost double that of a SMR with the same blades for hover. Therefore, the coaxial rotor aerodynamic environment improves the lag mode stability of the stiff hingeless blade. The stability of the first lag mode is relatively insensitive to increase in collective pitch and rotor thrust.

6. A new graphical method for examining modal coupling in coaxial rotors was developed and presented. The method allows the identification of coupling of modes between the upper and lower rotor. The upper and lower rotor first flap modes are strongly coupled in hover due to aerodynamic interaction effects captured using a combination of CFD-RFA and VVPM. Increasing the collective pitch increases the elastic coupling between the flap and lag modes of each blade. Therefore, at high hover thrust, the coupling between the flap and lag modes increases. Due to the increased collective pitch, the aerodynamic loads on both rotors are also increased. The increase in aerodynamic loads increases the aerodynamic interactions between the two rotors, and therefore the inter-rotor coupling also increases.

7. Two types of forward flight trim procedures were considered: one with propulsor off and one with propulsor on at level attitude. In trim with propulsor off,

the fuselage tilt increases from $\alpha_f = 5^o$ at an advance ratio of $\mu = 0.3$ to nearly $\alpha_f = 14^o$ at an advance ratio of $\mu = 0.5$. In trim at level attitude, the fuselage tilt is maintained at $\alpha_f = 0^o$ at all advance ratios. The forward thrust is provided by the propulsor, therefore the main rotor only generates lift to balance the weight of the helicopter.

8. In trim with propulsor off, the collective pitch and cyclic requirements are greater compared to trim at level attitude. The control inputs required increase because the rotor provides both lift and forward thrust with the propulsor off. For trim in level attitude, the control inputs do not change significantly ($|\Delta\theta| < 2^o$) between advance ratios of $\mu = 0.3$ and $\mu = 0.5$.

9. Increasing the LO from 0.2 to 0.4 at an advance ratio of $\mu = 0.3$ changes the control input for both types of trim. The fuselage tilt increases by 1.75^o for trim with propulsor off. The collective pitch decreases by 0.5^o for trim with propulsor off, and decreases by 1.5^o for trim at level attitude. The collective pitch decreases because as the LO increases, the center of lift of each rotor moves towards the advancing side. The dynamic pressure increases, therefore less collective pitch is required to generate the same amount of force. The lateral cyclic increases by 2^o for both types of trim to balance the change in rolling and pitching moment due to the change in LO. The longitudinal cyclic increases by nearly 4^o with increase in LO. The longitudinal cyclic primarily controls the roll moment at the hub, therefore it affects the LO more than the rest of the control inputs.

10. A coaxial rotor trimmed at level attitude is more efficient compared to a coaxial rotor with propulsor off. The coaxial rotor power requirement at zero fuselage tilt is nearly one-third compared to the power requirement with propulsor off at $\mu = 0.5$. Increasing the advance ratio increases the power requirement for

trim with propulsor off, however it decreases the power requirement for trim at level attitude. Similarly, increasing the LO increases the power requirement for trim with propulsor off, however it decreases the power requirement for trim at level attitude. Therefore, a coaxial rotor at level attitude is capable of using a combination of LO and higher advance ratio more efficiently.

11. In forward flight, the coaxial rotor experiences both 4/rev and 8/rev hub loads. The magnitude of the vertical hub force, roll moment and pitch moment are highest. These oscillatory loads are due to the complex inflow distribution generated by the wake and blade bound circulation on the upper and lower rotors. The 8/rev vertical hub force is greater than the 4/rev component at both advance ratios. This implies that the blade passage effect is significant in forward flight.

12. The vibratory vertical hub force and pitching moments on the coaxial rotor hub are larger for trim with propulsor off compared to trim at level attitude. The loads are increased due to the strong region of upflow near the hub with propulsor off. The upflow is due to the bound circulation induced component of the inflow. Hence, an accurate model of blade circulation and unsteady spanwise aerodynamic loads is required to capture the vibratory hub loads for a coaxial rotor in forward flight.

13. The separated wake modifies the inflow distribution over the rotor, and therefore affects the vibratory loads. The 4/rev and 8/rev vertical hub shears increase by 8-9% due to the inclusion of the separated wake. The 8/rev pitching moment increases by 18% due to the separated wake. Therefore, modeling the separated wake is important for accurate computation of the vibratory hub loads of the coaxial rotor in forward flight.

14. Increasing the LO from 0.2 to 0.4 decreases the hub loads. Increasing the LO

offloads the retreating side and increases the loads on the advancing side of the rotor. Therefore, the vibratory loads due to the DS effects, on the retreating side, are reduced with increase in advance ratio.

15. The coaxial rotor aeroelastic modes were stable at all advance ratios and LOs considered in this study. The least stable modes at $\mu = 0.3$ were the first lag modes of the lower rotor and upper rotor. However, in hover, the upper rotor first lag mode was less stable compared to the lower rotor. In addition, the stability of the first lag modes at $\mu = 0.3$ decreased by a factor of two compared to the least stable modes in hover. Therefore, the lag mode aeroelastic stability margin decreases from hover to advance ratios of $\mu = 0.3$.

16. For trim with propulsor off, increasing the advance ratio from $\mu = 0.3$ to $\mu = 0.5$ increases the stability margin of the least stable modes of the coaxial rotor. However, for trim at level attitude, the stability margin improves only marginally. Therefore, the lag modes are less stable in trim with level attitude compared to trim with propulsor off.

17. For trim with propulsor off, the first lag mode of the lower rotor was the least stable mode at $\mu = 0.3$. At $\mu = 0.5$, the least stable modes are the second lag modes due to the increased aeroelastic coupling in trim with propulsor off. In comparison, for trim at level attitude, the first lag modes are the least stable at both advance ratios.

18. Increasing the LO increases the inter-rotor coupling of the flap and lag modes of the coaxial rotor when trimmed at level attitude. The inter-rotor coupling is due only to the aerodynamic interactions between the two rotors, since the inertial and elastic loads of the hub connecting the two rotors are not modeled. The periodic blade passage effect combined with the high dynamic pressure on the advancing side of the rotor to produce the inter-rotor flap-lag coupling.

19. The tip path plane of the upper rotor and lower tilts by approximately 3.5^o towards the retreating side of each rotor at $\mu = 0.4$. Due to the close proximity of the blades, the influence of the bound circulation and wake between the two rotors increases. Therefore, the interaction effect between the two rotors is not symmetric about the $\boldsymbol{X}$ axis. This result implies that structural deformations of the stiff blades have to be included in order to capture the blade passage effect in forward flight.

8.2 Summary of key contributions

The formulation and solution of the coaxial rotor aeromechanical problem in this dissertation resulted in a number of new contributions to the field as summarized next:

1. A novel comprehensive coaxial rotor aeroelastic analysis was developed combining hingeless non-uniform blade structural dynamics, unsteady spanwise aerodynamic loading with the CFD-RFA approach, and wake modeling using the VVPM. The combination of the CFD-RFA model and the VVPM is a major advancement over conventional lifting-line and free wake models, and can capture the unsteady loads and complex rotor-wake interactions present in a coaxial rotor environment.

2. The ONERA-DS model was extended to capture 3D effects of DS and flow separation. A separated wake structure was modeled using vortex particles generated from the LE. The inclusion of the separated wake system modified the rotor vibratory loads, indicating its importance in a high speed coaxial rotor system. The separated wake has not been modeled in previous rotorcraft research.

3. Two different types of trim procedures were developed for a coaxial rotor in forward flight: one with propulsor off, and another one at level attitude. These trim formulations for coaxial rotor have not been described in literature previously. The results indicated that the level attitude trim is beneficial in reducing the rotor power requirement.

4. For the first time in literature, the coaxial rotor in hover was identified as a periodic system and an appropriate periodic aeroelastic stability analysis was used. A new graphical approach for identifying the modal coupling of the coaxial rotor aeroelastic modes was developed. A unique inter-rotor coupling of modes due to aerodynamic interactions was identified.

5. In forward flight, the trim condition, advance ratio and LO had a significant effect on the stability of blade modes. The lag mode stability was reduced at $\mu = 0.3$ compared to hover. For trim with propulsor off, the stability increased at $\mu = 0.5$. However, for trim at level attitude, the stability did not change. This result is different from the behavior of the lag mode of the SMR hingeless blade, where high advance ratios are destabilizing.

6. The effects of collective pitch, advance ratio, LO and separated wake on the vibratory hub loads and inflow distribution were studied in detail. The vibratory hub loads were examined using detailed comparison of the wake induced and bound circulation induced inflow distributions. The bound circulation induced inflow was identified as the primary source of the blade passage effect.

8.3 Recommendations for future research

The aeromechanical analysis of coaxial rotors in this dissertation has revealed several avenues for future research with potential for improving the aeroelastic modeling of

the coaxial rotor wake systems.

A Finite Element (FE) based hingeless blade model is required for modeling advanced composite coaxial rotor configurations. The FE blade model can represent the complex geometry including blade tip sweep and anisotropic material properties accurately.

The aeroelastic effects of slowing the coaxial rotor were not studied in this dissertation. Therefore, the current analysis has to be extended to examine the effect of reduced rotor RPM at high speed.

The trim analysis can be improved by including propulsor, fuselage and empennage models. At high speed flight, the aerodynamic loads on the fuselage and tail surfaces make significant contributions to the trim. Furthermore, the propulsor thrust and rotor RPM should be included as additional trim variables. In addition, the control settings can be optimized to reduce vibratory hub loads.

The VVPM calculations required the largest computational effort in the simulations. The development of fast algorithms for computing N-body particle interactions is an active area of research in applied mathematics. Algorithms for efficient implementation of FMM on exascale parallel systems have been developed [216, 217]. Fast parallel *TreeCodes* can improve computational times for VVPM calculations [218–220]. Therefore, the improvement in computational algorithms for VVPM calculations can permit using a larger number of vortex particles, thus enhancing the wake resolution.

A hybrid CFD-VVPM analysis can be developed to improve the unsteady spanwise

aerodynamic load calculations. The CFD-RFA and ONERA-DS are fundamentally 2D models. Therefore, they lack the accuracy required to capture pressure distributions over the blade surface, as well as high speed flow effects at the tip. A few preliminary studies have applied a hybrid CFD-VVPM method to helicopter configurations [95, 96]. However, the effectiveness of this approach has not been explored.

The acoustic characteristics of the coaxial configuration have not been studied in detail. Experimental acoustic data is limited [221]. The recent interest in coaxial helicopters has led to preliminary aeroacoustic studies [222–225]. The aeromechanical analysis presented in this dissertation is an improvement over previous studies, and therefore can be extended to improve the acoustic models of coaxial helicopters.

Other potential applications of this research include structural optimization of the rotor blade and control studies to reduce rotor vibrations.

APPENDIX A

Blade Kinematics

A.1 Counter-clockwise rotating blade

The angular velocity of the point $\boldsymbol{P}$ due to the rotation of the blade is:

$$\boldsymbol{\omega}_b = \Omega \widehat{\boldsymbol{k}}_h \tag{A.1}$$

The angular velocity of the deformed blade frame with respect to the point P:

$$\boldsymbol{\omega}_d = \dot{v}_{,x} \widehat{\boldsymbol{k}}_b - \dot{w}_{,x} \widehat{\boldsymbol{j}}_b \tag{A.2}$$

The total velocity of the point $\boldsymbol{P'}$ is:

$$\boldsymbol{v}_{P'} = \dot{\boldsymbol{P}}' + \boldsymbol{\omega}_b \times \boldsymbol{P}' + \boldsymbol{\omega}_d \times (\boldsymbol{P}' - \boldsymbol{P}) \tag{A.3}$$

The net velocity in the undeformed blade frame is:

$$\begin{aligned} \boldsymbol{v}_{P'} &= [\dot{u} - (\Omega + \dot{v}_{,x})v - \dot{w}_{,x} w] \widehat{\boldsymbol{i}}_b \\ &\quad + [\dot{v} + \Omega(x + e + u) + u\dot{v}_{,x} - \Omega\beta_p(w - e\beta_p)] \widehat{\boldsymbol{j}}_b \\ &\quad + [\dot{w} + \Omega v \beta_p + \dot{w}_{,x} u] \widehat{\boldsymbol{k}}_b \end{aligned} \tag{A.4}$$

The total acceleration of the point P' is calculated using the kinematic expression:

$$\boldsymbol{a}_{P'} = \dot{\boldsymbol{v}}_{P'} + \boldsymbol{\omega}_b \times \boldsymbol{v}_{P'} + \boldsymbol{\omega}_d \times (\boldsymbol{v}_{P'} - \boldsymbol{v}_P) \tag{A.5}$$

The acceleration in the undeformed blade coordinate system is:

$$\begin{aligned}
\boldsymbol{a}_{P'} &= \{\ddot{u} - \Omega^2(x+e+u) + \Omega^2\beta_p(w-\beta_p e) - 2\Omega(\dot{v} + \dot{v}_{,x}u + \dot{v}\dot{v}_{,x} + \dot{w}\dot{w}_{,x}) \\
&\quad +\Omega\beta_p(\dot{v}_{,x}w - \dot{w}_{,x}v) - (\ddot{v}_{,x}v + \ddot{w}_{,x}w) - u(\dot{v}_{,x}^2 + \dot{w}_{,x}^2)\}\widehat{\boldsymbol{i}}_b \\
&\quad +\{\ddot{v} + \ddot{v}_{,x}u - \Omega^2 v(1+\beta_p^2) + 2\Omega(\dot{u} - \dot{v}_{,x}v - \dot{w}\beta_p) \\
&\quad -\Omega\dot{w}_{,x}(\beta_p u + w) + 2\dot{u}\dot{v}_{,x} - \dot{v}_{,x}(\dot{v}_{,x}v + \dot{w}_{,x}w)\}\widehat{\boldsymbol{j}}_b \\
&\quad +\{\ddot{w} + \ddot{w}_{,x}u + \Omega^2\beta_p[x + e + u - \beta_p(w - \beta_p e)] \\
&\quad +2[\Omega\dot{v}\beta_p + \dot{u}\dot{w}_{,x}] + \Omega[\dot{v}_{,x}\beta_p u - \dot{w}_{,x}v] - \dot{w}_{,x}(\dot{v}_{,x}v + \dot{w}_{,x}w)\}\widehat{\boldsymbol{k}}_b
\end{aligned} \tag{A.6}$$

A.2 Clockwise rotating blade

For a clockwise rotating blade, the sign of the angular velocities changes:

$$\boldsymbol{\omega}_{b^*} = -\Omega\widehat{\boldsymbol{k}}_h^* \tag{A.7}$$

$$\boldsymbol{\omega}_{d^*} = -\dot{v}_{,x}\widehat{\boldsymbol{k}}_b^* + \dot{w}_{,x}\widehat{\boldsymbol{j}}_b^* \tag{A.8}$$

In the undeformed clockwise blade system, the velocity of the point is similar to that previously calculated:

$$\begin{aligned}
\boldsymbol{v}_{P^{*\prime}} &= [\dot{u} - (\Omega + \dot{v}_{,x})v - \dot{w}_{,x}w]\widehat{\boldsymbol{i}}_b^* \\
&\quad +[\dot{v} + \Omega(x+e+u) + u\dot{v}_{,x} - \Omega\beta_p(w - e\beta_p)]\widehat{\boldsymbol{j}}_b^* \\
&\quad +[\dot{w} + \Omega v\beta_p + \dot{w}_{,x}u]\widehat{\boldsymbol{k}}_b^*
\end{aligned} \tag{A.9}$$

The acceleration in the undeformed blade coordinate system is:

$$
\begin{aligned}
\boldsymbol{a}_{P^{*\prime}} &= \{\ddot{u} - \Omega^2(x+e+u) + \Omega^2\beta_p(w-\beta_p e) - 2\Omega(\dot{v} + \dot{v}_{,x}u + \dot{v}\dot{v}_{,x} + \dot{w}\dot{w}_{,x}) \\
&\quad +\Omega\beta_p(\dot{v}_{,x}w - \dot{w}_{,x}v) - (\ddot{v}_{,x}v + \ddot{w}_{,x}w) - u(\dot{v}_{,x}^2 + \dot{w}_{,x}^2)\}\widehat{\boldsymbol{i}}_b^* \\
&\quad +\{\ddot{v} + \ddot{v}_{,x}u - \Omega^2 v(1+\beta_p^2) + 2\Omega(\dot{u} - \dot{v}_{,x}v - \dot{w}\beta_p) \\
&\quad -\Omega\dot{w}_{,x}(\beta_p u + w) + 2\dot{u}\dot{v}_{,x} - \dot{v}_{,x}(\dot{v}_{,x}v + \dot{w}_{,x}w)\}\boldsymbol{y}_b^* \\
&\quad +\{\ddot{w} + \ddot{w}_{,x}u + \Omega^2\beta_p[x+e+u-\beta_p(w-\beta_p e)] \\
&\quad +2[\Omega\dot{v}\beta_p + \dot{u}\dot{w}_{,x}] + \Omega[\dot{v}_{,x}\beta_p u - \dot{w}_{,x}v] - \dot{w}_{,x}(\dot{v}_{,x}v + \dot{w}_{,x}w)\}\widehat{\boldsymbol{k}}_b^* \qquad \text{(A.10)}
\end{aligned}
$$

Therefore, the choice of this clockwise rotating coordinate system is advantageous because the expressions for velocity and accelerations are the same as that of the counter-clockwise system.

APPENDIX B

Free Vibration Mode Shapes and Frequencies

The general expression of the vibration problem is:

$$[\boldsymbol{M}]\ddot{\boldsymbol{\chi}} + [\boldsymbol{K}]\boldsymbol{\chi} = \mathbf{0} \tag{B.1}$$

The $\boldsymbol{\chi}$ vector represents the generalized coordinates, i.e. the coefficients of the *non-rotating* mode shapes $\varphi_n(x)$ and $\vartheta_n(x)$ of a uniform cantilevered beam. The mass $[\boldsymbol{M}]$ and stiffness $[\boldsymbol{K}]$ matrices are calculated using the blade flap, lag and torsional equations of motion. The rotational mode shapes and frequencies are obtained by solving the eigenvalue problem:

$$[\boldsymbol{K}]\boldsymbol{\chi} = \omega^2[\boldsymbol{M}]\boldsymbol{\chi} \tag{B.2}$$

where $\boldsymbol{\chi}$ is the eigenvector, and ω^2 is the eigenvalue. The frequency ω is the square root of the eigenvalue.

B.1 Torsion

The torsional shape functions of the non-rotating beam are:

$$\varphi_n(x) = \sin\left(\frac{(2n-1)\pi x}{2l}\right) \tag{B.3}$$

These shape functions satisfy the boundary conditions:

$$\varphi_n(0) = 0 \tag{B.4}$$

$$GJ\frac{\mathrm{d}\varphi_n}{\mathrm{d}x}(l) = 0 \tag{B.5}$$

The mass and stiffness matrices for the torsional degree of freedom are calculated using:

$$M_{ij} = \int_0^l I_{m_x}\varphi_i\varphi_j \mathrm{d}x \tag{B.6}$$

$$K_{ij} = \int_0^l [GJ\varphi_{i,x}\varphi_{j,x} - \Omega^2\overline{I}_{m_{(y-z)}}\varphi_i\varphi_j]\mathrm{d}x \tag{B.7}$$

The i^{th} rotating mode shape Φ_i is obtained from the i^{th} eigenvector $\boldsymbol{\chi}_i$:

$$\Phi_i(x) = \sum_{n=0}^{m_T} \boldsymbol{\chi}_{i_n}\varphi_n(x) \tag{B.8}$$

where m_T are the number of non-rotating torsional modes.

B.2 Bending

The non-rotating bending modes of the cantilevered beam are identical in flap and lag.

$$\begin{aligned}\vartheta_n(x) &= \frac{1}{2}\left[\left\{\cosh\left(\frac{\varsigma_n x}{l}\right) - \cos\left(\frac{\varsigma_n x}{l}\right)\right\}\right. \\ &\quad \left. + \left\{\sin\left(\frac{\varsigma_n x}{l}\right) - \sinh\left(\frac{\varsigma_n x}{l}\right)\right\}\left(\frac{\cosh(\varsigma_n) + \cos(\varsigma_n)}{\sin(\varsigma_n) + \sinh(\varsigma_n)}\right)\right]\end{aligned} \tag{B.9}$$

where ς_n is the n^{th} root of

$$\cos(\varsigma_n)\cosh(\varsigma_n) + 1 = 0 \tag{B.10}$$

These bending shapes satisfy the following boundary conditions:

$$\vartheta_n(0) = 0 \tag{B.11}$$

$$\frac{\mathrm{d}\vartheta_n}{\mathrm{d}x}(0) = 0 \tag{B.12}$$

$$-EI\frac{\mathrm{d}^2\vartheta_n}{\mathrm{d}x^2}(l) = 0 \tag{B.13}$$

$$-EI\frac{\mathrm{d}^3\vartheta_n}{\mathrm{d}x^3}(l) = 0 \tag{B.14}$$

Lag

The lag mass and stiffness matrices are calculated using the following equations:

$$M_{ij} = \int_0^L [m\vartheta_i\vartheta_j + \overline{I}_{m_z}\vartheta_{i,x}\vartheta_{j,x}]dx \tag{B.15}$$

$$K_{ij} = \int_0^L [T_c\vartheta_{i,x}\vartheta_{j,x} - m\Omega^2\vartheta_i\vartheta_j + \overline{EI}_z\vartheta_{i,xx}\vartheta_{j,xx}]dx \tag{B.16}$$

The i^{th} rotating mode shape V_i is obtained from the i^{th} eigenvector $\boldsymbol{\chi}_i$:

$$V_i(x) = \sum_{n=0}^{m_L} \boldsymbol{\chi}_{i_n}\vartheta_n(x) \tag{B.17}$$

where m_L are the number of non-rotating lag modes of the blade.

Flap

Similarly, the flap mass and stiffness matrices are:

$$M_{ij} = \int_0^L [m\vartheta_i\vartheta_j + \overline{I}_{m_y}\vartheta_{i,x}\vartheta_{j,x}]dx \tag{B.18}$$

$$K_{ij} = \int_0^L [T_c\vartheta_{i,x}\vartheta_{j,x} - \Omega^2\overline{I}_{m_y}\vartheta_{i,x}\vartheta_{j,x} + \overline{EI}_y\vartheta_{i,xx}\vartheta_{j,xx}]dx \tag{B.19}$$

The i^{th} rotating mode shape W_i is obtained from the i^{th} eigenvector $\boldsymbol{\chi}_i$:

$$W_i(x) = \sum_{n=0}^{m_F} \boldsymbol{\chi}_{i_n} \vartheta_n(x) \tag{B.20}$$

where m_F are the number of non-rotating flap modes of the blade.

APPENDIX C

Jacobian of Residual Equations

The Jacobian matrix required for the solution of the generalized degrees of freedom is derived analytically from Eqns. 2.52 - 2.54 and 2.58 - 2.60. The inertial term of the residual vector comprises of flap, lag and torsion components:

$$\boldsymbol{\epsilon}^I = \begin{Bmatrix} \boldsymbol{\epsilon}^I_F \\ \boldsymbol{\epsilon}^I_L \\ \boldsymbol{\epsilon}^I_T \end{Bmatrix} \tag{C.1}$$

The derivatives of the i^{th} flap component of the inertial residual term are:

$$\begin{aligned} \frac{\partial \epsilon^I_{F_i}}{\partial \ddot{a}_{F_j}} &= \int_0^l \left[-m(1+\beta_p^2) W_i W_j \right. \\ &\quad \left. + \left(\widetilde{v}_{,x}^2 \overline{I}_{m_z} - \overline{I}_{m_y} + \widetilde{v}_{,x} \beta_p \overline{I}_{m_{(y-z)_1}} \right) W_{i,x} W_{j,x} \right] \mathrm{d}x \qquad \text{(C.2)} \\ \frac{\partial \epsilon^I_{F_i}}{\partial \ddot{a}_{L_j}} &= \int_0^l \left(\widetilde{v}_{,x} \widetilde{w}_{,x} \overline{I}_{m_z} + \overline{I}_{m_{(y-z)_1}} \right) W_{i,x} V_{j,x} \mathrm{d}x \qquad \text{(C.3)} \\ \frac{\partial \epsilon^I_{F_i}}{\partial \ddot{a}_{T_j}} &= -\int_0^l \left[\widetilde{v}_{,x} \beta_p \left(\widetilde{w}_{,x} + \beta_p \right) \overline{I}_{m_x} W_{i,x} \Phi_j \right] \mathrm{d}x \qquad \text{(C.4)} \end{aligned}$$

The derivatives of the i^{th} lag component of the inertial residual term are:

$$\frac{\partial \epsilon^I_{L_i}}{\partial \ddot{a}_{F_j}} = \int_0^l \left[\left(1 - \widetilde{w}_{,x}\beta_p\right) \overline{I}_{m_{(y-z)_1}} - \widetilde{v}_{,x} \left(\widetilde{w}_{,x} + \beta_p\right) \overline{I}_{m_z} \right] \mathrm{d}x \tag{C.5}$$

$$\frac{\partial \epsilon^I_{L_i}}{\partial \ddot{a}_{L_j}} = -\int_0^l \left[\left(1 + \widetilde{w}_{,x}\beta_p + \widetilde{w}^2_{,x} + \beta_p^2\right) \overline{I}_{m_z} V_{i,x} V_{j,x} + m V_i V_j \right] \mathrm{d}x \tag{C.6}$$

$$\frac{\partial \epsilon^I_{L_i}}{\partial \ddot{a}_{T_j}} = \int_0^l \left[\widetilde{w}_{,x}\beta_p \left(\widetilde{w}_{,x} + \beta_p\right) \overline{I}_{m_x} V_{i,x} \Phi_j \right] \mathrm{d}x \tag{C.7}$$

The derivatives of the i^{th} torsion component of the inertial residual term are:

$$\frac{\partial \epsilon^I_{T_i}}{\partial \ddot{a}_{F_j}} = \int_0^l \left[\left(1 - \widetilde{w}_{,x}\beta_p\right) \overline{I}_{m_z} + \left(\widetilde{w}_{,x} + \beta_p\right) \overline{I}_{m_{(y-z)_1}} \right] \Phi_i W_{j,x} \mathrm{d}x \tag{C.8}$$

$$\frac{\partial \epsilon^I_{T_i}}{\partial \ddot{a}_{L_j}} = -\int_0^l \left[\widetilde{w}_{,x}\beta_p \left(\widetilde{w}_{,x} + \beta_p\right) \overline{I}_{m_z} + \widetilde{v}_{,x} \overline{I}_{m_{(y-z)_1}} \right] \Phi_i V_{j,x} \mathrm{d}x \tag{C.9}$$

$$\frac{\partial \epsilon^I_{T_i}}{\partial \ddot{a}_{T_j}} = -\int_0^l \left[\overline{I}_{m_x} \left(1 + \widetilde{w}_{,x}\beta_p + \widetilde{v}^2_{,x} + \widetilde{w}^2_{,x} + \beta_p^2\right) \Phi_i \Phi_j \right] \mathrm{d}x \tag{C.10}$$

Therefore, the Jacobian matrix can be assembled as:

$$\left[\frac{\partial \boldsymbol{\epsilon}^I}{\partial \ddot{\boldsymbol{a}}}\right] = \begin{bmatrix} \dfrac{\partial \boldsymbol{\epsilon}^I_F}{\partial \ddot{\boldsymbol{a}}_F} & \dfrac{\partial \boldsymbol{\epsilon}^I_F}{\partial \ddot{\boldsymbol{a}}_L} & \dfrac{\partial \boldsymbol{\epsilon}^I_F}{\partial \ddot{\boldsymbol{a}}_T} \\ \dfrac{\partial \boldsymbol{\epsilon}^I_L}{\partial \ddot{\boldsymbol{a}}_F} & \dfrac{\partial \boldsymbol{\epsilon}^I_L}{\partial \ddot{\boldsymbol{a}}_L} & \dfrac{\partial \boldsymbol{\epsilon}^I_L}{\partial \ddot{\boldsymbol{a}}_T} \\ \dfrac{\partial \boldsymbol{\epsilon}^I_T}{\partial \ddot{\boldsymbol{a}}_F} & \dfrac{\partial \boldsymbol{\epsilon}^I_T}{\partial \ddot{\boldsymbol{a}}_L} & \dfrac{\partial \boldsymbol{\epsilon}^I_T}{\partial \ddot{\boldsymbol{a}}_T} \end{bmatrix} \tag{C.11}$$

Bibliography

[1] Sikorsky, S. I., *Images of Aviation: The Sikorsky Legacy*, Arcadia Publishing, Charleston, SC, 2007.

[2] "Uncle Igor and the Chinese Top," *Time Magazine*, 16 November 1953.

[3] "Cierva C.1," jefflewis.net, Accessed: 26 March 2020, URL: http://www.jefflewis.net/graphics/aircraft/commercial_C.1.html.

[4] "Sikorsky S-69," Wikipedia, Accessed: 29 March 2020, URL: https://commons.wikimedia.org/wiki/File:XH-59_U.S._Army_demonstrator.jpg.

[5] "Mars Helicopter," NASA/JPL-Caltech, Accessed: 15 April 2020, URL: https://mars.nasa.gov/resources/24821/artists-concept-mars-helicopter/.

[6] "X2 Technology TM," Lockheed Martin, Accessed: 27 March 2020, URL: https://www.lockheedmartin.com/en-us/products/x2-helicopter-technology-demonstrator.html.

[7] "S-97 RAIDER," Lockheed Martin, Accessed: 27 March 2020, URL: https://www.lockheedmartin.com/en-us/products/s-97-raider-helicopter.html.

[8] "SB>1 Defiant," Lockheed Martin, Accessed: 27 March 2020, URL: https://www.lockheedmartin.com/en-us/products/sb1-defiant-technology-demonstrator.html.

[9] "RAIDER X TM," Lockheed Martin, Accessed: 27 March 2020, URL: https://www.lockheedmartin.com/en-us/products/fara-raider-x.html.

[10] "Lomonosov Aerodynamic Helicopter," All the World's Helicopters and Rotorcraft, Accessed: 26 March 2020, URL: http://www.aviastar.org/helicopters_eng/lomonosov.php.

[11] "Launoy & Bienvenu Helicopter," Stingray's List of Rotorcraft, Accessed: 26 March 2020, URL: https://sites.google.com/site/stingrayslistofrotorcraft/launoy--bienvenu.

[12] "Henry Bright's Helicopter," All the World's Helicopters and Rotorcraft, Accessed: 26 March 2020, URL: http://www.aviastar.org/helicopters_eng/bright.php.

[13] Leishman, J. G., *Principles of Helicopter Aerodynamics*, 2nd ed., Cambridge University Press, New York, NY, 2016.

[14] "Antonov "Helicoplane"," All the World's Helicopters and Rotorcraft, Accessed: 28 March 2020, URL: http://www.aviastar.org/helicopters_eng/antonov.php.

[15] "Ellehammer Helicopter," All the World's Helicopters and Rotorcraft, Accessed: 26 March 2020, URL: http://www.aviastar.org/helicopters_eng/ellehammer.php.

[16] "Petróczy-Kármán-Žurovec," Wikipedia, Accessed: 26 March 2020, URL: https://commons.wikimedia.org/w/index.php?curid=7930380.

[17] "Berliner Helicopter," Stingray's List of Rotorcraft, Accessed: 26 March 2020, URL: https://sites.google.com/site/stingrayslistofrotorcraft/berliner-helicopter.

[18] Boulet, J., *History of the Helicopter: as told by its Pioneers, 1907-1956*, Editions France-Empire, 1984.

[19] "Pescara Model 3 Helicopter," Wikipedia, Accessed: 28 March 2020, URL: https://commons.wikimedia.org/wiki/File:Pescara_helicopers.jpg.

[20] "Corradino D'Ascanio," Wikipedia, Accessed: 29 March 2020, URL: https://commons.wikimedia.org/wiki/File:D'Ascanio_D'AT3.jpg.

[21] "Bréguet-Dorand Gyroplane Laboratoire," Wikipedia, Accessed: 29 March 2020, URL: https://commons.wikimedia.org/wiki/File:Gyroplane-Laboratoire1.jpg.

[22] "Hiller XH-44 Hiller-Copter," Smithsonian National Air and Space Museum, Accessed: 26 March 2020, URL: https://airandspace.si.edu/collection-objects/hiller-xh-44-hiller-copter/nasm_A19530081000.

[23] "Rare Birds: No. 30's Bell's Coaxial," *Vertiflite*, March/April 1974.

[24] "Sources "probables" de Jacobs," Centaur Club, Accessed: 29 March 2020, URL: https://www.centaurclub.com/forum/viewtopic.php?f=72&t=2286&p=42881&hilit=bendix#p42881.

[25] "Gyrodyne Model 2C," Cradle of Aviation Museum and Education Center, Accessed: 29 March 2020, URL: https://www.cradleofaviation.org/history/exhibits/exhibit-galleries/the_jet_age/gyrodyne_model_2c.html.

[26] "Gyrodyne RON Rotorcycle," Wikipedia, Accessed: 26 March 2020, URL: https://commons.wikimedia.org/w/index.php?curid=8995202.

[27] "Kamov Ka-15," All the World's Helicopters and Rotorcraft, Accessed: 26 March 2020, URL: http://www.aviastar.org/helicopters_eng/ka-15.php.

[28] Burgess, R. K., "The ABC Rotor - A Historical Perspective," *American Helicopter Society 60th Annual Forum*, AHS International Inc., Baltimore, MD, June 2004.

[29] Escobar, D., Chopra, I., and Datta, A., "Aeromechanical loads on a Mars coaxial rotor," *74th Annual Forum & Technology Display*, AHS International Inc., Phoenix, Arizona, May 2018.

[30] Escobar, D., Chopra, I., and Datta, A., "Aeromechanics of a coaxial Mars helicopter using High-Fidelity CFD/CA," *75th Annual Forum & Technology Display*, Vertical Flight Society, Philadelphia, Pennsylvania, May 2019.

[31] Pipenberg, B. T., Keennon, M. T., Langberg, S. A., and Tyler, J. D., "Development of the Mars helicopter rotor system," *75th Annual Forum & Technology Display*, Vertical Flight Society, Philadelphia, Pennsylvania, May 2019, pp. 1–10.

[32] Coleman, C. P., "A Survey of Theoretical and Experimental Coaxial Rotor Aerodynamic Research," *NASA Technical Paper 3675*, Moffett Field, California, March 1997.

[33] Harrington, R. D., "Full-Scale-Tunnel Investigation of the Static-Thrust Performance of a Coaxial Helicopter Rotor," *NACA Technical Note 2318*, Langley Aeronautical Laboratory, Langley Field, Virginia, March 1951.

[34] Dingeldein, R. C., "Wind-Tunnel Studies of the Performance of Multi Rotor Configurations," *NACA Technical Note 3236*, Langley Aeronautical Laboratory, Langley Field, Virginia, August 1954.

[35] Akimov, A. I., Butov, V. P., Bourtsev, B. N., and Selemenev, S. V., "Flight Investigation of Coaxial Rotor Tip Vortex Structure," *American Helicopter Society 50th Annual Forum*, AHS International Inc., Washington, D.C., May 1994, p. 1431.

[36] McAlister, K., and Tung, C., "Experimental Study of a Hovering Coaxial Rotor with Highly Twisted Blades," *American Helicopter Society 64th Annual Forum*, Vol. 64, AHS International Inc., Montreal, Canada, April-May 2008.

[37] Ramasamy, M., "Hover Performance Measurements Toward Understanding Aerodynamic Interference in Coaxial, Tandem, and Tilt Rotors," *Journal of the American Helicopter Society*, Vol. 60, No. 3, 2015, pp. 1–17.

[38] Mula, S., Cameron, C., Tinney, C., and Sirohi, J., "Low-Dimensional Characteristics of Tip Vortices from a Coaxial Rotor in Hover," *American Helicopter Society 70th Annual Forum*, AHS International Inc., Montreal, Canada, May 2014.

[39] Cameron, C. G., Karpatne, A., and Sirohi, J., "Performance and Vibratory Hub Loads of a Mach-Scale Coaxial Rotor in Hover," *American Helicopter Society 70th Annual Forum*, AHS International Inc., Montreal, Canada, May 2014.

[40] Cameron, C. G., Uehara, D., and Sirohi, J., "Transient Hub Loads and Blade Deformation of a Mach-Scale Coaxial Rotor in Hover," *56th AIAA/ASCE/AHS/ASC Structures, Structural Dynamics, and Materials Conference*, AIAA Scitech 2015, AIAA Paper No. 2015-1412, Kissimmee, Florida, January 2015.

[41] Cameron, C., and Sirohi, J., "Performance and Loads of a Model Coaxial Rotor Part I : Wind Tunnel Testing," *72nd Annual Forum & Technology Display*, AHS International Inc., West Palm Beach, May 2016.

[42] Feil, R., Rinker, M., and Hajek, M., "Flight Testing of a Coaxial Ultralight Rotorcraft," *73rd Annual Forum Proceedings*, AHS International Inc., Fort Worth, Texas, May 2017, pp. 1–14.

[43] Feil, R., Eble, D., and Hajek, M., "Comprehensive Analysis of a Coaxial Ultralight Rotorcraft and Validation with Full-Scale Flight-Test Data," *Journal of the American Helicopter Society*, Vol. 63, 2018, pp. 042004–1–12. https://doi.org/10.4050/JAHS.63.042004.

[44] Cheney, M. C., "The ABC helicopter," *Journal of the American Helicopter Society*, Vol. 14, No. 4, 1969, pp. 10–19.

[45] Felker III, F. F., "Performance and Loads Data from a Wind Tunnel Test of a Full-Scale, Coaxial, Hingeless Rotor Helicopter," *NASA TM 81329*, Aeromechanics Laboratory, AVRADCOM Research and Technology, Ames Research Center, Moffett Field, California, October 1981.

[46] Bagai, A., "Aerodynamic Design of the X2 Technology Demonstrator™ Main Rotor Blade," *American Helicopter Society 64th Annual Forum*, AHS International Inc., Montreal, Canada, April-May 2008.

[47] Blackwell, R., and Millott, T., "Dynamics Design Characteristics of the Sikorsky X2 Technology™ Demonstrator Aircraft," *American Helicopter Society 64th Annual Forum*, AHS International Inc., Montreal, Canada, April-May 2008.

[48] Walsh, D., Weiner, S., Bagai, A., Lawerence, T., and Blackwell, R., "Development Testing of the Sikorsky X2 Technology Demonstrator," *65th Annual Forum Proceedings*, AHS International Inc., Grapevine, Texas, May 2009.

[49] Walsh, D., Weiner, S., Arifian, K., Lawrence, T., Wilson, M., Millott, T., and Blackwell, R., "High Airspeed Testing of the Sikorsky X2 Technology™ Demonstrator," *American Helicopter Society 67th Annual Forum*, AHS International Inc., Virginia Beach, Virginia, May 2011.

[50] Bowles, P. O., Geiger, D., Botros, B. B., Matalanis, C. G., , Min, B.-y., and Wake, B. E., "Experimental Investigation of Passive and Active Flow Control for X2 Technology ™ Hub and Fuselage Drag Reduction," *72nd Annual Forum & Technology Display*, AHS International Inc., West Palm Beach, Florida, May 2016, pp. 1–15.

[51] Lorber, P. F., Law, G. K., and Neill, J. J. O., "Overview of S-97 Raider™ Scale Model Tests," *72nd Annual Forum & Technology Display*, AHS International Inc., West Palm Beach, Florida, May 2016.

[52] Lorber, P. F., Bowles, P., Fox, E., Wang, Z. K., Hein, B., and Mayrides, B., "Wind Tunnel Testing for the SB>1 Defiant Joint Multi-Role Technology Demonstrator," *73rd Annual Forum & Technology Display*, AHS International Inc., Fort Worth, Texas, May 2017, pp. 1–18.

[53] Newman, J., Forster, W., Gatley, C., Pinney, T. R., Kinlan, J., and Saha, A. B., "SB > 1 Defiant™ Joint Multi-Role Technology Demonstrator: The way forward for rotorcraft manufacturing," *73rd Annual Forum & Technology Display*, AHS International Inc., Fort Worth, Texas, May 2017.

[54] Tuozzo, N., Fox, E., Eller, E., Mayrides, B., Zientek, T. A., Lorber, P., Narducci, R. P., and Sproul, T., "Analytic tool correlation status for the Joint Multi-Role Technology Demonstrator Program," *73rd Annual Forum & Technology Display*, AHS International Inc., Fort Worth, Texas, May 2017.

[55] McCarthy, D. K., Solari, D., Toni, D., Maack, J., and Spies, M., "Joint multi-role technology demonstrator fuselage proof test," *74th Annual Forum & Technology Display*, AHS International Inc., Phoenix, Arizona, May 2018.

[56] Bowles, P. O., Matalanis, C., Battisti, M., Min, B. Y., Wake, B. E., Tuozzo, N., and Lorber, P. F., "Full-configuration CFD analysis of the S-97 RAIDER™," *75th Annual Forum & Technology Display*, Vertical Flight Society, Philadelphia, Pennsylvania, May 2019, pp. 1–12.

[57] Gessow, A., and Myers Jr., G. C., *Aerodynamics of the Helicopter*, College Park press, 1985.

[58] Johnson, W., *Helicopter Theory*, Princeton University Press, New Jersey, NJ, 1980.

[59] Leishman, J. G., and Ananthan, S., "Aerodynamic Optimization of a Coaxial Proprotor," *American Helicopter Society 62nd Annual Forum*, AHS International Inc., Phoenix, Arizona, May 2006.

[60] Leishman, J. G., and Syal, M., "Figure of Merit Definition for Coaxial Rotors," *Journal of the American Helicopter Society*, Vol. 53, No. 3, 2008, pp. 290–300. https://doi.org/10.4050/JAHS.53.290.

[61] Leishman, J. G., and Ananthan, S., "An Optimum Coaxial Rotor System for Axial Flight," *Journal of the American Helicopter Society*, Vol. 53, No. 4, 2008, pp. 366–381. https://doi.org/10.4050/JAHS.53.366.

[62] Rand, O., and Khromov, V., "Aerodynamic Optimization of Coaxial Rotor in Hover and Axial Flight," *27th International Congress of the Aeronautical Sciences*, Nice, France, September 2010.

[63] Giovanetti, E. B., Hall, K. C., and Francis, J., "Axisymmetric Potential Flow Model of Single or Coaxial Actuator Disks," *72nd Annual Forum & Technology Display*, AHS International Inc., West Palm Beach, May 2016.

[64] Kong, Y.-b., Prasad, J. V. R., and Peters, D. A., "Development of a Finite State Dynamic Inflow Model for Coaxial Rotor using Analytical Methods School of Aerospace Engineering," *73rd Annual Forum & Technology Display*, AHS International Inc., Fort Worth, Texas, May 2017.

[65] Rand, O., and Khromov, V., "Parametric Study of Dynamic Inflow for Single and Coaxial Rotor Systems," *Journal of the American Helicopter Society*, Vol. 63, No. 4, 2018, pp. 1–14. https://doi.org/10.4050/JAHS.63.042007.

[66] Guner, F., Kong, Y. B., Prasad, J. V., Peters, D., and He, C., "Development of finite state inflow models for multi-rotor configurations using analytical approach," *74th Annual Forum & Technology Display*, AHS International Inc., Phoenix, Arizona, May 2018.

[67] Seidel, C., and Peters, D., "Simple inflow and structural dynamics of a coaxial rotor with time delays and adjoint variables," *75th Annual Forum & Technology Display*, Vertical Flight Society, May 2019, pp. 1–21.

[68] Kong, Y.-b., Prasad, J. V. R., Sankar, L. N., and Kim, J., "Finite State Coaxial Rotor Inflow Model Improvements via System Identification," *72nd Annual Forum & Technology Display*, AHS International Inc., West Palm Beach, May 2016.

[69] Hersey, S., Celi, R., Juhasz, O., and Tischler, M. B., "Accurate state-space inflow modeling for flight dynamics and control of a coaxial-pusher rotorcraft," *74th Annual Forum & Technology Display*, AHS International Inc., Phoenix, Arizona, May 2018.

[70] Zhao, J., and He, C., "Real-Time Simulation of Coaxial Rotor Configurations with Combined Finite State Dynamic Wake and VPM," *American Helicopter Society 70th Annual Forum*, AHS International Inc., Montreal, Canada, May 2014.

[71] Zhao, J., and He, C., "A Finite State Dynamic Wake Model Enhanced with Vortex Particle Method - Derived Modeling Parameters for Coaxial Rotor Simulation and Analysis," *Journal of the American Helicopter Society*, Vol. 61, No. 2, 2016, pp. 1–9. https://doi.org/10.4050/JAHS.61.022011.

[72] He, C., Syal, M., Tischler, M. B., and Juhasz, O., "State-Space Inflow Model Identification from Viscous Vortex Particle Method for Advanced Rotorcraft Configurations," *73rd Annual Forum & Technology Display*, AHS International Inc., Fort Worth, Texas, May 2017.

[73] Chen, P. W., Sankar, L. N., Prasad, J. V., Schatzman, N. L., and Rajagopalan, R. G., "Extraction of dynamic inflow models for coaxial and tandem rotors from CFD simulations," *75th Annual Forum & Technology Display*, Vertical Flight Society, Philadelphia, Pennsylvania, May 2019.

[74] Nagashima, T., and Nakanishi, K., "Optimum Performance and Wake Geometry of a Co-axial Rotor in Hover," *Vertica*, Vol. 7, No. 3, 1983, pp. 225–239.

[75] Bagai, A., and Leishman, J. G., "Free-Wake Analysis of Tandem, Tilt-Rotor and Coaxial Rotor Configurations," *Journal of the American Helicopter Society*, Vol. 41, No. 3, 1996, pp. 196–207. https://doi.org/10.4050/JAHS.41.196.

[76] Wachspress, D. A., and Quackenbush, T. R., "Impact of Rotor Design on Coaxial Rotor Performance, Wake Geometry and Noise," *62nd Annual Forum Proceedings*, Vol. 62, AHS International Inc., Phoenix, Arizona, May 2006.

[77] Lee, J., Yee, K., and Oh, S., "Numerical Investigation of Dual Rotors Using a Time-Marching Free-Wake Method," *American Helicopter Society 64th Annual Forum*, AHS International Inc., Montreal, Canada, April-May 2008.

[78] Lim, J. W., McAlister, K. W., and Johnson, W., "Hover Performance Correlation for Full Scale and Model Scale Coaxial Rotors," *Journal of the American Helicopter Society*, Vol. 54, No. 3, 2009, p. 32005.

[79] Spalart, P. R., "Vortex methods for separated flows," Tech. Rep. 100068, NASA Ames Research Center, Moffett Field, California, June 1988.

[80] Eldredge, J. D., and Jones, A. R., "Leading-Edge Vortices: Mechanics and Modeling," *Annual Review of Fluid Mechanics*, Vol. 51, No. 1, 2018, pp. 75–104. https://doi.org/10.1146/annurev-fluid-010518-040334.

[81] Hockney, R. W., and Eastwood, J. W., *Computer Simulation using Particles*, CRC Press, 1988.

[82] Cantaloube, B., and Huberson, S., "A New Approach Using Vortex Point Method For Prediction Of Rotor Performance In Hover And Forward Flight," *Ninth European Rotorcraft Forum*, ONERA, Stresa, Italy, September 1983.

[83] Teixeira, P. C., and Cesnik, C. E., "Propeller Effects on the Response of High-Altitude Long-Endurance Aircraft," *AIAA Journal*, 2019, pp. 1–15. https://doi.org/10.2514/1.J057575.

[84] Teixeira, P. C., and Cesnik, C., "Propeller influence on the aeroelastic stability of High Altitude Long Endurance aircraft," *The Aeronautical Journal*, Vol. 124, No. 1275, 2020, pp. 703–730. https://doi.org/10.1017/aer.2019.165.

[85] Alvarez, E. J., and Ning, A., "Development of a Vortex Particle Code for the Modeling of Wake Interaction in Distributed Propulsion," *2018 Applied Aerodynamics Conference*, American Institute of Aeronautics and Astronautics, Atlanta, Georgia, June 2018. https://doi.org/10.2514/6.2018-3646.

[86] Winckelmans, G. S., and Leonard, A., "Contributions to vortex particle methods for the computation of three-dimensional incompressible unsteady flows," *Journal of Computational Physics*, Vol. 109, No. 2, 1993, pp. 247–273. https://doi.org/10.1006/jcph.1993.1216.

[87] Saffman, P. G., *Vortex dynamics*, Cambridge University Press, 1992.

[88] Cottet, G.-H., and Koumoutsakos, P. D., *Vortex Methods: Theory and Practice*, Cambridge University Press, Cambridge, UK, 2000.

[89] Lee, D. J., and Na, S. U., "Numerical simulations of wake structure generated by rotating blades using a time marching, free vortex blob method," *European Journal of Mechanics - B/Fluids*, Vol. 18, No. 1, 1999, pp. 147–159. https://doi.org/10.1016/S0997-7546(99)80011-9.

[90] Opoku, D. G., Triantos, D. G., Nitzsche, F., and Voutsinas, S. G., "Rotorcraft Aerodynamic and Aeroacoustic Modelling Using Vortex Particle Methods," *ICAS 2002 Congress*, Toronto, Canada, September 2002, pp. 299.1–299.11.

[91] Cesnik, C., Opoku, D., Nitzsche, F., and Cheng, T., "Active twist rotor blade modelling using particle-wake aerodynamics and geometrically exact beam structural dynamics," *Journal of Fluids and Structures*, Vol. 19, No. 5, 2004, pp. 651 – 668. https://doi.org/10.1016/j.jfluidstructs.2004.01.007.

[92] Voutsinas, S. G., "Vortex Methods in Aeronautics: How to make things work," *International Journal of Computational Fluid Dynamics*, Vol. 20, No. 1, 2006, pp. 3–18. https://doi.org/10.1080/10618560600566059.

[93] He, C., and Zhao, J., "Modeling rotor wake dynamics with viscous vortex particle method," *AIAA Journal*, Vol. 47, No. 4, 2009, pp. 902–915. https://doi.org/10.2514/1.36466.

[94] Zhao, J., and He, C., "A Viscous Vortex Particle Model for Rotor Wake and Interference Analysis," *Journal of the American Helicopter Society*, Vol. 55, No. 1, 2010, p. 12007. https://doi.org/10.4050/JAHS.55.012007.

[95] Rajmohan, N., Zhao, J., and He, C., "A Coupled Vortex Particle / CFD Methodology for Studying Coaxial Rotor Configurations," *Fifth Decennial AHS Aeromechanics Specialists' Conference*, San Francisco, California, January 2014.

[96] He, C., and Rajmohan, N., "Modeling the Aerodynamic Interaction of Multiple Rotor Vehicles and Compound Rotorcraft with Viscous Vortex Particle Method," *72nd Annual Forum & Technology Display*, AHS International Inc., West Palm Beach, Florida, May 2016.

[97] Tan, J., Sun, Y., and Barakos, G. N., "Unsteady loads for coaxial rotors in forward flight computed using a vortex particle method," *The Aeronautical Journal*, Vol. 122, No. 1251, 2018, pp. 693–714. https://doi.org/10.1017/aer.2018.8.

[98] Passe, B. J., Sridharan, A., and Baeder, J. D., "Computational Investigation of Coaxial Rotor Interactional Aerodynamics in Steady Forward Flight," *33rd AIAA Applied Aerodynamics Conference*, American Institute of Aeronautics and Astronautics, Reston, Virginia, June 2015, pp. 1–29. https://doi.org/10.2514/6.2015-2883.

[99] Lakshminarayan, V. K., and Baeder, J. D., "High-Resolution Computational Investigation of Trimmed Coaxial Rotor Aerodynamics in Hover," *Journal of the American Helicopter Society*, Vol. 54, No. 4, 2009, p. 42008. https://doi.org/10.4050/JAHS.54.042008.

[100] Egolf, T. A., Reed, E., Rajmohan, N., and Sankar, L., "A Hybrid CFD Method for Coaxial Rotor Performance Prediction in Forward Flight," *AHS Specialist's Conference on Aeromechanics*, AHS International Inc., San Francisco, California, January 2010.

[101] Heyong, X. U., and Zhengyin, Y. E., "Numerical Simulation of Unsteady Flow around Forward Flight Helicopter with Coaxial Rotors," *Chinese Journal of Aeronautics*, Vol. 24, No. 1, 2011, pp. 1–7.

[102] Singh, R., Kang, H., and Sirohi, J., "Computational Investigations of Transient Loads and Blade Deformations on Coaxial Rotor Systems," *33rd AIAA Applied Aerodynamics Conference*, AIAA Aviation, AIAA Paper No. 2015-2884, Dallas, Texas, June 2015.

[103] Juhasz, O., Syal, M., Celi, R., Khromov, V., Rand, O., Ruzicka, G. G. C., and Strawn, R. R. C., "Comparison of Three Coaxial Aerodynamic Prediction Methods Including Validation with Model Test Data," *Journal of the American Helicopter Society*, Vol. 59, No. 3, 2014, p. 032006. https://doi.org/10.4050/JAHS.59.032006.

[104] Bhagwat, M. J., and Leishman, J. G., "Rotor Aerodynamics during Maneuvering Flight using a Time-Accurate Free-Vortex Wake," *Journal of the American Helicopter Society*, Vol. 48, No. 3, 2003, pp. 143–158. https://doi.org/10.4050/JAHS.48.143.

[105] Barbely, N. L., Field, M., Komerath, N. M., and Novak, L. A., "A Study of Coaxial Rotor Performance and Flow Field Characteristics," *Technical Meeting on Aeromechanics Design for Vertical Lift*, AHS International Inc., San Francisco, California, January 2016.

[106] Barbely, N. L., and Komerath, N. M., "Compressible 2D Flowfield Interaction of Two Contra-Rotating Blades," *Proceedings of the ASME 2016 International Mechanical Engineering Congress and Exposition*, American Society of Mechanical Engineers, Phoenix, Arizona, November 2016, pp. 1–15.

[107] Barbely, N. L., and Komerath, N. M., "Coaxial Rotor Flow Phenomena in Forward Flight," *SAE 2016 Aerospace Systems and Technology Conference*, SAE International, Hartford, Connecticut, September 2016, p. 10. https://doi.org/10.4271/2016-01-2009.

[108] Schatzman, N. L., Romander, E. A., and Komerath, N. M., "Modeling Shed Vorticity from Coaxial Blade Interactions," *2018 Fluid Dynamics Conference*, American Institute of Aeronautics and Astronautics, Reston, Virginia, June 2018. https://doi.org/10.2514/6.2018-2901.

[109] Passe, B., Sridharan, A., Baeder, J., and Singh, R., "Identification of Rotor-Fuselage Aerodynamic Interactions in a Compound Coaxial Helicopter using CFD-CSD Coupling," *AHS Technical Meeting on Aeromechanics Design for Vertical Lift*, AHS International Inc., San Francisco, California, January 2016.

[110] Yoon, S., Lee, H. C., and Pulliam, T. H., "Computational Study of Flow Interactions in Coaxial Rotors," *AHS Technical Meeting on Aeromechanics Design for Vertical Lift*, AHS International Inc., San Francisco, California, January 2016, pp. 1–8.

[111] Kim, J., and Sankar, L., "Application of a Navier-Stokes Free Wake Hybrid Methodology to the Harrington Coaxial Rotor," *AHS Technical Meeting on Aeromechanics Design for Vertical Lift*, San Francisco, California, January 2016, pp. 1–7.

[112] Kim, H. W., and Brown, R. E., "A Comparison of Coaxial and Conventional Rotor Performance," *Journal of the American Helicopter Society*, Vol. 55, No. 1, 2010, p. 012004. https://doi.org/10.4050/JAHS.55.012004.

[113] Klimchenko, V., Sridharan, A., and Baeder, J. D., "CFD/CSD Study of the Aerodynamic Interactions of a Coaxial Rotor in High-Speed Forward Flight," *35th AIAA Applied Aerodynamics Conference*, American Institute of Aeronautics and Astronautics, Reston, Virginia, June 2017. https://doi.org/10.2514/6.2017-4454.

[114] Klimchenko, V., and Baeder, J. D., "CFD/CSD Study of Interactional Aerodynamics of a Coaxial Compound Helicopter in High-Speed Forward Flight,"

AIAA Scitech 2020 Forum, American Institute of Aeronautics and Astronautics, Reston, Virginia, January 2020. https://doi.org/10.2514/6.2020-0304.

[115] Kim, H. W., and Brown, R. E., "Coaxial Rotor Performance and Wake Dynamics in Steady and Manoeuvring Flight," *62nd Annual Forum Proceedings*, AHS International Inc., Phoenix, Arizona, May 2006, pp. 1–21.

[116] Kim, H. W., Duraisamy, K., and Brown, R., "Aeroacoustics of a Coaxial Rotor in Level Flight," *American Helicopter Society 64th Annual Forum*, AHS International Inc., Montreal, Canada, April-May 2008.

[117] Kim, H. W., and Brown, R. E., "Modelling the Aerodynamics of Coaxial Helicopters - from an Isolated Rotor to a Complete Aircraft," *EKC2008 - Proceedings of the EU-Korea Conference on Science and Technology*, Heidelberg, Germany, August 2008.

[118] Kim, H. W., Kenyon, A. R., Duraisamy, K., and Brown, R. E., "Interactional Aerodynamics and Acoustics of a Propeller-Augmented Compound Coaxial Helicopter," *9th American Helicopter Society Aeromechanics Specialists' Meeting*, AHS International Inc., San Francisco, California, January 2008.

[119] Kim, H. W., Brown, R. E., Duraisamy, K., and Brown, R. E., "Effect of Rotor Stiffness and Lift Offset on the Aeroacoustics of a Coaxial Rotor in Level Flight," *65th American Helicopter Society Annual Forum*, AHS International Inc., Ft. Worth, Texas, May 2009.

[120] Kim, H. W., Kenyon, A. R., Duraisamy, K., and Brown, R. E., "Interactional Aerodynamics and Acoustics of a Hingeless Coaxial Helicopter with an Auxiliary Propeller in Forward Flight," *The Aeronautical Journal*, Vol. 113, No. 1140, 2009, pp. 65–78. https://doi.org/10.1017/S0001924000002797.

[121] Kim, H. W., and Brown, R. E., "A Rational Approach to Comparing the Performance of Coaxial and Conventional Rotors," *Journal of the American Helicopter Society*, Vol. 55, No. 1, 2010, p. 12003. https://doi.org/10.4050/JAHS.55.012003.

[122] Schmaus, J., and Chopra, I., "Aeromechanics for a High Advance Ratio Coaxial Helicopter," *American Helicopter Society 71st Annual Forum*, AHS International Inc., Virginia Beach, Virginia, May 2015.

[123] Schmaus, J., and Chopra, I., "Performance and Loads of a Model Coaxial Rotor Part II : Prediction Validations with Measurements," *72nd Annual Forum & Technology Display*, AHS International Inc., West Palm Beach, May 2016.

[124] Schmaus, J. H., and Chopra, I., "Aeromechanics of Rigid Coaxial Rotor Models for Wind-Tunnel Testing," *Journal of Aircraft*, Vol. 54, No. 4, 2017, pp. 1486–1497. https://doi.org/10.2514/1.c034157.

[125] Schmaus, J. H., "Aeromechanics of a High Speed Coaxial Helicopter Rotor," Ph.D. thesis, University of Maryland, College Park, 2017.

[126] Sunada, S., Sumino, H., Matsue, A., and Tokutake, H., "Analysis of Flapping Motion of Rotors of Small Coaxial Helicopter," *Transactions of the Japan Society for Aeronautical and Space Sciences*, Vol. 49, No. 164, 2006, pp. 101–108.

[127] Jacobellis, G., and Gandhi, F., "Investigation of Performance , Loads , and Vibrations of a Coaxial Helicopter in High Speed-Flight," *72nd Annual Forum & Technology Display*, AHS International Inc., West Palm Beach, May 2016.

[128] Kelly, M. E., and Brown, R. E., "Influence of Blade Aerodynamic Model on the Prediction of Helicopter High-Frequency Airloads," *Journal of Aircraft*, 2011. https://doi.org/10.2514/1.C031086.

[129] Rosen, A., and Friedmann, P. P., "Nonlinear Equations of Equilibrium for Elastic Helicopter or Wind Turbine Blades Undergoing Moderate Deformation," Tech. Rep. CR-159478, University of California at Los Angeles, Los Angeles, California, December 1978.

[130] Millott, T. A., "Vibration Reduction in Helicopter Rotors Using an Actively Controlled Partial Span Trailing Edge Flap Located on the Blade," Ph.D. thesis, University of California Los Angeles, 1994.

[131] Myrtle, T. F., "Development of an Improved Aeroelastic Model for the Investigation of Vibration Reduction in Helicopter Rotors Using Trailing Edge Flaps," Ph.D. thesis, University of California Los Angeles, 1998.

[132] Cribbs, R. C., "Vibration Reduction in Helicopters Using Active Control of Structural Response with Improved Aerodynamic Modeling," Ph.D. thesis, University of California Los Angeles, 1999.

[133] Patt, D. A., "Simultaneous BVI Noise and Vibration Reduction in Rotorcraft Using Actively-Controlled Flaps and Including Performance Considerations," Ph.D. thesis, University of Michigan, 2004.

[134] Padthe, A. K., "Active Vibration and Noise Alleviation in Rotorcraft Using Microflaps," Ph.D. thesis, University of Michigan, 2011.

[135] Sun, C.-T., *Mechanics of Aircraft Structures*, John Wiley & Sons, 2006.

[136] Holten, T. V., "Some notes on unsteady lifting-line theory," *Journal of Fluid Mechanics*, Vol. 77, No. 3, 1976, pp. 561–579. https://doi.org/10.1017/S0022112076002255.

[137] Johnson, W., "Airloads, wakes, and aeroelasticity," *NASA Contractor Report 177551*, Johnson Aeronautics, Palo Alto, California, 1990.

[138] Katz, J., and Plotkin, A., *Low-speed aerodynamics*, Cambridge University Press, 2001.

[139] Drela, M., *Flight vehicle aerodynamics*, MIT press, 2014.

[140] Singh, P., and Friedmann, P. P., "Application of Vortex Methods to Coaxial Rotor Wake and Load Calculations in Hover," *Journal of Aircraft*, Vol. 55, No. 1, 2018, pp. 373–381. https://doi.org/10.2514/1.C034520.

[141] Singh, P., and Friedmann, P. P., "A Computational Fluid Dynamics–Based Viscous Vortex Particle Method for Coaxial Rotor Interaction Calculations in Hover," *Journal of the American Helicopter Society*, Vol. 63, No. 4, October 2018, pp. 1–13. https://doi.org/10.4050/JAHS.63.042002.

[142] Tan, J., and Wang, H., "Highly Efficient Unsteady Panel Time-Marching Free Wake for Aerodynamics of Rotorcraft," *Journal of Aircraft*, Vol. 51, No. 1, 2014, pp. 54–61. https://doi.org/10.2514/1.C031807.

[143] Tan, J. F., and Wang, H. W., "Simulating unsteady aerodynamics of helicopter rotor with panel/viscous vortex particle method," *Aerospace Science and Technology*, Vol. 30, No. 1, 2013, pp. 255–268. https://doi.org/10.1016/j.ast.2013.08.010.

[144] Friedmann, P. P., "Arbitrary motion unsteady aerodynamics and its application to rotary-wing aeroelasticity," *Journal of Fluids and Structures*, Vol. 1, No. 1, 1987, pp. 71–93. https://doi.org/10.1016/S0889-9746(87)90194-0.

[145] Liu, L., Padthe, A. K., Friedmann, P. P., Quon, E., and Smith, M. J., "Unsteady Aerodynamics of an Airfoil/Flap Combination on a Helicopter Rotor Using Computational Fluid Dynamics and Approximate Methods," *Journal of the American Helicopter Society*, Vol. 56, No. 3, 2011, pp. 1–13. https://doi.org/10.4050/JAHS.56.032003.

[146] Bisplinghoff, R. L., Ashley, H., and Halfman, R. L., *Aeroelasticity*, Courier Corporation, 2013.

[147] Myrtle, T. F., and Friedmann, P. P., "Application of a new compressible time domain aerodynamic model to vibration reduction in helicopters using an actively controlled flap," *Journal of the American Helicopter Society*, Vol. 46, No. 1, 2001, pp. 32–43. https://doi.org/10.4050/JAHS.46.32.

[148] Liu, L., "BVI Induced Vibration and Noise Alleviation by Active and Passive Approaches," Ph.D. thesis, University of Michigan, 2005.

[149] Patt, D., Liu, L., and Friedmann, P. P., "Rotorcraft Vibration Reduction and Noise Prediction Using a Unified Aeroelastic Response Simulation," *Journal of the American Helicopter Society*, Vol. 50, No. 1, 2005, pp. 95–106. https://doi.org/10.4050/1.3092846.

[150] Glaz, B., "Active/Passive Optimization of Helicopter Rotor Blades for Improved Vibration, Noise, and Performance Characteristics," Ph.D. thesis, University of Michigan, 2008.

[151] Roger, K. L., *Airplane Math Modeling Methods for Active Control Design*, AGARD-CP-228, April 1997.

[152] Venkatesan, C., and Friedmann, P., "New approach to finite-state modeling of unsteady aerodynamics," *AIAA Journal*, Vol. 24, No. 12, 1986, pp. 1889–1897. https://doi.org/10.2514/3.9545.

[153] Patt, D., Liu, L., and Friedmann, P. P., "Simultaneous Vibration and Noise Reduction in Rotorcraft Using Aeroelastic Simulation," *Journal of the American Helicopter Society*, Vol. 51, No. 2, 2006, pp. 127–140. https://doi.org/10.4050/JAHS.51.127.

[154] Liu, L., Friedmann, P. P., Kim, I., and Bernstein, D. S., "Rotor Performance Enhancement and Vibration Reduction in Presence of Dynamic Stall Using Actively Controlled Flaps," *Journal of the American Helicopter Society*, Vol. 53, No. 4, 2008, pp. 338–350. https://doi.org/10.4050/JAHS.53.338.

[155] Friedmann, P. P., "On-Blade Control of Rotor Vibration, Noise, and Performance: Just Around the Corner? The 33rd Alexander Nikolsky Honorary Lecture," *Journal of the American Helicopter Society*, Vol. 59, No. 4, 2014, pp. 1–37. https://doi.org/10.4050/JAHS.59.041001.

[156] Chakravarthy, S., Peroomian, O., Goldberg, U., and Palaniswamy, S., "The CFD++ computational fluid dynamics software suite," *AIAA and SAE, 1998 World Aviation Conference*, American Institute of Aeronautics and Astronautics, Anaheim, California, September 1998. https://doi.org/10.2514/6.1998-5564.

[157] Gough, B., *GNU scientific library reference manual*, Network Theory Ltd., 2009.

[158] Harris, C. D., "Two-Dimensional Aerodynamic Characteristics of the NACA0012 Airfoil in the Langley 8-Foot Transonic Pressure Tunnel," *NASA Technical Memorandum 81927*, Hampton, Virginia, April 1981.

[159] Theodorsen, T., "General Theory of Aerodynamic Instability and the Mechanism of Flutter," *NACA Report 496*, National Advisory Committee for Aeronautics, 1935.

[160] Greenberg, J. M., "Airfoil in Sinusoidal Motion in a Pulsating Stream," *NACA TN 1326*, Langley Memorial Aeronautical Laboratory, Langley Field, Virginia, 1947.

[161] Ladson, C. L., "Effects of Independent Variation of Mach and Reynolds Numbers on the Low-Speed Aerodynamic Characteristics of the NACA 0012 Airfoil

Section," *NASA TM 4074*, Langley Research Center, Hampton, Virginia, October 1988.

[162] Petot, D., "Differential Equation Modeling of Dynamic Stall," *La Recherche Aerospatiale*, Vol. 1989, No. 5, 1989, pp. 59–72.

[163] Leishman, J. G., and Beddoes, T. S., "A semi-empirical model for dynamic stall," *Journal of the American Helicopter Society*, Vol. 34, No. 1, 1986, pp. 3–17. https://doi.org/10.4050/JAHS.34.3.

[164] Carr, L. W., McAlister, K. W., and McCroskey, W. J., "Analysis of the development of dynamic stall based on oscillating airfoil experiments," *NASA Technical Note D-8382*, January 1977, pp. 1–99.

[165] Johnson, W., "Rotorcraft Aerodynamics Models for a Comprehensive Analysis," *54th Annual Forum Proceedings*, American Helicopter Society, Washington, D.C., May 1998.

[166] Jain, R. K., Yeo, H., Ho, J. C., and Bhagwat, M., "An Assessment of RCAS Performance Prediction for Conventional and Advanced Rotor Configurations," *Journal of the American Helicopter Society*, Vol. 61, No. 4, 2016, pp. 1–12. https://doi.org/10.4050/JAHS.61.042005.

[167] Depailler, G., and Friedmann, P. P., "Reduction of vibrations due to dynamic stall in helicopters using an actively controlled flap," *Collection of Technical Papers - AIAA/ASME/ASCE/AHS/ASC Structures, Structural Dynamics and Materials Conference*, Vol. 3, April 2002, pp. 1826–1839. https://doi.org/10.2514/6.2002-1431.

[168] Smith, M. J., Liggett, N. D., and G. Koukol, B. C., "Aerodynamics of Airfoils at High and Reverse Angles of Attack," *Journal of Aircraft*, Vol. 48, No. 6, 2011, pp. 2012–2023. https://doi.org/10.2514/1.C031428.

[169] Lind, A. H., and Jones, A. R., "Vortex shedding from airfoils in reverse flow," *AIAA Journal*, Vol. 53, No. 9, 2015, pp. 2621–2633. https://doi.org/10.2514/1.J053764.

[170] Lind, A. H., and Jones, A. R., "Unsteady aerodynamics of reverse flow dynamic stall on an oscillating blade section," *Physics of Fluids*, Vol. 28, No. 7, 2016, p. 077102. https://doi.org/10.1063/1.4958334.

[171] Lind, A. H., Smith, L. R., Milluzzo, J. I., and Jones, A. R., "Reynolds Number Effects on Rotor Blade Sections in Reverse Flow," *Journal of Aircraft*, Vol. 53, No. 5, 2016, pp. 1248–1260. https://doi.org/10.2514/1.C033556.

[172] Powell, M. J., "An efficient method for finding the minimum of a function of several variables without calculating derivatives," *The Computer Journal*, Vol. 7, No. 2, 1964, pp. 155–162. https://doi.org/10.1093/comjnl/7.2.155.

[173] Sarpkaya, T., "Computational Methods With Vortices — The 1988 Freeman Scholar Lecture," *Journal of Fluids Engineering*, Vol. 111, No. 1, 1989, pp. 5–52. https://doi.org/10.1115/1.3243601.

[174] Wang, C., and Eldredge, J. D., "Low-order phenomenological modeling of leading-edge vortex formation," *Theoretical and Computational Fluid Dynamics*, Vol. 27, No. 5, 2013, pp. 577–598. https://doi.org/10.1007/s00162-012-0279-5.

[175] Katz, J., "A discrete vortex method for the non-steady separated flow over an airfoil," *Journal of Fluid Mechanics*, Vol. 102, 1981, p. 315–328. https://doi.org/10.1017/S0022112081002668.

[176] Eldredge, J. D., "Numerical simulation of the fluid dynamics of 2D rigid body motion with the vortex particle method," *Journal of Computational Physics*, Vol. 221, No. 2, 2007, pp. 626–648. https://doi.org/10.1016/j.jcp.2006.06.038.

[177] Gogulapati, A., Friedmann, P. P., Kheng, E., and Shyy, W., "Approximate Aeroelastic Modeling of Flapping Wings in Hover," *AIAA Journal*, Vol. 51, No. 3, 2013, pp. 567–583. https://doi.org/10.2514/1.J051801.

[178] Zanon, A., Giannattasio, P., and Ferreira, C. J. S., "Wake Modelling of a VAWT in dynamic stall: impact on the prediction of flow and induction fluids," *Wind Energy*, Vol. 18, No. 11, 2015, pp. 1855–1874. https://doi.org/10.1002/we.1793.

[179] Winckelmans, G. S., "Topics in vortex methods for the computation of three and two dimensional incompressible unsteady flows," Ph.D. thesis, California Institute of Technology, 1989.

[180] Zhao, J., and He, C., "Physics-Based Modeling of Viscous Ground Effect for Rotorcraft Applications," *Journal of the American Helicopter Society*, Vol. 60, No. 3, 2015, pp. 032006–1–13. https://doi.org/10.4050/JAHS.60.032006.

[181] Backaert, S., Chatelain, P., and Winckelmans, G., "Vortex particle-mesh with immersed lifting lines for aerospace and wind engineering," *Procedia IUTAM*, Vol. 18, 2015, pp. 1–7.

[182] Ploumhans, P., and Winckelmans, G., "Vortex Methods for High-Resolution Simulations of Viscous Flow Past Bluff Bodies of General Geometry," *Journal of Computational Physics*, Vol. 165, No. 2, 2000, pp. 354–406. https://doi.org/10.1006/jcph.2000.6614.

[183] Beale, J. T., and Majda, A., "Vortex methods. I. Convergence in three dimensions," *Mathematics of Computation*, Vol. 39, No. 159, 1982, pp. 1–1. https://doi.org/10.1090/S0025-5718-1982-0658212-5.

[184] Beale, J. T., and Majda, A., "Vortex Methods. II: Higher Order Accuracy in Two and Three Dimensions," *Mathematics of Computation*, Vol. 39, No. 159, 1982, p. 29. https://doi.org/10.2307/2007618.

[185] Anderson, C., and Greengard, C., "On Vortex Methods," *SIAM Journal on Numerical Analysis*, Vol. 22, No. 3, 1985, pp. 413–440. https://doi.org/10.1137/0722025.

[186] Choquin, J.-P., Cottet, G.-H., and Dautray, R., "Sur l'analyse d'une classe de méthodes de vortex tridimensionnelles (On the analysis of three dimensional vortex methods)," *Comptes rendus de l'Académie des sciences. Série 1, Mathématique*, Vol. 306, No. 17, 1988, pp. 739–742.

[187] Knio, O. M., and Ghoniem, A. F., "Numerical study of a three-dimensional vortex method," *Journal of Computational Physics*, Vol. 86, No. 1, 1990, pp. 75–106. https://doi.org/10.1016/0021-9991(90)90092-F.

[188] Singh, P., and Friedmann, P. P., "Modeling Coaxial Rotor Wakes in Forward Flight using Viscous Vortex Particle Method with Refined Blade Loads," *Technical Meeting on Aeromechanics Design for Transformative Vertical Flight*, AHS International Inc., San Francisco, California, January 2018, pp. 1–10.

[189] Singh, P., and Friedmann, P. P., "Dynamic stall modeling using Viscous Vortex Particle Method for Coaxial Rotors," *75th Annual Forum & Technology Display*, Philadelphia, Pennsylvania, May 2019, pp. 1–17.

[190] Riziotis, V. A., and Voutsinas, S. G., "Dynamic stall modelling on airfoils based on strong viscous–inviscid interaction coupling," *International Journal for Numerical Methods in Fluids*, Vol. 56, No. 2, 2008, pp. 185–208. https://doi.org/10.1002/fld.1525.

[191] Wachspress, D. A., Quackenbush, T. R., and Boschitsch, A. H., "Rotorcraft Interactional Aerodynamics with Fast Vortex/Fast Panel Methods," *Journal of the American Helicopter Society*, Vol. 48, No. 4, 2003, pp. 223–235. https://doi.org/doi:10.4050/JAHS.48.223.

[192] Zhao, J., He, C., Zhang, L., Zhao, H., and Hu, P., "Coupled Viscous Vortex Particle Method and Unstructured Computational Fluid Dynamics Solver for Rotorcraft Aerodynamic Interaction Analysis," *49th AIAA Aerospace Sciences Meeting including the New Horizons Forum & Aerospace Exposition*, Orlando, Florida, January 2011, pp. 1–13. https://doi.org/10.2514/6.2011-1121.

[193] Beatson, R., and Greengard, L., "A short course on fast multipole methods," *Wavelets, multilevel methods and elliptic PDEs*, Vol. 1, 1997, pp. 1–37.

[194] Greengard, L., and Rokhlin, V., "A new version of the Fast Multipole Method for the Laplace equation in three dimensions," *Acta Numerica*, Vol. 6, No. 1997, 1997, pp. 229–269. https://doi.org/10.1017/S0962492900002725.

[195] Greengard, L., and Strain, J., "The Fast Gauss Transform," *SIAM Journal on Scientific and Statistical Computing*, Vol. 12, No. 1, 1991, pp. 79–94. https://doi.org/10.1137/0912004.

[196] Greengard, L., and Sun, X., "A new version of the fast Gauss transform," *Documenta Mathematica*, Vol. 3, 1998, pp. 575–584.

[197] Spivak, M., Veerapaneni, S. K., and Greengard, L., "The Fast Generalized Gauss Transform," *SIAM Journal on Scientific Computing*, Vol. 32, No. 5, 2010, pp. 3092–3107. https://doi.org/10.1137/100790744.

[198] Abramowitz, M., and Stegun, I. A., *Handbook of mathematical functions with formulas, graphs, and mathematical tables*, Vol. 55, US Government printing office, 1948.

[199] Singh, R., Kang, H., Bhagwat, M. J., Cameron, C., and Sirohi, J., "Computational and Experimental Investigations of Coaxial Rotor Unsteady Loads," *54th AIAA Aerospace Sciences Meeting*, 2016, pp. 1–10. https://doi.org/10.2514/6.2016-1787.

[200] Jacobellis, G., Gandhi, F., and Floros, M., "A Physics-Based Approach to Trim Optimization of Coaxial Helicopters in High-Speed Flight," *AHS 71st Annual Forum*, American Helicopter Society International, Inc, Virginia Beach, Virginia, May 2015.

[201] Yeo, H., and Johnson, W., "Investigation of Maximum Blade Loading Capability of Lift-Offset Rotors," *Journal of the American Helicopter Society*, Vol. 59, No. 1, 2014, pp. 1–12. https://doi.org/10.4050/JAHS.59.012005.

[202] Cameron, C., Sirohi, J., Schmaus, J., and Chopra, I., "Performance and Loads of a Reduced-Scale Coaxial Counterrotating Rotor," *Journal of the American Helicopter Society*, Vol. 64, No. 4, 2019, pp. 1–15. https://doi.org/10.4050/JAHS.64.042003.

[203] Han, D., Wang, J., Smith, E. C., and Lesieutre, G. A., "Transient Loads Control of a Variable Speed Rotor During Lagwise Resonance Crossing," *AIAA Journal*, Vol. 51, No. 1, 2013, pp. 20–29. https://doi.org/10.2514/1.J050598.

[204] Torok, M. S., and Chopra, I., "Hingeless Rotor Aeroelastic Stability Analysis with Refined Aerodynamic Modeling," *Journal of the American Helicopter Society*, Vol. 36, No. 4, 1991, pp. 48–56. https://doi.org/10.4050/jahs.36.48.

[205] Klingloff, R. F., "Rigid Coaxial (ABC)^{TM} Rotor System Stability and Control Characteristics," *32nd Annual Forum*, American Helicopter Society, Washington, D.C., May 1976, pp. 1045–1–16.

[206] Burtsev, B. N., "Aeroelasticity of a Coaxial Helicopter Rotor," *17th European Rotorcraft Forum*, Deutschen Gesellschaft für Luft- und Raumfahrt, Berlin, Federal Republic of Germany, 1991.

[207] Friedmann, P. P., "Rotary-Wing Aeroelasticity: Current Status and Future Trends," *AIAA Journal*, Vol. 42, No. 10, 2004, pp. 1953–1972. https://doi.org/10.2514/1.9022.

[208] Kang, H., and Glaz, B., "Aeroelastic Stability Analysis of Stiff-in-plane Hingeless Rotors," *74th Annual Forum & Technology Display*, AHS International Inc., May 2018, pp. 1–9.

[209] Friedmann, P. P., and Kottapalli, S. B. R., "Coupled Flap-Lag-Torsional Dynamics of Hingeless Rotor Blades in Forward Flight," *Journal of the American Helicopter Society*, Vol. 27, No. 4, 1982, pp. 28–36. https://doi.org/10.4050/JAHS.27.28.

[210] Bousman, W. G., "An Experimental Investigation of the Effects of Aeroelastic Couplings on Aeromechanical Stability of a Hingeless Rotor Helicopter," *Journal of the American Helicopter Society*, Vol. 26, No. 1, 1981, pp. 46–54. https://doi.org/10.4050/JAHS.26.1.46.

[211] Friedmann, P. P., Hammond, C. E., and Woo, T.-H., "Efficient numerical treatment of periodic systems with application to stability problems," *International Journal for Numerical Methods in Engineering*, Vol. 11, No. 7, 1977, pp. 1117–1136. https://doi.org/10.1002/nme.1620110708.

[212] Friedmann, P. P., "Numerical Methods for the Treatment of Periodic Systems with Applications to Structural Dynamics and Helicopter Rotor Dynamics," *Computers & Structures*, Vol. 35, No. 4, 1990, pp. 329–347. https://doi.org/10.1016/0045-7949(90)90059-B.

[213] Mohan, R., and Gaonkar, G. H., "A unified assessment of fast Floquet, generalized Floquet, and periodic eigenvector methods for rotorcraft stability predictions," *Journal of the American Helicopter Society*, Vol. 58, No. 4, 2013. https://doi.org/10.4050/JAHS.58.042002.

[214] Peters, D. A., Lieb, S. M., and Ahaus, L. A., "Interpretation of Floquet eigenvalues and eigenvectors for periodic systems," *Journal of the American Helicopter Society*, Vol. 56, No. 3, 2011, pp. 1–11. https://doi.org/10.4050/JAHS.56.032001.

[215] Nagabhushanam, J., and Gaonkar, G. H., "Automatic Identification of Modal Damping from Floquet Analysis," *Journal of the American Helicopter Society*, Vol. 40, No. 2, 1995, pp. 39–42. https://doi.org/10.4050/JAHS.40.39.

[216] Sheel, T. K., and Obi, S., "High-performance computing techniques for vortex method calculations," *Theoretical and Computational Fluid Dynamics*, Vol. 24, No. 1-4, 2010, pp. 175–179. https://doi.org/10.1007/s00162-009-0149-y.

[217] Chandramowlishwaran, A., "The fast multipole method at exascale," Ph.D. thesis, Georgia Institute of Technology, 2013.

[218] Salmon, J. K., and Warren, M. S., "Fast Parallel Tree Codes for Gravitational and Fluid Dynamical N-Body Problems," *The International Journal of Supercomputer Applications and High Performance Computing*, Vol. 8, No. 2, 1994, pp. 129–142. https://doi.org/10.1177/109434209400800205.

[219] Lindsay, K., and Krasny, R., "A Particle Method and Adaptive Treecode for Vortex Sheet Motion in Three-Dimensional Flow," *Journal of Computational Physics*, Vol. 172, No. 2, 2001, pp. 879–907. https://doi.org/10.1006/JCPH.2001.6862.

[220] Vaughn, N., Wilson, L., and Krasny, R., "A GPU-Accelerated Barycentric Lagrange Treecode," *arXiv:2003.01836*, arXiv, eprint, March 2020.

[221] Mosher, M., and Peterson, R. L., "Acoustic measurements of a full-scale coaxial helicopter," *8th Aeroacoustics Conference*, American Institute of Aeronautics and Astronautics, Moffett Field, California, April 1983.

[222] Jia, Z., Lee, S., Sharma, K., and Brentner, K. S., "Aeroacoustic analysis of a lift-offset coaxial rotor using high-fidelity CFD-CSD loose coupling simulation," *74th Annual Forum & Technology Display*, AHS International Inc., Phoenix, Arizona, May 2018, pp. 1–15.

[223] Zhu, Z., Zhao, Q., Jing, S., Yuan, X., and Wang, B., "Analyses on aeroacoustic characteristics of coaxial rotor in forward flight," *74th Annual Forum & Technology Display*, AHS International Inc., Phoenix, Arizona, May 2018.

[224] Jia, Z., Lee, S., Sharma, K., and Brentner, K. S., "Effect of pitch attitude on the performance and acoustics of a lift-offset coaxial rotor based on high-fidelity CFD/CSD simulations," *75th Annual Forum & Technology Display*, Vertical Flight Society, Philadelphia, Pennsylvania, May 2019.

[225] Sharma, K., Brentner, K. S., Jia, Z., and Lee, S., "Aeroacoustic study of lift offset coaxial rotor using free wake analysis," *75th Annual Forum & Technology Display*, Vertical Flight Society, Philadelphia, Pennsylvania, May 2019.